5-14-2010

Comprehensive Modeling and Numerical Investigation of Entrained-Flow Coal Gasifiers

Armin Silaen
University of New Orleans

Comprehensive Modeling and Numerical Investigation of Entrained-Flow Coal Gasifiers

A Dissertation

Submitted to the Graduate Faculty of the
University of New Orleans
in partial fulfillment of the
requirements for the degree of

Doctor of Philosophy
in
Engineering and Applied Science

by

Armin Karen Silaen

B.S. University of New Orleans, 2002
M.S. University of New Orleans, 2004

May, 2010

ACKNOWLEDGEMENT

I would like to thank my advisor, Dr. Ting Wang, for his guidance and support while working under him while I pursued both my master's and doctorate degrees. None of this would be made possible without Dr. Ting Wang's hard work and dedication to his students and the University of New Orleans. I would also like to thank Dr. Kazim Akyuzlu, Dr. Martin Guillot, Dr. Carsie Hall, and Dr. Dongming Wei to serve in my dissertation committee.

I would like to acknowledge the support from the Louisiana Governor's Energy Initiative, administered by the Louisiana Board of Regents via the Clean Power and Energy Research Consortium (CPERC).

Furthermore, I would also like to thank my fellow students and researchers, Lei Zhao, Liang Wang, Jason Kent, and other from the Energy Conversion and Conservation Center (ECCC) for their help and support. Finally, I would like to thank all my family and friends for their constant support.

TABLE OF CONTENTS

LIST OF FIGURES

LIST OF TABLES

NOMENCLATURE

a	local speed of sound (m/s)
c	concentration (mass/volume, moles/volume)
c_p	heat capacity at constant pressure (J/kg-K)
c_v	heat capacity at constant volume (J/kg-K)
D	mass diffusion coefficient (m^2/s)
D_H	hydraulic diameter (m)
D_{ij}	mass diffusion coefficient (m^2/s)
D_t	turbulent diffusivity (m^2/s)
E	total energy (J)
g	gravitational acceleration (m/s^2)
G	incident radiation
Gr	Grashof number ($L^3.\rho^2.g.\beta.\Delta T/\mu^2$)
H	total enthalpy (W/m^2-K)
h	species enthalpy (W/m^2-K)
J	mass flux; diffusion flux (kg/m^2-s)
k	turbulence kinetic energy (m^2/s^2)
k	thermal conductivity (W/m-K)
m	mass (kg)
M_W	molecular weight (kg/kgmol)
M	Mach number
p	pressure (atm)
Pr	Prandtl number (ν/α)
q	heat flux
q_r	radiation heat flux
R	universal gas constant
Sc	Schmidt number (ν/D)
S_f	source term due to exchange of momentum
S_h	source term due to exchange of energy
S_m	source term due to exchange of mass
t	time (s)
T	temperature (K)
U	mean velocity (m/s)
X	mole fraction (dimensionless)
Y	mass fraction (dimensionless)

Greek letter

β	coefficient of thermal expansion (K^{-1})
ε	turbulence dissipation (m^2/s^3)
ε_w	wall emissivity
κ	von Karman constant
μ	dynamics viscosity (kg/m-s)
μ_k	turbulent viscosity (kg/m-s)
ν	kinematic viscosity (m^2/s)
ν'	stoichiometric coefficient of reactant

ν'' stoichiometric coefficient of product
ρ density (kg/m^3)
ρ_w wall reflectivity
σ Stefan-Boltzmann constant
σ_s scattering coefficient
τ stress tensor ($kg/m\text{-}s^2$)

Subscript
i index notation
j index notation

ABSTRACT

Numerical simulations of coal gasification process inside a generic 2-stage entrained-flow gasifier are carried out using the commercial CFD solver ANSYS/FLUENT. The 3-D Navier-Stokes equations and eight species transport equations are solved with three heterogeneous global reactions, three homogeneous reactions, and one thermal cracking equation of volatiles. Finite rates are used for the heterogeneous solid-gas reactions. Both finite rate and eddy-breakup combustion models are calculated for each homogeneous gas-gas reaction, and the smaller of the two rates is used. Lagrangian-Eulerian method is employed. The Eulerian method calculates the continuous phase while the Lagrangian method tracks each coal particle.

Fundamental study is carried out to investigate effects of five turbulence models (standard k-ε, k-ω, RSM, k-ω SST, and k-ε RNG) and four devolatilization models (Kobayashi, single rate, constant rate, and CPD) on gasification simulation. A study is also conducted to investigate the effects of different operation parameters on gasification process including coal mixture (dry vs. slurry), oxidant (oxygen-blown vs. air-blown), and different coal distributions between two stages. Finite-rate model and instantaneous gasification model are compared. It is revealed that the instantaneous gasification approach can provide an overall evaluation of relative changes of gasifier performance in terms of temperature, heating value, and gasification efficiency corresponding to parametric variations, but not adequately capture the local gasification process predicted by the finite rate model in most part of the gasifier.

Simulations are performed to help with design modifications of a small industrial demonstration entrained-flow gasifier. It is discovered that the benefit of opening the slag tap on the quench-type gasifier wider by allowing slag to move successfully without clogging is compromised by increased heat losses, reduced gasification performance, downgraded syngas heating value, and increased unburned volatiles. The investigation of heat transfer on fuel injectors shows that blunt tip fuel injector is less likely to fail compared to conical tip fuel injector because the maximum high temperature on the injector is scattered. Two concentric fuel/oxidant injections provide better fuel-oxidant mixing and higher syngas heating value than four separate fuel and oxidant injections.

Keywords: Gasification modeling, entrained-flow gasifier, clean coal technology, syngas production, multiphase flow.

CHAPTER ONE
INTRODUCTION

1.1 Background

Coal is the most abundant fossil fuel. Archeologists have found evidence that the Romans in England used coal in the 100-200 AD. The overwhelming need of energy to run the machinery during the Industrial Revolution pushed coal to become a dominant worldwide energy source. During the 1800's, steamships and steam-powered railroads, which used coal to fuel their boilers, became the leading modes of transportation.

During the Civil War, weapon factories began to use coal, and by 1875, coke replaced charcoal as the primary fuel for iron blast furnaces in steel factories. In 1880, coal was first used to generate electricity for homes and factories.

One quarter of the world's coal reserves are found in the United States. Energy content of those reserves exceeds the energy content of the world's known oil reserves. Coal is the United States' largest domestic energy resource, and coal generates more than 50 percents of the United States' electricity. At the current rates of use, United States' coal reserves are enough to last for 250 years. The dependence by the U.S. on coal as source of energy will continue as the Energy Information Administration projects a 26 percent increase in the United States' electricity demand from 2007 to 2030 with coal remaining as the main fuel source.

Unfortunately, coal is not a perfect fuel. Coal contains impurities such as nitrogen and sulfur. Burning coal will release these impurities (NO_x and SO_x) into the air, which can react with the air's water vapor and form "acid rain." In addition, as with any other carbon-based fuel, burning coal produces carbon dioxide. Carbon dioxide in the atmosphere can trap the earth's heat causing the "greenhouse effect" and changes the earth's climate.

Methods of using coal can be divided into (a) combustion, (b) pyrolysis, (c) liquefaction, and (d) gasification. In combustion, coal is directly burned to produce heat. In pyrolysis, coal is decomposed through heating, which releases volatile matter inside the coal leaving only carbon (char) and tar. In liquefaction, coal is converted into liquid fuel. In gasification, coal is converted into synthetic gas (syngas).

Gasification is a process that converts any carbon-based materials, such as coal, petcoke, biomass, or various wastes, into a synthetic gas (syngas) through an oxygen-limited reaction.

The clean syngas can be used as a fuel to produce electricity or valuable products such as chemicals, fertilizers, and transportation fuels. In contrast to the combustion process, which takes place in excess oxidant conditions, the gasification process takes place in substoichiometric conditions. Generally, the amount of O_2 used is only 35% or less of the amount required for complete combustion. The main differences between combustion and gasification are listed in Table 1.1.

Table 1.1 Comparison between combustion and gasification.

Combustion	**Gasification**
▪ Occurs in excess-oxidant conditions ▪ Releases heat (exothermic) ▪ Produces heat	▪ Occurs in oxidant-lean conditions ▪ Absorbs heat (endothermic) ▪ Produces sygas

A very efficient way to use the syngas as fuel for electricity generation is by employing the Integrated Gasification Combined Cycle (IGCC). A schematic of an IGCC system is presented in Figure 1.1. IGCC combines gas and steam turbine systems. The syngas produced by the gasifier is cleaned and used as a fuel for the gas turbine. The high pressure and hot gases produced in the combustor then expand through the gas turbine to drive the air compressor and an electric generator. The hot exhaust gases from the gas turbine are sent to a HRSG (Heat Recovery Steam Generator), producing steam that expands through a steam turbine to drive another electric generator.

Gasification has a lower environmental impact compared to traditional combustion technologies because:

(a) Syngas is cleaned before combustion, reducing air pollutants such as NO_x and SO_x.
(b) Gasification can recover available energy from low-value materials such as petcoke and municipal solid waste.
(c) The by-products of gasification (sulfur and slag) are nonhazardous and marketable.
(d) High efficiency/low CO_2 production.
(e) Carbon dioxide (CO_2) can be captured prior to syngas combustion, which is the least costly and most efficient way of capturing CO_2 from a fossil-fuel based power plant.

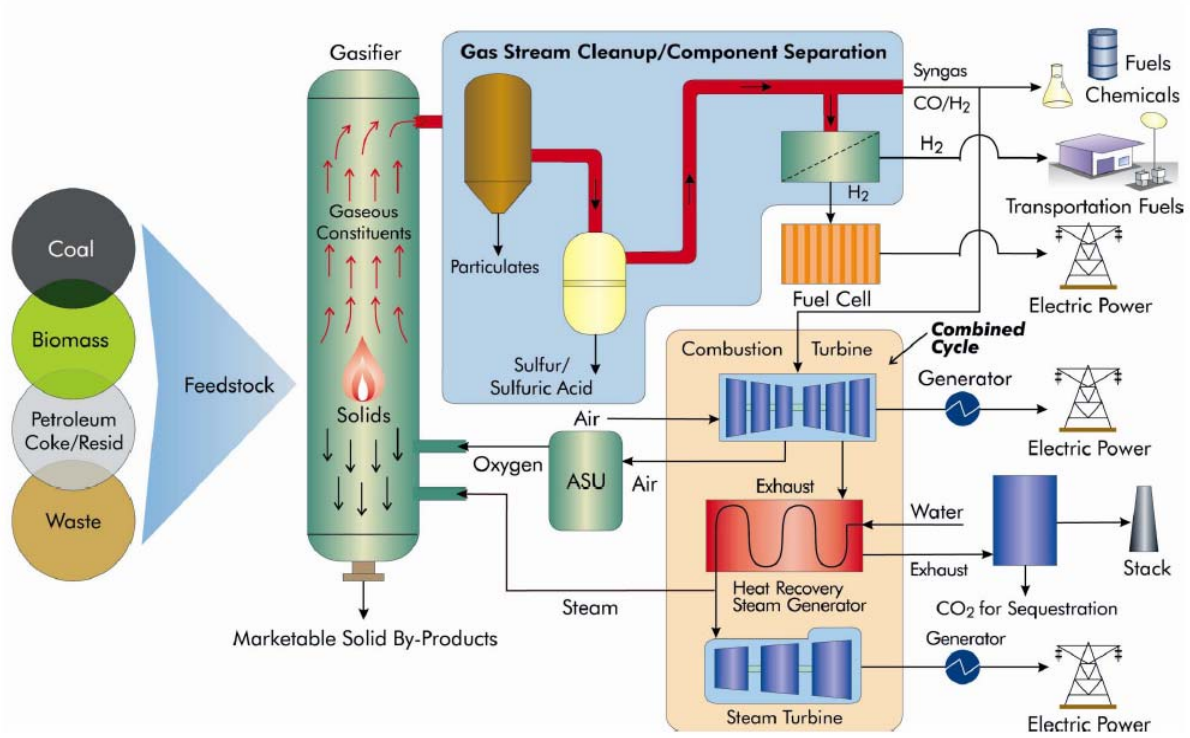

Figure 1.1 Schematic of an IGCC system (Source: National Energy Technology Laboratory).

1.2 Objectives

(a) There are a lot of parameters that affect the performance, efficiency, and reliability of an entrained-flow gasifier. The motivation of this study is to help improve the performance, efficiency, and reliability of entrained-flow gasifiers. A good understanding of the gasification process inside a gasifier is needed to help achieve these goals. An economical way to achieve this is through numerical modeling. The **objective** of this research is to perform a comprehensive numerical investigation of entrained-flow coal gasifiers with the specific goals of establishing a robust and reliable gasification computational model by:

- selecting appropriate global reaction equations
- examining and selecting appropriate reaction rate
- incorporating two-layer solid-gas heterogeneous reaction model
- investigating various turbulence and devolatilization models
- incorporating thermal cracking of volatiles

- incorporating droplet coalescence and break-up models

(b) Investigate the effect of various operating conditions on gasification performance including dry vs. slurry feed, oxygen vs. air blown, single vs. two stage, and different fuel injection angles.

(c) Use the gasification numerical model developed to help industry find ways to improve gasifier performance and reliability. Through a collaborative study with industry, the following items are studied:

- Fuel injection direction and location
- Fuel injector design
- Design of gasifier
- Syngas cooling method

1.3 Literature Review

1.3.1 History of Gasification

The gasification process has been used for hundreds of years, with the earliest practical gasification process being reported to have taken place in 1792. Murdoch, a Scottish engineer, pyrolyzed coal to produce gas that he then used to light his home. In 1812, the first gas company was established in London to produce gas from coal to light the Westminster Bridge. The first gas plant to manufacture syngas from coal was built in the United States in 1816 to light the streets of Baltimore. Soon, more gas plants followed in Boston and New York. By 1875, manufactured gas was being widely used for home lighting. More than 1,200 gas plants were in operation in the United States by the late 1920s as manufactured gas was used in domestic and industrial applications. During World War II, over 1 million air-blown gasifiers were in operation to generate synthetic gas from wood and charcoal to power vehicles and generate steam and electricity. However, the discovery of large quantities of low-cost natural gas after World War II put an end to the synthetic gas manufacturing industry. It wasn't until the 1960's and 1970's that the interest in gasification technologies was renewed.

1.3.2 Gasification Global Reactions

Coal gasification occurs when the coal is heated with limited oxygen and steam in a gasification reaction chamber. The main global reactions involved in a gasification process are as follows:

Heterogeneous reactions:

$C(s) + ½\ O_2 \rightarrow CO$	$\Delta H°_R$ = -110.5 MJ/kmol	(R1.1)
$C(s) + CO_2 \rightarrow 2CO$	$\Delta H°_R$ = +172.0 MJ/kmol (Gasification, Boudouard reaction)	(R1.2)
$C(s) + H_2O(g) \rightarrow CO + H_2$	$\Delta H°_R$ = +131.4 MJ/kmol (Gasification)	(R1.3)

Homogeneous reactions:

$CO + ½\ O_2 \rightarrow CO_2$	$\Delta H°_R$ = -283.1 MJ/kmol	(R1.4)
$CO + H_2O(g) \rightarrow CO + H_2$	$\Delta H°_R$ = -41.0 MJ/kmol (Water-shift)	(R1.5)
$CH_xO_y \rightarrow a\ CO + b\ H_2 + c\ CH_4$	(Volatile cracking)	(R1.6)
$CH_4 + ½\ O_2 \rightarrow CO + 2\ H_2$	$\Delta H°_R$ = -35.7MJ/kmol	(R1.7)

The gasification of char by CO_2 and H_2O, reactions (R1.2) and (R.1.3), respectively, are endothermic reactions. The endothermic two-step char combustion, reactions (R1.1) and (R1.4), are needed to supply the energy needed in the gasification reactions. The sythentic gas produced mainly consists of CO and H_2. Reaction (R1.6) is the thermal cracking of the volatiles (CH_xO_y). The volatiles released from the coal particles are thermally cracked into lighter gases. The volatile species for different coals varies according to the ultimate composition of the coal. For example, the volatile species for Indonesian coal is $CH_{2.121}O_{0.5855}$.

1.3.3 Types of Gasifiers

There are four main gasifier types: (a) fluidized-bed gasifier, (b) moving-bed gasifier, (c) entrained-flow gasifier, and (d) transport gasifier. Explanations of each type and its examples are presented below. The comparison of these gasifiers is summarized in Table 1.2.

1.3.3.1 Fluidized-Bed Gasifier

In a fluidized-bed gasifier, air or oxygen is injected upward at the bottom of solid fuel bed, suspending the fuel particles. Schematic of a fluidized-bed gasifier is presented in Figure 1.2. The size (6-10mm) and weight of the particles prevent them from blowing out. The fuel feed rate and the gasifier temperature are lower compared to those of entrained-flow gasifiers. The operating temperature of a fluidized-bed gasifier is around 1000°C (~1800°F), which is roughly only half of the operating temperature of a coal burner. This lower temperature has several advantages:

- Lower NO_x emission; the temperature is not hot enough to break apart the nitrogen molecules and cause the nitrogen atoms to join with oxygen atoms to form NO_x.
- No slag formation; the temperature is not hot enough to melt ash. It is suitable for coals of any rank (high or low ash content).
- Lower syngas temperature; that means cheaper syngas cooling system prior to gas clean up.

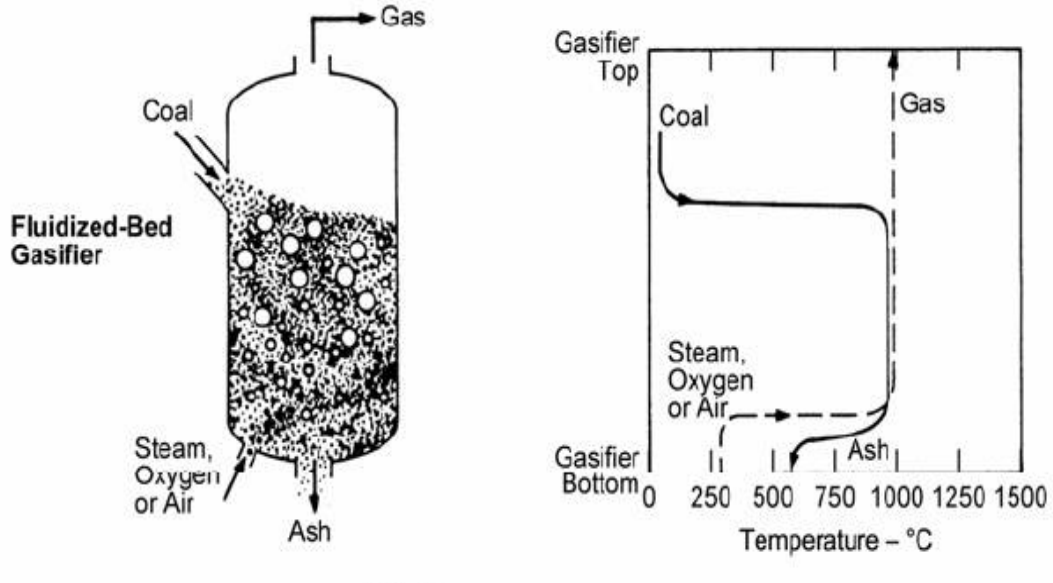

Figure 1.2 Schematic of fluidized-bed gasifier (Holt, 2004).

Fluidized-bed gasifiers require moderate supply of oxygen and steam. Examples of commercial fluidized-bed gasifier are:

(i) High Temperature Wrinkler (HTW)

HTW was developed by Rheinbraun in Germany to gasify lignites for the production of a reducing gas for iron ore. A schematic of an HTW gasifier is presented in Figure 1.3. The gasifier is a refractory-lined vessel equipped with water jacket. Coal is dropped into the fluidized bed that consists of particles, semi-coke, and coal. The gasifier is fluidized by the injection of air or oxygen/steam from the bottom. The temperature of the bed is kept at around 800°C, which is below the ash fusion temperature. An additional gasification gas is added at the freeboard to decompose undesirable byproducts formed during gasification. The operating pressure can vary from 1 to 3 MPa. The raw syngas exiting the top of gasifier is then passed through a cyclone to remove particulates and then cooled. Particulates recovered in the cyclone are recycled back into the gasifier.

HTW technology was successfully applied to produce methanol from lignites at Berrenrath, Germanybetween 1986 and 1997. The plant was shut down at the end of 1997 because the process was no longer considered economically viable. In 1989, a 140 ton/day plant was commission in Wesseling, Germany to supplement research and development of the HTW technology, including a study to find future applications for power generation through an Integrated Gasification Combined Cycle (IGCC) system. There is presently a project to build a 400MW IGCC plant in the Czech Republic using the HTW technology developed at the Wesseling plant.

(ii) Kellogg-Rust-Westinghouse (KRW)

A schematic of a KRW gasifier is shown in Figure 1.4. The fuel and oxidant enter the bottom of the gasifier through concentric high-velocity jets, ensuring thorough mixing of the fuel and oxidant and of the bed of char and limestone that collects in the gasifier. Upon entering the gasifier, the coal releases its volatiles which then immediately burns releasing heat needed for the gasification. The combusted volatiles form large bubbles that rise up to the center of the gasifier. This causes the char and the sorbent in the bed to move down the sides of the gasifier and back into the central jet. The char in the bed reacts with the steam, which is injected

together with the oxidant and also through multiple other injections on the bottom of the gasifier to form syngas. The ash particles formed are denser than the coal; thus they settle down to the bottom of the gasifier and are then removed. Any particles that escaped the gasifier through the exit at the top is recaptured in the cyclone gas clean-up system and is injected back into the gasifier.

From 1997 through 2000, a 965MW Integrated Gasification Combined Cycle (IGCC) demonstration plant using the KRW technology was carried out in Pinon Pine, Nevada by Sierra Pacific Resources and was sponsored by the US Department of Energy as part of its Clean Coal Technology Program. It was the only large-scale, coal-based IGCC plant using the KRW technology. Unfortunately, the plant faced numerous problems. It had 18 gasifier start-ups and all of them failed due to equipment design.

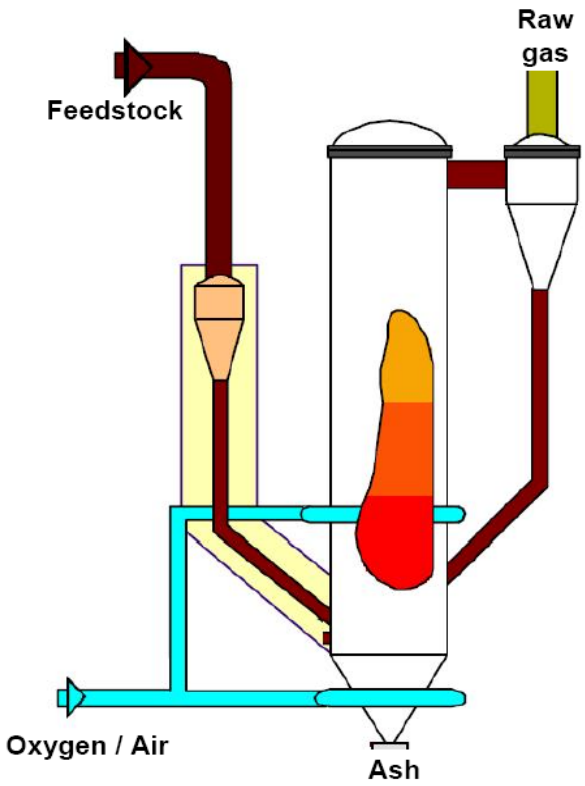

Figure 1.3 High Temperature Wrinkler (HTW) Gasifier.

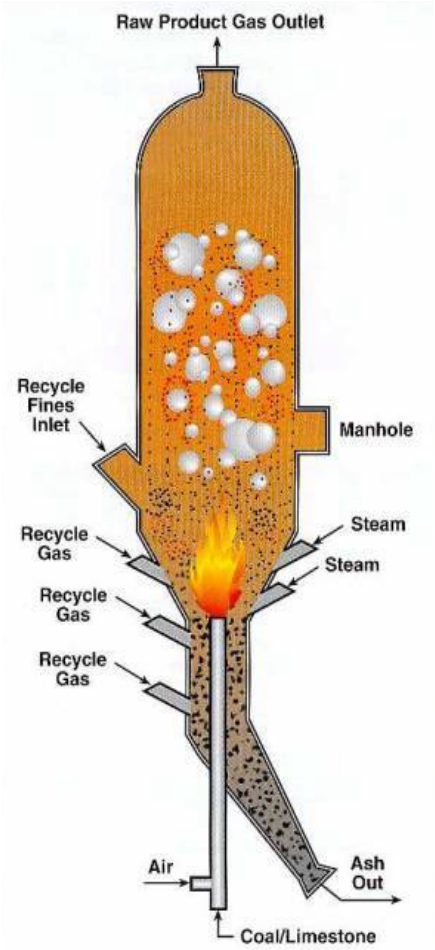

Figure 1.4 Schematic of a KRW gasifier.

1.3.3.2 Moving-Bed Gasifier

In a moving-bed gasifier, steam and air/oxygen flows through a fixed bed of solid fuel particles as shown in Figure 1.5. Fresh coal is fed from the top, while air or oxygen is injected from the bottom. This configuration, the steam and oxygen/air feed is counter-current to the coal feed, is referred to as "updraft" or counter-current moving-bed gasifier. Coal moves downward slowly. Its residence time can reach 1 hour. The syngas exits from the upper part of the gasifier. Ash and unreacted char are removed from the bottom. The depth of coal bed is kept constant by adding fresh coal from the top. Another configuration is the "downdraft" or co-current moving-bed gasifier, where steam and air/oxygen are fed from the top, co-current to the coal feed.

A counter-current moving-bed gasifier can be divided into four zones (from top to bottom): (i) the drying/preheating zone, (ii) the devolatilization zone, (iii) the gasification zone, and (iv) the combustion zone. The coal in the top zone is dried/preheated by hot gas that is

flowing from the bottom. The coal moves down to the devolatilization zone where heat from the hot gas drives volatiles out of coal particles. Gasification occurs in the next zone, and any remaining char is then burned in the gasification zone. Syngas produced by an updraft moving-bed gasifier has high tar content because the tar released during the devolatilization process is carried away by the hot gas that is flowing up from gasification zone.

Ash can be removed from the bottom in the form of dry ash or slag. If dry ash is desired, the gasifier temperature is usually kept below ash fusion temperature (1300°C or 2300°F). Moving-bed gasifiers have the advantage of high char conversion, high thermal efficiency, and low exit gas temperature (450-600°C or 850-1100°F). However, they have the disadvantage of low throughput.

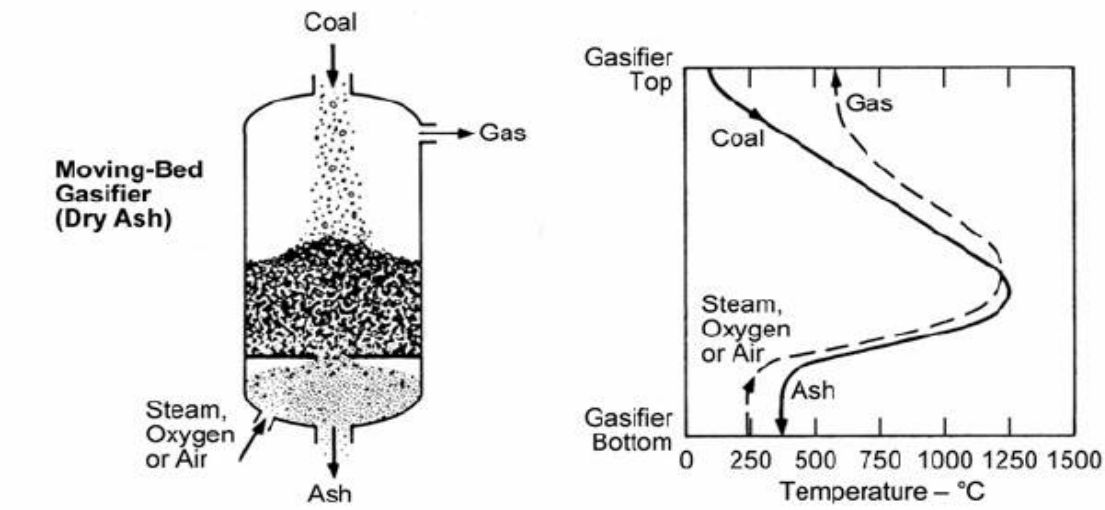

Figure 1.5 Schematic of a counter-current moving-bed gasifier (Holt, 2004).

Examples of moving-bed gasifier are:

(i) British Gas/Lurgi (BGL)

The British Gas/Lurgi (BGL) coal gasifier (Figure 1.6) is a dry-fed, pressurized, fixed-bed, slagging gasifier. The reactor wall is water cooled and refractory lined. The coal mixture enters from the top of the gasifier via a lock hopper system. Oxygen and steam enter through injector on the sidewall. A motor-driven coal distributor/mixer stirs and evenly distributes the incoming coal mixture inside the gasifier. The coal mixture descends gradually through several process zones. The top layer of the bed is the pyrolysis and devolatilization layer. The coal is

transformed into char and moves down to the next zone, which is the gasification zone. Below the gasification zone any remaining carbon is oxidized, and the ash content melts and becomes slag. The slag flows down through the opening on the bottom of the gasifier into a quench chamber. The syngas leaves the reactor through the exit at the top of the gasifier at a temperature of approximately 550°C (~1020°F).

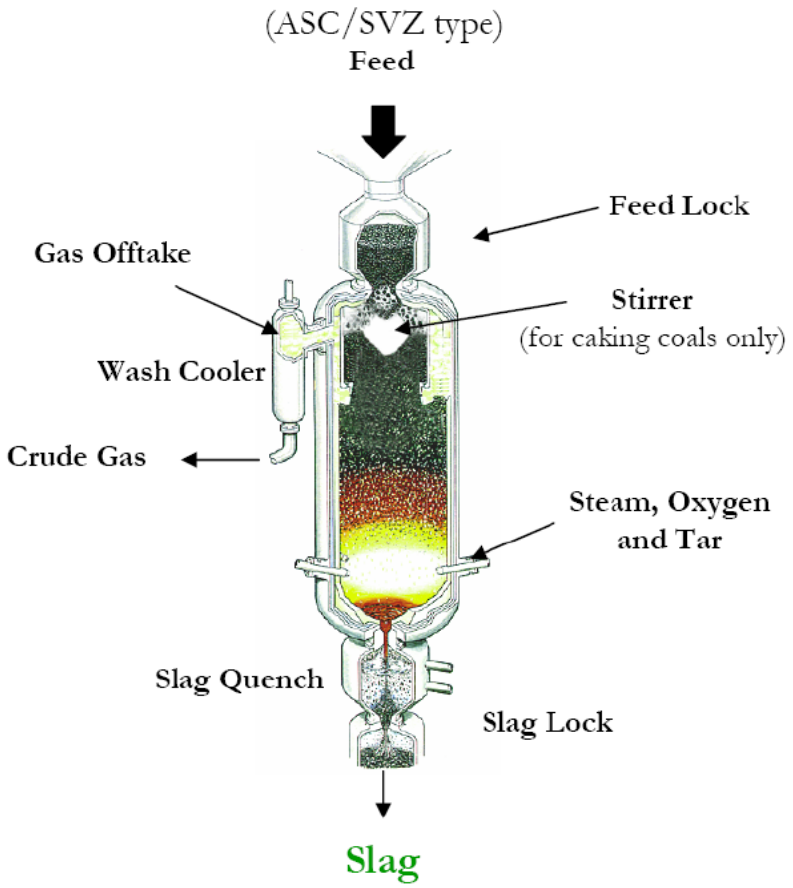

Figure 1.6 Schematic of Britigh Gas Lurgi moving-bed gasifier.

1.3.3.3 Entrained-Flow Gasifier

Figure 1.7 presents an illustration of an entrained-flow gasifier. In an entrained-flow gasifier, very fine fuel particles (< 100 μm) are suspended in a stream of oxygen/air and steam. Coal particles mix thoroughly with steam and oxygen, and the syngas produced exits through the outlet. Entrained-flow gasifiers operate at very high temperatures (1400-1650°C or 2500-3000°F). Ash in the coal melts and is discharged as liquid slag from the bottom of the gasifier.

Entrained-flow gasifiers are available in larger capacities compared to other types. The flow residence time is about 3~5 seconds. Better mixing of fuel and oxidant in the entrained-flow gasifier, when compared to moving-bed and fluidized-bed gasifiers, results in a higher efficiency. However, an entrained-flow gasifier does have disadvantages as it requires the highest amount of oxygen and produces the lowest heating value gas.

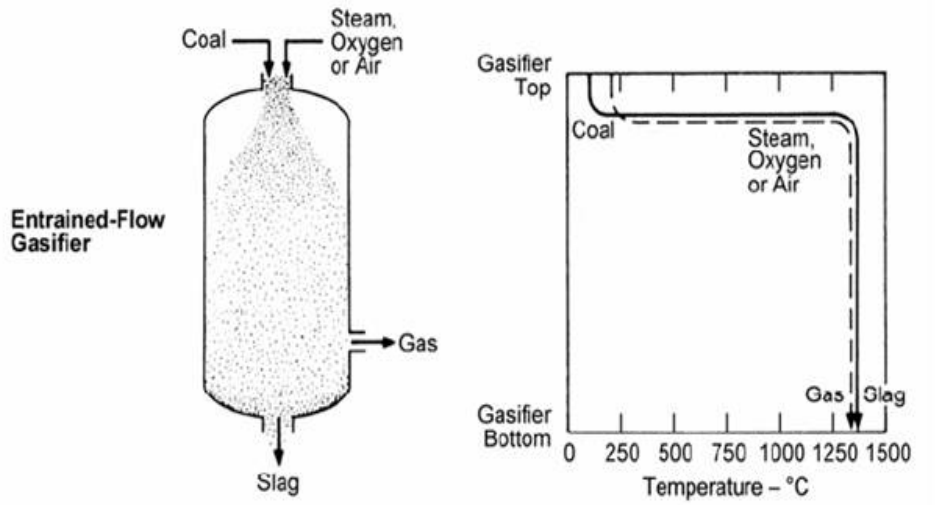

Figure 1.7 Schematic of an entrained-flow gasifier (Holt, 2004).

Examples of entrained-flow gasifiers:

(i) Shell Coal Gasification Process (SCGP)

The Shell gasifier is a high-pressure, dry-fed, oxygen-blown, entrained-flow gasifier. Dry pulverized coal is fed into the high-pressure vessel with transport gas, which is usually nitrogen, through a lock hopper system. Shell gasifier does not use refractory bricks for its wall, but instead uses membrane walls. Steam and oxygen enter into the gasifier together with dry coal particles. The gas temperature can reach 1400°C (~2500°F). Because of the high temperature, no hydrocarbon volatile and moisture will be left. At such high operating temperature, ash in the coal melts and flows down the membrane wall. When the raw syngas at the temperature of 1400-1650°C (~2500-3000°F) leaves the vessel, it contains a small amount of unburned carbon as well as about half of the molten ash. To prevent the molten ash from sticking to the wall, the raw syngas is partially cooled down to around 870°C (~1600°F) by quenching it with cooled recycle product gas. The raw syngas goes through a further cooling

process in the syngas cooler unit for further clean up. The first commercial IGCC plant using the Shell gasifier is Buggenum, Netherlands, which was built in 1993. The plant is able to achieve an overall efficiency of 43%. It can process up to 2000 tons of coal per day.

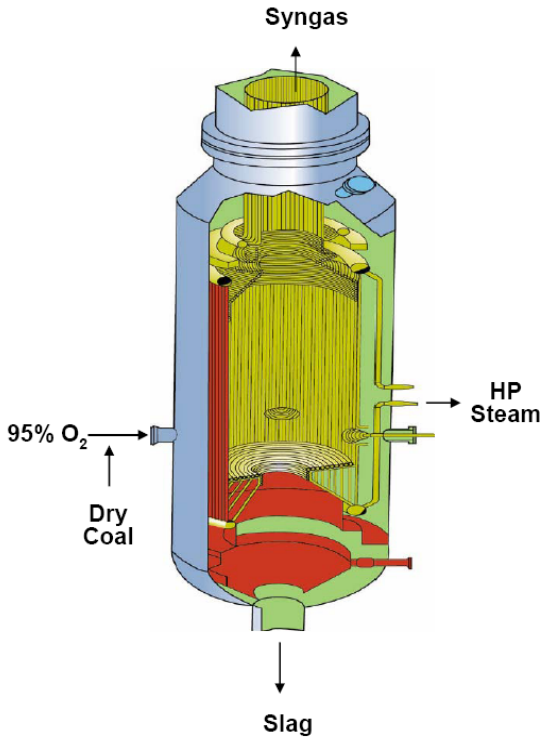

Figure 1.8 Schematic of Shell gasifier.

(ii) General Electric Gasifier (Previously Texaco gasifier)

The General Electric (GE) gasifier (Figure 1.9) operates in the temperature range of 1250-1450°C and pressure of 3 MPa for power generation and 6-8 MPa for H_2 and chemical synthesis. Coal slurry and oxidant are introduced from the top of the gasifier. The water in the slurry mixture replaces the steam, which is normally injected into the system. The hot raw gas produced during the gasification process flow toward the bottom of the gasifier. The molten ash flows down the refractory-lined walls. The hot raw gas temperature is around 1400°C (2500°F). Two ways of cooling raw syngas are available: (a) cooling by water quenching or (b) cooling in a radiant cooler. When water quench is used, the raw syngas is also cleaned from molten ash.

The first true IGCC demonstration technology was at the Southern California Edison Cool Water Station in 1984 and used a GE (Texaco) gasifier. The Cool Water gasifier was

moved to a commercial installation at the Coffeyville refinery in Kansas after the completion of the demonstration program in 1989. The gasifier is still in operation at the refinery where it converts petroleum coke into ammonia. There are currently 64 plants with GE gasifiers operating worldwide with 10 more plants being planned.

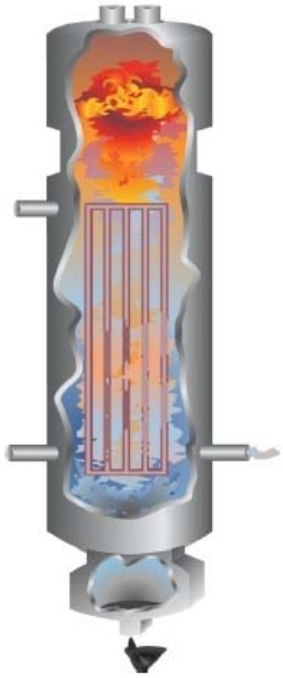

Figure 1.9 Schematic of General Electric gasifier.

(iii) Conoco-Phillips (E-Gas) Gasifier

The E-Gas gasifier is a two-stage, high-pressure, oxygen-blown, slurry-fed, slagging gasifier. Coal is mixed with water to make coal-slurry. About 80% of the coal slurry and 100% of the oxidant are injected into the first stage, while the remaining coal slurry is injected into the second stage. The first stage is located at the bottom part of the gasifier, a horizontal cylinder with one burner at each end. One is used for fresh coal slurry, and the other is for recycled unburned char. Oxidation is dominant in the first stage, increasing the temperature to about 1300-1425°C (~2400-2600°F). The ash melts and forms molten slag, which flows down and out of the vessel through a tap hole. The molten ash is quenched in a water bath and is removed.

The hot gas from the first stage flows up to the second stage where the remaining 20% coal slurry is injected. The slow endothermic gasification reactions are dominant in the second

stage. Gas temperature reduces to around 1025°C (~1900°F). The syngas and the unburned char leave the gasifier from the top. The unburned char is removed from the syngas in the gas clean-up system and is recycled back into the gasifier's first stage.

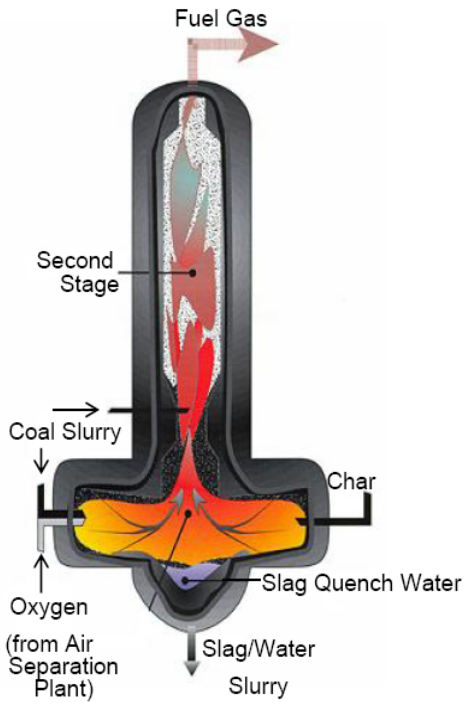

Figure 1.10 Schematic of Conoco-Phillips (E-Gas) gasifier.

(iv) PRENFLO (PREssurized ENtrained-FLOw) Gasifier

PRENFLO, which operates at atmospheric pressure, is a further development of the Kopper-Totzek process developed in the 1940's. PRENFLO was developed by Uhde, which later merged with Krupp Koppers. PRENFLO is a one-stage, high pressure, dry-fed, oxygen-blown, slagging gasifier. The gas temperature inside a PRENFLO gasifier can exceed 2000°C (3600°F) and uses a membrane wall. PRENFLO gasifiers are used in the world's largest solid-feedstock-based IGCC power plant in Puertolanno, Spain.

Figure 1.11 shows an illustration of a PSG (PRENFLO with Steam Generation) gasifier. Coal is injected together with oxygen and steam through several injectors in the lower part of the gasifier. Raw syngas is then sent through the waste heat boiler to cool down and produce steam. The exit gas temperature is 1350-1600°C (~2450-2900°F). In a PDQ (PRENFLOW with Direct

Quench), illustrated in Figure 1.11b, coal and oxygen/steam are injected in the upper part of the gasifier. Raw syngas is quenched by water in the direct quench in the lower part of the gasifier. The syngas is cooled down to 200-250°C (~390-480°F).

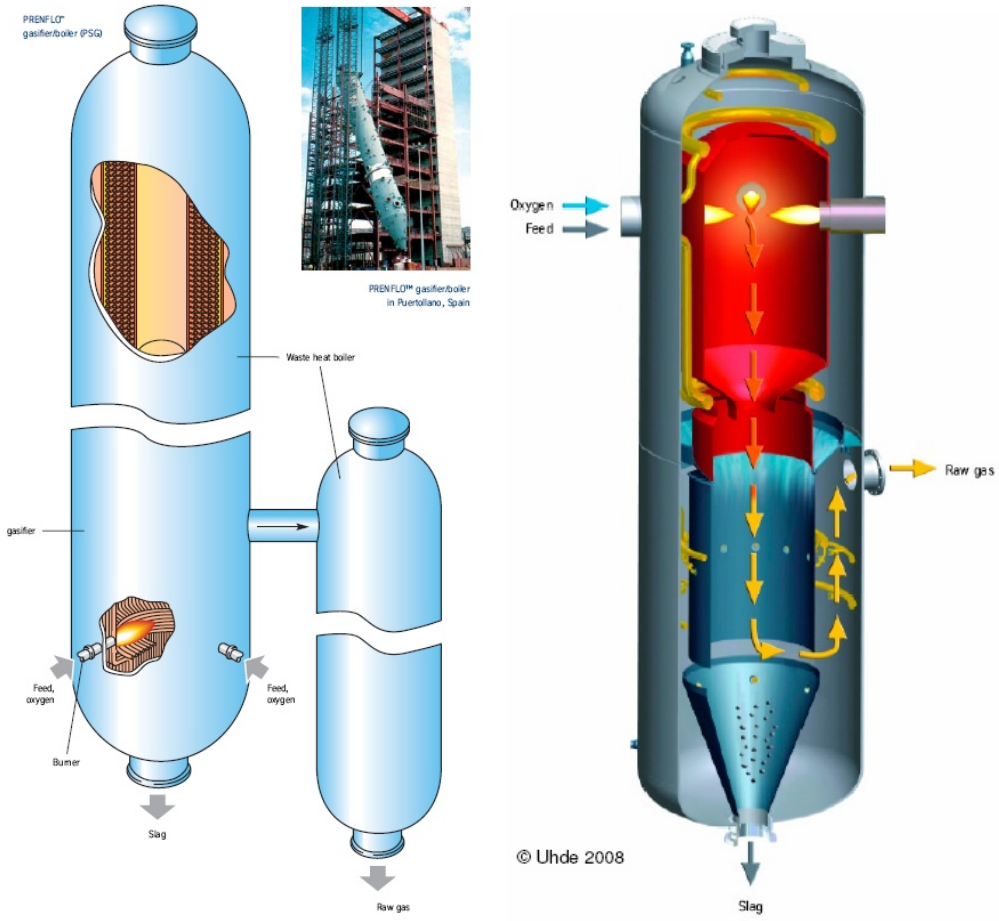

(a) PSG (b) PDQ

Figure 1.11 (a) PRENFLO with Steam Generation (PSG) and (b) PRENFLO with Direct Quench (PDQ).

1.3.3.4 Transport Gasifier

The Kellogg Brown & Root (KBR) transport gasifier, whose schematic is shown in Figure 1.12, is a circulating-bed reactor that uses fine pulverized coal and limestone. The reactor consists of a mixing zone, a riser, cyclones, and a standpipe. Oxidant and steam are fed at the bottom of the gasifier in the mixing zone. The amount of oxidant fed is carefully controlled to limit char combustion inside the gasifier. The steam added to the gasifier functions as a reactant

and moderator to control the gas temperature. Oxidant reacts with the recycled unburned char. To avoid premature combustion with oxygen, coal (and lime) is injected in the upper section of the mixing zone. The endothermic char gasification primarily occurs in the riser. The gas and particles flow up through the riser and into the cyclones, where the syngas and solids are separated by gravity and/or centrifugal forces. The syngas exits the reactor and passes through the gas cooler, while the solids are discharged back into the mixing zone through the standpipe. The entrained-solids circulate the reactor through the riser, the cyclone, and the standpipe. The KBR transport gasifier is a non-slagging gasifier. The moderate operating temperature and the use of dry coal mean that the syngas has low tar and oil contents. The exit syngas temperature is around 1000°C (~1800°F). One of the advantages of the transport gasifier is that coal is injected in the relatively low-temperature region (gasification region), so a typical problem related to the fuel-injector's reliability does not present itself.

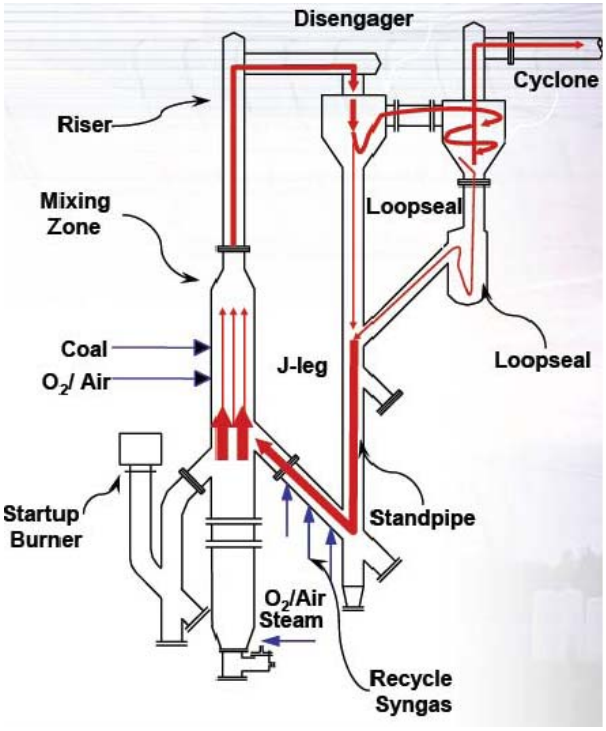

Figure 1.12 Kellogg Brown & Root (KBR) transport gasifier.

Table 1.2 Summary of coal gasifier comparisons.

Gasifier Type	Moving-bed	Fluidized-bed	Entrained-flow	Transport
Process Description	Coal is fed from top and moves down by gravity. Air and steam are injected from	Solid particle bed is fluidized by air and steam.	Solid particles are mixed thoroughly with air and steam and are entrained by the flow.	Circulating-bed reactor consist of mixing zone, riser, cyclones, and stand pipe
Technology Providers	BGL, Lurgi	HTW, KRW	Conoco-Phillips (E-Gas), GE, Shell, PRENFLO, Future Energy, sSiemens	Kellogg-Brown Root (KBR)
Fuel feed:				
Size	6-50mm	6-10mm	<100μm	< 400μm
Caking coal	Yes	Yes	No	Yes
Coal rank	Any	Any	Dry feed -- any. Slurry feed -- high rank.	Any
Operating issues:				
Syngas temperature	Low (around 600ºC)	Moderate (1000ºC)	High (1300-1600ºC)	Moderate (1000ºC)
Oxidant demand	Low	Moderate	High	Moderate
Steam demand	High	Moderate	Low	Moderate
Throughput	Low (residence time is 30 minutes to 1 hour)	Low	High (residence time is 3-5 seconds)	High
Feed rate	Low	Low	High	High
Internal moving parts	Yes (needs reactor stirrer)	No	No	No

1.3.4 Coal Combustion or Gasification

Figure 1.13 presents the typical processes undergone by coal particles in gasification. The combustion of coal particles involves two major steps: (a) thermal decomposition (pyrolysis and devolatilization) and (b) combustion of solid residue from the first step. Coal particles undergo pyrolysis when they enter the hot combustion environment. Moisture contained in the particles boils and leaves the particles once the particle temperature reaches the boiling temperature. The volatiles are then released as particle temperature continues to increase. This volatile release process is called devolatilization. The volatiles are then thermally cracked into lighter gases, such as H_2, CO, C_2H_2, CH_4, etc. These lighter gases can react with O_2, releasing some of the heat needed for the pyrolysis. With only char and ash left, the particles undergo combustion to produce CO and CO_2, leaving only ash. The thermal decomposition occurs rapidly, while the combustion step is slow.

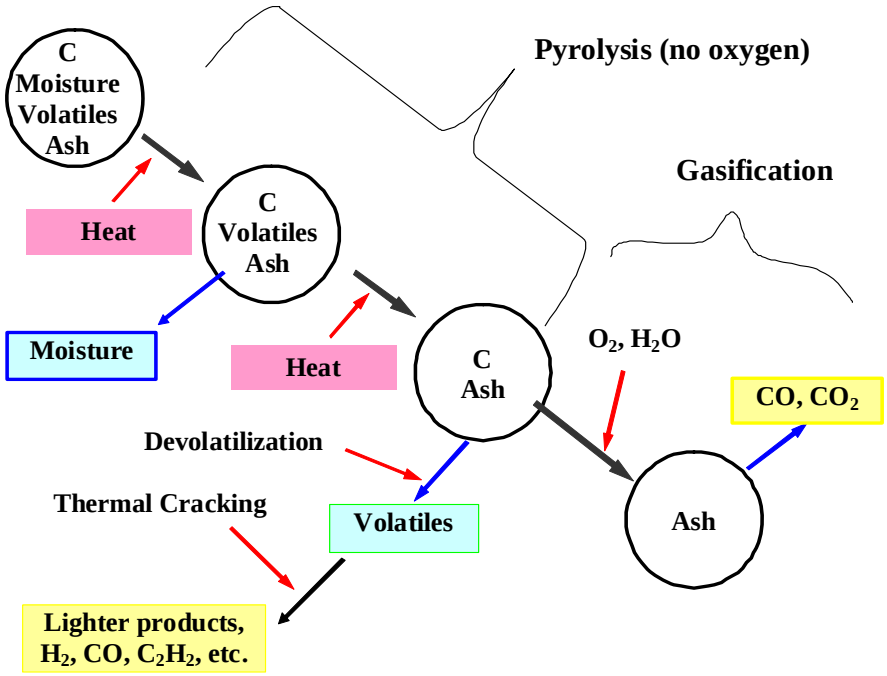

Figure 1.13 Simplified global gasification processes of coal particles (sulfur and other minerals are not included in this figure). Heat can be provided externally or internally through combustion of char, volatiles, and CO.

1.3.4.1 Devolatilization

Devolatilization is a decomposition process of hydrocarbon materials when they are heated. Devolatilization rates are influenced by temperature, residence time, particle size, and coal type. The heating causes bonds to rupture and both of coal's organic and mineral parts to decompose. The process starts at a temperature of around 373 K with desorption of gases, such as water steam, CO_2, CH_4, and N_2, which are stored in the coal pores. When temperature reaches above 573 K, the released liquid hydrocarbon called tar becomes important. Gaseous hydrocarbons such as CO, CO_2, and water steam are also released. The coal particle is in a plastic state where it undergoes a drastic change in size and shape when the temperature is above 773 K. When the temperature reaches around 823 K, the coal particle then becomes hard again and is called char. As heating continues, H_2 and CO are released.

Coal particles undergo swelling as they are heated. Small particles behave differently than larger particles. Smaller particles expand at a lower temperature than larger particles. Aside from expanding, particles also change shape during swelling. Usually, the sharp edges of the particles become rounded off. The structure of the coal particles at the end of

devolatilization is influenced by the amount of volatile contained in the coal. Intensive volatile release in high volatile coal results in larger particle porosity; low volatile particles have smaller porosity and burn on the surface.

The pyrolysis conditions affect the physical properties of coal chars. Experiments by Gale et al. (1995), conducted at maximum particle temperatures between 840 and 1627 K and heating rates between 10^4 and 2 x 10^5 K/s, showed that micropore (CO_2) surface area generally increases with increasing residence time and mass releases for lignite and bituminous coals. It also showed that the micropore surface area of char increases with increasing maximum particle temperature and heating rate.

The volatile matters generated during heating can significantly influence the temperature distribution in the particle. The volatiles generated near the center of the particle travel to the particle surface and escape. The flow of these volatiles from the particle center to the particle surface can reduce the convective heat transfer from surroundings to the particles surface. It is reported that the heat transfer coefficient decreases 10 times during fast heating of coal particles mixed with hot solid heat carrier. This reduced heat transfer rate to the particle surface results in a temperature plateau of the particle surface on the level of about 673 K and lasts during the whole time of volatiles release. Davies and Brown's (1969) explanation for this temperature plateau is that this is due to a strong effect of devolatilization.

In general, the larger the particle size, the smaller the volatile yields. This is because larger particles compared to smaller particles are more volatiles and may crack, condense, or polymerize with some carbon deposition occurring during their migration from inside the particle to the particle surface. High pressure has similar effect on the devolatilization rates. Anthony et al. (1975) reported that devolatilization rates are higher at lower pressures. An increase in pressure increases the transit time of volatiles to reach the particle surface.

Seebauer et al. (1997) investigated the effects of pressure, particle size and heating rate on coal pyrolysis using thermogravimeteric analysis. The pressure used in the study ranged from 1 to 40 atm and the heating rate was from 0.03 to 0.1 K/s. Seebauer et al. found that the total volatile yield decreased with increasing pressure. Sun et al. (1997) studied the pyrolysis of two Chinese coals under pressure ranging from 1 to 13 atm with a heating rate as low as 0.33 K/s. It was reported that at high pressure the total volatile yield decreases with increasing pressure. The

total weight loss is almost independent of the pressure at low temperatures (about less than 837 K).

Fatemi et al. (1987) studied the pressure effects on devolatilization of pulverized coal up to temperature 1373 K and pressure 68 atm in an entrained-flow reactor. They indicated that the tar yield decreases significantly with increasing pressure up to 13.8 atm. Weight loss and gas yield decreases with increasing pressure up to 13.8 atm, and there is no significant effect above this pressure.

Wall et al. (2002) reviewed the pressure effect on variety aspects of coal reactions reported in open literature. In general the total volatile and tar yields decrease with increasing pressure. This effect is more pronounced at higher temperatures and is less pronounced at high pressures. Increasing pressure improves fluidity of the coal melt and reduces char reactivity.

1.3.4.2 Carbon Particle Combustion/Gasification

The steps involved in a reaction between gas and a solid particle are as follows:

1. Transport of reactants to solid surface by convection and/or diffusion
2. Adsorption of reactant molecule on the surface
3. Reaction steps involving various combinations of adsorbed molecules, the surface, and the gas-phase molecules
4. Desorption of product molecules from the surface
5. Transport of product molecules away from solid surface by convection and/or diffusion

Due to the porous structure of char particles, chemical reactions between gases and the solid surface occur both on the outer and the inner surfaces of the particles. Reacting gases diffuse from the free space to the particle outer surface and then diffuse into the particle through the porous structure. As the reaction proceeds, the size of the available pores increases, which increases the inner particle surface. The particle active surface reaches a maximum at burnout of about 40%. The total active surface area is then decrease as a result of connection of enlarging neighboring pores.

Based on the assumption made for the solid surface and gas phase chemistry, solid carbon combustion model can be divided into (a) one-film model, (b) two-film model, and (c) continuous film model.

(A) One-film model

The one-film model uses a single step reaction, $C(s) + O_2 \rightarrow CO_2$. Figure 1.14 below illustrates gas concentration and temperature distributions near the particle surface in the one-film model. O_2 diffuses inward and reacts with the surface to form CO_2 which then diffuses outward. This model ignores the intra-particle diffusion.

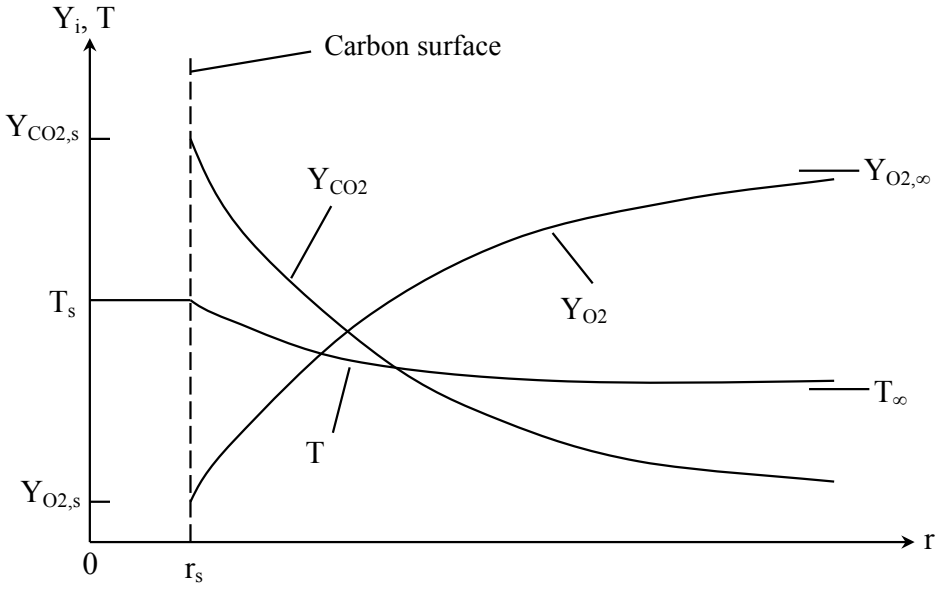

Figure 1.14 Schematic of gas concentration and temperature distributions for one-film particle combustion model.

(B) Two-film model

The two-film model involves two reactions: $C(s) + CO_2 \rightarrow 2CO$ and $CO + \frac{1}{2}O_2 \rightarrow CO_2$. Figure 1.15 illustrates the gas concentration and temperature distributions for the two-film model. CO_2 diffuses inward and attacks the particle surface. Reaction between CO_2 and the surface is $C(s) + CO_2 \rightarrow 2CO$. The CO formed then diffuses outward and is consumed at the flame sheet by O_2, which is diffusing inward according to reaction $CO + \frac{1}{2}O_2 \rightarrow CO_2$. The reaction is assumed to be infinitely fast. Thus, CO and O_2 concentrations are both zero at the flame sheet.

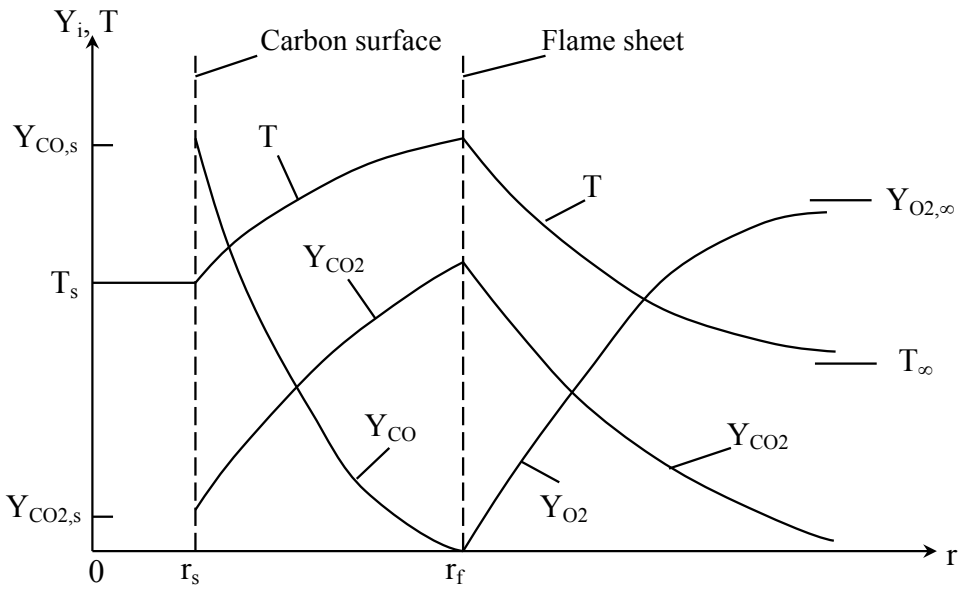

Figure 1.15 Schematic of gas concentration and temperature distributions for two-film particle combustion model.

1.3.4.3 Modeling Particle Combustion

(A) Kinetics/Diffusion Fixed-Core Model

The kinetics/diffusion fixed-core model takes into account the diffusion and kinetic rates of the combustion. The size of the particle during the combustion is assumed to be constant. The particle consumption rate is defined as follow

$$\frac{dm_p}{dt} = \frac{P_g}{\frac{1}{k_d} + \frac{1}{k_s}} A_0 \tag{1.1}$$

where m_p is the particle mass, P_g is the partial pressure of the gas phase species, A_0 is the original particle surface area, k_d is the diffusion rate constant and k_s is the kinetics rate constant.

(B) Shrinking Core Model

The shrinking core model accounts for the reduction in the particle radius as the combustion occurs. The effect of diffusion through the ash layer surrounding the particle is also taken into account. The particle consumption rate is defined as

$$\frac{dm_p}{dt} = \frac{P_g A_0}{\frac{1}{k_d} + \frac{1}{k_s}\left(r_p / R_p\right)^2 + \frac{1}{k_{dash}}\left(\frac{R_p}{r_p} - 1\right)} \tag{1.2}$$

where m_p is the particle mass, P_g is the partial pressure of the gas phase species, k_d is the diffusion rate constant, k_s is the kinetics rate constant, and k_{dash} is the ash diffusion constant. r_p is the instantaneous radius of the particle, R_p is initial radius of the particle, and A_0 is the initial particle surface area.

(C) Random Pore Model

The random pore model (Bhatia and Perlmutter, 1980) accounts for the evolution of the particle reactive surface during the combustion. The rate of mass change of the particle is defined as

$$\frac{dm_p}{dt} = R_k m_{po}\left(S + A_o\right) \tag{1.3}$$

where m_p is the particle mass, m_{po} is the initial particle mass, R_k is the kinetic rate, and A_0 is the initial particle surface area. S is the instantaneous internal reactive surface area, which is defined as

$$\frac{S}{S_o} = 1 - x\sqrt{1 - \psi \ln\left(1 - x\right)} \tag{1.4}$$

where S_o is the initial reactive area, x is the conversion factor, and ψ is the structure parameter for the particular char/coal type.

1.3.4.3 Carbon Combustion Reaction Rates

Hurt and Mitchell (1992) investigated coal char combustion kinetics for ten U.S. coals of various ranks. They observed that char reactivity decreased with increasing rank of the coal. Char reactivity decreases with increasing carbon content of the coal. The reactivity differences are more pronounced at low temperatures than at high temperatures. Hurt and Mitchell provided a char reactivity correlation, which is based on carbon content (coal rank) of the coal under conditions relevant to pulverized coal fired combustors.

Field (1968) conducted an experiment to measure rate of reaction $C(s) + ½\ O_2 \rightarrow CO$. Gas temperature used by Field ranged from 1200 K to 1720 K at atmospheric pressure. Oxygen

concentrations used ranged from 1% to 20%, and particle size ranged from 20 μm to 100 μm. The measured particle temperatures ranged from 1200 K to 2000 K.

It was assumed that the product formed inside the char and on the surface of the char was carbon monoxide and that on average CO was transported to some distance from the particle before it could combine with oxygen to form carbon dioxide. The reaction rate was calculated from the weight loss of a char sample in a given transit time at a given oxygen concentration. An overall reaction rate coefficient is defined as the rate of removal of carbon per surface unit external surface area per unit atmosphere partial pressure of oxygen in the gas. Field found that the variation of the diffusional reaction rate coefficient was not strong. The experiment did not detect any effect of particle size on the reaction rate. The kinetic reaction rate was found to be $k = T(A+BT)$ where $A = -0.067$ m/(s-K) and $B = 5.26 \times 10^{-5}$ m/s-K^2.

Mayers (1934(a)) conducted an experiment to determine the rate of reaction $C(s) + CO_2 \rightarrow 2CO$, where graphite was used as the C. The experiment was conducted at atmospheric pressure. Mayers measured the reduction rate of CO_2. The effects of diffusion as the rate determining factor were eliminated by increasing the gas velocity across the particle surface, thus removing the concentration gradients.

The rate of reduction of CO_2 through the reaction appeared in two temperature ranges: (a) between 1125 K and 1225 K and (b) 1225 K and 1575 K. Mayers found that when CO_2 reacted with carbon at low temperatures ($T < 1250$ K), CO was formed at the same rate as that at which CO_2 disappeared. This is explained by the retention of half of the oxygen of the carbon dioxide by the graphite ($C + CO_2 \rightarrow CO + C\text{-}O_{solid}$). Mayers indicated that the CO_2 reduction rate at the high temperature range might be represented by two reactions: $C + CO_2 \rightarrow CO + C\text{-}O_{solid}$ and $C\text{-}O_{solid} \rightarrow CO$, where the second reaction follows so rapidly on the first that there is no accumulation of $C\text{-}O_{solid}$. Thus the product of the CO_2 reduction is CO only. The CO_2 reduction rate is expressed in Arrhenius form $k = AT^n(-E/RT)$ where $n = 1.0$, $A = 4.4$ m/s-K, and $E = 1.62 \times 10^{+8}$ J/kmol.

Mayers (1934(b)) conducted another experiment to measure the rate of $C(s) + H_2O(g) \rightarrow CO + H_2$, where graphite was used as the source of C, at atmospheric pressure in the temperature range of 1123-1433 K under conditions which eliminated the effects of diffusion as the rate determining process. Mayers found that the appearance CO and of CO_2 varied rather widely within the same temperature group, but their sum was found to be constant. The ratio CO/CO_2

of the products of reaction depends on the speed of the secondary reaction ($CO + H_2O \rightarrow CO_2 + H_2$) and on the time during which the mixture of gases remains in the heated zone. The rate of oxidation of carbon by steam appeared in temperature ranges 1133-1233 K and 1273-1433 K. Mayers reported that the rate of oxidation of C was of the same order of magnitude as the rate of appearance of C as CO when graphite was oxidized by CO_2. The kinetic reaction rate was found to be $k = AT^n(-E/RT)$ where $n = 1.0$, $A = 1.33$ m/s-K, and $E = 1.47 \times 10^{+8}$ J/kmol.

CHAPTER TWO
COMPUTATIONAL MODEL

2.1 Problem Statement

This study will investigate the thermal-flow and gasification process in a two-stage entrained-flow gasifier as shown in Figure 2. Four tangential fuel injectors are located in the first stage at the bottom, and four opposing fuel injectors are located in the second stage. The gas flows upward and exits the gasifier from the top.

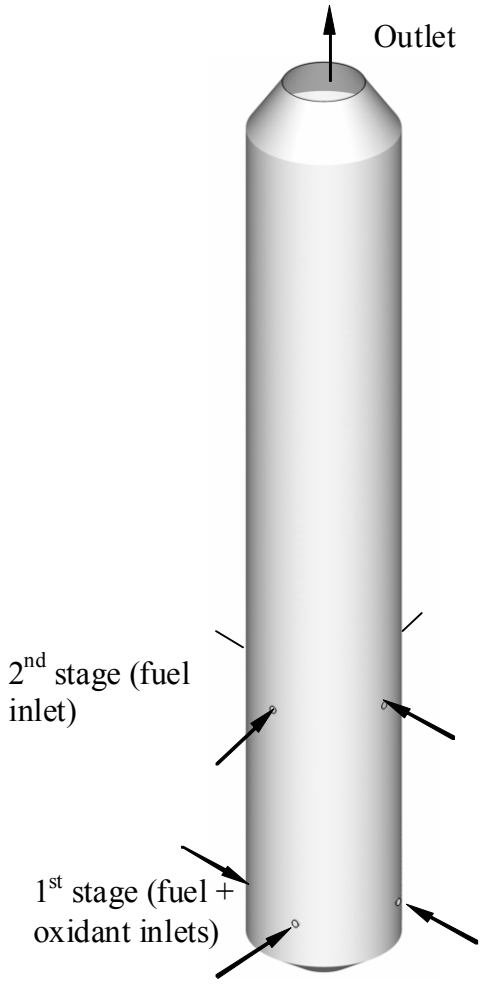

Figure 2.1 Two-stage entrained-flow gasifier studied.

Coal gasification is a multiphase reactive flow problem. It is a multiphase problem between gas and coal particles, and is also a reactive flow which involves homogeneous reactions between gases and heterogeneous reactions between solid and gas. The Eulerian-Lagrangian method is adopted in this study. Gas phase (continuous phase) is solved using Eulerian method, while solid phase (discrete phase) is solved using Lagrangian method. Gas phase is first calculated. Once the solution for gas phase is obtained, the calculations for solid phase are performed. All of solid particles are tracked one by one. The paths taken by these particles are determined by calculating force balance on the particles based on gas flow field obtained earlier. The heterogeneous solid-gas phase reactions are also calculated. After completion of the solid phase calculations, gas phase is updated with the depletion or production of a species and the energy change due to the heterogeneous reactions.

Using Computational Fluid Dynamics (CFD) simulation is an economical and effective tool to study coal gasification. Summary of researches of coal gasification conducted using CFD simulation is presented in below.

2.1.1 Recent Researches

Numerical analysis of entrained-flow coal gasifier has been widely studied since the early 1980's (Tyrkiel and Cudnok (1981), Lasa and Mok (1981), Rabbitts et al. (1983), Chapyak et al. (1983), Boysan et al. (1983), and Fletcher (1983)). Fletcher et al. (1984) developed a computer code called PCGC-2 (Pulverized Coal Gasification or Combustion) to model coal gasification and combustion. The code was made available to the public. Celik and Chattree (1990) used PCGC-2 to study gasification of Montana Rosebud-subbituminous pulverized coal in an entrained-flow reactor and compared the results with experimental data. They found that the particle residence times significantly different from the commonly calculated gas residence times and suggested that the use of gas residence time alone as a parameter might lead to erroneous conclusions regarding char burnout.

Chen et al. (2000) developed a comprehensive three-dimensional simulation model for entrained coal gasifiers which applied an extend coal gas mixture fraction model with the Multi Solids Progress Variables (MSPV) method to simulate the gasification reaction and reactant mixing process. The model employed four mixture fractions separately track the variable coal off-gas from the coal devolatilization, char-O_2, char-CO_2, and char-H_2O reactions. Chen et al.

performed a series of numerical simulations for a 200 ton per day (tpd) two-stage air blown entrained flow gasifier developed for an IGCC process under various operation conditions (heterogeneous reaction rate, coal type, particle size, and air/coal partitioning to the two stages).

Chen et al.'s model predicted that coal devolatilization and char oxidation were responsible for most of the carbon conversion (up to 80%) in the two-stage air blown entrained flow gasifier. It was found that carbon conversion was independent of devolatilization rate, sensitive to the chemical kinetics of heterogeneous reactions on the char surface, and less sensitive to a change in coal particle size. They found that increasing air ratio (or reducing equivalence ratio) leads to increased CO_2 and decreased CO and H_2 concentrations.

Chen et al. (2000) also predicted that increasing the average coal particle size decreases the carbon conversion, which results in an increase in the exit gas temperature and lower heating value. They also predicted that dry feed yields more CO mole fraction than wet feed does due to injecting less moisture into the system. Chen et al. model shows that an increase in the system pressure increases the average residence time due to the reduced average gas velocity which further results in increased particle residence time and increased carbon conversion.

Bockelie et al. (2002(a)) of Reaction Engineering International (REI) developed a CFD modeling capability for entrained flow gasifiers that focus on two gasifier configurations: single-stage down fired system and two-stage updraft system with multiple feed inlets. The model was constructed using GLACIER, an REI in-house comprehensive coal combustion and gasification tool. The basic combustion flow field was established by employing full equilibrium chemistry. Gas properties were determined through local mixing calculations and are assumed to fluctuate randomly according to a statistical probability density function (PDF) which is characteristic of the turbulence. Gas-phase reactions were assumed to be limited by mixing rates for major species as opposed to chemical kinetic rates. Gaseous reactions were calculated assuming local instantaneous equilibrium. The particle reaction processes include coal devolatilization, char oxidation, particle energy, particle liquid vaporization and gas-particle interchange. The model also includes a flowing slag sub-model.

U.S. Department of Energy/National Energy Technology Laboratory (NETL) developed 3D CFD model of two commercial-sized coal gasifiers (Guenther and Zitney, 2005). The commercial FLUENT CFD software is used to model the first gasifier, which is a two-stage entrained-flow coal slurry-fed gasifier. The Eulerian-Lagrangian approach is applied. The

second gasifier is a scaled-up design of transport gasifier. The NETL open source MFIX (Multiphase Flow Interphase eXchanges) Eulerian-Eulerian model is used for this dense multiphase transport gasifier. NETL also developed an Advanced Process Engineering Co-Simulator (APECS) that combines CFD models and plant-wide simulation. APECS enables NETL to couple its CFD models with steady-state process simulator Aspen Plus.

Watanabe and Otaka (2006) developed a numerical simulation of coal gasification in an entrained-flow gasifier. They modeled CRIEPI (Central Research Institute of Electric Power Industry) 2-tons/day research scale coal gasifier. Influence of the air ratio on gasification performance, such as syngas composition, char conversion, and cold gas efficiency, was studied and compared to experimental data. The model was able to provide quite accurate results. It was reported that increasing the air ratio increased the char conversion. However, increasing the air ratio caused the atmosphere inside the gasifier to become more oxidative, and as a result it reduced the calorific value of the syngas.

Choi et al. (2001) performed numerical parametric analysis of flow field of an entrained-flow gasifier. Choi et al. changed the gas injection angle, gas inlet diameter, gas inlet velocity, extension in burner length, and gasifier geometry and found that the basic patterns of the flow field inside the gasifier were nearly the same with a parabolic distribution. They reported that the geometric parameters of the burner, such as the oxygen inlet diameter and angle, influenced the flow field at the inlet region near the burner; but the flow field was nearly the same after a certain length along the gasifier.

Chen et al. (1999) studied the flow field inside a two-stage entrained-flow gasifier. They reported that the swirl flow is sensitive to the gasifier throat diameter. To prevent sticky particles from moving toward the reductor walls, Chen et al. recommended a small swirl diameter for the lower combustor burner and an intermediate swirl diameter for the reductor burner. They reported that the Swirl number was the most important hydrodynamic scaling law for multi-stage injecting swirl flow gasifiers.

Matsushita et al. (2006) conducted numerical analysis of an entrained-flow gasifier. Matsushita et al. reported that the CO mole fraction in the upper part of the combustor is higher for the smaller gasifier throat diameter. Vincente et al. (2003) used Eulerian-Eulerian concept in their numerical simulation of entrained-flow gasifier. Tominaga et al. (2000) used ash viscosity

as the criteria for slagging in their numerical model and indicated that the results matched fairly well with the measured data they had.

Ajilkumar et al. (2007) performed numerical study of gasification of Indian coal which has high ash content. They observed that as the ash content increases, the heat and mass transfer are affected and the gasification performance decreases. They suggested that this is attributed to the lower char reactivity due to thick ash layers and lower oxygen and other gas diffusion rates. They also found that increasing the temperatures of inlet air and steam reduces CO, but increases H_2, CO_2, and carbon conversion. Steam addition decreases the temperature but increases H_2 production at the expense of CO.

Govind and Shah (1984) conducted a numerical study on Texaco downflow entrained-flow which used coal liquefaction residues and coal-water slurries as feedstocks. They reported that oxygen-fuel ratio affects carbon conversion more than the steam-fuel ratio. The steam-fuel ratio significantly affects the syngas composition. The optimum oxygen-fuel ratio is between 0.8-0.9 to achieve 98-99% carbon conversion.

2.2 Governing Equations for Continuous Phase

As mentioned earlier, the Eulerian-Lagrangian method is adopted for this study. In the Eulerian method for continuous phase, the 3-D time-averaged steady-state Navier-Stokes equations as well as mass and energy conservation equations are solved. The governing equations for the conservations for conservation of mass, momentum and energy are given as:

$$\frac{\partial}{\partial x_i}\left(\rho u_{i\,j}\right) = S_m \tag{2.1}$$

$$\frac{\partial}{\partial x_i}\left(\rho u_i u_j\right) = \rho \bar{g}_j - \frac{\partial P}{\partial x_j} + \frac{\partial}{\partial x_i}\left(\tau_{ij} - \rho\overline{u_i' u_j'}\right) + S_f \tag{2.2}$$

$$\frac{\partial}{\partial x_i}\left(\rho c_p u_i T\right) = \frac{\partial}{\partial x_i}\left(\lambda \frac{\partial T}{\partial x_i} - \rho c_p \overline{u_i' T'}\right) + \mu\Phi + S_h . \tag{2.3}$$

The symmetric stress tensor, τ_{ij}, is given by

$$\tau_{ij} = \mu\left(\frac{\partial u_j}{\partial x_i} + \frac{\partial u_i}{\partial x_j} - \frac{2}{3}\delta_{ij}\frac{\partial u_k}{\partial x_k}\right). \tag{2.4}$$

Species transport model is used to model the mixing and transport of the chemical species. The equation for species transport is

$$\frac{\partial}{\partial x_i}\left(\rho u_i C_j\right) = \frac{\partial}{\partial x_i}\left(\rho D_i \frac{\partial C_j}{\partial x_i} - \rho\overline{u_i' C_j'}\right) + S_j . \tag{2.5}$$

S_j in Eq. 2.5 is the source term to accept increased or decreased chemical species resulted from chemical reactions.

2.3 Turbulence Models

The velocity field in turbulent flows always fluctuates. As a result, the transported quantities such as momentum, energy, and species concentration fluctuate as well. The fluctuations can be small scale and high frequency, which is computationally expensive to be directly simulated. To overcome this, a modified set of equations that are computationally less expensive to solve can be obtained by replacing the instantaneous governing equations with their time-averaged, ensemble-averaged, or otherwise manipulated to remove the small time scales. However, the modifications of the instantaneous governing equations introduce new unknown variables. Many turbulence models have been developed to determine these new unknown variables (such as Reynolds stresses or higher order terms) in terms of known variables.

2.3.1 Standard k-ε Model

The standard k-ε model defines the Reynolds stresses as

$$-\rho\overline{u_i' u_j'} = \mu_t\left(\frac{\partial u_i}{\partial x_j} + \frac{\partial u_j}{\partial x_i}\right) - \frac{2}{3}\rho k \delta_{ij} \tag{2.6}$$

where k is the turbulence kinetic energy, and μ_t is the turbulence viscosity given by

$$\mu_t = \rho C_\mu k^2 / \varepsilon \tag{2.7}$$

where C_μ is a constant and ε is the turbulence dissipation rate. The equations for the turbulence kinetic energy (k) and dissipation rate (ε) are

$$\frac{\partial}{\partial x_i}\left(\rho u_i k\right) = \frac{\partial}{\partial x_i}\left[\left(\mu + \frac{\mu_t}{\sigma_k}\right)\frac{\partial k}{\partial x_i}\right] + G_k - \rho\varepsilon \tag{2.8}$$

$$\frac{\partial}{\partial x_i}\left(\rho u_i \varepsilon\right) = \frac{\partial}{\partial x_i}\left[\left(\mu + \frac{\mu_t}{\sigma_\varepsilon}\right)\frac{\partial \varepsilon}{\partial x_i}\right] + C_{1\varepsilon} G_k \frac{\varepsilon}{k} - C_{2\varepsilon} G_k \rho \frac{\varepsilon^2}{k} . \tag{2.9}$$

G_k is the generation of turbulence kinetic energy due to the mean velocity gradients. The turbulent heat flux and mass flux can be modeled with the turbulent heat conductivity (λ_t) and the turbulent diffusion coefficient (D_t), respectively.

$$\rho c_p \overline{u'_i T'} = -\lambda_t \frac{\partial T}{\partial x_i} = -c_p \frac{\mu_t}{Pr_t} \frac{\partial T}{\partial x_i}, \tag{2.10}$$

$$\rho \overline{u'_i C'} = -\rho D_t \frac{\partial C}{\partial x_i} = -\frac{\mu_t}{Sc_t} \frac{\partial C}{\partial x_i}. \tag{2.11}$$

The constants $C_{1\varepsilon}$, $C_{2\varepsilon}$, C_μ, σ_k, and σ_ε used are: $C_{1\varepsilon} = 1.92$, $C_{2\varepsilon} = 0.09$, $C_\mu = 1.0$, $\sigma_k = 1.3$ (Launder and Spalding, 1972). The turbulence Prandtl number, Pr_t, is set to 0.85, and the turbulence Schmidt number, Sc_t, is set to 0.7.

The turbulence models are valid for the turbulent core flows, i.e. the flow in the regions somewhat far from walls. The flow very near the walls is affected by the presence of the walls. Viscous damping reduces the tangential velocity fluctuations and the kinematic blocking reduces the normal fluctuations. The solution in the near-wall region can be very important because the solution variables have large gradients in this region.

However, the solution in the boundary layer is not important in this study. Therefore, the viscous sublayer, where the solution variables change most rapidly, does not need to be solved. Instead, wall functions, which are a collection of semi-empirical formulas and functions, are employed to connect the viscosity-affected region between the wall and the fully-turbulent region. The wall functions consist of:

- laws-of-the-wall for mean velocity and temperature (or other scalars)
- formulas for near-wall turbulent quantities.

There are three types of wall function: (a) standard wall function, (b) non-equilibrium wall function, and (c) enhanced wall function.

Standard Wall Function – The momentum is expressed as

$$U^+ = \frac{1}{\kappa} \ln\left(Ey^+\right) \tag{2.12}$$

where

$$U^+ \equiv \frac{U_P C_\mu^{1/4} k_P^{1/2}}{\tau_w / \rho} \tag{2.13}$$

$$y^+ \equiv \frac{\rho C_\mu^{1/4} k_P^{1/2} y_P}{\mu} \tag{2.14}$$

and

κ = von Karman constant (= 0.42)

E = empirical constant (= 9.793)

U_P = mean velocity of fluid at point P

k_P = turbulence kinetic energy at point P

y_P = distance from point P to the wall

μ = dynamic viscosity of the fluid.

The wall function for the temperature is given as

$$T^+ \equiv \frac{(T_w - T_P)\rho c_p C_\mu^{1/4} k_P^{1/2}}{\dot{q}} = \begin{cases} Pry^+, y^+ \langle y_T^+ \\ Pr_t \left[\frac{1}{\kappa} \ln(Ey^+) + P \right], y^+ \rangle y_T^+ \end{cases} \tag{2.15}$$

where P is given as

$$P = 9.24 \left[\left(\frac{Pr}{Pr_T} \right)^{3/4} - 1 \right] \left[1 + 0.28 e^{-.007 Pr/Pr_T} \right] \tag{2.16}$$

and

r = density of the fluid

c_p = specific heat of fluid

q = wall heat flux

T_P = temperature at cell adjacent to the wall

T_W = temperature at the wall

Pr = molecular Prandtl number

Pr_t = turbulent Prandtl number (0.85 at the wall)

A = 26 (Van Driest constant)

κ = 0.4187 (von Karman constant)

E = 9.793 (wall function constant)

U_c = mean velocity magnitude at $y^+ = y^+_T$

y^+_T = non-dimensional thermal sublayer thickness.

The species transport is assumed to behave analogously to the heat transfer. The equation is expressed as

$$Y^+ \equiv \frac{\left(Y_{i,w} - Y_i\right)\rho c_p C_\mu^{1/4} k_P^{1/2}}{J_{i,w}} = \begin{cases} Scy^+, y^+ < y_c^+ \\ Sc_t\left[\frac{1}{\kappa}\ln\left(Ey^+\right) + P_c\right], y^+ > y_c^+ \end{cases} \tag{2.17}$$

where Y_i is the local mass fraction of species i, Sc and Sc_t are the molecular and turbulence Schmidt numbers respectively, and $J_{i,w}$ is the diffusion flux of species i at the wall. The molecular Schmidt number, Sc, is given as $\mu/\rho D$, where μ is the viscosity and D is the diffusivity. The P_c and y^+_c are calculated in a similar way as P and y^+_T, with the difference being that the Prandtl numbers are replaced by the corresponding Schmidt numbers.

In the k-ε model, the k equation is solved in the whole domain, including the wall-adjacent cells. The boundary condition for k imposed at the wall is

$$\frac{\partial k}{\partial n} = 0 \tag{2.18}$$

where n is the local coordinate normal to the wall. The production of kinetic energy, G_k, and its dissipation rate, ε, at the wall-adjacent cells, which are the source terms in k equation, are computed on the basis of equilibrium hypothesis with the assumption that the production of k and its dissipation rate assumed to be equal in the wall-adjacent control volume. The production of k and ε is computed as

$$G_k \approx \tau_w \frac{\partial U}{\partial y} = \tau_w \frac{\tau_w}{\kappa \rho C_\mu^{1/4} k_p^{1/4} y_P} \tag{2.19}$$

and

$$\varepsilon_P = \tau_w \frac{C_\mu^{3/4} k_p^{3/2}}{k y_P}. \tag{2.20}$$

Notice that in the wall-adjacent control volume when the equilibrium hypothesis is employed, the k-transport Eq. 2.8 is solved, while the ε-transport Eq. 2.9 is not solved but is replaced by Eq. 2.20.

Enhanced Wall Function – The k-ε model is mainly valid for high Reynolds number fully turbulent flow. Special treatment is needed in the region close to the wall. The enhanced wall

function is one of several methods that model the near-wall flow. In the enhanced wall treatment, the two-layer model is combined with the wall functions. The whole domain is separated into a viscosity-affected region and a fully turbulent region by defining a turbulent Reynolds number, Re_y,

$$Re_y = yk^{1/2} / \nu \tag{2.21}$$

where k is the turbulence kinetic energy and y is the distance from the wall. The standard k-ε model is used in the fully turbulent region where $Re_y > 200$, and the one-equation model of Wolfstein (1969) is used in the viscosity-affected region with $Re_y < 200$. The turbulent viscosities calculated from these two regions are blended with a blending function (θ) to smoothen the transition.

$$\mu_{t,enhanced} = \theta\mu_t + (1-\theta)\mu_{t,l} \tag{2.22}$$

where μ_t is the viscosity from the k-ε model of high Reynolds number, and $\mu_{t,l}$ is the viscosity from the near-wall one-equation model. The blending function is defined so it is equal to 0 at the wall and 1 in the fully turbulent region. The linear (laminar) and logarithmic (turbulent) laws of the wall are also blended to make the wall functions applicable throughout the entire near-wall region. A similar thermal wall function equation is employed for temperature calculation.

2.3.2 Reynolds Stress Model

The Reynolds stress model (RSM), a second-moment closure, is considered in this study. The Reynolds stress transport equation can be given as

$$\frac{\partial}{\partial x_k}\left(\rho u_k \overline{u'_i u'_j}\right) = -\frac{\partial}{\partial x_k}\left[\rho u_k \overline{u'_i u'_j u'_k} + \overline{P(\delta_{kj}u'_i + \delta_{ik}u'_j)} + \mu\frac{\partial}{\partial x_k}\left(\overline{u'_i u'_j}\right)\right]$$
$$-\rho\left(\overline{u'_i u'_k}\frac{\partial u_j}{\partial x_k} + \overline{u'_j u'_k}\frac{\partial u_i}{\partial x_k}\right) + \overline{P\left(\frac{\partial u'_i}{\partial x_j} + \frac{\partial u'_j}{\partial x_i}\right)} - 2\mu\overline{\frac{\partial u'_i}{\partial x_k}\frac{\partial u'_j}{\partial x_k}} \tag{2.23}$$

The diffusive term on the right-hand side can be modeled as

$$-\frac{\partial}{\partial x_k}\left[\rho u_k \overline{u'_i u'_j u'_k} + \overline{P(\delta_{kj}u'_i + \delta_{ik}u'_j)} + \mu\frac{\partial}{\partial x_k}\left(\overline{u'_i u'_j}\right)\right] = \frac{\partial}{\partial x_k}\left(\frac{\mu_t}{\sigma_k}\frac{\partial}{\partial x_k}\left(\overline{u'_i u'_j}\right)\right) \tag{2.24}$$

The second term on the right-hand side of Eq. 2.23 is the production term, and it is notated as G_{ij}

$$G_{ij} = -\rho\left(\overline{u'_i u'_k}\frac{\partial u_j}{\partial x_k} + \overline{u'_j u'_k}\frac{\partial u_i}{\partial x_k}\right) \tag{2.25}$$

The third term is the pressure-strain term, which can be modeled as

$$\overline{P\left(\frac{\partial u'_i}{\partial x_j} + \frac{\partial u'_j}{\partial x_i}\right)} = C_1\rho\frac{\varepsilon}{k}\left(\overline{u'_i u'_j} - \frac{2}{3}\delta_{ij}k\right) - C_2\left[A_{ij} - \frac{1}{3}\delta_{ij}A_{kk}\right] \tag{2.26}$$

where $A_{ij} = G_{ij} - \frac{\partial}{\partial x_k}\left(\rho u_k \overline{u'_i u'_j}\right)$. The constants C_1 and C_2 are 1.8 and 0.6, respectively. The last term in Eq. 2.23 can be approximated by

$$2\mu\overline{\frac{\partial u'_i}{\partial x_k}\frac{\partial u'_j}{\partial x_k}} = \frac{2}{3}\delta_{ij}\rho\varepsilon \tag{2.27}$$

and assumes this dissipation term isotropic.

Modeling of the turbulent heat flux and mass flux are similar as in the k-ε model. The turbulent kinetic energy and its dissipation rate can be calculated from the Reynolds stresses.

2.3.3 Other Models

Ignoring details here, the turbulent models adopted in this study also include the RNG k-ε model, k-ω model, and the shear-stress transport (SST) k-ω model. RNG k-ε model was derived using renormalization group theory (Choudhury, 1993). It has an additional term in the ε-equation to improve the accuracy for rapidly strained flows. It uses the effective viscosity to account for low-Reynolds-number effects. Theoretically, this model is more accurate and reliable than the standard k-ε model. The standard k-ω model is an empirical model based on transport equations for the turbulence kinetic energy (k) and the specific dissipation rate (ω), which can also be considered as the ratio of ε to k (Wilcox, 1998). The low-Reynolds-number effect is accounted for in the k-ω model. The SST model is mixture of the k-ω model and the k-ε model: close to the wall it becomes the k-ω model while in the far field the k-ε model is applied (Menter, 1993).

2.4 Radiation Model

The P-1 radiation model is used to calculate the flux of the radiation at the inside walls of the gasifier. The P-1 radiation model is the simplest case of the more general P-N radiation model that is based on the expansion of the radiation intensity I. The P-1 model requires only a little CPU demand and can easily be applied to various complicated geometries. It is suitable for applications where the optical thickness aL is large where "a" is the absorption coefficient and L is the length scale of the domain.

The heat sources or sinks due to radiation is calculated using the equation

$$-\nabla.q_r = aG - 4a\sigma T^4 \tag{2.28}$$

where

$$q_r = -\frac{1}{3(a+\sigma_s) - C\sigma_s}\nabla G \tag{2.29}$$

and q_r is the radiation heat flux, a is the absorption coefficient, σ_s is the scattering coefficient, G is the incident radiation, C is the linear-anisotropic phase function coefficient, and σ is the Stefan-Boltzmann constant. The gases are assumed to be the participating media. However, when the effect of particles is included in the radiation model, the heat sources or sinks due to radiation become,

$$-\nabla \cdot q_r = -4\pi\left(a\frac{\sigma T^4}{\pi} + \varepsilon_p\right) + (a + a_p)\nabla G \tag{2.30}$$

where ε_p and a_p are the equivalent emissivity and equivalent absorption of the particle, respectively.

The flux of the radiation, $q_{r,w}$, at walls caused by incident radiation G_w is given as

$$q_{r,w} = -\frac{4\pi\varepsilon_w\frac{\sigma T_w^4}{\pi} - (1-\rho_w)G_w}{2(1+\rho_w)} \tag{2.31}$$

where ε_w is the emissivity and is defined as

$$\varepsilon_w = 1 - \rho_w \tag{2.32}$$

and ρ_w is the wall reflectivity.

2.5 Discrete Phases (Solid Particles or Liquid Particles)

Discrete phases include coal particles and liquid particles. Lagrangian method to track each particle is adopted in this study. The discrete phase is justified in entrained-flow gasification process because the particle concentration is lower than 10%. Particles in the airflow can encounter inertia and hydrodynamic drags. Because of the forces experienced by the particles in a flow field, the particles can be either accelerated or decelerated. The velocity change is determined by the force balance of the particle, which can be formulated by

$$m_p dv_p/dt = F_d + F_g + F_o \tag{2.33}$$

where F_d is the drag force of the fluid on the particle and F_g is the gravity. F_o represents the other body forces, typically include the "virtual mass" force, thermophoretic force, Brownian force, Saffman's lift force, etc**.**

The drag force, F_d, is calculated as

$$F_D = \frac{18\mu}{\rho_p d_p^2}\frac{C_D Re}{24}\left(v - v_p\right)m_p \tag{2.34}$$

and the gravity force, F_g, is calculated using the following equation

$$F_g = \frac{g\left(\rho_p - \rho\right)}{\rho_p} m_p \tag{2.35}$$

where m_p is particle mass, d_p is particle diameter, v is the fluid phase velocity, v_p is the particle velocity, ρ is the fluid phase density, ρ_p is the particle density, g is gravity, μ is the fluid phase molecular viscosity, and C_D is the drag coefficient. The relative Reynolds number, Re, is defined as

$$Re = \frac{\rho d_p \left|v_p - v\right|}{\mu}. \tag{2.36}$$

2.5.1 Coal particles

Gasification or combustion of coal particles undergoes the following global processes: (i) evaporation of moisture, (ii) devolatilization, (iii) gasification to CO and (iv) combustion of volatiles, CO, and char. (See Figure 1.12)

2.5.1.1 Devolatilization Model

After all the moisture contained in the coal particle has evaporated, the particle undergoes devolatilization. Four different devolatilization models widely used are the Kobayashi model, single rate model, constant rate model, and CPD (Chemical Percolation Devolatilization) model.

(a) Kobayashi model --- The Kobayashi model (Kobayashi, 1976) with two-competing devolatilization rates are expressed as a weighted function of two competing rates, R_1 and R_2, as shown below,

$$\frac{m_v(t)}{(1-f_{w,0})m_{p,0}-m_a} = \int_0^t (\alpha_1 R_1 + \alpha_2 R_2)\exp\left(-\int_0^t (R_1+R_2)dt\right)dt \tag{2.37}$$

where α_1 and α_2 are yield factors, f_w is mass fraction of moisture, m_p is mass of particle, m_a is mass of ash, and R_1 and R_2 are given as,

$$R_1 = A_1 e^{-(E_1/RT_p)} \tag{2.38}$$

and,

$$R_2 = A_2 e^{-(E_2/RT_p)}. \tag{2.39}$$

The value of the constants are $A_1 = 2\text{x}10^5$, $A_2 = 1.3\text{x}10^7$, $E_1 = 1.046\text{x}10^8$ J/kgmol, and $E_2 = 1.67\text{x}10^8$ J/kgmol.

(b) Single rate model --- The devolatilization rate is dependent on the amount of volatiles remaining in the particle (Badzioch and Hawsley, 1970). The devolatilization kinetic rate is defined in Arrhenius form below

$$k = Ae^{-(E/RT)} \tag{2.40}$$

where the pre-exponential factor, A, used in this study is $4.92\text{x}10^5$ and the activation energy, E, is $7.4\text{x}10^7$ J/kgmol.

(c) Constant rate model --- This model assumes that volatiles are released at a constant rate (Baum and Street, 1971). The rate used in this study is 12/s (Pillai, 1981).

(d) Chemical Percolation Devolatilization (CPD) model --- The CPD model considers the chemical transformation of the coal structure during devolatilization. It models the coal

structure transformation as a transformation of chemical bridge network which result in release of light gas, char, and tar (Fletcher and Kerstein (1992), Fletcher et al. (1990), and Grant et al. (1989)). In this study, the volatile contained in the coal is assumed to be C_6H_6. The initial fraction of the bridges in the coal lattice is 1, and the initial fraction of char is 0. The lattice coordination number is 5. The cluster molecular weight is 400 and the side chain molecular weight is 50.

Volatiles released by coal particles contain a lot of various lighter gases. When simulating coal gasification, decision has to be made as to what lighter gases are released during the devolatilization.

The study by Chen et al. (2000) modeled that hydrogen, oxygen, nitrogen, and sulfur in the coal particles to be released as a volatile species. The volatile species then reacts with oxygen according to Eq. 2.41 below for oxygen-rich conditions and Eq. 2.42 for oxygen-lean conditions.

For oxygen-rich conditions,

$$\begin{aligned} C_{m1}H_{m2}O_{m3}N_{m4}S_{m5}mois_{m6} + \left(m_1 + \frac{m_2}{4} - \frac{m_3}{2} + m_5\right)O_2 \rightarrow m_1CO_2 \\ + \left(m_7 + \frac{m_2}{4}\right)H_2O + m_5SO_2 + \frac{m_4}{2}N_2 \end{aligned} \quad . \tag{2.41}$$

For oxygen-lean conditions $\left(\varphi < \left(m_1 + \frac{m_2}{4} - \frac{m_3}{2} + m_5\right)\right)$,

$$\begin{aligned} C_{m1}H_{m2}O_{m3}N_{m4}S_{m5} + \varphi O_2 \rightarrow \alpha_1 CO_2 + \alpha_2 CO + m_1(1-\alpha_1-\alpha_2)CO_2 \\ + \left[\frac{(1-\alpha_1)}{2}(m_2 - 2m_5) - 2(1-\alpha_1-\alpha_2)\right]H_2 \\ + \frac{\alpha_1(m_2-2m_5)}{2}H_2O + \frac{\alpha_1(m_2-2m_5)}{2}H_2O + m_5H_2S + \frac{m_4}{2}N_2 \end{aligned} \quad . \tag{2.42}$$

The values of m_1 through m_6, which determine the composition of the volatile, in Eqs. 2.41 and 2.42 above are calculated from the proximate and ultimate analyses of the coal. The coefficient φ is the criteria for which the condition is considered oxygen-lean.

Kumar et al. (2009) modeled that volatiles are broken up as follow,

$$\text{Volatiles} \rightarrow \alpha_1\, CO + \alpha_2\, H_2O + \alpha_3\, CO_2 + \alpha_4\, H_2 + \alpha_5\, CH_x + \alpha_6\, N_2 \tag{2.43}$$

where the stoichiometric coefficients α_i's and value of x in CH_x are determined by the proximate and ultimate analyses of the coal. In this study, the volatile matters contained in the coal are assumed to be composed of CO, H_2, N_2, and C_6H_6 (Tomeczek, 1994). However, the devolatilization model used can only model the release of one volatile gas. Thus, the devolatilization model is divided into two steps:

(i) Release of a volatile gas modeled using the devolatilization model. All of the volatile matters are lumped into one intermediate gas species ($C_xH_yO_z$), whose release rate is given by the devolatilization model.

(ii) Thermal cracking of the volatile gas into several different gases. Once this intermediate is released, it is decomposed into the volatile gases – CO, H_2, and C_6H_6 – through chemical reaction: $C_xH_yO_z \rightarrow aCO + bH_2 + cC_6H_6$

To model part (i), the chemical formula of the intermediate gas species ($C_xH_yO_z$) has to be known. However, coal composition does not provide the volatiles' chemical formula. Thus, the chemical formula needs to be found out. Based on the proximate and ultimate analyses, the elemental composition of the volatiles is calculated. The enthalpy of the volatiles is calculated from the coal heating value. The detailed calculation is presented in Appendix.

2.5.2 Liquid droplets

Theoretically, evaporation occurs at two stages: (a) when temperature is higher than the saturation temperature (based on local water vapor concentration), water evaporates from the particle's surface, and the evaporation is controlled by the water vapor partial pressure until 100% relative humidity is achieved; (b) when the boiling temperature (determined by the air-water mixture pressure) is reached, water continues to evaporate even though the relative humidity reaches 100%. After the moisture is evaporated due to either high temperature or low moisture partial pressure, the vapor diffuses into the main flow and is transported away. The rate of vaporization is governed by concentration difference between surface and gas stream, and the corresponding mass change rate of the particle can be given by,

$$\frac{dm_p}{dt} = \pi d^2 k_c (C_s - C_\infty) \tag{2.44}$$

where k_c is the mass transfer coefficient and C_s is the concentration of the vapor at the particle's surface, which is evaluated by assuming that the flow over the surface is saturated. C_∞ is the

vapor concentration of the bulk flow, obtained by solving the transport equations. The values of k_c can be calculated from empirical correlations by (Ranz and Marshall, 1955):

$$Sh_d = \frac{k_c d}{D} = 2.0 + 0.6 Re_d^{0.5} Sc^{0.33} . \tag{2.45}$$

where Sh is the Sherwood number, Sc is the Schmidt number (defined as ν/D), D is the diffusion coefficient of vapor in the bulk flow. Re_d is the Reynolds number, defined as uν/d, where u is the particle slip velocity relative to the gas flow.

When the droplet temperature reaches the boiling point, the following equation can be used to evaluate its evaporation rate (Kuo, 1986):

$$\frac{dm_p}{dt} = \pi d^2 \left(\frac{\lambda}{d}\right)(2.0 + 0.46 Re_d^{0.5}) \ln\left(1 + c_p (T_\infty - T)/h_{fg}\right)/c_p \tag{2.46}$$

where λ is the heat conductivity of the gas/air, h_{fg} is the droplet latent heat, and c_p is the specific heat of the bulk flow.

The droplet temperature can also be changed due to heat transfer between droplets and the continuous phase. The droplet's sensible heat change of the droplet is shown in the following equation

$$m_p c_p \frac{dT}{dt} = \pi d^2 h(T_\infty - T) + \frac{dm_p}{dt} h_{fg} + \varepsilon_p A_p \sigma\left(\theta_R^4 - T^4\right) \tag{2.47}$$

where θ_R is the radiation temperature. The convective heat transfer coefficient (h) can be obtained with a similar empirical correlation to equation (2.35):

$$Nu_d = \frac{hd}{\lambda} = 2.0 + 0.6 Re_d^{0.5} Pr^{0.33} \tag{2.48}$$

where Nu is the Nusselt number, and Pr is the Prandtl number.

2.5.3 Stochastic Tracking

The various turbulence models are based on the time-averaged equations. Using this flow velocity to trace the droplet will result in an averaged trajectory. In the real flow, the instantaneous velocity fluctuation would make the droplet dance around this average track. However, the instantaneous velocity is not calculated in the current approach as the time averaged Navier-Stokes equations are solved. One way to simulate the effect of instantaneous turbulence on droplets dispersion is to use the stochastic tracking scheme (Fluent, 2006).

Basically, the droplet trajectories are calculated by using the instantaneous flow velocity ($\overline{u} + u'$) rather than the average velocity ($\overline{u}$). The velocity fluctuation is then given as:

$$u' = \zeta\left(\overline{u'^2}\right)^{0.5} = \zeta(2k/3)^{0.5} \tag{2.49}$$

where ζ is a normally distributed random number. This velocity will apply during a characteristic lifetime of the eddy (t_e), given from the turbulence kinetic energy and dissipation rate. After this time period, the instantaneous velocity will be updated with a new ζ value until a full trajectory is obtained. When the stochastic tracking is applied, the basic interaction between droplets and continuous phase keeps the same, accounted by the source terms in the conservation equations. The source terms are not directly but rather indirectly affected by the stochastic method. For example, the drag force between droplets and the airflow depends on the slip velocity calculated by the averaged Navier-Stokes equations if without the stochastic tracking. With the stochastic tracking a random velocity fluctuation is imposed at an instant of time, and the drag force and additional convective heat transfer will be calculated based on this instantaneous slip velocity. The source terms associated with this instantaneous drag force and convective heat transfer enter the momentum and energy equations without any additional formulation. For a steady-state calculation, the "instant of time" means "each iteration step." Therefore, the averaged momentum equation will not be affected by the stochastic tracking scheme; rather the trajectory of the droplet will reflect the effect of the imposed instantaneous perturbation.

2.6 Reaction Models

2.6.1 Particle Reactions

The reaction of particle occurs after the devolatilization process has finished. The rate of depletion of solid due to a surface reaction is expressed as (Smith, 1982),

$$\overline{R} = A\eta Y R \tag{2.50}$$

$$R = k\left(p_n - \frac{R}{D}\right)^N \tag{2.51}$$

where

$\overline{R}$ = rate of particle surface species depletion (kg/s)

A = particle surface area (m^2)

Y = mass fraction of surface the solid species in the particle

η = effectiveness factor (dimensionless)

R = rate of particle surface species reaction per unit area (kg/m^2-s)

p_n = bulk partial pressure of the gas phase species (Pa)

D = diffusion rate coefficient for reaction

k = kinetic reaction rate constant (units vary)

N = apparent order of reaction.

The kinetic rate of reaction is usually defined in an Arrhenius form as

$$k = AT^n e^{-(E/RT)} . \tag{2.52}$$

For reaction order N = 1, the rate of particle surface species depletion is given by

$$\overline{R} = A\eta Y p_n \frac{kD}{D+k} . \tag{2.53}$$

For reaction order N = 0,

$$\overline{R} = A\eta Y k . \tag{2.54}$$

For reaction order N = 0, the unit for the kinetic reaction rate constant, k, is kg/m^2-s.

In the CFD software used, FLUENT, the reaction order of the particle reaction is 0. Thus, Eq. 2.50 is used to calculate rate of depletion of the solid, $\overline{R}$ (kg/s). The kinetic reaction rate constant, k (kg/m^2-s), is to be supplied by the user.

The kinetic reaction rate constants, k, for the solid-gas char reactions are determined by kinetic reaction rate constants adopted from published literatures as presented in Table 2.1. These rate constants are taken from Chen et al. (2000(a)). These kinetic reaction rate constants have to be carefully checked and adjusted if necessary so that their units are consistent with the unit of k (kg/m^2-s) in Eq. 2.54. The sources of these kinetic reaction rate constants are introduced and discussed below.

Table 2.1 Kinetic reaction rate constants for solid-gas reactions.

Reaction	***Rate Constant***	***Parameters***
$C(s) + ½O_2 \rightarrow CO$ (Combustion)	$k = AT^n \exp(-E/RT)$ $(kg/m^2\text{-}s\text{-}Pa^{0.5})$	$n = 0$ $A = 0.052\ kg/m^2\text{-}s\text{-}Pa^{0.5}$ $E = 6.1 \times 10^7\ J/kmol$
$C(s) + CO_2 \rightarrow 2CO$ (Gasification, Boudouard reaction)	$k = AT^n \exp(-E/RT)$ $(kg/m^2\text{-}s\text{-}Pa^{0.5})$	$n = 0$ $A = 0.0732\ kg/m^2\text{-}s\text{-}Pa^{0.5}$ $E = 1.125 \times 10^8\ J/kmol$
$C(s) + H_2O(g) \rightarrow CO + H_2$ (Gasification)	$k = AT^n \exp(-E/RT)$ $(kg/m^2\text{-}s\text{-}Pa^{0.5})$	$n = 0$ $A = 0.0782\ kg/m^2\text{-}s\text{-}Pa^{0.5}$ $E = 1.15 \times 10^8\ J/kmol$

2.6.2 Gas Phase (Homogeneous) Reactions

Three approaches are adopted to solve homogenenous gas- phase reactions: (a) eddy-dissipation model, (b) global equilibrium model, and (c) finite-rate kinetic model.

(a) Eddy-dissipation model takes into account the turbulent mixing of the gases. It assumes that the chemical reaction is faster than the time scale of the turbulence eddies. Thus, the reaction rate is determined by the turbulence mixing of the species. The reaction is assumed to occur instantaneously when the reactants meet. The net rate of production or destruction of a species (in kg/s) is given by the smaller of the two expressions below.

$$R = \nu' M A \rho \frac{\varepsilon}{k} \min\left(\frac{Y}{\nu' M}\right) \tag{2.55}$$

and

$$R = \nu' M B \rho \frac{\varepsilon}{k} \min\left(\frac{\Sigma Y}{\Sigma \nu' M}\right) \tag{2.56}$$

where ν' is the stoichiometric coefficient of reactant, ν'' is stoichiometric coefficient of product, M is the molecular weight of the species, ρ is the density of the species, A and B are constants. The chemical reaction is governed by large-eddy mixing time scale, k/ε. The smaller of the two Eqs. 2.55 and 2.56 is used because it is the limiting value that determines the reaction rate.

(b) Global equilibrium model.

(c) The finite-rate kinetic model calculates the reaction rate using an expression that takes into account temperature, and does not take into account the turbulent mixing of the species. The rate of destruction or production of a species, R (kg/m^3-s), in a reaction is calculated using Eq. 2.57 below,

$$R = M_W\left(\nu' - \nu''\right)\left(k\prod_{j=1}^{N}\left[C_j\right]^{\left(\eta' - \eta''\right)}\right) \tag{2.57}$$

where,

M_W = molecular weight (kg/kgmol)

ν' = stoichiometric coefficient of reactant

ν'' = stoichiometric coefficient of product

k = kinetic reaction rate constant (s^{-1})

$[C_j]$ = molar concentration of species j ($kgmol/m^3$)

η' = rate exponent of reactant species

η'' = rate exponent of product species.

Reaction rate constant, k, is usually expressed in an Arrhenius form, $k = AT^n\exp(-E/RT)$. The unit of k is s^{-1}. (Note that this is different from unit in Eq. 2.54 because it is reaction rate constant for homogenous gas phase reaction while Eq. 2.54 is for heterogeneous gas-solid reaction)

For each gas-phase homogeneous reaction in this study, the reaction rates based on both the eddy-dissipation and finite-rate kinetic rate are calculated. The smaller of the two is used as the reaction rate. The summary of the kinetic reaction rate constants for the gas-phase homogeneous reactions are presented in Table 2.2. The reaction rate constant for the reaction $CO + ½\ O_2 \rightarrow CO_2$ is taken from Westbrook and Dryer (1981). The reaction rate constant for the water-shift reaction ($CO + H_2O_{(g)} \rightarrow CO_2 + H_2$) listed in the table has been reduced from the original value by Jones and Lindstedt (1988). Jones and Lindstedt obtained the reaction rate constant through experiment where catalyst was used. Since catalyst is not used in this study, the reaction rate constant would not be correct. The original reaction rate constant by Jones and Lindstedt was used in the preliminary study. It was found that the syngas contained no H_2O with very low CO and very high H_2 and CO_2. This indicates that the water-shift reaction was dominant. However, it is known that water-shift reaction is a slow reaction at temperature above

1400 K, which where the gasifier operation temperature is. The reaction rate constant for the water-shift was then purposely slowed down to make the syngas composition consistent with that in the actual similar commercial entrained-flow gasifier with coal-slurry feed from bottom operated by Wabash River Energy Ltd. (Wabash River Energy Ltd., 2000).

Table 2.2 Kinetic reaction rate constants for finite-rate gas phase reactions.

Reaction	**Rate Constant**	**Parameters**
$CO + ½\ O_2 \rightarrow CO_2$	$k = AT^n \exp(-E/RT)$ (s^{-1})	$n = 0$ $A = 2.2x10^{12}$ $E = 1.67x10^8$ J/kmol
$CO + H_2O(g) \rightarrow CO_2 + H_2$ (Watershift)	$k = AT^n \exp(-E/RT)$ (s^{-1})	$n = 0$ $A = 2.75x10^2$ $E = 8.38x10^7$ J/kmol
$C_2H_2 + O_2 \rightarrow 2CO + H_2$	Eddy-dissipation only	

2.7 Gasification Models

There are two gasification models used in this study: (a) finite-rate gasification model and (b) instantaneous gasification model.

2.7.1 Finite-Rate Model

In the finite-rate model, the flow (continuous phase) is solved in Eulerian form as a continuum while the particles (dispersed-phase) are solved in Lagrangian form as a discrete phase. Stochastic model is employed to model the effects of turbulence on the particles. The continuous phase and discrete phase are communicated through drag forces, lift forces, heat transfer, mass transfer, and species transfer. The finite-rate combustion model is used for the heterogeneous reactions. Both the finite-rate and eddy-dissipation models are used for the homogeneous reactions, and the smaller of the two is used as the reaction rate. The finite-rate model calculates the reaction rates based on the kinetics, while the eddy-dissipation model calculates based on the turbulent mixing rate of the flow. Gasification or combustion of coal particles undergoes the following global processes: (i) evaporation of moisture, (ii) devolatilization, (iii) gasification to CO and (iv) combustion of volatiles, CO, and char.

For solid particles, the rate of depletion of the solid due to a surface reaction is expressed as a function of kinetic rate, solid species mass fraction on the surface, and particle surface area

as described in Section 2.6.1 earlier. The reaction rates are all global net rates, i.e., the backward reaction, calculated by equilibrium constants, are included in the global rate. The water evaporation for the liquid droplets is calculated as described in Section 2.5.2.

2.7.2 Instantaneous Gasification Model

The interphase exchange rates of mass, momentum and energy are assumed to be infinitely fast. Carbon particles are made to gasify instantaneously, thus the solid-gas reaction process can be modeled as homogeneous gas combustion reactions. This approach is based on the locally-homogeneous flow (LHF) model proposed by Faeth (1987), implying infinitely-fast interphase transport rates. The instantaneous gasification model can effectively reveal the overall reaction process and results without dealing with the details of the otherwise complicated heterogeneous particle surface reactions, heat transfer, species transport, and particle tracking in turbulent reacting flow. The eddy-dissipation model is used to model the chemical reactions. This model can significantly reduce the computational time but can only provide a qualitative trend of gasification process. Although the instantaneous gasification model is crude, it catches the effect of thermal-fluid field (including turbulence structure) on chemical reactions, which are not readily available from the global equilibrium method.

CHAPTER THREE
COMPUTATIONAL METHOD

3.1 Computational Scheme

The major steps in the CFD simulation are divided into three: (a) preprocessing, (b) processing, and (c) postprocessing.

3.1.1 Preprocessing

Preprocessing refers to the geometry generation, geometry mesh, model specifications and boundary specifications. Before any calculation can be done, computational domain has to be created. The commercial preprocessing software GAMBIT is used to generate and then mesh geometries (computational domains) in this study. In this study, quad meshes are used in simple 2-D domains, while tetrahedral meshes are used in 3-D domains. Once a computational domain geometry has been meshed in GAMBIT, it is imported into the commercial CFD code FLUENT (Version 6.3.23) from ANSYS, Inc.. Then, the appropriate models and boundary conditions are set.

3.1.2 Processing

In the processing step, calculations are performed to obtain the solution for the governing equations. As indicated earlier, FLUENT is used in this study. FLUENT is a finite-volume based CFD solver. Solution is obtained through iteration until convergence criteria, which are set by the user, are satisfied. Residuals are used as means to determine the convergence. Residuals are the imbalanced errors in the governing equations over all the cells in the computational domain.

3.1.3 Postprocessing

Postprocessing involves analyzing and interpreting solution obtained. Charts and various visualization schemes can be employed to aid in understanding the physics of the solution.

3.2 Numerical Procedures

Segregated solution method is employed in solving the governing equations. Segregated solution method means that governing equations of continuity, momentum, energy, and species transport are solved sequentially (segregated from one another). The non-linear governing equations are implicitly linearized, which means that each unknown value is computed using a relation that includes both existing and unknown values from neighboring cells. As a result, each unknown will appear in more than one equation in the linear system produced. Thus, these equations must be solved simultaneously in order to obtain the unknown quantities.

The governing equations are discretized spatially to yield discrete algebraic equations for each control volume. The second order scheme is used as the discretization scheme. The SIMPLE algorithm (Patankar, 1980) is used to couple the pressure and velocity.

There are three types of boundary conditions used:

a. Mass flow rate inlet – All the inlet surfaces are defined as mass flow rate inlets. Mass flow rate, temperature of the gas mixture, and mass fractions of all species are specified.
b. Pressure outlet – The outlet surface is assigned as a pressure outlet boundary. Pressure, temperature, and species mass fractions of the gas mixture just downstream of the outlet (outside of the domain) are specified. This information does not affect the calculations inside the computational domain but will be used if backflow occurs at the outlet.
c. Walls – The outside surfaces are defined as wall boundary. The walls are stationary with no-slip condition imposed (zero-velocity) on the surface. The heat flux on the walls is set to 0 (adiabatic walls).

The dispersed phase enters the computational domain through injection points. Each injection is modeled as a group streams. It is through each of this stream the particles enter the computational domain. When the geometry is 2D, the fuel injections are "group" injections (terminology in the FLUENT software) where mass flow rate for each stream is specified. In this study, each injection is set to have 20 streams. When the geometry is 3D, the "surface" injections are used. The surface where an injection is located is specified. A stream will then be placed at the center of each face on that particular surface. The total mass flow rate for the injection is specified, and is equally divided among the streams. For both "group" and "surface" injections, velocity, size, and temperature of the particles at these injection points are specified.

As mentioned in Chapter 2, the Eulerian-Lagrangian method is adopted to solve the multiphase problem. Eulerian method is used for the continuous phase, and the Lagrangian method for the disperse phase. The iterations are conducted alternatively between the continuous and the dispersed phases. The continuous phase is updated in the next iteration based on the dispersed phase calculation results, and the process is repeated.

The detailed steps of the calculation process are given below. Figure 3.1 depicts the flow chart of these steps.

1. Fluid properties are updated based on the current solution or the initialized solution.
2. The momentum equations are solved using the current values of pressure and face mass fluxes to get the updated velocity field.
3. Equation for the pressure correction is calculated from the continuity equation and the linearized momentum equations since the velocity field obtained in step (2) may not satisfy the continuity equation.
4. The pressure correction equations obtained from step (3) are solved to correct the pressure and velocity fields, and face mass such that the continuity equation is satisfied.
5. The equations for turbulence are solved using the updated values of the other variables.
6. The homogeneous gas phase reactions are solved. Production and consumptions of each species are calculated.
7. Enthalpy change due to reaction is calculated.
8. The species transport equations are solved. Changes in the species mass fraction due to reactions in steps 6 and 12 appear as source or sink terms in the species transport equation.
9. The energy equation is solved. This includes source or sink terms due to reactions in steps 6 and 7.
10. Particles (dispersed phase) are tracked one by one. Forces on the particles (drag, lift) are calculated.
11. Particle heat transfer is calculated.
12. Heterogeneous reactions (gas-solid) are calculated. Production and consumptions of each species are calculated.
13. Enthalpy changes due to reaction are calculated.

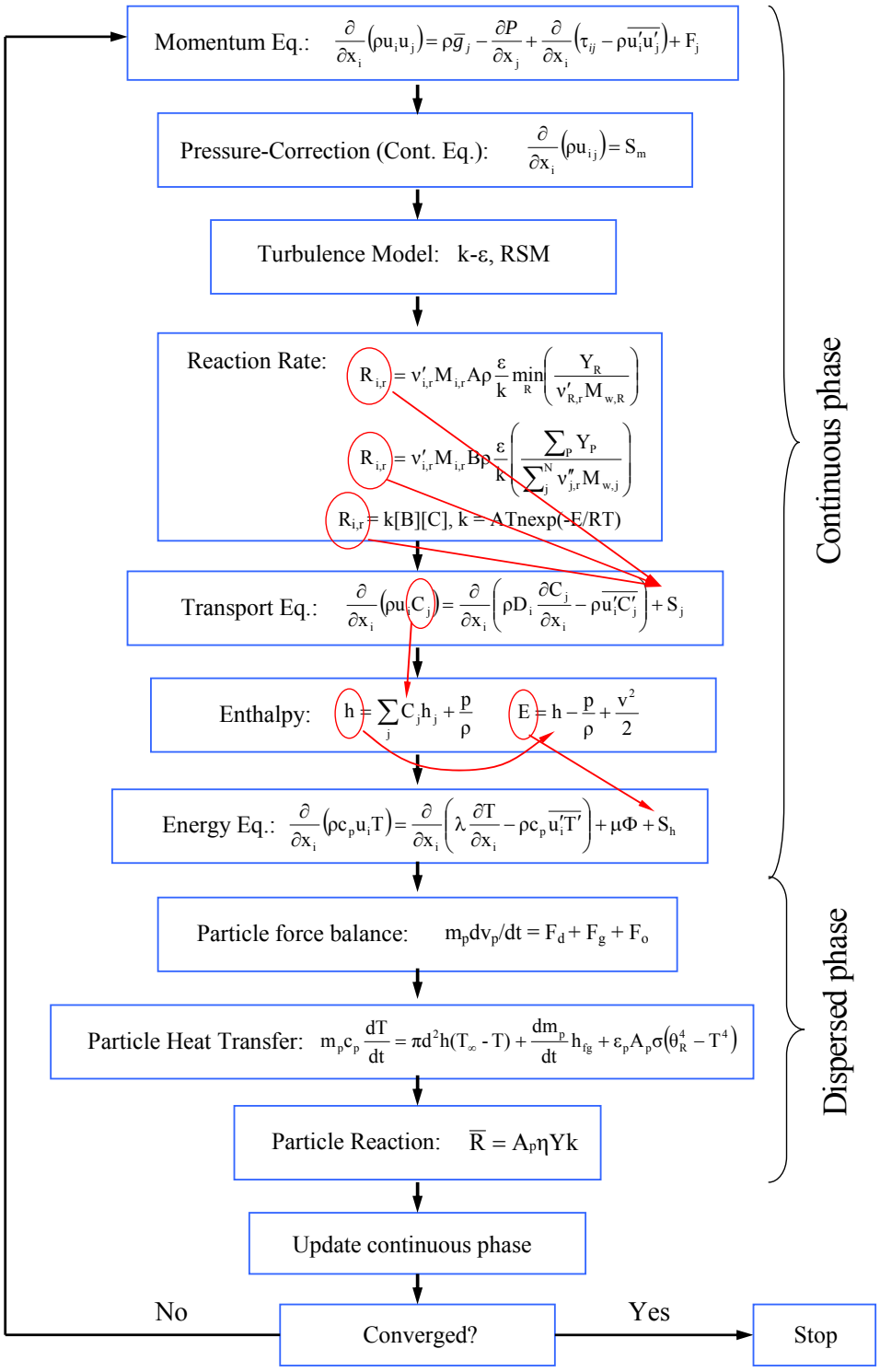

Figure 3.1 Outline of numerical procedures.

14. The species transport equations are solved. Changes in the species mass fraction due to reactions in step 12 appear as source or sink terms in the species transport equation.
15. The energy equation is solved. This includes source or sink terms due to reactions in steps 13 and 14.
16. Continuous phase properties are updated based on the dispersed phase.
17. The equation is checked for convergence.
18. If convergence criteria are met, the process is stopped. Otherwise, the process is repeated from step 1.

Converged results are obtained when the residuals satisfy mass residual of 10^{-3}, energy residual of 10^{-5}, momentum and turbulence kinetic energy residuals of 10^{-4}. These residuals are the summation of the imbalance in each cell, scaled by a representative for the flow rate. Figure 3.2 shows a graph of typical variable residuals. The fluctuation shown in Fig. 3.2 is a normal display of calculation alternating between continuous and dispersed phases. The computation was carried out in parallel processing on two dual-core Pentium clusters with 12 nodes each.

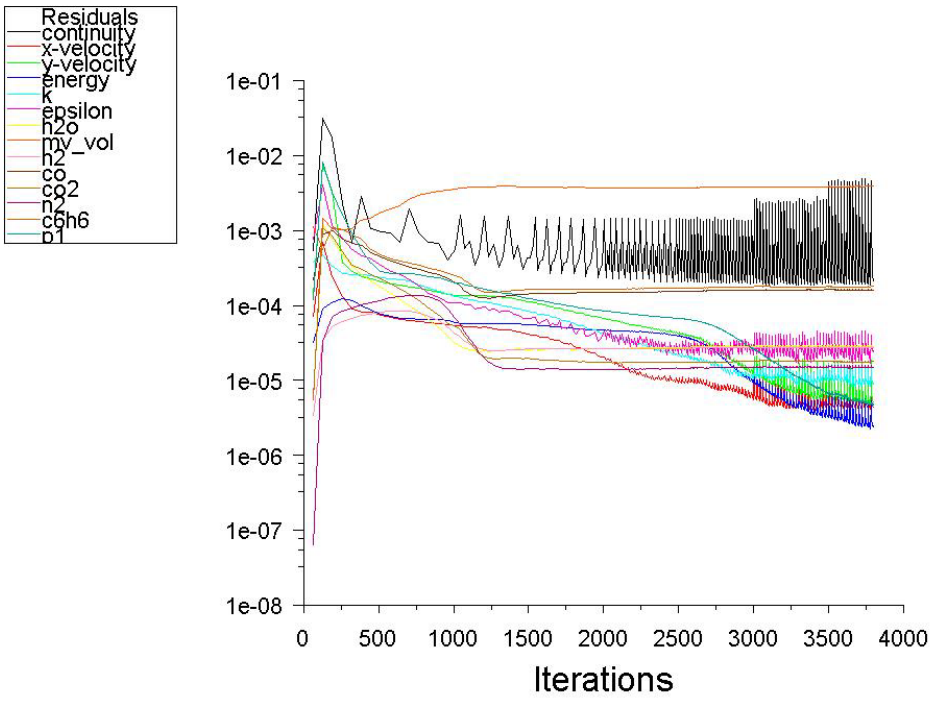

Figure 3.2 Typical variable residuals during calculation.

Material properties:

Variable properties for enthalpy, specific heat and conductivity are used for each species. The specific heat is calculated using piecewise-polynomial relation as a function of temperature defined as

$$\text{For } T_{min1} < T < T_{max1},\ F(T) = A_1T + A_2T^2 + A_3T^3 + ...$$
$$\text{For } T_{min2} < T < T_{max2},\ F(T) = B_1T + B_2T^2 + B_3T^3 + ... \quad (3.1)$$

The specific heat of the whole continuous phase, which is a mixture of species, is also variable and is calculated as a mass fraction average of the pure species heat capacities defined as

$$F = \sum_i Y_i F_{,i} \quad (3.2)$$

Where F is the property (enthalpy, specific heat, or conductivity), Y_i is the mass fraction of species i and F_i is the property of species i.

Simulation procedures:

As mentioned earlier, the calculations for the continuous phase and the dispersed phase are performed alternately. The pathlines of the particles are calculated based on the continuous phase flow field. Thus, a good continuous phase flow field is needed. This can be a problem in the beginning of the simulation where usually the flow field has not yet been established. As a remedy, only the equations for the continuous phase are solved in the beginning of a simulation while the equations for the dispersed phase and chemical reactions are not solved. The purpose is to obtain a good flow field before incorporating the dispersed phase. Usually 300 iterations are performed to let the continuous phase flow field develop. After this, the dispersed phase equations and chemical reactions equations are solved.

Patching temperature:

The initial gas temperature in the gasifier is set the same as the gas temperature at inlets, which is 420 K in this study. Gasification will not occur at this temperature. The energy at this temperature is below the activation energy of the reactions, thus the reactions will not occur. High temperature is needed to start the reactions. Thus, the domain needs to be patched with high temperature. This process is akin to using a lighter to ignite combustion inside a combustor. This temperature patching is done by setting the temperature of the cells near the injections to

1500 K, which is high enough to start the reactions. After the temperature patching, one dispersed phase iteration step is performed, followed by one continuous phase iteration.

Dispersed phase and continuous phase iterations:

As shown in Figure 4.1, the continuous phase is updated after each iteration in dispersed phase. The dispersed phase affects the continuous phase through source terms in the momentum, species transport, and energy equations. These changes in the continuous phase equations will affect the convergence. Normally, twenty continuous phase iterations are performed before changing to the dispersed phase iteration. This allows the continuous phase to settle down before the next dispersed phase iteration and can help the simulation converge faster.

However, it was found during preliminary study, that the practice of performing 20 continuous phase iterations per iteration in dispersed phase in the beginning can sometimes cause the flame to die out. Theoretically, once the char combustion occurs, the energy released should be enough to maintain the flame. However, this is not the case in the simulation.

The reason the flame dies out is the following. During the dispersed phase calculation, char particles are tracked and the heterogeneous reaction ($C + ½ O_2 \rightarrow CO$) is calculated. The heterogeneous reaction produces CO and releases energy. In the next continuous phase iteration, the homogeneous reaction is calculated where CO produced by the heterogeneous reaction is combusted. This continuous phase iteration is repeated 20 times without performing any dispersed phase iteration at all. In each continuous phase iteration, CO is combusted but no CO is being produced by the heterogeneous reaction. As a result, CO in cells near the injector will be totally consumed. Once CO in a particular cell is totally consumed, no reaction will happen and the temperature in that cell will decrease as gasification reactions (endothermic) take place. If the temperature decreases below the minimum temperature required for char combustion, char will not react in the next dispersed phase iteration.

As the iterations continue in the continuous phase, it can be seen that hot temperature region near the injections/inlets is slowly convected downstream and is replaced by the cold gas from the inlets. Thus, the particles will not react near the injector but instead further downstream. The location where char combustion starts to occur slowly moves downstream toward the outlet until it finally moves out of the computational domain. All the flames die out and no reaction will occur any more inside the computational domain.

To avoid the flame from dying out, the number of continuous phase iterations per dispersed phase iteration is gradually increased -- 1, 5, 10, and finally 20. After temperature patching, one dispersed phase iteration is performed followed by one continuous phase iteration. Then one dispersed phase iteration is done followed by five (5) continuous phase iterations until the flame is stabilized. Typically this would take about 200 steps. Then, ten (10) continuous phase iteration per dispersed phase iteration is done for a total of 200 steps. Finally, it is increased to 20 continuous phase iterations per discrete phase iteration until convergence is achieved. In an extreme case, one continuous phase iteration per single dispersed phase iteration is performed as long as is needed to ensure the flame stabilizes.

Under-relaxation factor:

The under-relaxation factor for variables can help convergence behavior of the variables. Equation 3.3 defines how the under-relaxation factor, α, affects the value of the variable.

$$\phi = \phi_{old} + \alpha \, \Delta\phi \tag{3.3}$$

ϕ is the variable and $\Delta\phi$ is the change in the variable. The value of under-relaxation factor, α, ranges from 0 to 1. The smaller the under-relaxation factor is, the smaller the change in the variable during the iteration. It can help stabilize the convergence but requires more iteration steps to reach convergence.

The under-relaxation factors are set to 0.3 for pressure, 0.7 for momentum, 0.1 for dispersed phase, and 0.8 for species, k and ε. The under-relaxation factor for the energy is set to 0.4 in the early stage of the simulation to aid in ensuring the flame or char combustion does not die out (as explained earlier). The under-relaxation factor is then increased to 0.7 once the reactions have stabilized.

Temperature Limits:

During preliminary study, it was found that the temperature during iterations could sometimes go as low as 1 K and as high as 5000 K. It is known that the gas temperature in a real gasifier will never reach 1 K or 5000 K. Thus, these extremely low temperature (1 K) and extremely high temperature (5000 K) are not realistic. To avoid these non-realistic temperatures, the lower and the upper temperature limits are set to 273 K and 3500 K, respectively. It is obvious that the gas temperature inside gasifier will never go below 273 K. The upper limit

3500 K is well above the typical adiabatic flame temperature of coal (2500 K). These temperature upper and lower limits give the CFD solver a good temperature range of where the solution should be bounded. It will prevent the CFD solver from going astray and getting the wrong or unrealistic solutions.

CHAPTER FOUR
RESULTS AND DISCUSSIONS

The study begins with parametric study of effects of various models which are involved in the numerical simulation, such as turbulence and devolatilization models. Findings from parametric study are then applied to the investigation of finite-rate model vs. instantaneous gasification model. The parametric study is concluded with investigation of actually gasifier operation parameters, such as dry-fed vs. wet-fed, oxygen-blown vs. air-blown, and fuel distributions.

Although a two-stage gasifier is used, most of the parametric study is conducted without turning on the second-stage. The results of employing the second stage is specifically investigated when study of other parameters are completed.

4.1 Effect of Turbulence and Devolatilization Models on Gasification Simulation

In the gasification, the transports of CO concentration and heat from the coal particle surface layer to the surrounding gases depend on the thermal-flow behavior. Therefore, turbulence modeling and stochastic tracking of fluctuating particles will affect the simulated results. In addition, the different coal particle size will affect coal surface/volume ratio and result in different gasification performance. To shed some light on the effect of above variables, a study is conducted to investigate the effects of different turbulence models, devolatilization models, coal particle diameters, and stochastic tracking time constant on the outcome of the simulation.

A comprehensive fundamental investigation starts on 2-D geometry. Based on the 2-D results, more adequate models are selected and implemented in the 3-D study. In the simulations, the buoyancy force is considered, varying fluid properties are calculated for each species and the gas mixture, and the walls are assumed impermeable and adiabatic. The flow is steady and no-slip condition (zero velocity) is imposed on wall surfaces.

Indonesian sub-bituminous coal is used as feedstock in this study. Its composition is given in Table 4.1 and the feed rates used are given in Table 4.2. The moisture content of the coal is 8.5 by weight. The 2-D feed rate is prorated lower from the 3D feed rate to an extent that the injection velocity is comparable to the 3-D case. The coal/water weight ratio of the coal

slurry is 60%-40%. The oxidant used is 95% O_2 and 5% N_2. Oxidant/coal slurry feed rate used in Table 4.2 gives O_2/coal equivalence ratio of 0.3. Gasifier operating pressure is 24 atm.

The walls are assigned as adiabatic with internal emissivity of 0.8. The boundary condition of the discrete phase at walls is assigned as "reflect", which means the discrete phase elastically rebound off once reaching the wall. At the outlet, the discrete phase simply escapes/exits the computational domain

The volatile ($CH_{2.121}O_{0.5855}$) is thermally cracked into CO, H_2, and C_6H_6 according to reaction,

$$CH_{2.121}O_{0.5855} \rightarrow 0.5855\ CO + 0.8532\ H_2 + 0.06907\ C_6H_6 \quad (4.1)$$

and the C_6H_6 is modeled to be further "gasified" into CO and H_2 by reaction

$$C_6H_6 + 3\ O_2 \rightarrow 6\ CO + 3\ H_2. \quad (4.2)$$

The meshed 2-D and 3-D computational domains are given in Figures 4.1(a) and (b), respectively. A grid sensitivity study of both the 2-D and 3-D geometries is conducted. Four different 2-D grids including the coarse grid (33k cells), medium grid (86k cells), and fine grids (135k and 215k cells) are used. In the 3-D geometry, three different grids are used including the coarse grid (148k cells), medium grid (969k cells) and fine grid (1,684k cells).

The difference of temperature distributions for all four different grids in the 2-D geometry is very small, as shown in Figure 4.2. Thus, to save the computational time, the medium grid of 86k cells is chosen for further parametric studies. The near-wall y+ of the 2-D grid is 118. The results of the 3-D geometries show that the temperature distributions of the medium and fine grids are almost identical. Again, to save computational time, the medium grid of 969k cells is chosen. The near-wall y+ of the 3-D grid is 190, which is adequate to use the wall-function for turbulence models.

Table 4.1 Moisture-free (MF) compositions of Indonesian sub-bituminous coal.

Proximate Analysis (MF), wt%		***Ultimate Analysis (MF), wt%***	
Volatile	51.29	C	73.32
Fixed Carbon (FC)	47.54	H	4.56
Ash	1.17	O	20.12
	100.00	N	0.72
		S	0.11
		Ash	1.17
			100.00

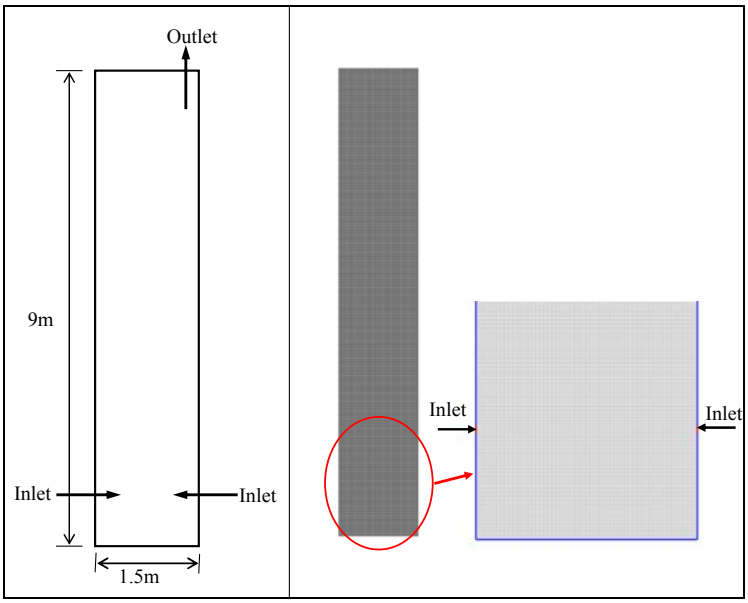

(a) Simplified 2-D entrained flow gasifier

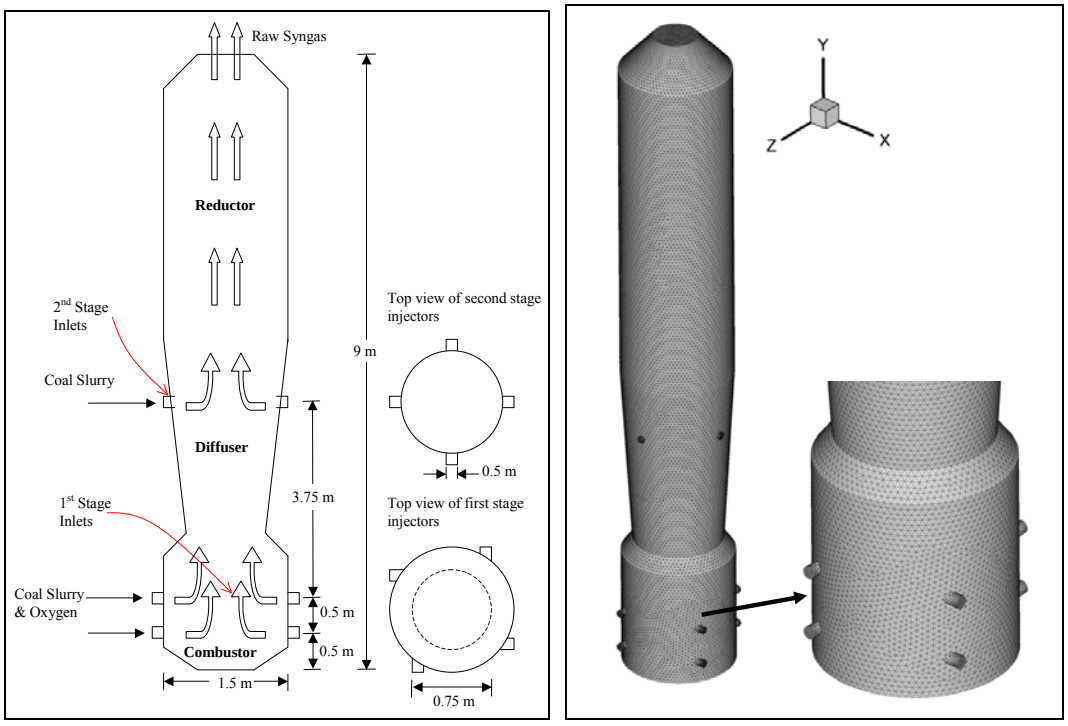

(b) 3-D one-stage entrained flow gasifier

Figure 4.1 Schematic and meshed computational domain of (a) a simplified 2-D entrained flow gasifier and (b) 3-D one-stage entrained flow gasifier (adopted from Bockelie et al., 2002a) configurations.

Table 4.2 Coal slurry and oxidant feed rates.

	Feed rate (kg/s)	
	2D gasifier	**3D gasifier**
Coal slurry	18.15	21.39
Oxidant	6.04	7.12

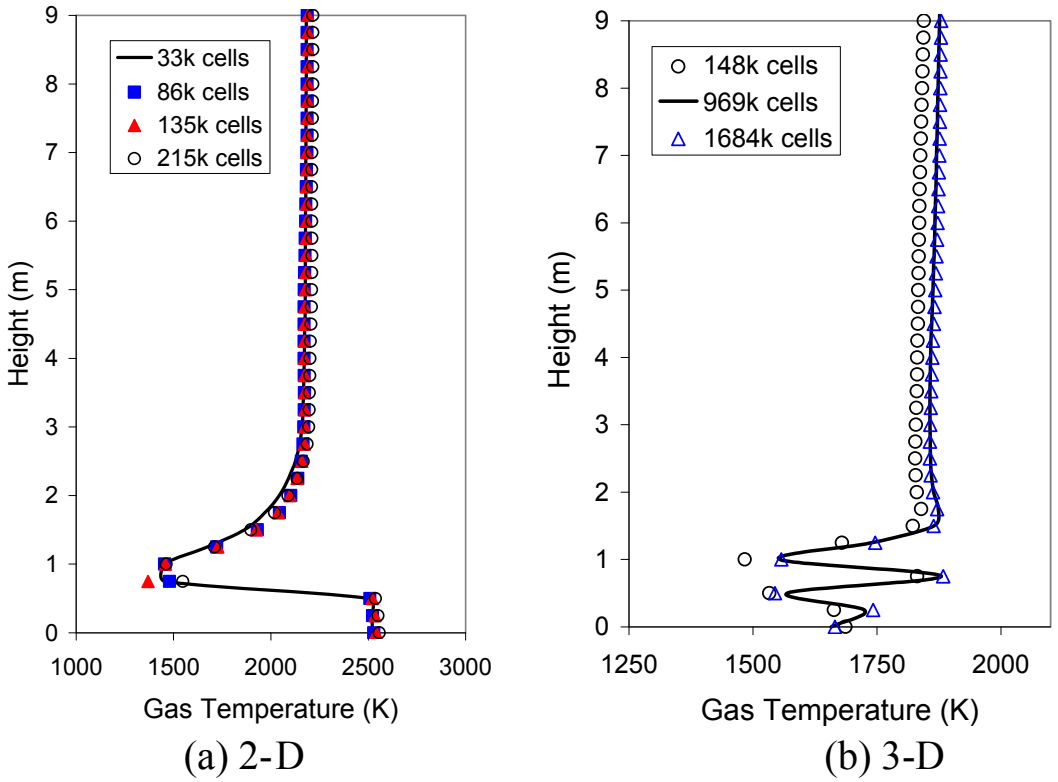

Figure 4.2 Grid sensitivity study: temperature distributions for the different grid sizes of the 2-D and 3-D geometries.

4.1.1 Effects of Time Scale in the Stochastic Particle Tracking

Stochastic particle tracking employs the concept of integral time scale, which defines the time spent in turbulent motion along the particle path. The integral time scale can be calculated using the empirical formula $T = T_C\, k/\varepsilon$, where T_C is the time constant, k is the turbulence kinetic energy and ε is the turbulence dissipation rate. The suggested value of T_C is 0.15. However, since this value of 0.15 was empirically obtained for a specific flow, it is not clear whether this value is adequate for the present thermal-flow field in a gasifier. Hence, a sensitivity study is

conducted by comparing the results of using various T_C values with the reference case without stochastic tracking (i.e. $T_C = 0$). The result in Figure 4.3 shows that the mass-weighted temperature and various species distribution curves move closer to the reference curve when the T_C value is decreased from 0.15 to 0.00015. The moderate value of 0.015 is chosen so the artificial turbulence perturbation will not be overdone.

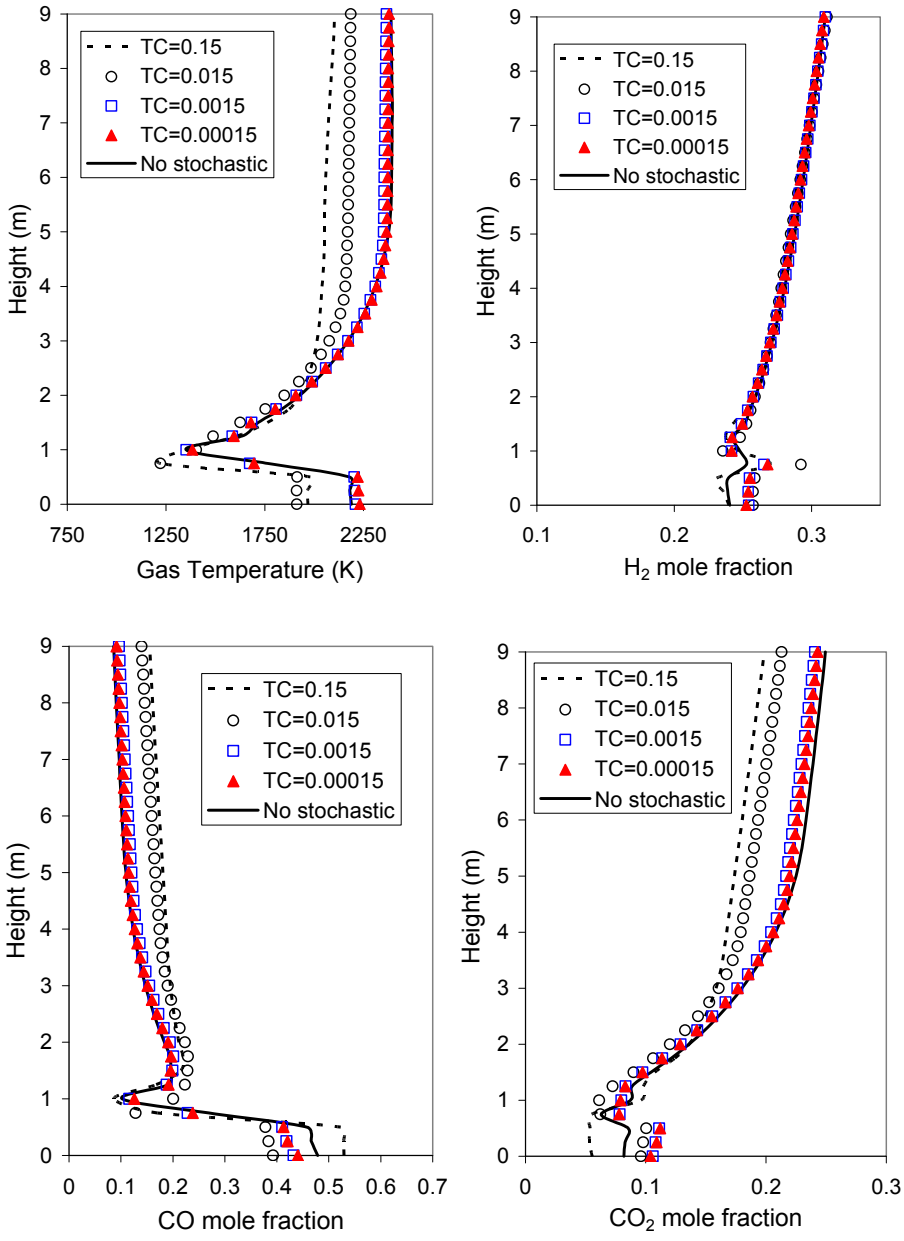

Figure 4.3 Mass-weighted average temperature and species using standard k-ε model with different stochastic tracking T_C (time scale) constants.

4.1.2 Effects of Five Turbulence Models

The effects of turbulence models are shown in Figure 4.4 in terms of mass-weighted averages of temperature and species distribution along the height of the gasifier. The comparison shows that standard k-ε, RSM, and k-ω SST models give consistent and similar results while the results from the k-ω and k-ε RNG models deviate from the consistent trend. Further examination shows although standard k-ε, RSM, and k-ω SST give similar results above the fuel injection location, the results below the injection location show the k-ω SST model deviates from the standard k-ε and the RSM models. The similar results from the standard k-ε and the RSM models provide the advantage of using the standard k-ε model to conduct parametric studies to significantly save the computational time while the high-order RSM model is used to "verify" the relatively simpler standard k-ε model.

Regarding the k-ω SST model, although it is more complicated than the standard k-ε model by incorporating the low-Reynolds number effect and near-wall dissipation rate, it does not model the anisotropic Reynolds stresses as in the RSM model. Since the k-ω SST model does also confirm the consistency of the results of the standard k-ε model above the injection location, all the parametric studies are then conducted by the standard k-ε model to significantly save the computational time with results acceptable to this study.

4.1.3 Effect of Devolatilization Models

Particle tracks for cases with different devolatilization rates are presented in Figure 4. 6. The overall tracks look very similar, except that the tracks for the Kobayashi model are a little bit longer. This means that the particle reaction (oxidation and gasification in Eq. R1.1. R1.2, and R1.3) finishes later than that of the other models. The volatile mole fraction concentration contour plot in Figure 4. 6 also confirms that the devolatilization process using the Kobayashi model seems to starts later compared to other models with a smaller high-concentration core. Thus, it appears that the Kobayashi devolatilization model, which utilizes two weighted competing rates, is slower than the other models. Since particle reaction occurs after most of the moisture and volatiles have been released from the particle, as a result of the relatively slow devolatilization rate, the particle reaction starts and finishes much later compared to the other models.

The particle tracks of the constant rate model and single rate model cases are very similar. The temperature and species distributions for both cases shown in Figure 4.5 as well as the exit syngas composition listed in Table 4.3 are also similar. In summary, Kobayashi models predicts higher exit gas temperature and CO_2, but lower CO and hence lower syngas heating value. CPD and single rate models produce more consistent results.

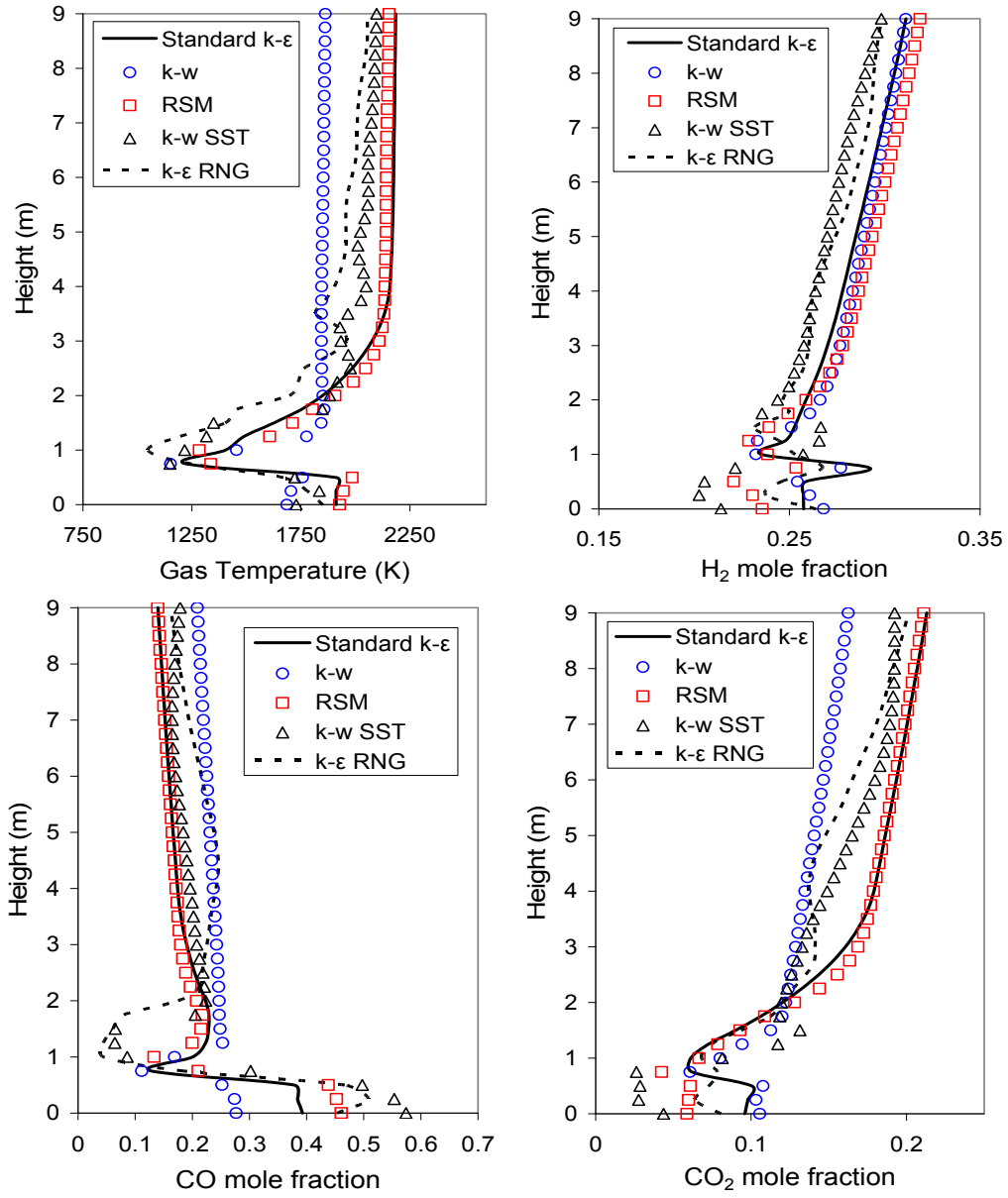

Figure 4.4 Mass-weighted average temperature and species for cases with five different turbulence models.

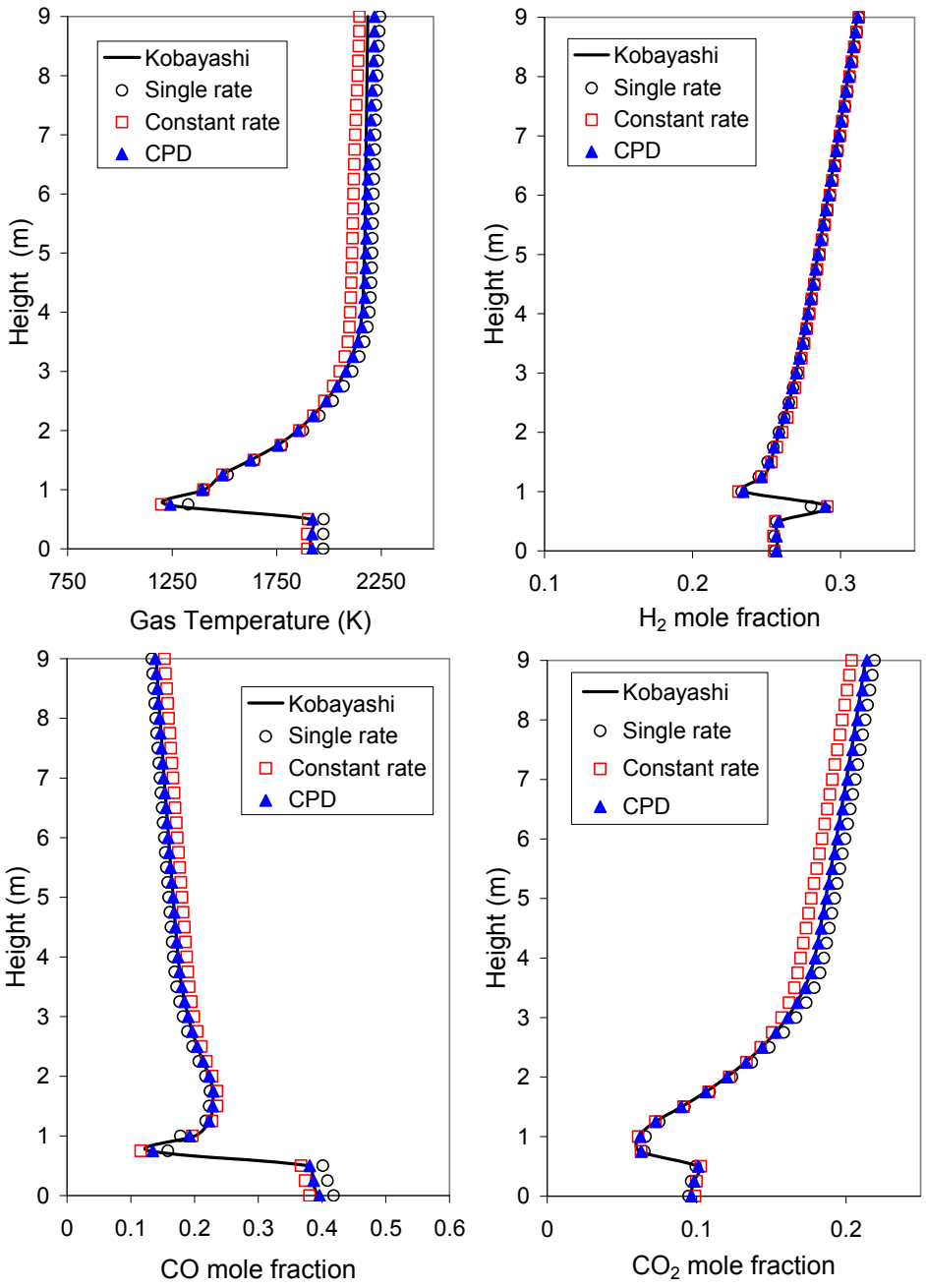

Figure 4.5 Mass-weighted average temperature and species for standard k-ε model with different devolatilization models.

4.1.4 Effect of Particle Size

The coal slurry particles are assumed to be spherical. The coal slurry particle of 200 μm is assigned to the baseline case. Two other different coal slurry particle diameters, 100 μm and 300 μm, are also simulated for comparison. It is understood that the particle distribution in the

real operation is not uniformly distributed. However, uniform particle size is assigned in each case to allow a more convenient way to track the change of particle size during the gasification process as well as to provide a clear comparison of the effect of particle sizes. The particle tracks presented in Figure 4.7 show that 100-μm particles require more time to completely react than the 200-μm particles, which seems to be counterintuitive because the surface/volume ratio of smaller particle is larger than the larger particles and they should react more quickly. To look for explanation to this phenomenon, the focus is moved towards examining the relative motion between the particles and gases. Figure 4.7 also presents side by side the particle tracks (discrete phase) and the streamlines of the continuous phase (gas). It can be seen that the tracks of the 100 μm particles follow the streamlines of the continuous flow; whereas the 200-μm particles deviate from the continuous flow streamlines. It seems that the deviation of the 200-μm particles from the streamlines increases the slip velocity which results in enhanced convective transports of heat and species concentrations. In the meantime, the mixing of the particles also augments particle reactions. Thus the 200-μm particles require less time to completely react than the 100-μm particles. When the particle diameter is increased to 300 μm, the residence time for reaction increases. Other than the factor of reduced surface/volume ratio, it can be seen that the particles actually have much more inertia after fuel injection and are able to impinge on the opposite jet and split the particle streams in both above and below the injection location. Strong recirculation zones, which contribute to trapping particles, lengthen the residence time.

Mass-weighted temperature and species distribution curves in Figure 4. 8 show that there is a large exit temperature difference about 640K (1779 K vs. 2426K) between using smaller and larger particles (100 μm vs. 300 μm). The temperature near the gasifier bottom for the 300-μm case is much higher than those of the 100-μm and 200-μm cases. This is because the particles that impinge at the center and then go downward eventually burn out near the gasifier bottom. The exit syngas composition listed in Table 6 shows that the smallest particles give the highest syngas heating value. Generally speaking, larger particles produce more H_2, less CO, higher exit gas temperature, and more CO_2, and hence less efficient.

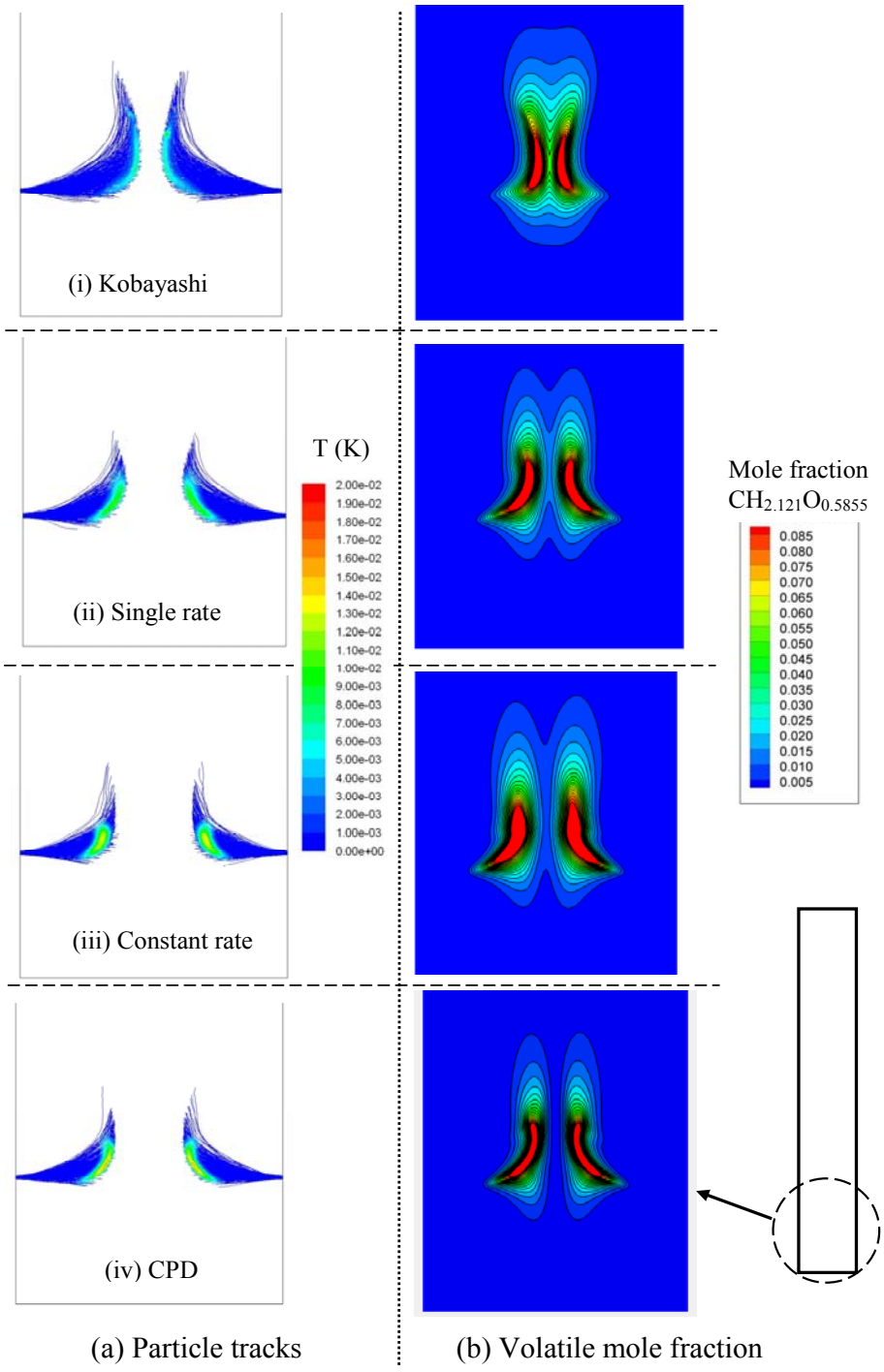

Figure 4.6 Effect of four devolatilization models of 200 μm particle: (a) particle tracks colored by devolatilization rate (kg/s) and (b) volatile mole fraction.

Table 4.3 Exit gas temperature and compositions for the 2-D case with different devolatilization models.

Parameters	***Kobayashi***		***Single rate***		***Constant rate***		***CPD***	
Exit temperature, K	2218		2133		1992		2100	
Components at exit:								
	Mole fraction	Mole no. (mole)	Mole fraction	Mole no. (mole)	Mole fraction	Mole no. (mole)	Mole fraction	Mole no. (mole)
CO	14.0%	72.86	15.4%	80.73	18.1%	95.80	15.8%	83.00
H_2	28.9%	150.41	28.5%	149.41	28.1%	148.72	28.2%	148.14
CO_2	22.9%	119.19	21.5%	112.71	19.5%	103.21	21.0%	110.31
$CH_{2.121}O_{0.5855}$	0.0%	0.00	0.0%	0.00	0.0%	0.00	0.0%	0.00
H_2O	33.3%	173.31	33.6%	176.14	33.4%	176.77	34.0%	178.60
C_6H_6	0.0%	0.00	0.0%	0.00	0.0%	0.00	0.0%	0.00
N_2	0.9%	4.68	1.0%	5.24	0.9%	4.76	1.0%	5.25
C	0.0%	0.00	0.0%	0.00	0.0%	0.00	0.0%	0.00
Heating value (MJ/kg)	5.9		6.1		6.5		6.1	

Table 4.4 Exit gas temperature and compositions for the 2-D case with different coal slurry sizes.

Parameters	***100 μm***		***200 μm***		***300 μm***	
Exit temperature, K	1839		2218		2252	
Components at exit:						
	Mole fraction	Mole no. (mole)	Mole fraction	Mole no. (mole)	Mole fraction	Mole no. (mole)
CO	24.0%	128.04	14.0%	72.86	12.9%	67.20
H_2	26.3%	140.31	28.9%	150.41	29.8%	155.25
CO_2	15.5%	84.13	22.9%	119.19	23.8%	123.99
$CH_{2.121}O_{0.5855}$	0.0%	0.00	0.0%	0.00	0.0%	0.00
H_2O	33.3%	180.75	33.3%	175.03	32.6%	171.03
N_2	0.9%	4.89	0.9%	4.73	0.9%	4.72
C	0.0%	0.00	0.0%	0.00	0.0%	0.00
Heating value (MJ/kg)	7.1		5.9		5.9	

4.1.5 Three-Dimensional Gasifier

Using the parametric study of 2-D results, the selected turbulence model (standard k-ε turbulence), devolatilization model (Kobayashi) and stochastic tracking time constant (T_C = 0.015) are employed to conduct 3-D gasifier simulation with 200 μm particles. The gasifier is a 2-stage gasifier, but only the first-stage injectors are used with the second-stage injectors being turned off in this study. The diameter and the height of the gasifier is the same as that of the 2-D one.

Figure 4.10 shows the temperature and species distributions on the vertical center plane of the gasifier. The close-up view of the combustor section is shown in Figure 4.11. The hottest region in the combustor section occurs in the region near the wall as pictured in Figure 4.11. The O_2 distribution, also pictured in Figure 4.11, shows that O_2 does not travel far from the injectors before it is fully depleted. Particle tracks from one injector given in Figure 4.9 show that particle temperatures do not reach above 1000 K until the particles nearly reach the area of the next injector downstream at higher elevation. During that time, water evaporates and devolatilization follows. Once the particles have passed the downstream first-stage second-level injectors, they react with the O_2 injected through the second-level injectors. The top view shows that some high-temperature particles burn out near the wall and contributes to the high-temperature region near the combustor wall.

Gas pathlines presented in Figure 4.12 show that the tangential injection creates a helical flow and particle paths which are essential for lengthening the residence time. The exit gas temperature and syngas compositions are listed in Table 4.5. Exit gas temperature in the 3-D case is 1883 K, which is roughly 400 K lower than that of the 2-D case indicating more energy is consumed for gasification. The 3-D case gives lower H_2 and CO_2 mole fractions (2.7 and 7.8 percentage points lower, respectively) and higher CO mole fraction (10.2 percentage points higher) than the 2-D case. The 3-D case results in 38% higher heating value (8.0 vs. 6.4 MJ/kg) as expected because 3-D domain provides longer residence time and allows better gasification performance.

Table 4.5 Exit gas temperature and compositions for the 3-D case compared to the 2-D case.

Parameters	***2-D***		***3-D***	
Exit temperature, K	2218		2133	
Components at exit:				
	Mole fraction	Mole no. (mole)	Mole fraction	Mole no. (mole)
CO	14.0%	72.86	23.5%	293.06
H_2	28.9%	150.41	24.7%	308.02
CO_2	22.9%	119.19	15.4%	192.05
VM	0.0%	0.00	0.0%	0.00
H_2O	33.3%	173.31	35.6%	443.95
N_2	0.9%	4.68	0.8%	9.98
C	0.0%	0.00	0.0%	0.00
Heating value (MJ/kg)	5.9		6.7	

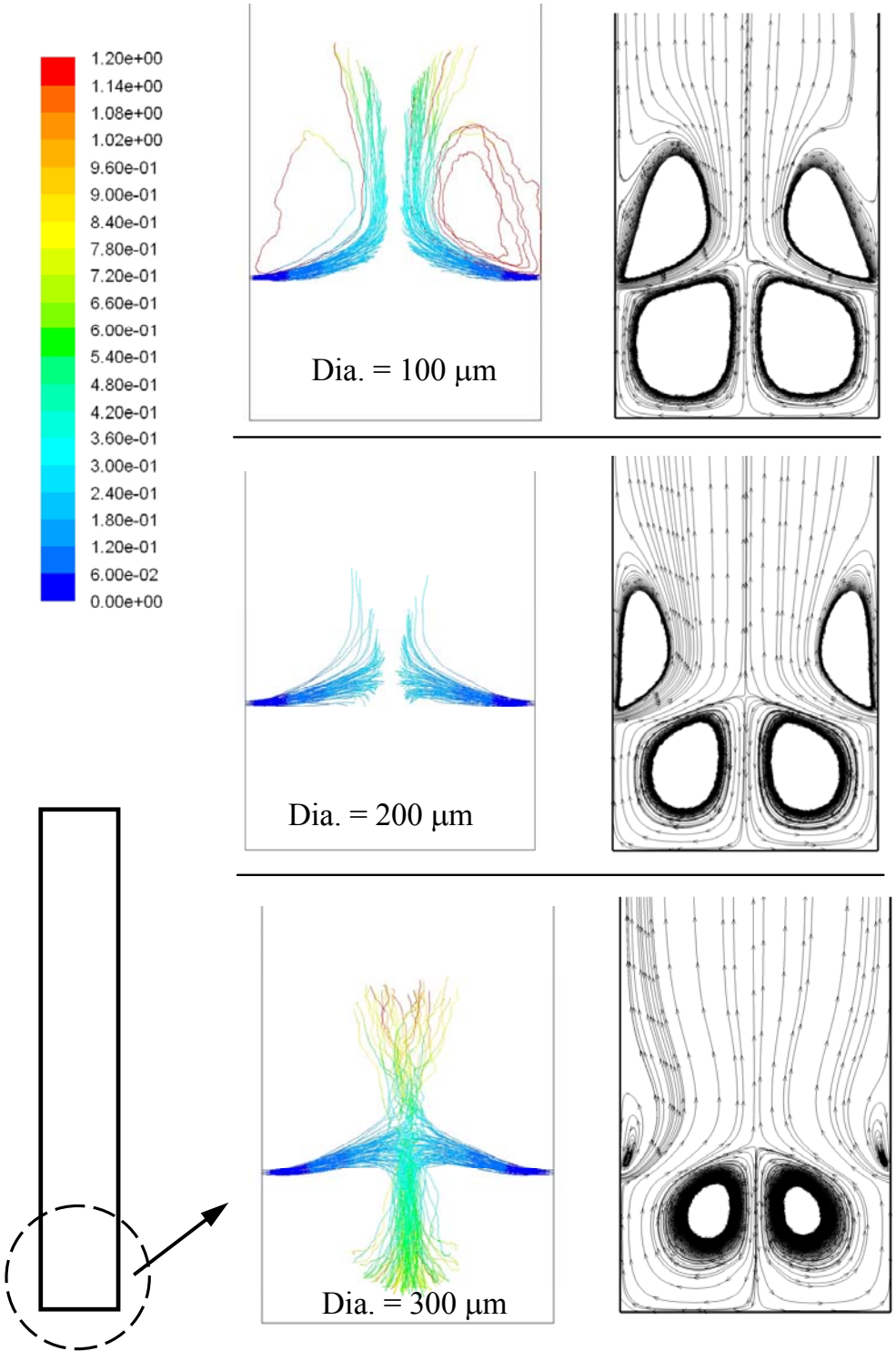

Figure 4.7 Particle tracks and gas streamlines show effect of different coal slurry particle sizes. The particle tracks are colored by residence time (s). Kobayashi devolatilization model is used.

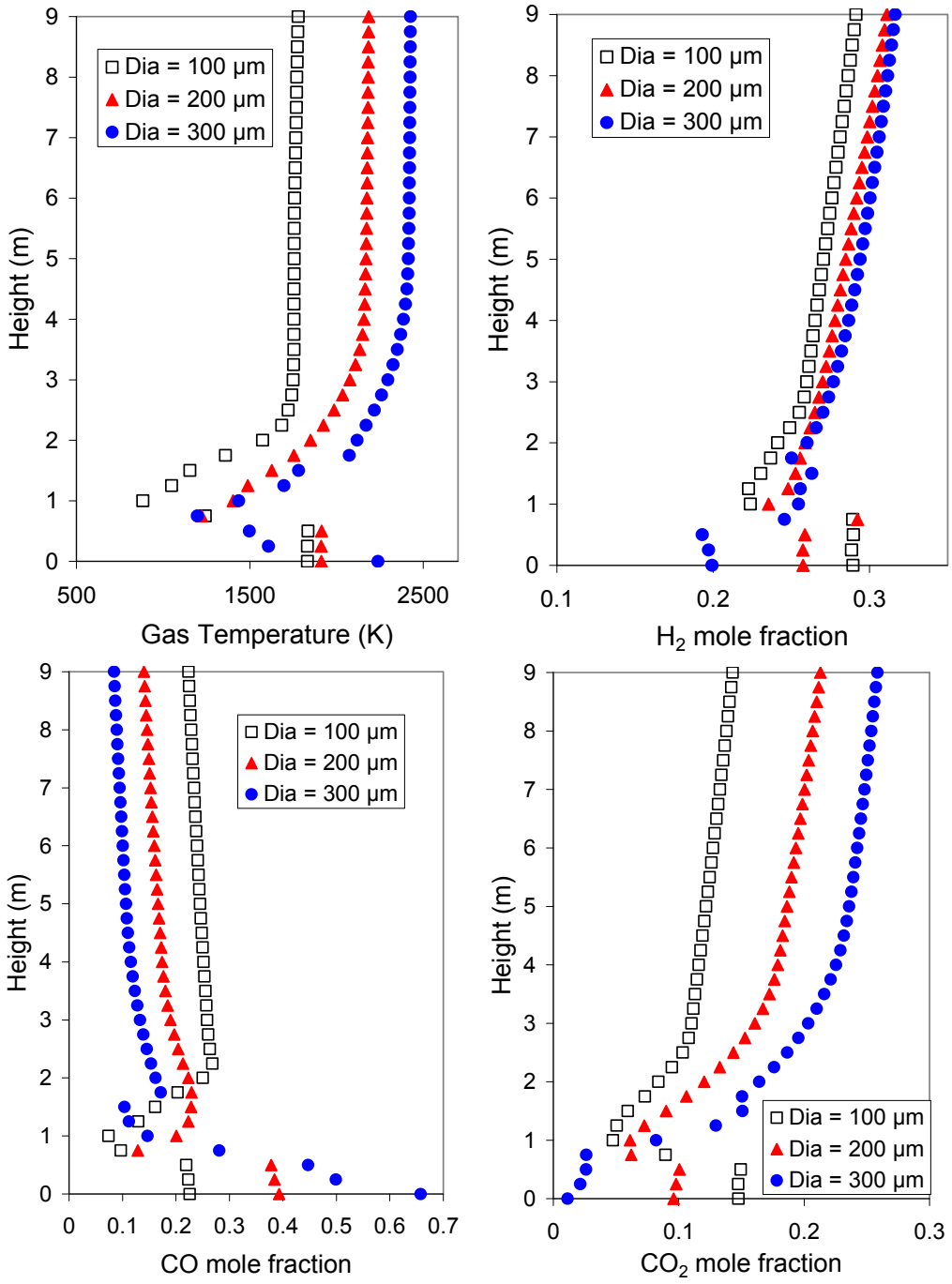

Figure 4.8 Mass-weighted average temperature and species distributions for cases with various particle sizes. Standard k-ε model turbulence model and Kobayashi devolatilization model are used.

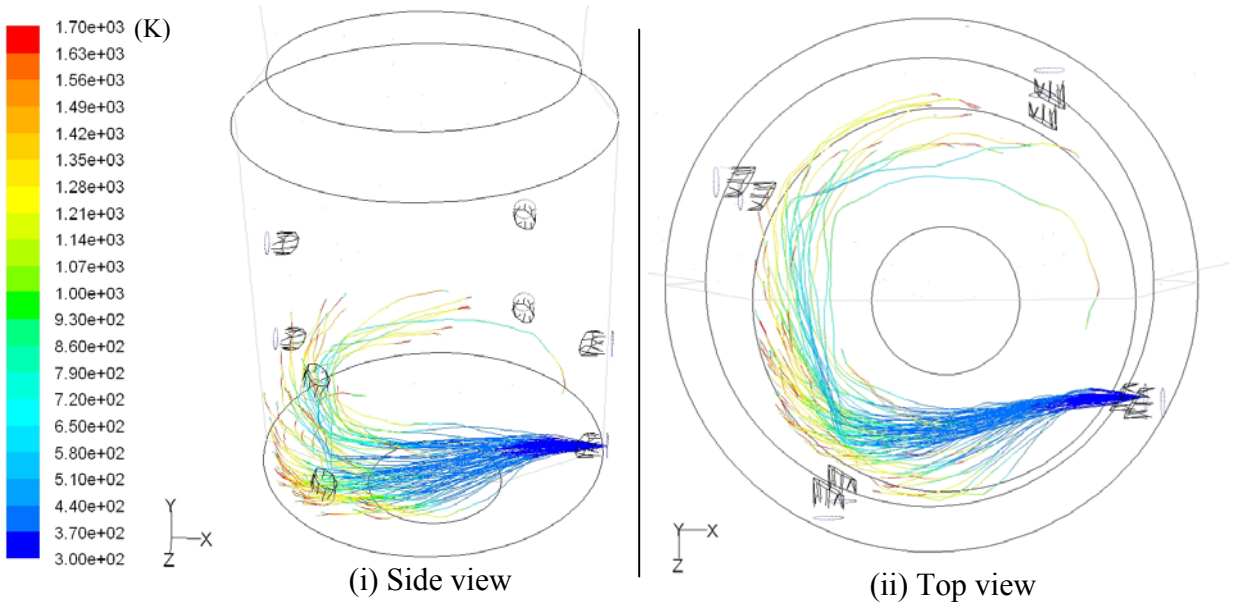

Figure 4.9 Particle tracks colored by particle temperature in the combustor section of the 3-D gasifier. For clarity, only one injection is shown.

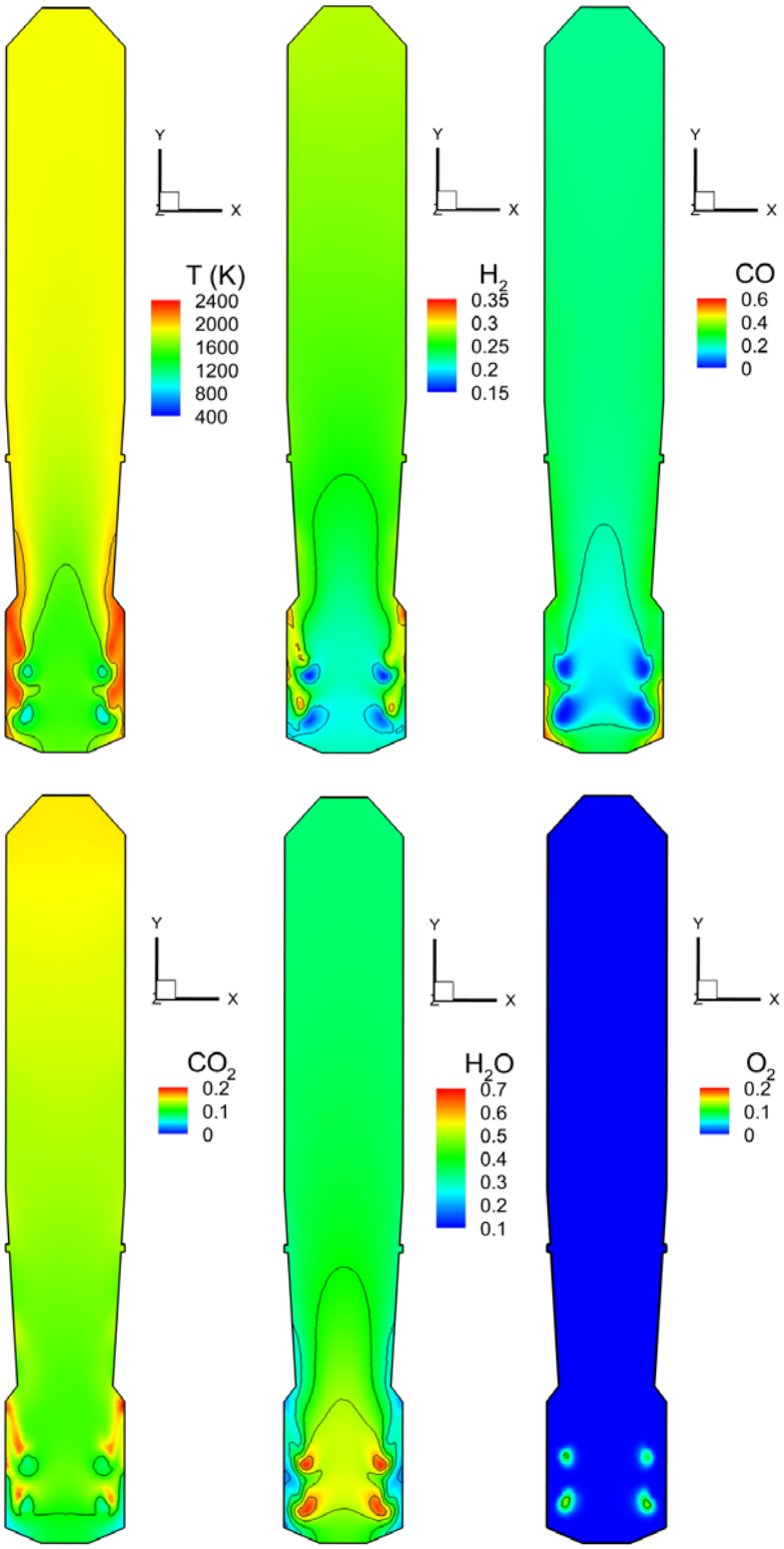

Figure 4.10 Temperature and species distributions on the vertical center plane in the 3-D gasifier.

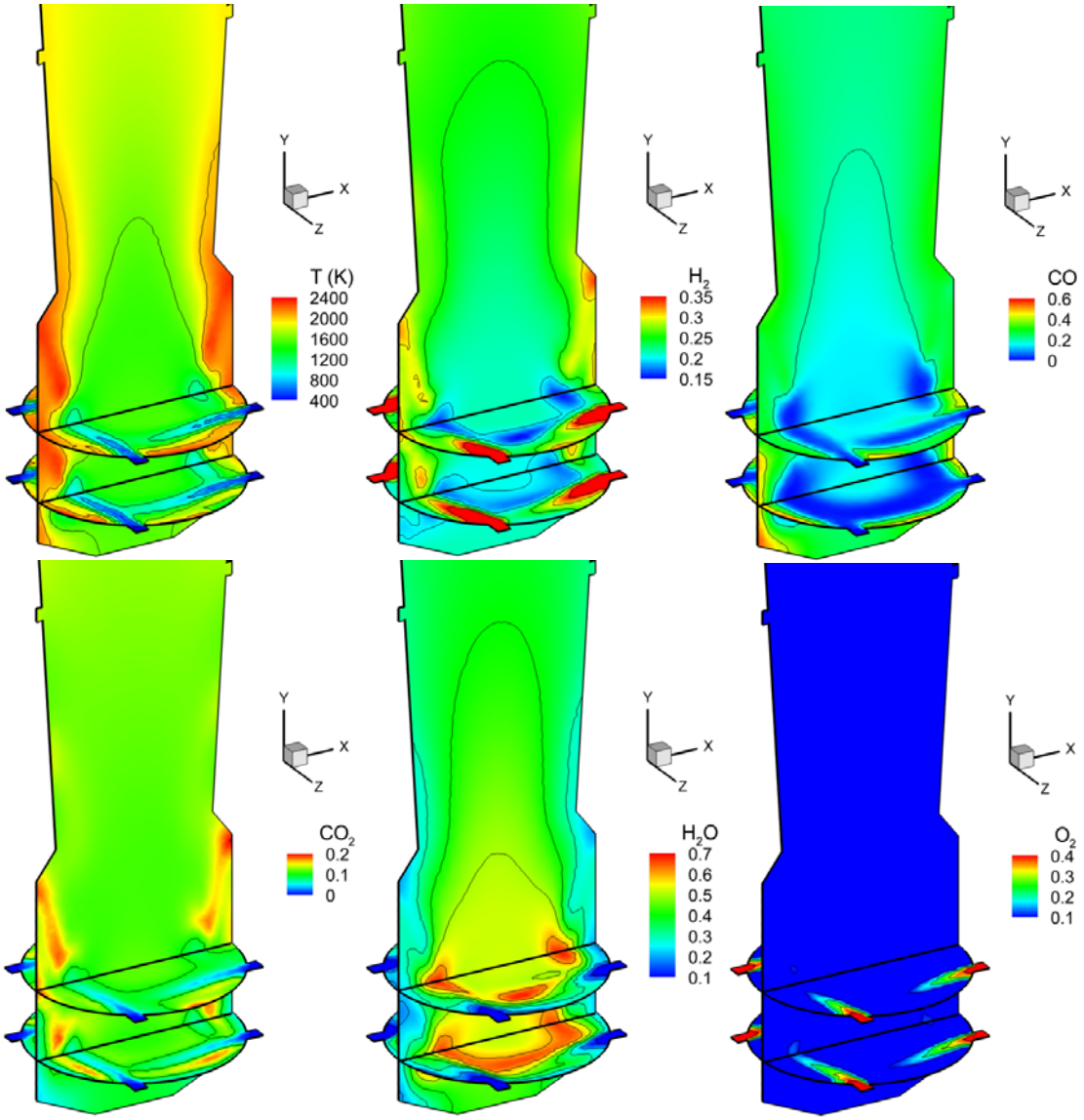

Figure 4.11 Close-up view of temperature and species distributions in the 3-D combustor section on a vertical center plane intersected with two horizontal fuel-injection planes.

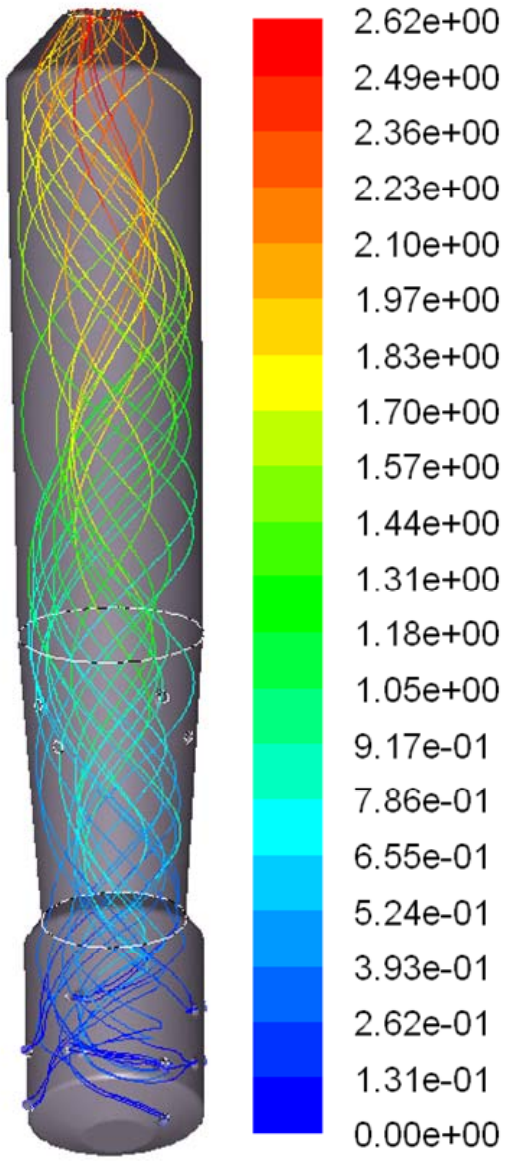

Figure 4.12 Gas path lines inside the 3-D gasifier colored by residence time (s).

4.2 Comparison between Finite-Rate Model and Instantaneous Gasification Model

A coal gasification simulation model involves many sub-models and each of the sub-models needs to be investigated and verified. Two different gasification reaction models (finite-rate model and instantaneous gasification model) are investigated. The **goal** is to determine if the simplified instantaneous gasification model can be used to quickly capture acceptable approximations of thermal-flow and reaction behaviors that can be used as a preliminary screening tool of new design ideas for improving gasifiers' performance.

A one-stage entrained flow coal gasifier is studied. Fundamental investigation is first conducted on a simplified 2-D geometry (Figure 4.1(a)) to perform a parametric study of the effect of coal particle sizes on gasification performance and two different approaches of modeling coal slurry. From the 2-D results, a fixed coal particle size and one coal slurry model are selected to conduct 3-D simulation. The geometry of the 3-D two stage gasifier is adopted from Bockelie el al. (2002(a)) and is shown in Figure 4.2(a). Two opposing injectors are located near the bottom of the gasifier. In this section, the second-stage is turned off.

In the finite-rate model, the oxidant is considered as a continuous flow and coal slurry is considered as a discrete flow. The discrete phase only includes the fixed carbon and water from the moisture content of coal and water added to make the slurry. Two approaches are adopted to model the coal slurry injection. The first approach injects the slurry coal with each particle containing both coal and liquid water. The second approach injects coal (as a solid particle) and liquid water (as droplets) separately. Other components of the coal, such as N, H, S, O, and ash, are injected as gas, together with the oxidant in the continuous flow. N is treated as N_2, H as H_2, and O as O_2. This treatment will not use additional energy to bind elements N, H, or O into molecules because the coal heating value has been included in the fixed carbon and the volatiles. S and ash are lumped into N_2. The coal slurry size is uniformly given as 50 μm respectively in the baseline case. In the instantaneous gasification model, all species are injected as gas.

In this study, the volatile ($CH_{2.121}O_{0.5855}$) is thermally cracked into CO, H_2, and C_2H_2 according to reaction,

$$CH_{2.121}O_{0.5855} \rightarrow 0.5855\ CO + 0.231\ H_2 + 0.414\ C_2H_2 \qquad (4.3)$$

and the C_2H_2 is gasified by reaction

$$C_2H_2 + 2\ O_2 \rightarrow 2\ CO + H_2. \qquad (4.4)$$

This treatment is a little different from using benzene (C_6H_6) in Eqs. 4.3 and 4.4 as the intermediate substance to be further "gasified" into CO and H_2.

4.2.1 Comparison between Results of Finite-Rate Case Instantaneous Gasification Case

Table 4.6 presents the exit syngas temperature and compositions for the finite-rate and instantaneous gasification cases. The gasification performance is evaluated by the syngas composition, syngas heating value, carbon version rate, and the cold gasification efficiency. Carbon conversion is defined as the amount of unburned char contained in the exit gas divided by the total char injected through the inlets (see Eq. 4.1). The char is treated as fixed carbon. Carbon conversion for the finite-rate case is 91% while the carbon conversion for the instantaneous gasification is 100%. As mentioned earlier, carbon particles are made to gasify instantaneously in the instantaneous gasification model. Thus, the solid-gas reaction process can be modeled as homogeneous combustion reactions. The homogenous reactions of char in the instantaneous gasification model are much faster than the heterogeneous reactions of char in the finite-rate model. In the instantaneous gasification, char is injected as gas which means that it can immediately react as soon as it leaves the inlets. Coal particles in the finite-rate model have to undergo evaporation and devolatilization before the char can be burned. The existence of unburned chars in the exit gas is consistent with the operating of current gasifiers reported in available literatures.

$$\text{Carbon conversion efficiency} = \frac{\text{mass of carbon at inlet - mass of carbon at exit}}{\text{mass of carbon at inlet}} \qquad (4.1)$$

Syngas temperature for both finite-rate and instantaneous gasification cases, listed in Table 4.6, are almost identical. However, Figure 4.13 shows very different temperature distribution for both cases. Gas temperature and species distributions presented in Figure 4.14 for the instantaneous gasification are pretty uniform. The reactions happen and finish very quickly as expected. On the other hand, the finite-rate model shows a hot region (around 2200 K) below the injection points and a gradual increase above the injection points.

Table 4.6 Exit syngas temperature and compositions for finite-rate and instantaneous gasification 2D cases with 50 μm particles.

	Finite rate	***Instantaneous gasification***
Temperature (K)	1181	1179
Carbon conversion	91.0%	100.0%
Cold gasification efficiency	78%	84%
Mole fraction:		
CO	28.4%	28.9%
H_2	29.7%	36.4%
CO_2	8.5%	10.5%
$CH_{2.121}O_{0.5855}$	0.0%	0.0%
H_2O	31.2%	23.1%
C_2H_2	1.0%	0.0%
N_2	1.0%	1.1%
O_2	0.0%	0.0%
HHV at 25°C (MJ/kg)	9.7	10.4

The preliminary result of the 2-D finite rate case shows almost no CO existing at the exit; this is apparently not consistent with a typical syngas produced by any existing commercial gasifier. A detailed analysis has been conducted and it is discovered that the water-shift reaction rate is based on the laboratory result in the presence of catalyst (Jones and Lindstedt, 1988). Considering no catalyst is added in a typical gasifier, the water-shift reaction rate constant is purposely slowed down in this study to make the syngas composition consistent with that in the actual production. This reduced reaction rate constant is used in both finite-rate model and instantaneous gasification model. With the modification of reduced water-shift reaction rate, the finite-rate reactions seem to complete at the location above gasifier height of 8 m, indicated by an almost zero change in the gas temperature and gas species distributions.

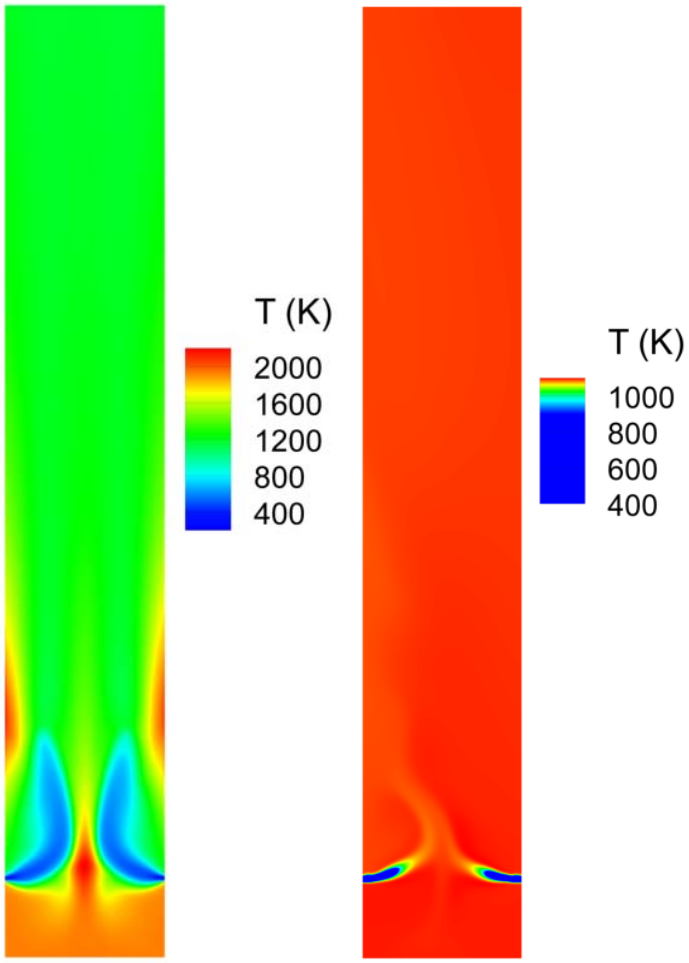

(a) Finite-rate (b) Instantaneous gasification

Figure 4.13 Temperature distributions for 2-D finite-rate case versus instantaneous gasification case.

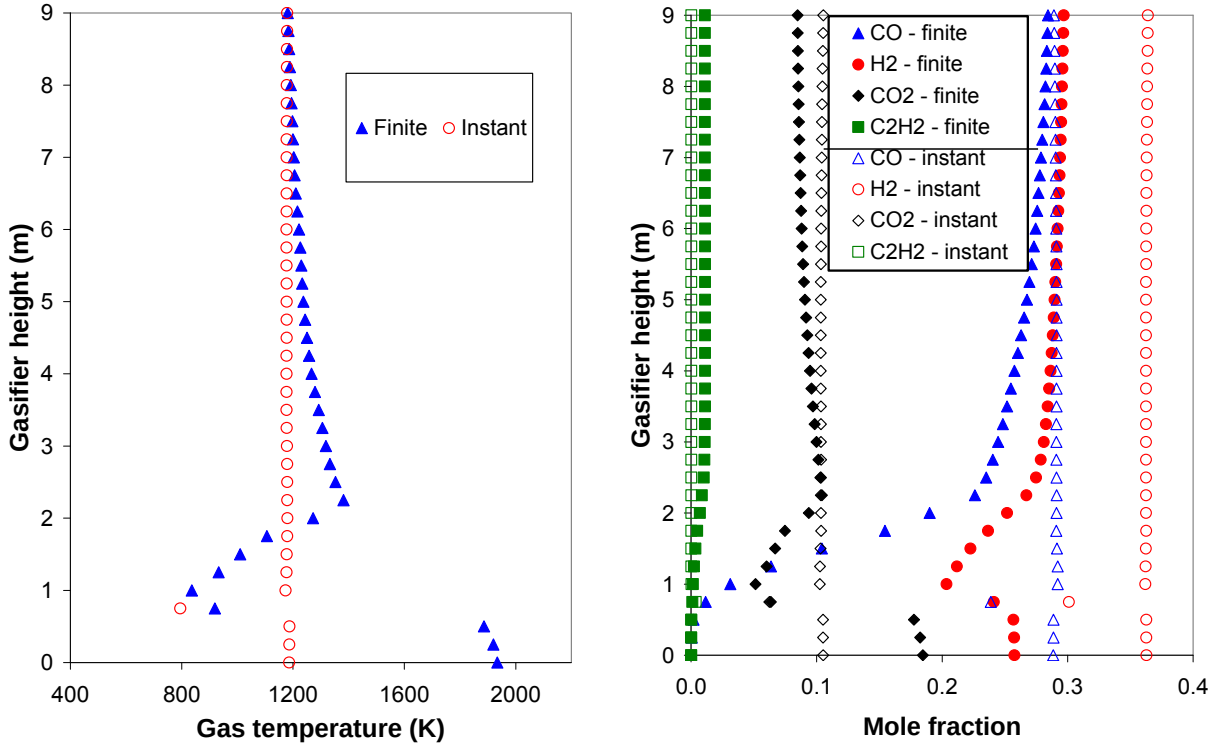

(a) Gas temperature (b) Mole fraction

Figure 4.14 Mass weighted average of (a) gas temperature and (b) species mole fraction for 2D finite-rate versus instantaneous gasification cases.

4.2.2 Effects of Different Coal Particle Sizes on Finite-Rate and Instantaneous Gasification Cases

As mentioned earlier, the reaction rates in the instantaneous gasification are much faster than those in the finite-rate model. Several cases with different coal particle diameters are studied to examine if perhaps the results would be similar if particle size is reduced because smaller particle sizes have larger surface/volume ratios, which can help expedite the reaction. Three other different coal slurry particle diameters used are 1 μm, 10 μm, and 100 μm. The results, along with the results for the 50-μm diameter coal slurry particle case above, are compared in Table 4.7.

The results show a trend that the carbon conversion increases as particle diameter reduces. The smaller particles require less time to burn out as expected. (Note that an exception occurs for the particle of 200 μm as discussed in 4.1.4). Carbon conversion is 100% for the 1

μm coal slurry diameter case. Syngas heating value becomes closer to that of the instantaneous gasification as particle diameter decreases. However, there is no clear trend in the change of syngas compositions.

Table 4.7 Exit syngas temperature and compositions for finite-rate with various coal slurry particle diameters and instantaneous gasification 2D cases.

Particle diameter (μm)	1	10	50	100	Instantaneous
Temperature (K)	1199	1189	1181	1387	1179
Carbon conversion	100.0%	99.7%	91.0%	70.0%	100.0%
Cold gasification efficiency	82%	82%	78%	67%	84%
Mole fraction:					
CO	30.5%	30.1%	28.4%	20.6%	28.9%
H_2	29.7%	30.1%	29.7%	31.5%	36.4%
CO_2	7.9%	8.2%	8.5%	13.2%	10.5%
$CH_{2.121}O_{0.5855}$	0.0%	0.0%	0.0%	0.0%	0.0%
H_2O	29.4%	29.2%	31.2%	33.2%	23.1%
C_2H_2	1.4%	1.3%	1.0%	0.4%	0.0%
N_2	1.1%	1.1%	1.0%	1.1%	1.1%
O_2	0.0%	0.0%	0.0%	0.0%	0.0%
HHV at 25°C (MJ/kg)	10.2	10.2	9.7	8.3	10.4

4.2.3 Comparison Between Two Different Slurry Coal Injection Models

In the finite-rate cases presented above, the coal slurry injection has been modeled following the first approach, i.e. each coal slurry particle consists of char, moisture contained in the coal, and water to make the slurry. The results are now compared with those obtained by employing the second approach, i.e. the water to make slurry is injected separately as water droplets from the coal particles. In this second approach, two adjacent injections are used at each inlet. One is the injection for the coal particle, which consists of char and moisture contained in the coal. The other is the injection for the water droplets to make the slurry.

It is initially thought that when the water slurry is included in the coal particles, the coal particles need longer time to complete the evaporation process due to more water content inside the particle than if the slurry water is injected separately as water droplets. Thus, the devolatilization and char reactions will be delayed, which could result in a lower carbon

conversion. However, the results listed in Table 4.8 shows that carbon conversion is almost the same but the cold gasification efficiency is eight percentage points higher when water slurry is injected as a part of the coal particles than when it is injected separately as water droplets. Particle concentration distributions shown in Figure 4.15 reveal that the particles react a little bit slower for the case where slurry water is injected separately from coal particles (approach 2).

Table 4.8 Exit syngas temperature and compositions for finite-rate 2-D cases with two different coal slurry injection models.

Water slurry injection	***Combined coal-water particles***	***Separated coal & water particles***
Temperature (K)	1181	987
Carbon conversion	91.0%	90.0%
Cold gasification efficiency	78%	70%
Mole fraction:		
CO	28.4%	22.5%
H_2	29.7%	29.5%
CO_2	8.5%	11.9%
$CH_{2.121}O_{0.5855}$	0.0%	0.0%
H_2O	31.2%	33.8%
C_2H_2	1.0%	1.2%
N_2	1.0%	1.1%
O_2	0.0%	0.0%
HHV at 25°C (MJ/kg)	9.7	8.7

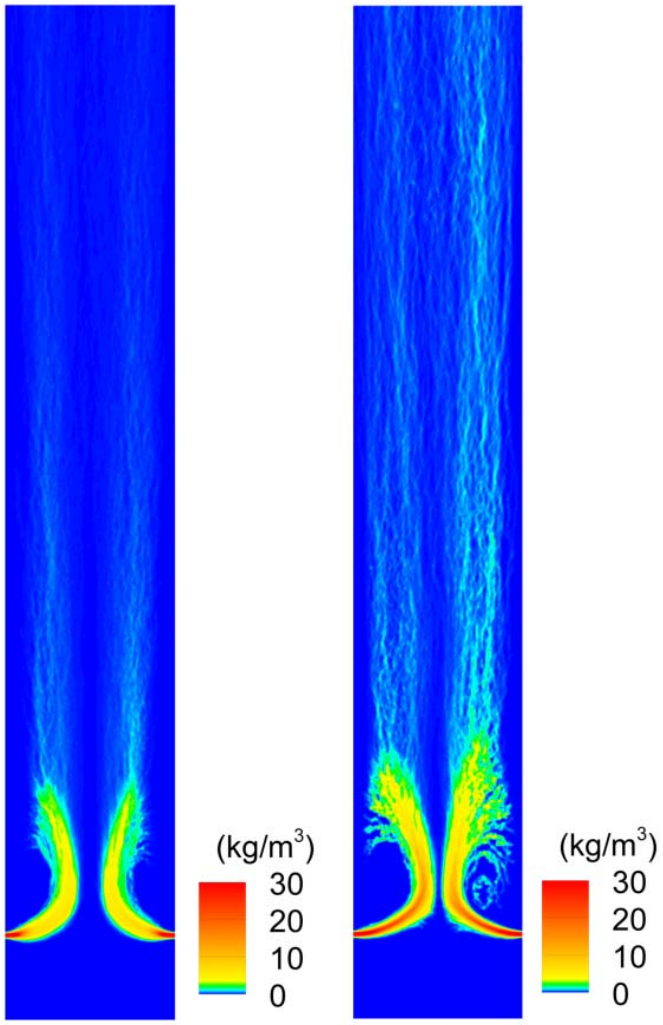

(a) Combined coal-water particles **(b) Separated coal & water particles**

Figure 4.15 Particle concentrations for finite-rate cases with (a) combined coal-water particles and (b) slurry water injected as separated water droplets from coal particles.

4.2.4 Comparison Between Finite-Rate and Instantaneous Gasification Results for the 3-D Gasifier

A similar comparison between the finite-rate model and the instantaneous gasification model in the 3-D gasifier follows by using 50 μm coal particles and water slurry in coal particles. Table 4.9 shows the results. Syngas temperature for the instantaneous gasification case is much lower compared to the temperature for the finite-rate case (874 K compared to 1221 K), which is different from the 2-D gasifier case where the syngas temperature for the instantaneous gasification case and the finite-rate case are almost identical (1179 K and 1181 K, respectively). The 3-D gasifier provides better mixing than the 2-D gasifier and results in more complete and faster endothermic char-CO_2 and char-steam gasification for the instantaneous gasification model.

Table 4.9 Comparison of exit syngas temperatures and compositions of the 3D gasifier between finite-rate model and instantaneous gasification model.

	Finite-rate	***Instantaneous gasification***
Temperature (K)	1221	874
Carbon conversion	98.1%	100.0%
Cold gasification efficiency	79%	88%
Mole fraction:		
CO	28.6%	31.0%
H_2	31.8%	36.3%
CO_2	9.9%	7.5%
$CH_{2.121}O_{0.5855}$	0.0%	0.0%
H_2O	28.0%	22.0%
C_2H_2	0.7%	0.0%
N_2	1.0%	3.2%
O_2	0.0%	0.0%
HHV at 25°C (MJ/kg)	9.8	10.9

The plots of the average gas temperature and species mole fractions along the gasifier's height in Figure 4.16 show that, similar to the 2-D gasifier, the instantaneous gasification model predicts faster reactions than the finite-rate model does.

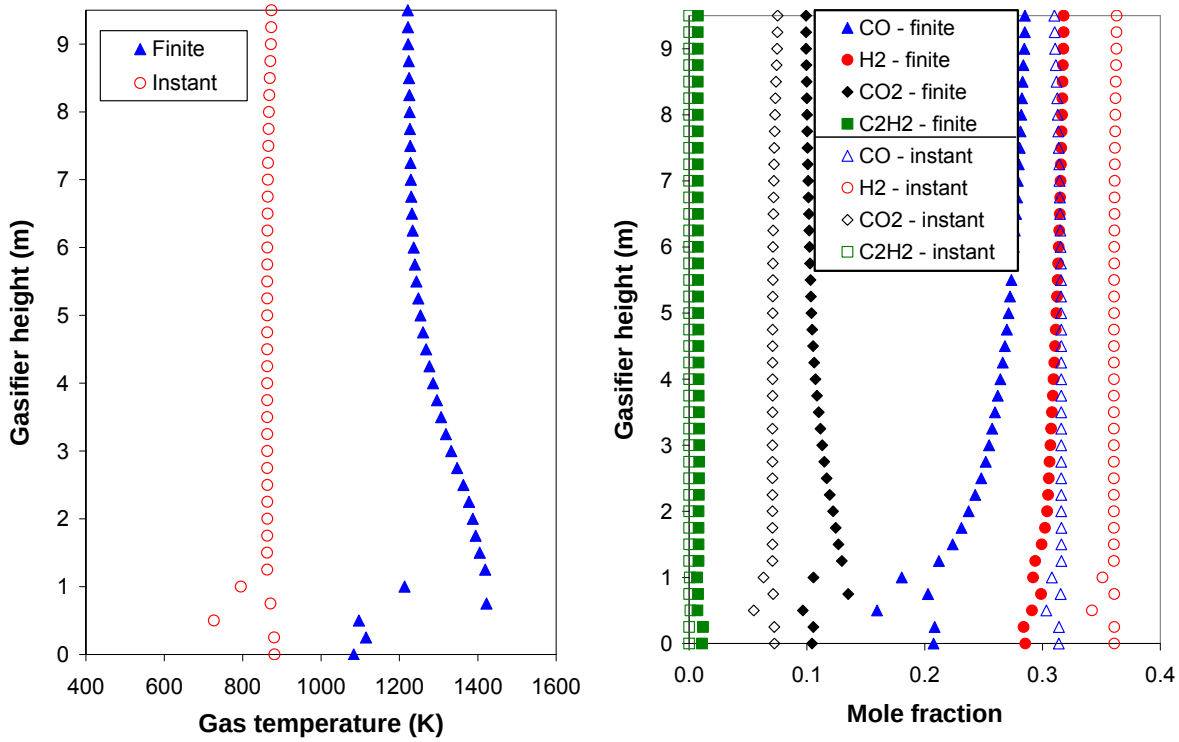

Figure 4.16 Mass weighted average of (a) gas temperature and (b) species mole fraction for 3-D gasifier finite-rate and instantaneous gasification cases.

Close-up views of the region near the injections for both the finite-rate case and the instantaneous gasification case are presented in Figure 4.17. In the finite-rate case, the hottest region is near the wall just downstream of the injectors. The CO_2 mole fraction in those locations is the highest. This may indicate that CO produced by the char combustion ($C + ½O_2 \rightarrow CO$) in that area is burned, which produces CO_2. The temperature and species distributions plot on vertical mid-plane for the finite-rate case shown in Figure 4.17. Figures 4.17 and 4.18 show that temperature and species distributions are still changing and reactions are still occurring away from the injection regions. On the other hand, the instantaneous gasification case shows that strong reaction and temperature changes occur not too far away from the injection points. The reactions occur very fast and also finish quickly. Finite-rate case shows a minor trace of unreacted C_2H_2 and more water vapor content in the syngas.

Similar to the 2-D cases, the carbon conversion for the instantaneous gasification model case is also 100%, while there are about 2% unburned chars in the finite-rate model case. Carbon conversion for the 3-D finite-rate model case (98.1%) is 7.1 percentage points higher

than that of the 2-D finite-rate model case (91.0%). The tangential fuel injection in 3-D gasifier causes the flow to swirl and lengthens particle residence time which benefits carbon conversion and fuel production. Without tangential swirl, the residence time of the through flow is around 1 second; the tangential injection increases the average particle residence time to 3.8 seconds. This tangential injection can't be simulated in the 2-D gasifier.

In summary, instantaneous gasification approach can provide approximately adequate syngas composition and heating value, but it can't adequately capture the local gasification process predicted by the finite rate model in most part of the gasifier.

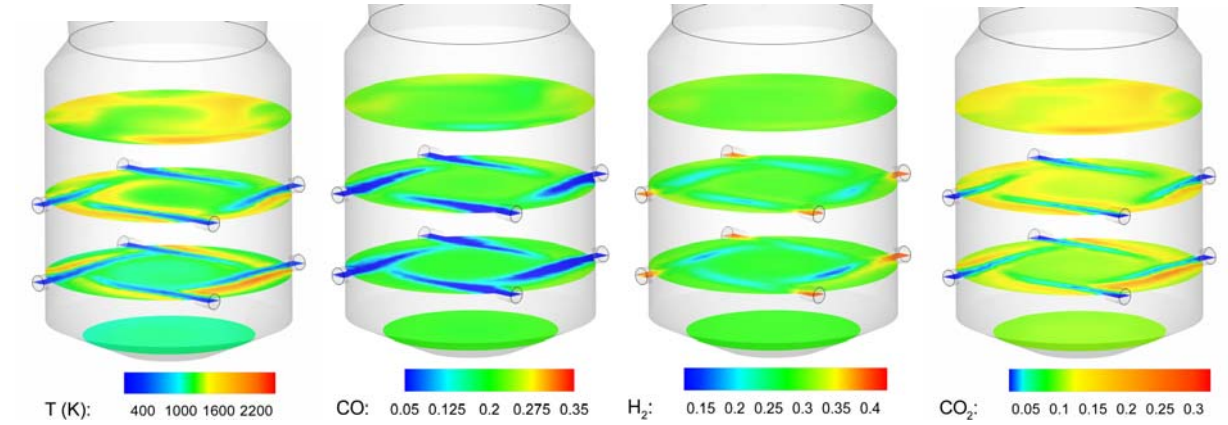

Figure 4.17 Comparison of gas temperature and species mole fraction distributions near the injection regions for the finite-rate and the instantaneous gasification cases. The same color map is used for both cases for an easy comparison.

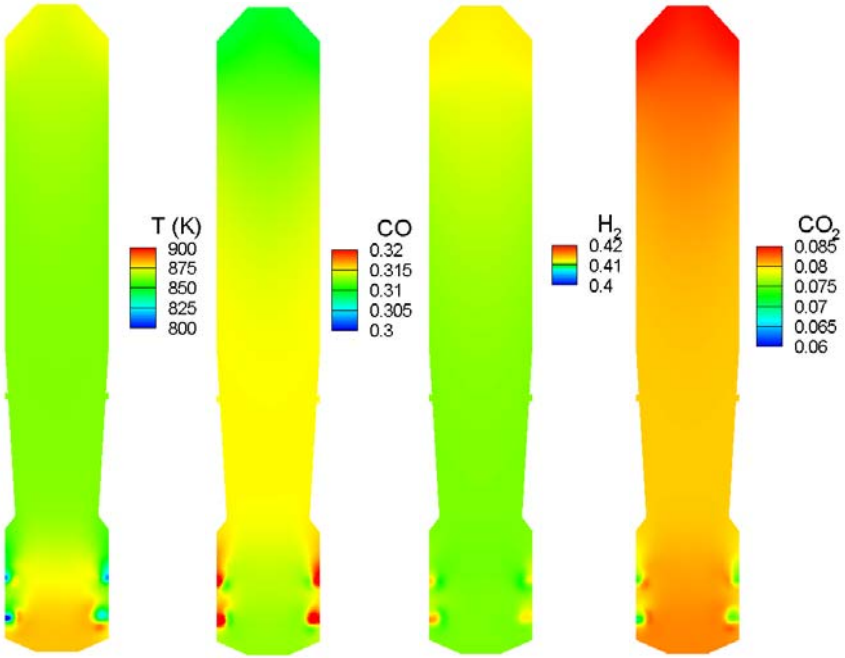

(a) Instantaneous gasification model

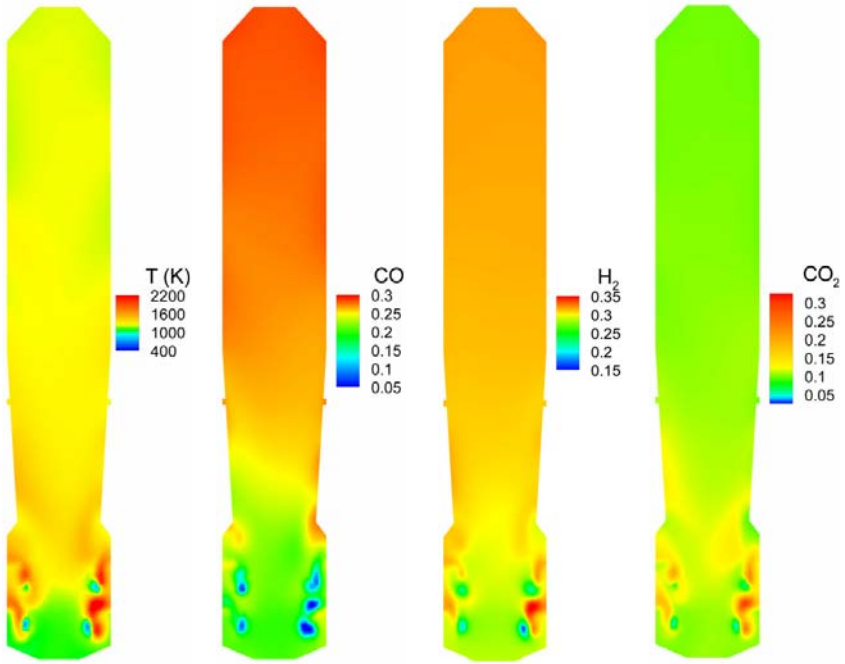

(b) Finite-rate model

Figure 4.18 Gas temperature and species mole fraction distributions on vertical mid-plane for 3-D gasifier with (a) Instantaneous gasification model (b) finite-rate model. Different color maps are used between these two cases to allow more clear presentations of local parametric distributions.

4.3 Two-Stage Entrained-Flow Gasifier

Based on the fundamental studies in the sections 4.1 and 4.2 above, a study is conducted to investigate the effects of different operation parameters by employing fuel injection at the second stage including changes of coal mixture (dry vs. slurry), oxidant (oxygen-blown vs. air-blown), and coal distribution between two stages. Schematic and meshed computational domain of the two-stage gasifier studied are presented in Figure 4.19. The second level injection on the first stage in Figure 4.1 is removed in the gasifier shown in Figure 4.19. Indonesian sub-bituminous coal is used and its compositions are shown in Table 4.1. Total coal feed rate is 13.14 kg/s. The O_2/C mole ratio is 0.4. The coal/H_2O mass ratio of the coal slurry mixture is 60%/40%. For the oxygen-blow operation, the oxidant composition by weight is 95% O_2 and 5% N_2. The gasifier operates at 24 atm.

The volatile ($CH_{2.121}O_{0.5855}$) is thermally cracked into CO, H_2, and CH_4 according to reaction,

$$CH_{2.121}O_{0.5855} \rightarrow 0.5855\ CO + 0.231\ H_2 + 0.414\ CH_4 \qquad (4.5)$$

and the CH_4 is gasified by reaction

$$CH_4 + 0.5\ O_2 \rightarrow CO + 2\ H_2. \qquad (4.6)$$

Methane (CH_4) is used to replace C_2H_2 in Eq. 4.1 or C_6H_6 in Eq. 4.3 is modeled after a recent report (Oka, 2004) that a large fraction of volatiles of certain coals consists of CH_4 versus a previous report (Tomeczek, 1994) stating benzene exists in volatiles of many types of coals.

4.3.1 Baseline Case (Case 1)

The baseline case (Case 1) is the two-stage oxygen-blown operation with coal distribution of 75%-25% between the first and the second stages. Gas temperature and species mole fraction distributions on the horizontal and center vertical planes in the gasifier are shown in Figure 4.20. It is seen that gas temperature is higher in the region between the first stage and second stage injection locations compared to the region above the second stage injection location. Maximum gas temperature in the first stage reaches 2400 K. The dominant reaction in the first stage is the intense char combustion ($C + ½\ O_2 \rightarrow CO$ and $CO + ½\ O_2 \rightarrow CO_2$) in the first stage and gasification reactions (mainly char-CO_2 gasification, $C + ½\ CO_2 \rightarrow CO$) in the second stage. Oxygen is completely depleted through the char combustion in the first stage. Char gasification is enhanced in the second stage with the injection of the remaining coal. Char

is gasified with CO_2 produced in the first stage through reaction $C + CO_2 \rightarrow CO$ and with H_2O through reaction $C + H_2O \rightarrow CO + H_2$.

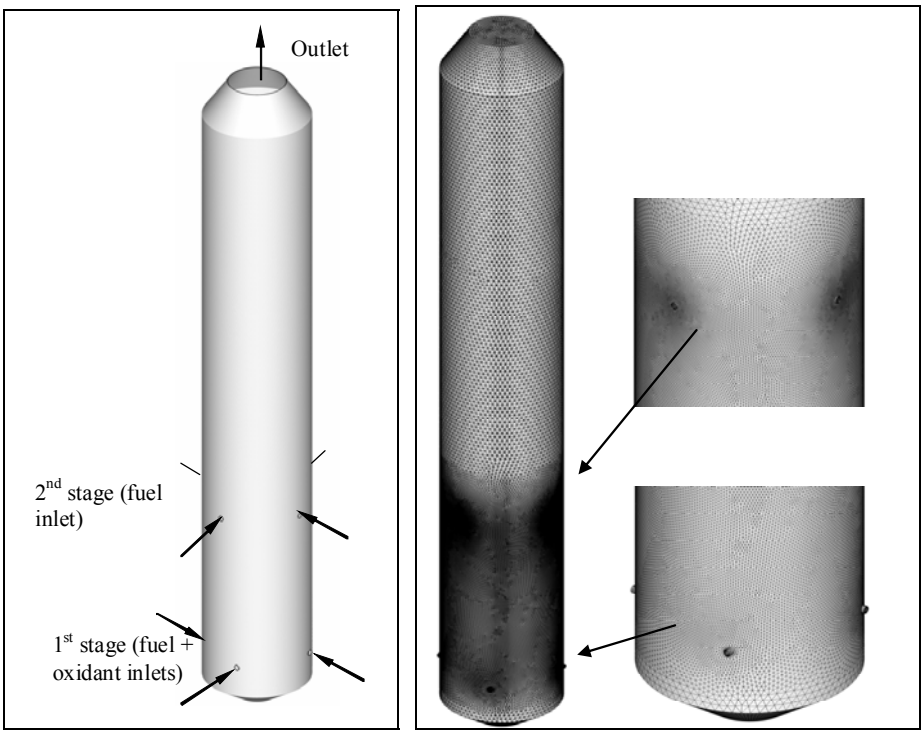

Figure 4.19 (a) Schematic and (b) meshed computational domain of the two-stage entrained-flow gasifier.

Mass-weighted averages of gas temperature and species mole fractions along the gasifier height for Case 1 are shown in Figure 4.21. The dips in the graphs occur at the injector elevations, at heights of 0.75 m for the first stage and 3 m for the second stage. The CO_2 mole fraction and the gas temperature decrease from roughly 27% to roughly 19% as the gas flows from the first stage to the second stage. On the other hand, CO mole fraction increases from 12% to 20%. This is due to the endothermic char-CO_2 gasification mentioned above. Meanwhile, the increase in the average mole fraction of H_2 in the second stage is negligible. This may indicate that char-CO_2 gasification is more dominant than char-H_2O gasification in the second stage.

At the gasifier height of 8.5 m, the graphs for the average gas temperature and gas mole fractions flatten out. This indicates that the rates of reactions are slowing down. Making the gasifier longer or higher would probably not make significant change in the syngas temperature

and compositions. Figure 4.22 shows helical flow pathlines inside the gasifier which lengthens the flow residence time to allow more time for the reactions to take place.

Exit syngas temperature and mole fraction compositions are listed in Table 4.10. Carbon conversion efficiency, which is the comparison of the total mass of carbon injected into the gasifier to the total mass of carbon at the gasifier exit, is 99.4%. The high heating value of the exit syngas is 8.24 MJ/kg.

Table 4.10 Exit syngas temperatures and compositions.

	Case 1	***Case 2***	***Case 3***	***Case 4***	***Case 5***
Fuel distribution	2-stage (75%-25%)	2-stage (75%-25%)	2-stage (50%-50%)	1-stage	2-stage (75%-25%)
Oxidant	oxygen	oxygen	oxygen	oxygen	air
Fuel type	slurry	dry	slurry	slurry	slurry
Exit syngas:					
T (K)	1310	1882	1250	1407	1143
Mole fraction:					
H_2	31.7%	33.8%	31.1%	32.2%	19.0%
CO	20.2%	31.4%	19.7%	21.5%	7.6%
CO_2	18.9%	19.0%	19.2%	18.0%	12.5%
CH_4	1.2%	1.7%	1.3%	0.7%	0.4%
H_2O	26.7%	0.8%	27.4%	26.3%	16.4%
N_2	1.3%	13.3%	1.3%	1.3%	44.1%
O_2	0.0%	0.0%	0.0%	0.0%	0.0%
Carbon conversion efficiency	99.4%	100.0%	98.3%	94.8%	77.3%
HHV at 25°C (MJ/kg)	8.24	9.45	9.03	7.68	4.40

4.3.2 Effects of Coal Mixture (Slurry vs. Dry)

Case 2 is conducted to investigate the effects of using dry coal as fuel. Coal and oxidant feed rates are kept the same as for Case 1. Nitrogen is used as transport gas for the coal powder. The amount of N_2 transport gas used is 0.3 times the mass of coal powder. The same fuel and oxidant distributions as in Case 1 are used, that is two-stage operation with 75%-25% fuel distribution between the first and second stages and 100% oxidant injected into the first stage (ie. no oxidant injection at the second stage).

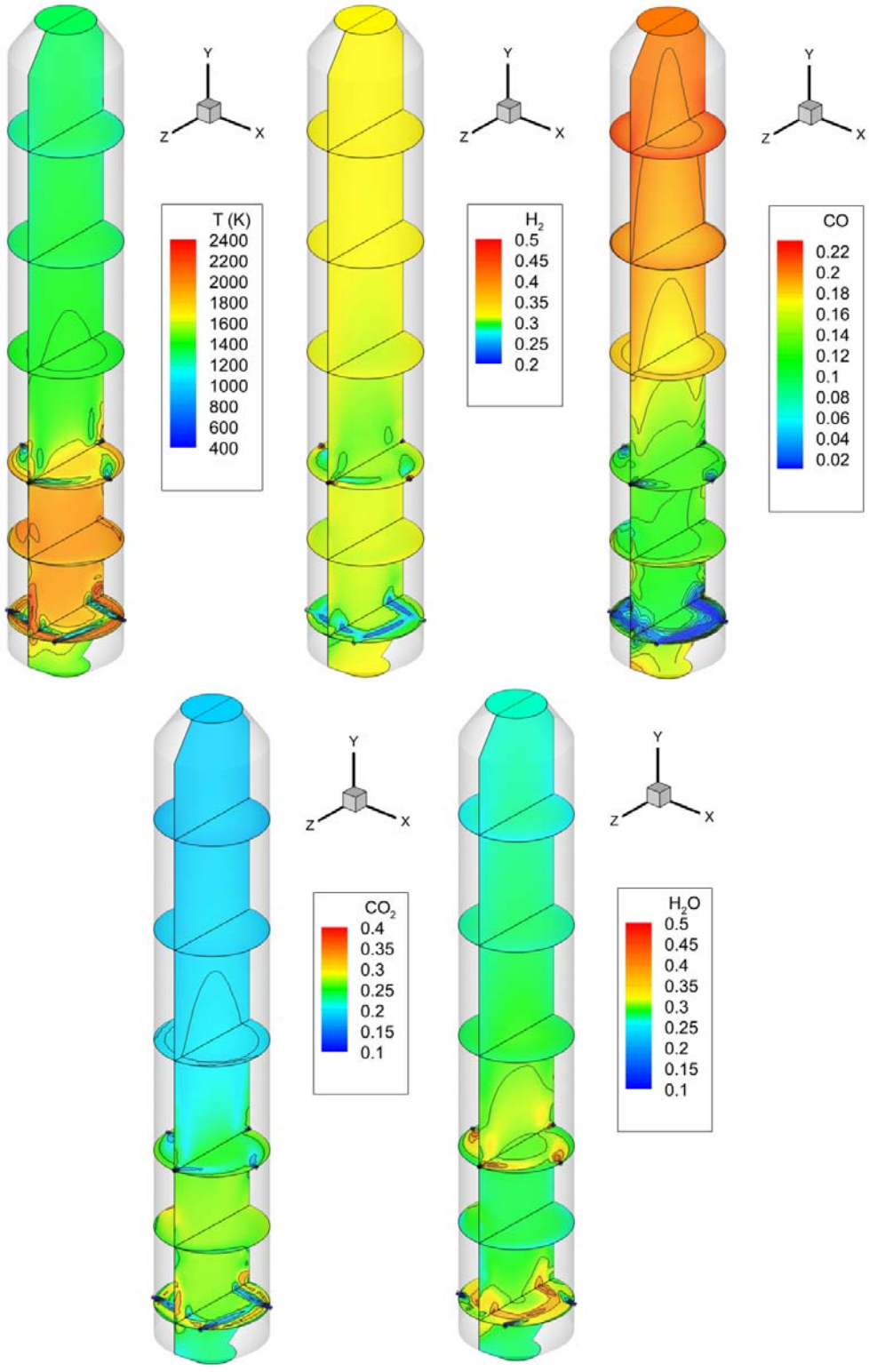

Figure 4.20 Gas temperature and species mole fraction distributions for Case 1 (2-stage, 75%-25%, coal slurry, oxygen-blown).

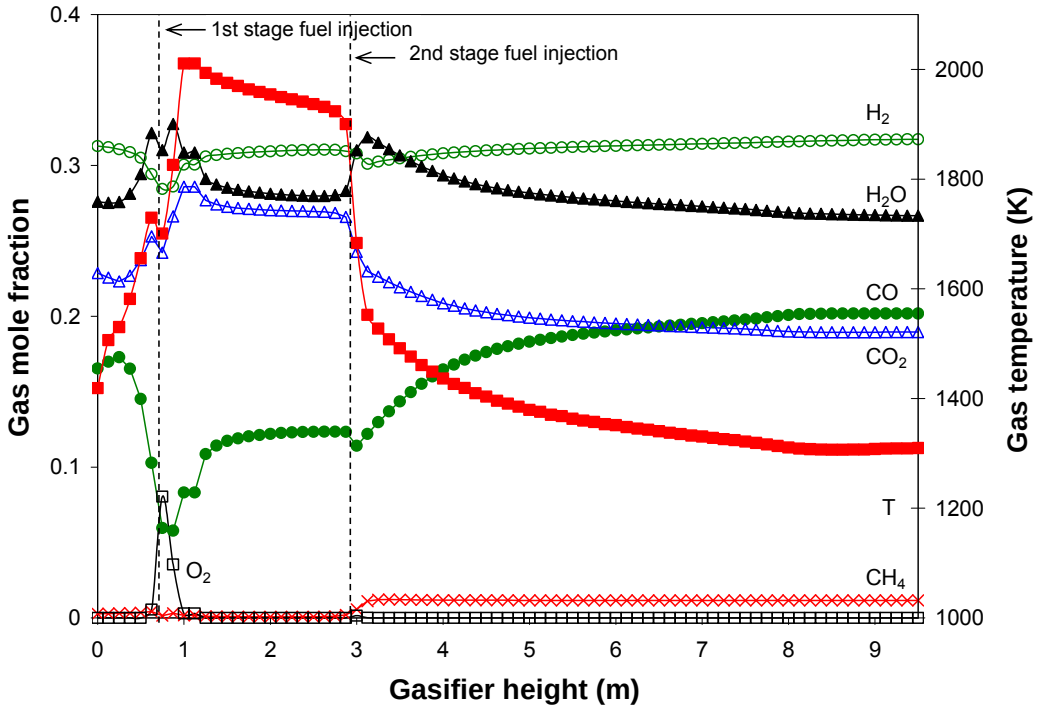

Figure 4.21 Mass-weighted averages of gas temperature and species mole fraction distributions along gasifier height for Case 1 (2-stage, 75%-25%, coal slurry, oxygen-blown).

The distribution of gas temperature presented in Figure 4.23 shows that the highest temperature in the first stage is approximately 3200 K, which is 800 K higher than that of the coal slurry case (Case 1). Unlike the coal slurry case, the dry coal case does not have a lot of H_2O to absorb the heat released by the char combustion, nor does much water react with char through the char-H_2O gasification. H_2O that presents in Case 2 comes from the moisture contained in the coal, while H_2O in Case 1 comes from both the moisture contained in the coal and water added to the coal to make the slurry. This higher gas temperature means that the refractory walls in the first stage will experience higher thermal loading than that in the coal slurry operation.

As seen in Figure 4.24, the average CO mole fraction in the first stage is slightly higher than that of the coal slurry case (Case 1), approximately 19% compared to approximately 12%. The same is observed for the average CO_2 and H_2 mole fractions, 30% for CO_2 and 34% for H_2 in the dry coal case compared to 27% for CO_2 and 31% for H_2 in the coal slurry case.

Similar to the coal slurry operation in Case 1, char gasification is enhanced in the second stage by injecting the remaining fresh coal. But because the coal injected is dry coal, char

gasification that occurs is mainly char-CO_2 gasification. Both Figures 4.22 and 4.23 show increase in CO (from approximately 19% to 31%) and decrease in CO_2 (from approximately 30% to 19%) in the second stage due to the char-CO_2 gasification. Char-H_2O ($C + H_2O \rightarrow CO + H_2$) also occurs in the second stage. The small decrease in H_2 in the second stage is due to dilution by the additional coal.

The temperature of the exit syngas, listed in Table 4.10, is 1882 K, which is 572 K higher than the syngas for the coal slurry case (Case 1). As stated earlier, this is due to the lower amount of H_2O injected into the gasifier in the dry coal operation. Compared to the coal slurry case, there is less H_2O to absorb the heat from the char combustion and less H_2O to react with C through the endothermic char-H_2O reaction ($C + H_2O \rightarrow CO + H_2$).

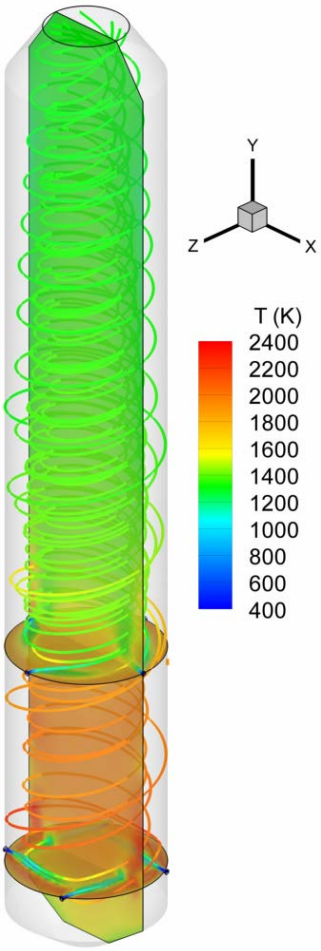

Figure 4.22 Flow pathline colored by the gas temperature for Case 1(2-stage, 75%-25%, coal slurry, oxygen-blown).

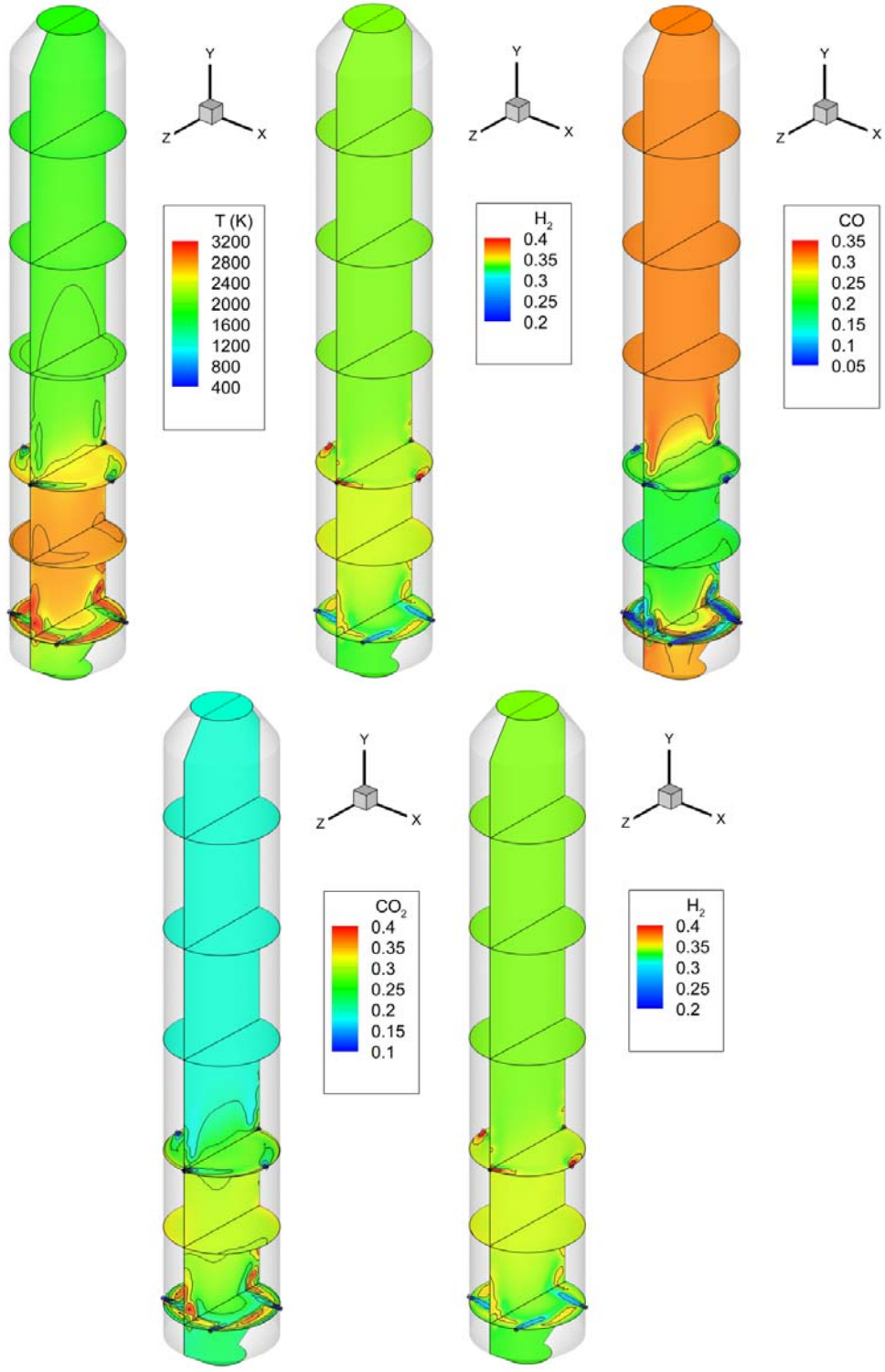

Figure 4.23 Gas temperature and species mole fraction distributions for Case 2 (2-stage, 75%-25%, dry coal, oxygen-blown).

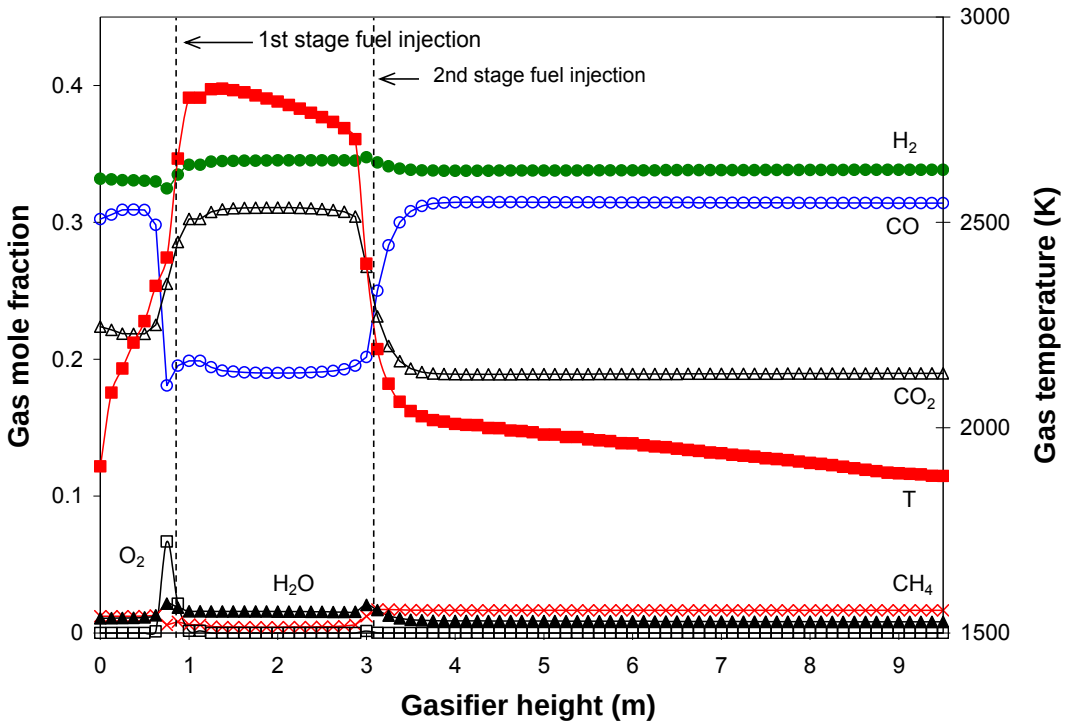

Figure 4.24 Mass-weighted averages of gas temperature and species mole fraction distributions along gasifier height for Case 2 (2-stage, 75%-25%, dry coal, oxygen-blown).

H_2 and CO_2 contents of the syngas are higher than those of the coal slurry case, 33.8% and 31.4% compared to 31.7% and 20.2%, respectively. The syngas high heating value of the dry coal case is also higher than that of the coal slurry case, 9.45 MJ/kg compared to 8.24 MJ/kg. Of course, higher heating value is better. However, the higher syngas temperature of the dry coal case means that it will have lower efficiency when it is put through the gas clean-up system downstream of the gasifier. A lot of energy will be wasted when the syngas is cooled down to the temperature acceptable for the gas clean-up system operation. Although syngas cooler can transfer the thermal energy of the high raw syngas temperature to high-pressure steam, degradation of the energy quality will inevitably affect the overall plant thermal efficiency.

4.3.3 Effects of Fuel Distribution

In the baseline case (Case 1), fuel is distributed 75%-25% between the first and the second stages. Cases 3 & 4 are conducted to study the effects of fuel distribution. In Case 3, the fuel is evenly distributed between the first and the second stages, ie. 50% injected in the first stage and 50% injected in the second stage. In Case 4, all (100%) of the fuel is injected in the

first stage. In other words, Case 4 simulates the one-stage operation of the gasifier. The same total feed rates of coal slurry and oxidant in Case 1 are used in Cases 3 & 4. As in Case 1, all of the oxidant is injected in the first stage.

Figure 4.25 presents the comparison of average gas temperature and species mole fractions for Cases 1, 3, and 4. Higher mass-weighted average gas temperature in the first stage for Case 3 (50%-50%) compared to that of Case 1 (75%-25%), 2500 K compared to 1900 K, is due to the higher O_2/char ratio in the first stage for Case 3. Higher O_2/char causes more char to burn, resulting in the higher gas temperature. Interestingly, gas temperature in the first stage for Case 4 (100%) is also higher than that of Case 1 (75%-25%). The lower average gas temperature in the injector area for Case 1 (75%-25%) has the benefit of helping prolong the injector's life.

The graph of O_2 mole fraction for Case 3 shows that there is still a little amount of O_2 when the gas reaches the second stage injection level. This means that char has a good opportunity to react with the abundant O_2 at the first stage. Meanwhile, for Case 1 (75%-25%) and Case 4 (100%-0%), O_2 is quickly completely depleted in the first stage. The comparison of CO and CO_2 mole fractions for all three cases confirms that char combustion is more intense in Case 3. Case 3 has the highest CO_2 mole fraction and the lowest CO mole fraction in the first stage. It means that a large amount of char in the first stage goes through complete combustion. Case 4 (100%-0%) which has the lowest O_2/char ratio in the first stage, on the other hand, has the lowest CO_2 mole fraction and the highest CO mole fraction.

The exit syngas composition listed in Table 4.10 indicates that among the three cases, Case 4 (100%-0%) yields the highest H_2 production – 32.2% compared to 31.7% for Case 1 (75%-25%) and 31.1% for Case 3 (50%-50%). Case 4 also has the highest CO production – 21.5% compared to 20.2% for Case 1 and 19.7% for Case 3. However, Case 4 has the highest exit syngas temperature, which is 1407 K. Syngas temperature for Cases 1 and 3 are 1310 K and 1250 K, respectively.

Even though Case 4 has the highest H_2, CO and CH_4 combined, its syngas high heating value is the lowest among three cases. High heating value of syngas for Case 4 is 7.68 MJ/kg, compared to 8.24 MJ/kg for Case 1 and 9.03 MJ/kg for Case 3. This is due to the lower carbon conversion efficiency of Case 4 (94.8%) compared to the other two cases (99.4% for Case 1 and 98.3% for Case 3). The exit syngas of Case 4 contains the most unreacted char, thus, combined with its high temperature, it has the lowest high heating value.

Based on the syngas temperature and composition, the 50%-50% fuel distribution (Case 3) give the best result. It has the highest syngas high heating value (9.03 MJ/kg) even though its carbon conversion efficiency (98.3%) is slightly lower than that of the 75%-25% case (Case 1 with carbon conversion efficiency of 99.4%). Besides the highest syngas high heating value, Case 3 has the lowest syngas temperature (1250 K). This lowest syngas temperature compared to the other cases means that there will be less energy lost during the syngas clean-up process. However, its mass-weighted average of gas temperature (2500 K) in the first stage is highest compared to those of the other cases (1900 K for Case 1 and 1500 K for Case 4). This higher gas temperature will put the gasifier's wall refractory bricks in higher thermal loading, which means that the refractory bricks will be more prone to failure and requires more maintenance.

4.3.4 Effects of Oxidant (Oxygen-Blown vs. Air-Blown)

Case 5 simulates the air-blown two-stage operation of the gasifier. Air with composition of 22% O_2 and 78% N_2 by weight is used as the oxidant. The O_2/C mole ratio is maintained the same as in Case 1 (oxygen-blown) which is 0.4. Total feed rate of coal and oxidant combined is the same as for Case 1. Similar to Case 1, the fuel is distributed 75% and 25% between the first and the second stages.

As expected, the mass-weighted average of gas temperature in the first stage shown in Figure 4.26 is lower than in Case 1 (oxygen-blown) due to the abundance of N_2 in the air-blown case. The average gas temperature is approximately 1450 K, while the average gas temperature in the oxygen-blown case is 2000 K.

The syngas composition listed Table 4.10 shows that the ratio of CO mole fraction compared to the H_2 mole fraction for the air-blown case is much lower than those of the oxygen-blown case (Case 1), which is 0.4 for Case 5 compared to 0.64 for Case 1. The syngas high heating value for Case 5 is approximately only half of that of Case 1, 4.40 MJ/kg compared to 8.24 MJ/kg for Case 1. The syngas is diluted with N_2 which causes this low heating value. However, its low carbon conversion efficiency also contributes to this low syngas heating value. Carbon conversion efficiency for the air-blown case is 77.3%. This low carbon conversion efficiency is due to the lower overall gas temperature inside the gasifier, which means there is less energy available to drive the endothermic gasification reactions.

To give a fair comparison between the syngas in Cases 1 and 5, syngas compositions and heating values for both cases are recalculated after N_2 contained in syngas are removed. This eliminates the effect of N_2 dilution on the syngas composition. The recalculated compositions are compared in Table 4.11. The mole fraction of H_2 for the air-blown case (Case 5) is slightly higher than that of the oxygen-blown case (Case 1), 34.0% compared to 32.1%. However, the CO mole fraction for the air-blown (13.6%) is 6.5 percentage points lower than for the oxygen-blown case. As expected, the heating value of the syngas becomes higher once N_2 is removed, which is 7.26 MJ/kg compared to 4.40 MJ/kg before N_2 is removed. However, that syngas heating value is still lower by roughly 1 MJ/kg than that of the oxygen-blown case (8.25 MJ/kg).

Table 4.11 Exit syngas temperatures and compositions for Cases 1 and 5 after N_2 is removed from the syngas.

	Case 1	***Case 5***
Fuel distribution	2-stage (75%-25%)	2-stage (75%-25%)
Oxidant	oxygen	air
Fuel type	slurry	slurry
Exit syngas:		
T (K)	1310	1143
Mole fraction:		
H_2	32.1%	34.0%
CO	20.5%	13.6%
CO_2	19.1%	22.4%
CH_4	1.2%	0.7%
H_2O	27.1%	29.3%
O_2	0.0%	0.0%
Carbon conversion efficiency	99.4%	77.3%
HHV at 25°C (MJ/kg)	8.25	7.26

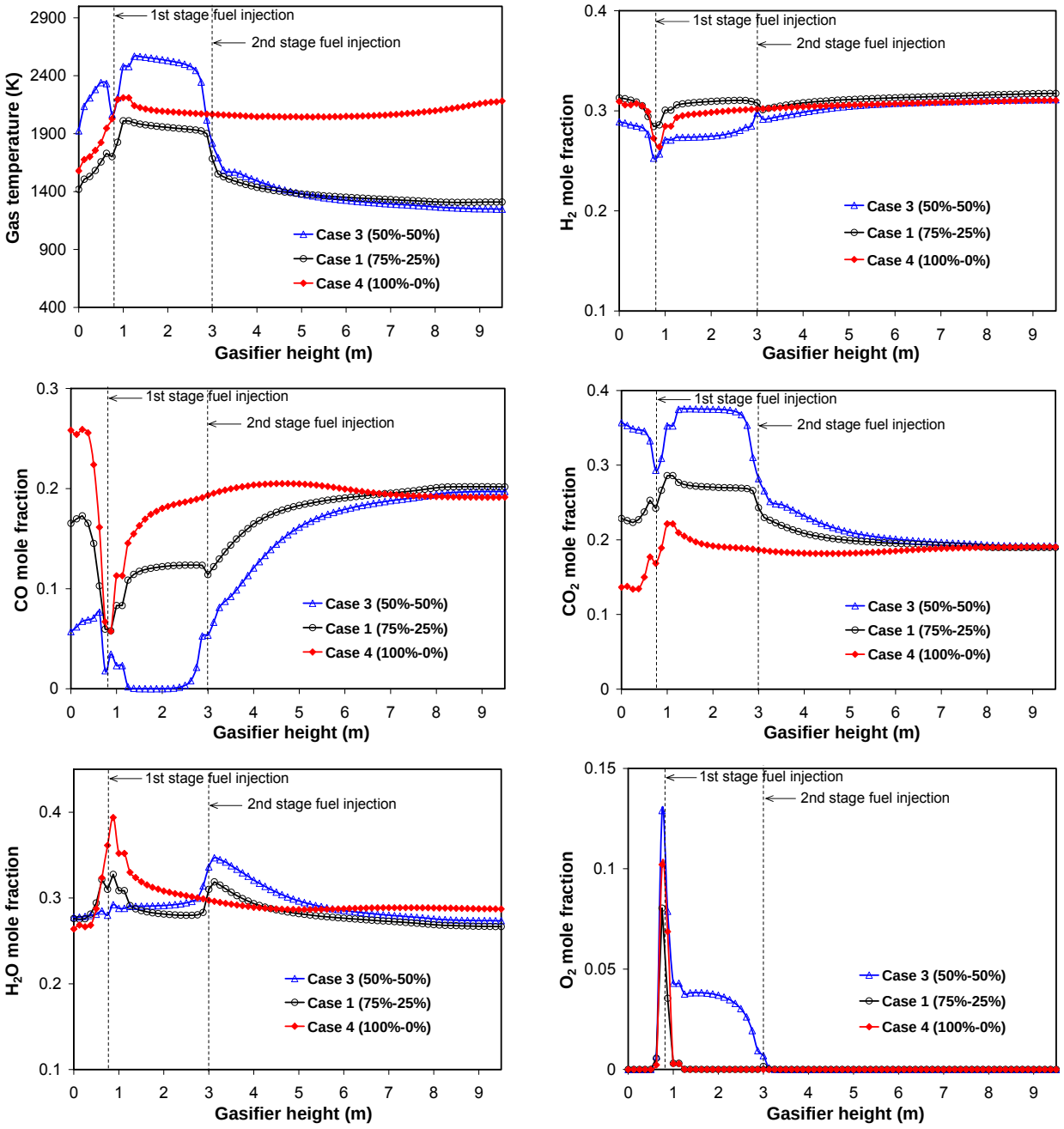

Figure 4.25 Mass-weighted averages of gas temperature and species mole fraction distributions along gasifier height for Cases 1, 3 and 4.

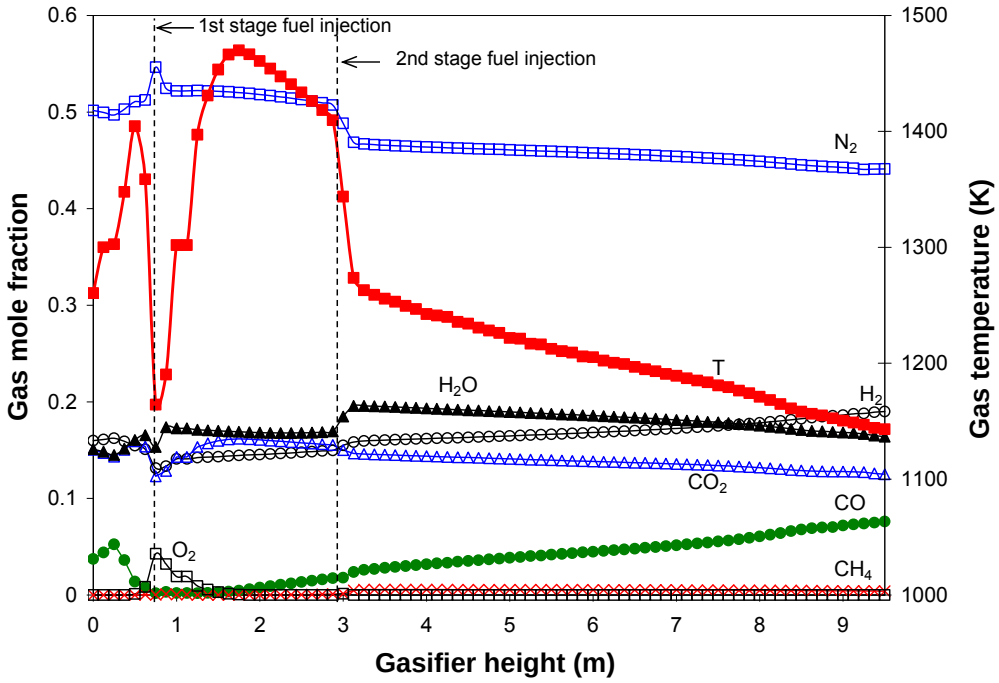

Figure 4.26 Mass-weighted averages of gas temperature and species mole fraction distributions along gasifier height for Case 5 (2-stage, 75%-25%, coal slurry, air-blown).

CHAPTER FIVE
INDUSTRIAL APPLICATIONS

A collaborative study has been conducted with the Industrial Technology Research Institute (ITRI) of Taiwan to help with its design and modifications of a demonstration coal gasifier. In return, ITRI's experimental data and operating experience are shared with University of New Orleans. The Energy and Resources Laboratories of the Industrial Technology Research Institute constructed a demonstration gasifier (Hsu et al., 2003) in the Southern Taiwan city of Kaohsiung. The gasifier, shown in Figure 5.1, is designed for a maximum load of two tons of coal per day. The gasifier is operated with oxygen-blown scheme. Coal powder is transported by nitrogen and feeds from the bottom. The hot gas flows upwards and exits from the top. A water spray device is installed on the top of the gasifier to cool the syngas temperature and adjust the H_2 or CO content of the syngas. If necessary, a water spray device is also used to control the exit gas temperature. Slag that forms on the inside wall flows to the bottom through a slag tap throat and is quenched in a water bath.

This facility is designed to convert pulverized coal and petroleum cokes into syngas at a pressure below 15 bars. The designed coal gasification efficiency under full-load operation is approximately 75% and carbon conversion exceeds 90%. The experimental system includes the following major sections: solids handling, solids feeding, gas feeding, gasification, syngas cooling, slag discharge, fines removal.

The solid feed materials include pulverized coal, petroleum cokes, and fluxing agents such as limestone. The feed materials are pulverized to a size distribution of greater than 70% by weight by passing through 200 mesh. The feed solids are discharged by the hoppers via rotary feeders and a screw conveyor, and are then transferred to the three feed injection vessels. The feed solids are discharged from the injection vessels by variable speed metering screws located at the bottom of the injection vessels. These screws are used to control the rate of the solids that are fed into the pipes of gasifier. The feed solids are mixed with oxygen and steam and are injected into the gasifier through three feed nozzles by a dense-phase pneumatic conveying system using high-pressure nitrogen.

The gasifier consists of a gasification section and a slag quench section. The gasification section is a single- stage, refractory-lined, entrained-flow reactor where the feed solids react with

oxidants and steam to be converted into syngas. The molten slag generated from the gasification section flows down through slag tap opening located at the bottom of the gasification section and falls into the slag quench section for water quenching. The designed slag tap opening size is 33% of the gasifier inner diameter.

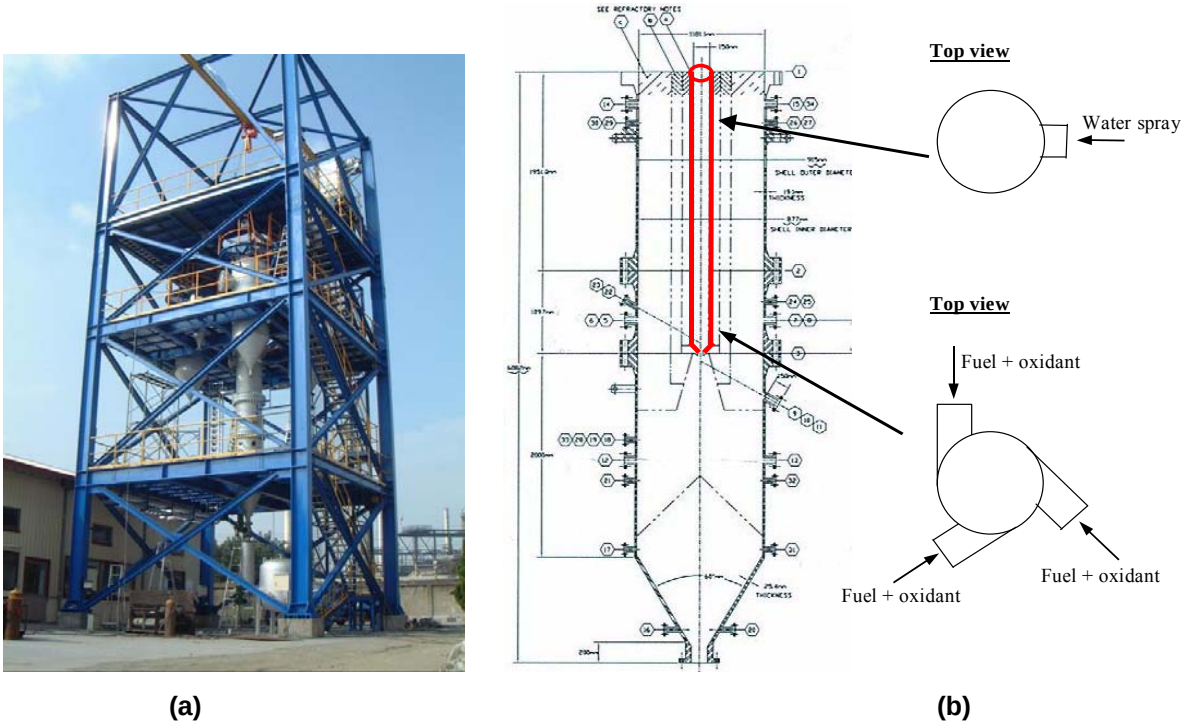

Figure 5.1 (a) Actual facility and (b) schematic of the ITRI Gasifier. The computational domain is highlighted red.

5.1 Part-Load Simulations

During the experiments, the ITRI's gasification system has not been able to maintain the full-load operation for an extended time. Various operational issues and maintenance calls have frequently affected the operation to be undertaken under part-load conditions. Therefore, it is desired to obtain some educated knowledge of the gasifier performance under various part-load conditions. To this end, specific tests are conducted to investigate the gasifier's performance and to gain operation experience under part-load conditions. In addition, computational simulations are conducted to help understand the gasifying characteristics of various part-load conditions. The ultimate goal is to compare the simulated and experimental results to improve the simulation

model. The improved model is expected to be used for providing guidance for selecting appropriate approaches for future part-load and off-design operations.

Indonesian coal is used as feedstock in this study. Its composition is given in Table 5.1. The inlet and boundary conditions are given in Table 5.2 and Figure 5.2a. A total of 204,509 tetrahedral meshes are used as shown in Figure 5.2b. The instantaneous gasification model is employed.

Table 5.1 Composition of Indonesia Coal. The 38.81% (wt) of volatiles are absorbed as C and H.

Solids or Liquids	**Weight %**
C	61.52
H	4.35
O	12.82
N	1.12
S	0.5
Ash	6.32
Moisture	13.37
Total, wt %	100
HHV kcal/kg	5690

Table 5.2 Input and boundary conditions for the baseline full-load case.

Coal feed rate (kg/h)	83.5
Steam feed rate (kg/h)	3.14
Oxidant feed rate (kg/h)	76.23
Transport nitrogen feed (kg/h)	24.05
Water spray (kg/h)	24.01

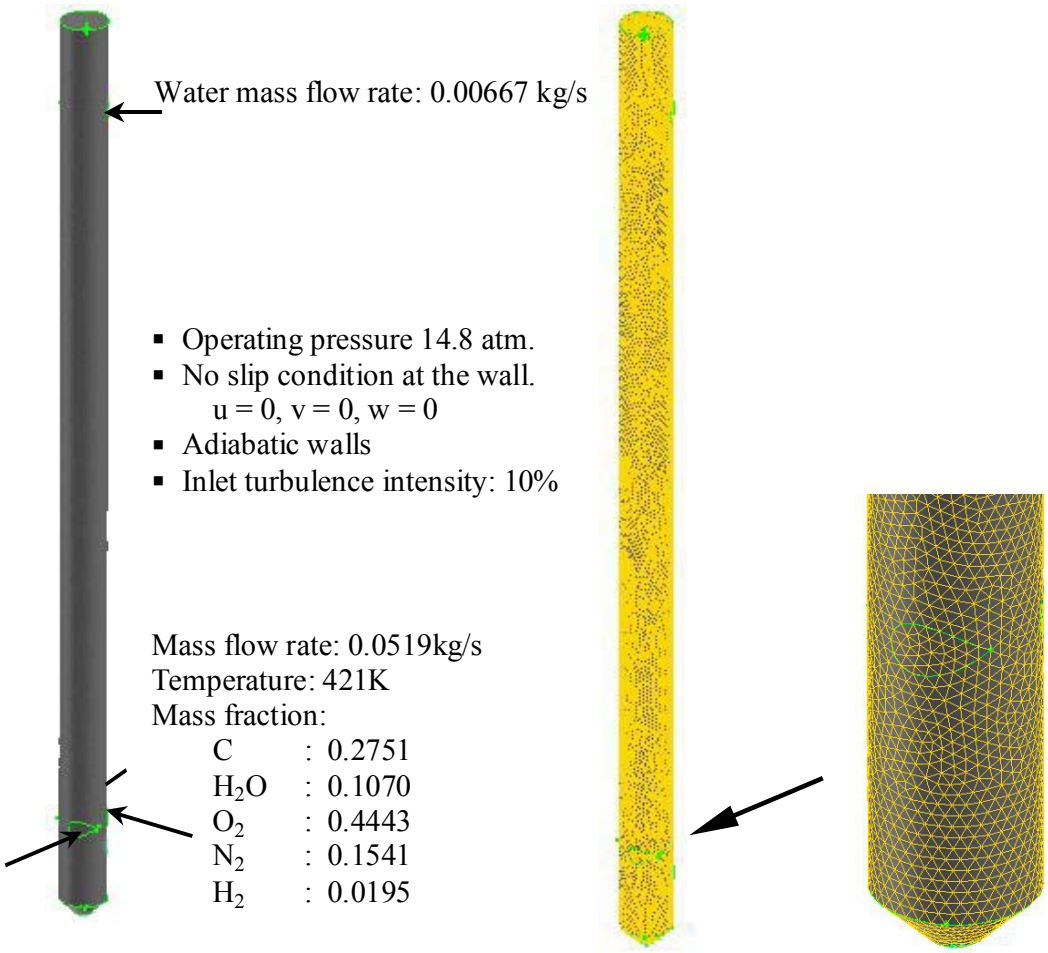

a) Boundary conditions b) Meshed computational domain

Figure 5.2 (a) Boundary conditions for the baseline case and (b) meshed computational domain.

Seven cases are simulated in this study are:

Case 1: Full load with water spray at 14.8 bars --- baseline.

Case 2: 50% load with prorated 50% water spray at 14.8 bars.

Case 3: Full load without water spray at 14.8 bars.

Case 4: Simulating experimental case at 49.7% load via one injector with prorated water spray at 2.04 bars.

Case 5: Simulating experimental case at 20.3% load via one injector with prorated water spray at 4.32 bars.

Case 6: Simulation of Case 4 with three fuel injectors feeding the same **total** mass flow as in Case 4. Each fuel injector in Case 6 is 1/3rd of the load in Case 4.

Case 7: Simulation of Case 4 with all three fuel injectors feeding the same mass flow as in Case 4. The total mass flow rate in Case 7 is three times the total load in Case 4.

The input parameters are listed in Table 5.3a and the simulation results on the gas temperature, carbon fuel conversion efficiency, and the mass-weighted average mole fractions of species at the gasifier outlet are listed in Table 5.3b.

Table 5.3a Parameters for simulated cases.

Parameters	***Case 1***	***Case 2***	***Case 3***	***Case 4***	***Case 5***	***Case 6***	***Case 7***
Fuel	100%	50%	100%	49.7%	20.3%	49.7%	149.1%
Spray	100%	50%	0%	49.7%	20.3%	49.7%	149.1%
Pressure, bar	14.8	14.8	14.8	2.04	4.32	2.04	2.04
Total mass flow rate, kg/s	0.0519	0.0258	0.0519	0.0241	0.0105	0.0241	0.0722
Coal mass flow rate, kg/s	0.0232	0.0116	0.0232	0.0115	0.0047	0.0115	0.0346
Water spray, kg/s	0.0067	0.0033	0.0000	0.0033	0.0014	0.0033	0.0099
Mass fraction at inlet							
C	0.2751	0.2751	0.2751	0.2947	0.2621	0.2947	0.2947
H_2O	0.107	0.107	0.107	0.1147	0.102	0.1147	0.1147
H_2	0.0195	0.0195	0.0195	0.0208	0.0185	0.0208	0.0208
O_2	0.4443	0.4443	0.4443	0.4072	0.467	0.4072	0.4072
N_2	0.1541	0.1541	0.1541	0.1625	0.154	0.1625	0.1625

Table 5.3b Summary of simulation results.

Parameters	***Case 1***		***Case 2***		***Case 3***		***Case 4***		***Case 5***		***Case 6***		***Case 7***	
Exit temperature, K	1774		1557		2032		1220		1308		1521		1896	
Carbon fuel conversion efficiency	20%		20%		54%		39%		9%		25%		50%	
Gasification efficiency, %	70%		70%		72%		81%		64%		71%		78%	
Fuel conversion efficiency, %	54%		54%		65%		65%		48%		57%		63%	
Components at exit:														
	Mole fraction	Mole no. (mole)	Mole fraction	Mole no. (mole)	Mole fraction	Mole no. (mole)	Mole fraction	Mole no. (mole)	Mole fraction	Mole no. (mole)	Mole fraction	Mole no. (mole)	Mole fraction	Mole no. (mole)
CO	9.0%	0.24	9.1%	0.12	28.0%	0.64	17.4%	0.23	4.0%	0.02	11.5%	0.15	23.8%	0.89
H_2	44.3%	1.17	44.3%	0.58	35.4%	0.81	44.3%	0.58	44.0%	0.23	44.7%	0.56	38.7%	1.44
CO_2	35.9%	0.95	35.8%	0.47	24.1%	0.55	27.6%	0.36	40.8%	0.21	33.1%	0.42	25.6%	0.95
H_2O	0.0%	0.00	0.0%	0.00	0.0%	0.00	0.0%	0.00	0.2%	0.00	0.0%	0.00	0.1%	0.01
N_2	10.8%	0.28	10.8%	0.14	12.5%	0.29	10.7%	0.14	11.0%	0.06	10.7%	0.13	11.8%	0.44
C	0.0%	0.00	0.0%	0.00	0.0%	0.00	0.0%	0.00	0.0%	0.00	0.0%	0.00	0.0%	0.00
Heating value (MJ/kg)	6.9		6.9		8.0		8.5		6.0		7.4		8.1	

5.1.1 Baseline Case (100% fuel load, 100% water spray)

The baseline case has a 100% fuel load with 100% water spray. Figure 5.3 illustrates the distributions of gas temperature and gas composition in the gasifier for Case 1. The plane in Figure 5.3 represents the vertical plane cutting through the center of the gasifier. The coal powder and oxygen reacts immediately as they enter the gasifier. The char burns to produce CO according to the exothermic reaction $C + 0.5O_2 \rightarrow CO$ (R1.1) and increase the temperature. The CO produced by reactions (R1.1) then reacts with the remaining O_2 to produce CO_2 through reaction $CO + 0.5O_2 \rightarrow CO_2$ (R1.4) which releases heat and further raises the temperature. The heat released from reactions (R1.1) and (R1.4) provides energy needed for all other endothermic reactions under a controlled condition with limited oxidations.

The H_2O distribution shows that H_2O is almost completely consumed as soon as it enters the gasifier. Water vapor reacts with char as soon as it enters the gasifier and produces CO and H_2 as described by the gasification reaction $C + H_2O \rightarrow CO + H_2$ (R1.3). Some of the CO reacts with the H_2O to produce CO_2 and H_2 via the water-shift reaction (R1.5). Figure 4.3 shows that all of the char is consumed through reactions (R1.1) to (R1.3). Water is injected in the upper part of the gasifier to produce more hydrogen as well as cool the syngas in this demonstration unit. When the gas reaches this location, water-shift reaction occurs again to convert more CO to CO_2 and H_2 (R1.5). The absorbed latent heat and the endothermic reaction lower the gas temperature.

To make analysis easier, a mass-flow-weighted average of each gas component is calculated across the cross-sectional area along the height of the gasifier as shown in Figure 5.4. The dips of temperature and CO curves in Figure 5.4 at height of 0.3 m are due to the injections of coal, steam, and oxygen. The highest mole fraction of C occurs at this level. The char is then quickly consumed and CO, CO_2 and H_2 are then produced. The overshoot of CO concentration immediate downstream of the injection indicates a vigorous reaction of $C + 0.5O_2 \rightarrow CO$ (R1.1). The second group of dips occurs at the height of where water is injected. As mentioned earlier, water-shift reaction takes place. CO reacts with the H_2O to produce CO_2 and H_2. Gas temperature and mole fractions of CO and H_2O reduce while mole fractions of H_2 and CO_2 increase. This water shift process is not an efficient process to produce fuel or heating value because it converts the fuel CO to H_2 and CO_2. The production of CO_2 reduces the fuel heating value. It is more efficient to produce H_2 from the gasification reaction $C + H_2O \rightarrow CO + H_2$

(R1.3), in which no CO_2 is produced. However, if more H_2 is needed as the end product, the water shift process is an optional process to produce H_2 among several other alternative methods.

As listed in Table 5.3, 100% of the carbon has reacted before the gas exits the gasifier. This fast reaction could be due to the eddy-dissipation model used in this study. In the eddy-dissipation model, the chemical reactions are assumed to be faster than the turbulence time scale; so for the size of this gasifier, the residence time is sufficient for all the reactions to be completed when the flow exits the gasifier. To evaluate the gasifier performance, four different indicators are defined in this study:

- The carbon conversion efficiency
- The carbon fuel conversion efficiency
- The fuel conversion efficiency
- Gasification efficiency.

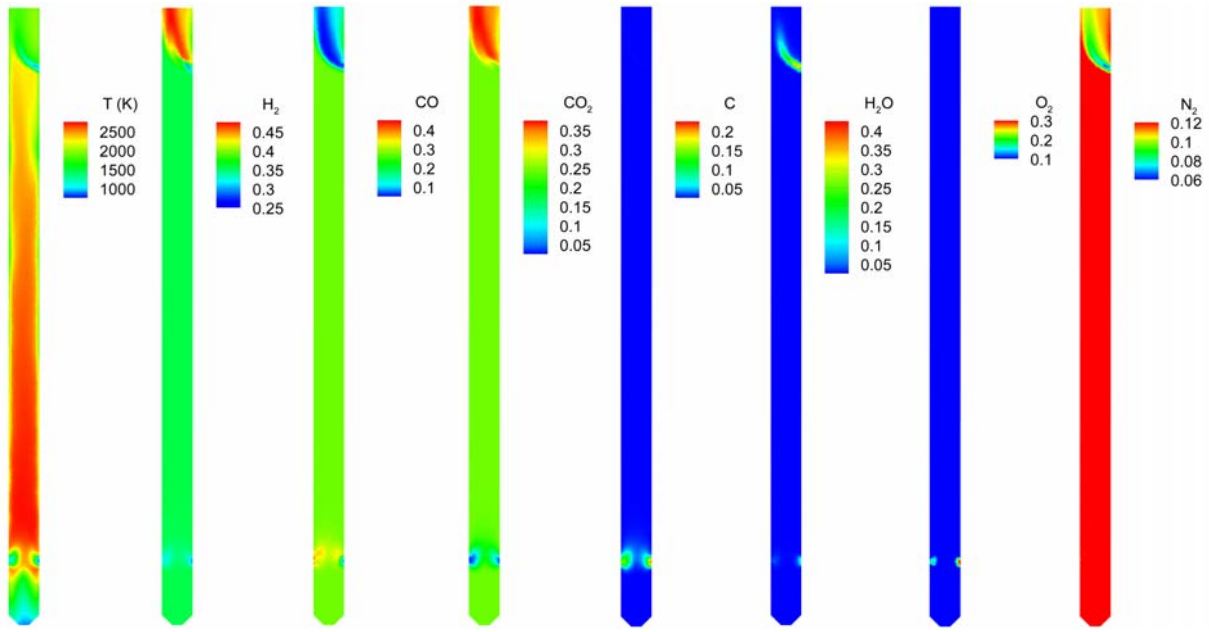

Figure 5.3 Midplane axial distribution of the gas temperature and the gas mole fraction at the center vertical plane for 100% fuel load and 100% water spray case (Case 1).

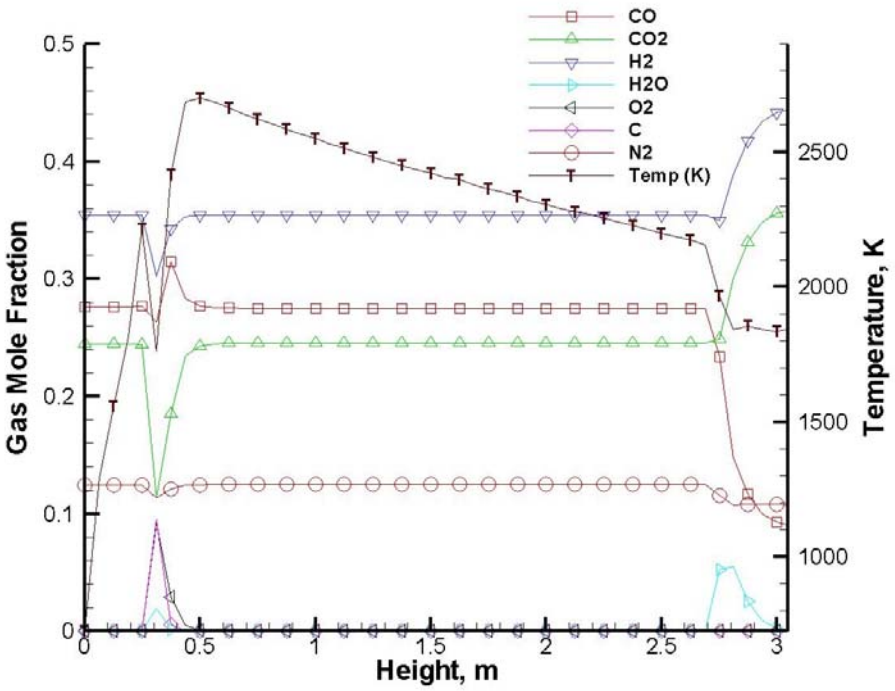

Figure 5.4 Mass-weighted average gas temperature and mole fraction along the gasifier height for 100% fuel load and 100% water spray case (Case 1).

The carbon conversion efficiency is defined as

$$\text{Carbon conversion efficiency} \equiv 1 - \frac{\text{carbon at the exit}}{\text{raw carbon} + \text{recycled carbon}} \tag{5.1}$$

Although the carbon conversion efficiency is 100% in Case 1 (i.e. no carbon is left, C = 0%), not all carbon is converted to useful fuel. The portion of carbon that is converted to CO_2 is not beneficial, so the indicator "carbon conversion efficiency" does not inform how much carbon is converted to the useful fuels, CO or CH_4, in this study. Therefore, another term "carbon **fuel** conversion efficiency" is adopted and defined as the percentage of carbon converted into the useful fuels, CO or CH_4, and written as,

$$\text{Carbon fuel conversion efficiency} \equiv \frac{[\text{CO} + \text{CH}_4]_{\text{mole}}}{[\text{raw carbon}]_{\text{mole}}} \tag{5.2}$$

So, the useful carbon conversion of Case 1 is not 100% even though 100% of carbon reacts, but rather 20% is converted to CO. Eighty percent of the carbon reacts to produce CO_2, which is not a useful fuel, in the final product.

The third performance indicator, **fuel conversion efficiency**, is defined as the ratio of the total moles of the useful fuel gases produced (H_2, CO, and CH_4) to the total moles of value of the raw carbon, water, and oxygen injected in the process. This definition can fairly compare the effectiveness of conversion of hydrogen and oxygen into useful fuels between oxygen-blown and air-blown schemes as well as dry and wet feed methods. The fuel conversion efficiency is written as,

$$\text{Fuel conversion efficiency} \equiv \frac{\left[H_2 + CO + CH_4\right]_{\text{moles}}}{\left[\text{raw carbon} + H_2O + O_2\right]_{\text{moles}}} \tag{5.3}$$

The ultimate gasification performance indicator, **gasification efficiency**, is defined as the ratio of the total heating value of the useful syngas produced (H_2, CO, and CH_4) to the total heating value of the coal injected in the process. The gasification efficiency is written as,

$$\text{Gasification efficiency} \equiv \frac{\left[H_2 + CO + CH_4\right]_{\text{heating value}}}{\left[\text{coal}\right]_{\text{heating value}}} \tag{5.7}$$

The fuel conversion efficiency and gasification efficiency in Case 1, as given in Table 5.3b, are 54% and 70%, respectively, which are relatively low. The heating value of the syngas is 6.9 MJ/kg, which is also low compared to a typical oxygen-blown gasifier. The reason for this low fuel conversion efficiency is postulated to be caused by the low steam injection accompanied by over-supplied oxygen (34% in Case 1 versus a typical 25%-30% of the stoichiometric value for a gasifier). When steam is not sufficiently available, the gasification process $C(s) + H_2O(g) \rightarrow CO + H_2$ (R1.3) only occurs in a limited fashion. With oversupplied oxygen, the condition is favorable for burning carbon monoxide via $CO + ½\ O_2 \rightarrow CO_2$ (R1.4). This can be evidenced by the very high temperature (2800K) in the gasifier as combustion is stronger than needed. A later stage of water spray near the gasifier exit exacerbates the endothermic water-shift reaction $CO + H_2O(g) \rightarrow CO_2 + H_2$ (R1.5), which produces H_2 in a less effective process (than the endothermic gasification process, R1.3) by producing CO_2. This can be evidenced by the drop of CO and rise of CO_2 at a height of 2.8 m in the gasifier in Figure 5.4. One approach to improve the fuel conversion efficiency is to take advantage of the gasification reaction R1.3 by injecting more steam near the fuel injector when carbon is still available rather than at the exit when carbon has been converted to CO.

5.1.2 Effect of Different Fuel Feed Rates with Prorated Water Spray

Case 2 is simulated to investigate the effects of using a different fuel feed rate. The fuel load percentage for Cases 2 is 50% of the full load. The water spray rate is also changed in proportion to the change of fuel feed rate. The result listed in Table 5.3 shows that Cases 1 and 2 have nearly the same exit gas temperature and compositions. Reducing fuel feed 50% does not affect the exit gas composition.

5.1.3 Effects of Removing Water Spray

Since Case 1 shows that water spray near the gasifier exit ineffectively converts CO to H_2 with co-production of CO_2, it is interesting to see if the syngas heating value can be improved by eliminating water spray. This is investigated as Case 3. The result given in Table 4 shows that the exit gas temperature (2032 K) is higher than that of Case 1 (1774 K). As expected, the exit gas contains a much higher mole fraction of CO (28%) than in Case 1 (9%), lower H_2 (35.4% vs. 44.3%) and lower CO_2 (24.1% vs. 35.9%). As a result, the fuel conversion efficiency is higher (65% vs. 54%) as well as the heating value (8.0 MJ/kg vs. 6.9 MJ/kg).

The mass-weighted averages of gas composition and temperature distributions are shown in Figure 5.5. The mole fractions of CO, H_2, and CO_2 maintain almost constant values in the gasifier higher than 0.5m after the fuel injection. In contrast, the gas temperature drops about 400 K from 0.5 m to the exit. This temperature drop is a manifestation of the two endothermic gasification reactions $C(s) + CO_2 \rightarrow 2CO$ and $C(s) + H_2O(g) \rightarrow CO + H_2$, even though the increases of CO and H_2 and the reduction of CO_2 are slight (see Fig. 5.5).

5.1.4 Comparison with the Experimental Data

Two experimental cases, Cases 4 and 5, are simulated, and their results are compared to the measured data. The experiments were conducted for part-load conditions with only one fuel injector in operation at low operating pressures. The exact water spray feed rates are not recorded, so amounts of water prorated from the full load are used in the simulation.

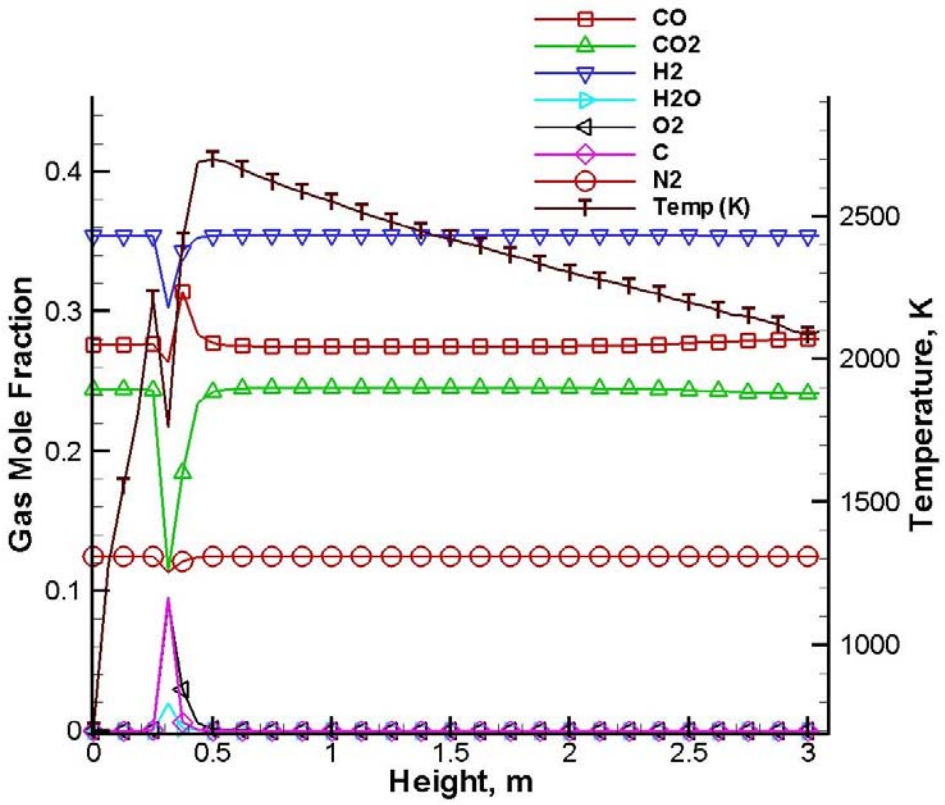

Figure 5.5 Mass-weighted average gas temperature and mole fraction along the gasifier height for 100% fuel load and without water spray case (Case 3).

The simulated results are listed in Table 5.3 and are compared with the measured data in Table 5.4. The gas mole fractions given in Table 5.4 are the values that have been normalized excluding N_2. This study does not include reactions that involve CH_4, so no CH_4 mole fractions are available from the CFD results in Table 5.3. The comparison shows CFD of Case 4 underpredicts CO and CO_2 by approximately 2.5 and 8 percentage points, respectively. On the other hand, it overpredicts H_2 by roughly 9 percentage points. This might be caused by injecting water in the simulation than actually being sprayed, so more CO is converted to H_2 via the water shift reaction. It also overpredicts the carbon conversion efficiency. The simulation predicts that all the carbon reacts, i.e. 100% carbon conversion efficiency, while the measured data shows that only 66% of carbon reacts. The gasification efficiency is significantly overpredicted. This could be contributed by the eddy-dissipation model which tends to overpredict the rates of the reactions that consume char (R1.1 through R1.3).

Table 5.4 Comparison of simulated result to measured data for Cases 4 and 5. N_2 is not included in the mole fraction calculation.

	Case 4		Case 5	
	Measured	CFD	Measured	CFD
Exit gas mole fraction:				
CO	22.00%	19.48%	36.86%	4.50%
H_2	38.52%	49.61%	26.49%	49.55%
CO_2	39.27%	30.91%	35.81%	45.95%
CH_4	0.21%	-	0.85%	-
Gas temp above inlet, K	1594	1700-2000	1495	1500-2500
Carbon conv. efficiency	66%	100%	94%	100%
Gasification efficiency	39%	81%	52%	64%

A reading from a thermocouple inserted immediately above the feedstock injection port recorded a local temperature at 1594 K. The simulated temperature at the same location is about 2000 K, which is approximately 400 K above the measured value. The temperature difference between the simulated and measured value seems large; however, the temperature field (Figure 5.6) near the thermocouple measuring location shows large temperature gradient and gives a gas temperature range from 1700 K to 2000 K within a few centimeters. Considering the uncertainty in accurately determining the measuring locations during the experiment and the uncertainty in predicting the flame fronts near the fuel injectors, it could be fair to state that the simulated temperature is roughly 100-400 K higher than the measured data. Similarly, strong temperature gradients, actually stronger than in Case 4, exist near the thermocouple measurement location in Case 5 (Figure 5.6). The temperature drops almost 1,000 K within a short distance above the fuel injectors. The higher predicted temperature is also attributed to the adiabatic wall assumption made for the simulation.

The comparison between the simulated and measured data for Case 5 shows the simulation significantly underpredicts the CO mole fraction but overpredicts H_2 and CO_2 mole fractions and the carbon conversion efficiency. This might be caused by injecting too much water before the gasifier exit in the simulation and consequently converts too much CO into H_2 and CO_2 than in the experiment. Predicted exit gas composition in Case 4 is closer to the experimental data than in Case 5; it seems also more water is injected in the simulation than in the experiment. Therefore, it is important to accurately record the amounts of water spray in

future experiments. The prediction of coal gasification efficiency is off by 12 percentage points in Case 5 but significantly overpredicted in Case 4.

The discrepancies between the simulated and the experimental results could be attributed by the following possible reasons:

- The eddy-dissipaton model of the reaction rates could provide faster rates and earlier equilibrium status than the real reaction, so the gasification efficiency and carbon conversion efficiency are both overpredicted. Finite rate reaction model is recommended for future analysis.
- Since the data were obtained under off-design, part-load conditions, the data could be taken under transient or non-equilibrium conditions, which might render less-efficient gasification than otherwise under the steady-state and equilibrium condition in simulations.
- Higher temperature gradients exist near the feedstock injection region. A minor mismatch in the measurement locations with those in the computational results would cause large temperature difference.
- The amount of water spray is not known. This would throw the simulations in either the under or over prediction direction.

5.1.5 Effects of Number of Injections

Cases 6 and 7 are simulated to investigate the effects of the number of injectors on the gasifier performance. In Case 6, the same total fuel feed rates as in Case 4 is used, but it is injected through all three injectors, as opposed to only one injector as in Case 4. Changing from Case 6 to Case 4 is similar to a situation when two of the three injectors are under maintenance, and the only operating injector has to take the entire load. In Case 7, the same fuel feed rate injected through the one injector in Case 4 is injected through each of the three injectors. Changing from Case 7 to Case 4 is similar to a situation when two of the three injectors fail and the remaining injector continues to inject at the same rate. The total fuel feed rate in Case 4 is therefore 1/3rd of Case 7.

The result in Table 5.3 shows that Case 4 has a better performance than Case 6. The exit gas for both cases have nearly the same H_2 content (roughly 44%), but the CO content of Case 4 (17.4%) is six percentage points higher than that of Case 6. As a result, the heating value of the

syngas for Case 4 (8.5 MJ/kg) is higher than Case 6 (7.4 MJ/kg). This is contrary to our intuition that employing three injectors would give a better performance because three injectors usually produces more uniform and stronger reactions than employing only one injector. Since the major difference between operating one and three injectors is associated with flow pattern, investigation is then directed towards studying the flow field of these two cases.

The flow pathlines for Cases 4, 6 and 7 are shown in Figures 5.7a, 5.7b, and 5.7c, respectively. The flow leaving the single injector in Case 4 is nine times stronger in momentum than the flow leaving each of the three injectors in Case 6. Thus, the cyclonic flow in Case 4 is stronger than in Case 6 and creates faster mixing and reactions. Flow animation movie (not shown here) shows that there is a strong twisting flow moves towards bottom in Case 4 due to the strong cyclone-induced low-pressure core. This patch of gas later spirals upward from the bottom moving opposite to the downward moving core. This downward moving flow is also observed in Case 6, but it is weaker. It is postulated that this downward mixing would enhance gasification and fuel conversion efficiencies.

The gasification performance and syngas composition of Case 7 are on par with Case 4 even though the total mass flow rate in Case 7 is three times more than Case 4. It is postulated that the strength of each injector is the primary factor that strongly affected the cyclone strength because the momentum and speed from each injector is identical between Cases 4 and 7. When compared with syngas composition in Case 4, the CO mole fraction is higher but the H_2 and CO_2 mole fractions are lower in Case 7. This may indicate that the water-shift reaction after the water injection in Case 7 is not as strong as in Case 4. The higher gas velocity induced by the higher total mass flow rate of Case 7 may lead to insufficient time to allow sprayed water to effectively react with CO through the water-shift reaction. As a result, less CO reacts with H_2O and less H_2 and CO_2 are produced. A small amount of water is noticed to remain at the exit. Figure 5.7 shows that flow pathlines of Case 7 is similar to Case 6 except the water-shift process downstream of the water injection is pushed towards the water injector site by the faster and stronger through-gas flow.

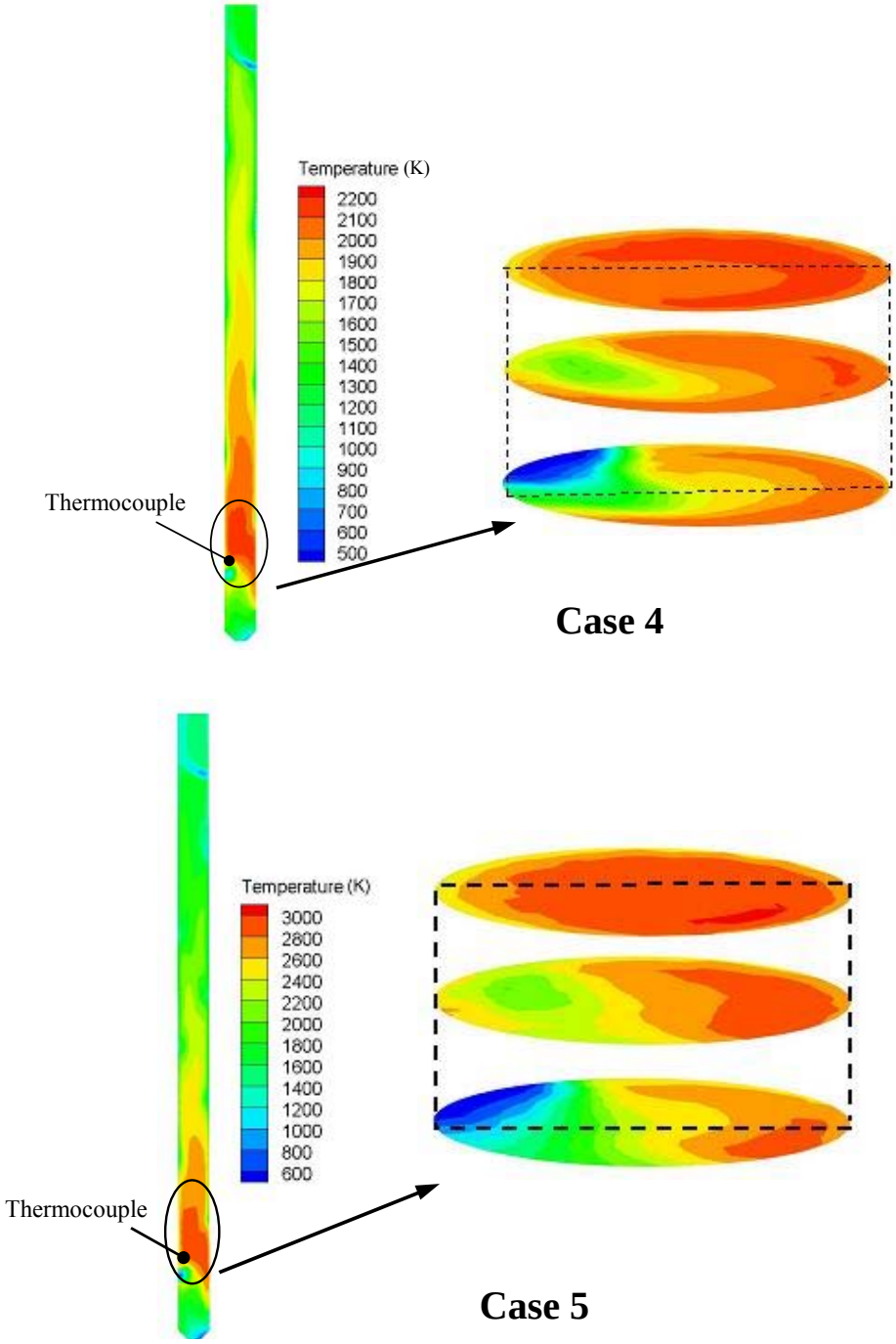

Figure 5.6 Temperature distributions for Cases 4 and 5.

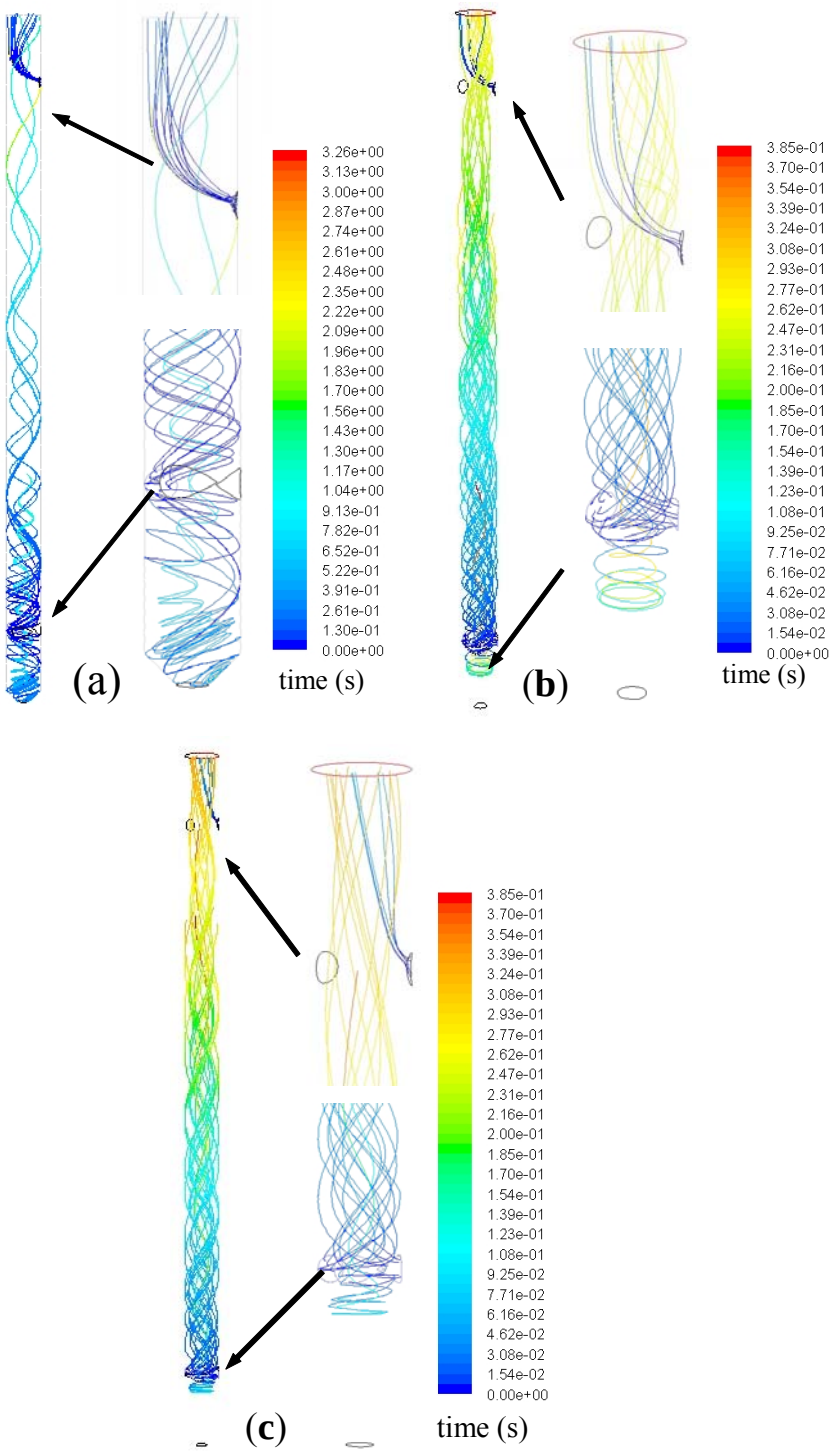

Figure 5.7 Flow pathlines for (a) Case 4 (1 injector), (b) Case 6 (3 injectors) and (c) Case 7 (3 injectors and 3 times more of feed mass flow rates).

5.1.6 Summary of Part-Load Analysis

The results of the baseline case (100% fuel feed rate, 100% water spray) shows that spraying water near the exit of the gasifier is not an effective approach to produce H_2 because the water shift process $CO + H_2O(g) \rightarrow CO_2 + H_2$, is likely to take place by converting CO (a good fuel) to CO_2 and H_2. The production of CO_2 during water shift process reduces the fuel heating value. Rather, it is more efficient to produce H_2 from the gasification reaction $C + H_2O \rightarrow CO + H_2$, in which no CO_2 is produced. If more H_2 is needed as the end product, it is recommended that steam be injected near the feedstock injection ports when plenty carbon is available and temperature is high. The steam can be generated from waste heat without consuming the gas flow energy. Spraying water will take energy away from the gas flow and reduce efficiency. Furthermore, with reduced temperature, the water shift reaction is more likely to take place than the more effective gasification reaction.

Comparison between the simulated and the part-load experimental data shows discrepancies. The CFD simulation usually overpredicts the carbon conversion efficiency and gasification performance. This could be attributed to the eddy-dissipation reaction rate model, which seems to produce faster than the actual reaction rates in this study. The simulation also overpredicts H_2 but underpredicts CO, possibly caused by injecting more water than the unknown actual amounts. The discrepancy in temperature comparison could be contributed by the uncertainty of thermocouple measurement location and the extremely large temperature gradients surrounding the measurement locations.

Employing fuel injection through a single injector unexpectedly performs better than applying three injectors. The results indicate the injection velocity speed and momentum strength of each injector, rather than the total momentum, could be more influential in affecting the gasification efficiency. The computational model developed in this study, although complex as it seems, is still rudimentary in predicting the complicated gasification process. Further improvements are required including incorporating finite rate reactions and imposing temperature and pressure factors upon the reaction rates.

5.2 Effect of Slag Tap Size on Gasification Performance and Heat Losses in a Quench-Type Coal Gasifier

With the current slag tap design, the problem of clogged slag tap is often encountered. The clogging problem can be temporarily resolved by employing a kerosene burner to melt the solidified slag. However, resolving this problem permanently by opening up the slag tap and/or directing the coal injector downward is more desirable. There is a concern that opening the slag tap wider would allow more heat losses to the water bath below and result in both reduced thermal efficiency and degraded gasification performance. Therefore, computational simulations are conducted to investigate the possibility of modifying the slag tap opening size or the fuel/oxidant injections direction to help avoid the clogged slag tap problem without adversely affecting the performance. This is one of the challenges between the scaling of larger and the smaller gasifiers. The slag tap opening of the larger gasifier can not be adequately scaled down to smaller gasifiers. Therefore, an independent study of slag tap opening size needs to be conducted for each different size of gasifier.

5.2.1 Studied Cases

A total of four cases are investigated in this study as shown in Figure 5.8. Case 1 is for the current slag tap opening which is 2 inches in diameter and is 33% of the gasifier's inner diameter (6 inches). Two other wider slag tap openings are also investigated with Case 2: 66% (4 inches) and Case 3: 100% (6 inches, i.e. no slag tap) of gasifier inner diameter. Cases 2 include two fuel injection arrangements: Case 2a has the current horizontal injection arrangement with an tangential angle of 45^{o} while Case 2b injects fuel 15° downward plus an tangential angle of 45^{o} intending to help further melt the slag near the slag tap throat to avoid clogging.

5.2.2 Results

The results are shown in Table 5.5. From the various conversion efficiency and syngas heating values, it can be clearly seen that increasing slag tap size from 2-inch to 6-inch diameter reduces the gasification performance and syngas heating value approximately 10%. The degradation of gasification performance is believed to be caused by increasing heat loss to cold water bath as slag tap opening widens. This is consistent with the concerns shared by the original gasifier's designer who designed the slag taps opening diameter to be 1/3 of the gasifier

main chamber diameter to reduce heat losses. The increased heat loss with larger slag tap opening is supported by data in Table 5.6 that shows that heat loss increases 13.5% when the slag tap opens up from 2-inch to 6-inch in diameter.

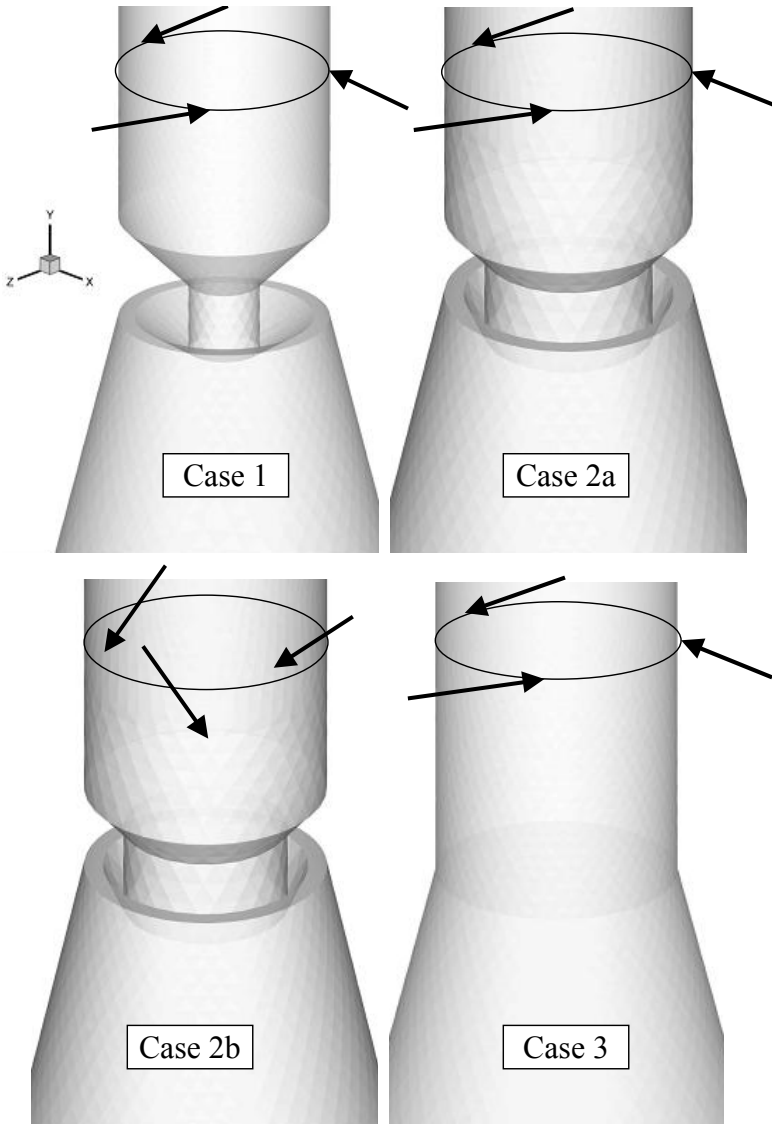

Figure 5.8 Four studied cases: (a) Case 1: 2 inch opening (b) Case 2a: 4-inch opening with horizontal injection. (c) Case 2b: 4-inch opening, injection 15^{o} downward (d) Case 3 6-inch opening (no slag tap).

Table 5.5 Results for the cases of various slag tap opening sizes.

Parameters	***Case 1***		***Case 2a***		***Case 2b***		***Case 3***	
Exit temperature, K	1342		1375		1360		1333	
Carbon fuel conversion efficiency, %	69%		63%		62%		52%	
Coal gasification conv. efficiency, %	61%		58%		59%		55%	
Fuel conversion efficiency, %	69%		66%		67%		62%	
Components at exit:	Mole fraction	Mole no. (mole)	Mole fraction	Mole no. (mole)	Mole fraction	Mole no. (mole)	Mole fraction	Mole no. (mole)
CO	9.4%	0.11	9.2%	0.11	7.8%	0.09	5.6%	0.07
H_2	39.2%	0.48	39.1%	0.46	40.0%	0.48	40.5%	0.47
CO_2	25.0%	0.30	26.5%	0.31	26.5%	0.32	29.0%	0.34
VM	14.1%	0.17	13.2%	0.16	13.5%	0.16	12.9%	0.15
H_2O	1.8%	0.02	1.5%	0.02	1.9%	0.02	2.7%	0.03
N_2	10.5%	0.13	10.5%	0.12	10.3%	0.12	10.2%	0.12
C	0.0%	0.00	0.0%	0.00	0.0%	0.00	0.0%	0.00
Heating value (MJ/kg)	7.9		7.6		7.7		7.2	

Table 5.6 Heat loss to the water bath for four cases.

	Heat flux, W/m²
Case 1	579
Case 2a	614
Case 2b	616
Case 3	685

The velocity vectors on a vertical midplane of the gasifier for Case 1 (2-inch opening) in Figure 5.9 show that the gas in the quench section is almost stagnant. Almost all of the gas that flows down (actually spirals down) from the gasification section is blocked by the constriction of the slag tap. Only a very small percentage of the gas spiraling through the slag tap throat and into the quench section. The spiraling down flow produces a core of upflowing breeze in the center of the downward spiraling column to maintain mass conservation, as can be seen in Figure 5.10. As the opening is widened (Cases 2 and 3), more gas spirals down from the gasification section into the water bath section.

The effects of widening the slag tap opening on the gas temperature are observed in Figure 5.11. Because of the small slag tap opening in Case 1, only a very small fraction of hot

gas from the gasification section flows down through the slag tap throat. There is a large temperature difference across the slag tap. As the opening size is increased, more of the hot gas flows down through the slag tap opening and into the cold quenching region. Thus the gas temperature in the quenching section just below the slag tap (or upper part of the quenching section) becomes several hundred degrees higher as the slag tap opening size is increased. However, lower half part of the quenching section maintains about the same temperature at near 350K irrespective of the slag tap opening sizes. Gas temperature in the gasification section does not show much variation between all cases. Since the flow in the quenching section is almost stagnant for all cases, the heat loss to the water bath is expected to be mainly transferred via radiation. Therefore, larger slag tap opening will induce a larger shape factor leading to larger heat transfer loss as previously shown in Table 5.6.

Gas composition plots in Figure 5.12 show that gas compositions in the gasification section are almost identical for all slag tap opening sizes, except after the water spray. Water shift reaction occurs ($CO + H_2O \rightarrow CO_2 + H_2$) when the water is sprayed. As a result, a decreased in CO and an increase in both CO_2 and H_2 are observed. Among the four cases, Case 1 (smallest opening) has the highest CO content at the exit and the lowest CO_2 and H_2 contents. Case 3 (no tap), on the other hand, has the least amount of CO content and the highest CO_2 and H_2 content. Changing the injection direction from horizontal to 15 degrees downward (Case 2a to Case 2b) does not make noticeable difference to the gas temperature and compositions. Unburned volatile fraction seems to increase in Case 3 with no slag tap arrangement (wide open). There is the concern that unburned volatile could be condensed into tar in the cooler downstream of gasifier during the cold-stream clean up process. Therefore, it is essential to know the benefit as well as drawbacks of opening the slap tap wider. By allowing slag to move successfully without clogging, about 10% of gasification performance and syngas fuel heating value are compromised and lost. It should be noted that the present simulation has not considered the formation and flowing of molten slag layer, so the heat loss is over predicted. This is because, in the real situation, the slag layer will reduce the effective slag tap opening and hence, the radiation loss will be proportionally reduced.

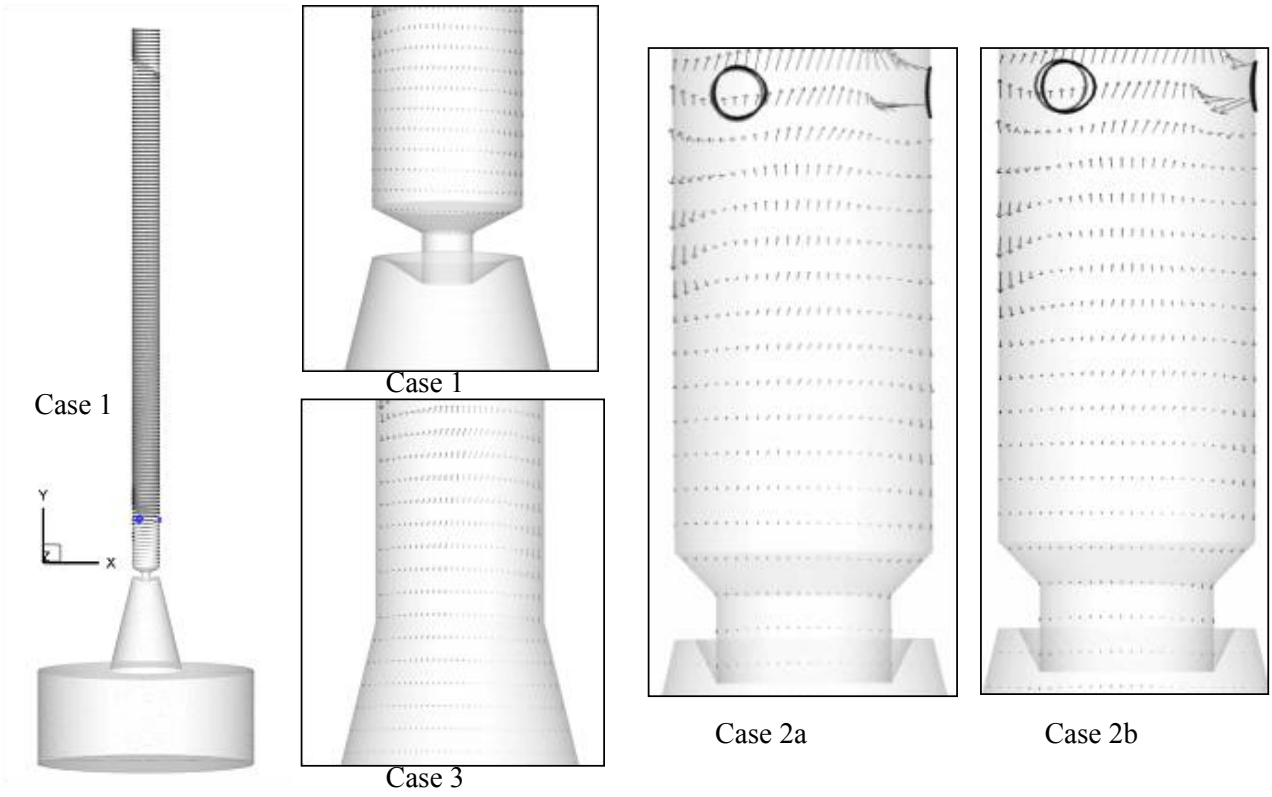

Figure 5.9 Velocity vectors on vertical midplane of gasifier for four cases. Flow in the quenching section is almost stagnant for all cases.

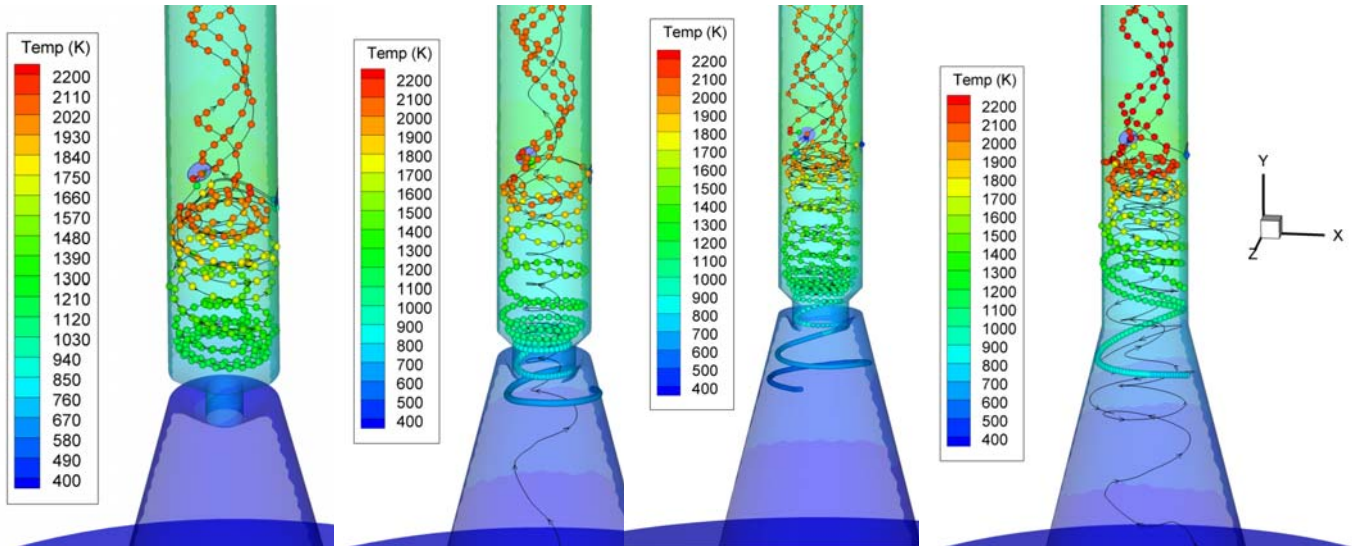

(a) Case 1 **(b) Case 2a** **(c) Case 2b** **(d) Case 3**

Figure 5.10 Flow pathline traces and temperature distributions for all cases. The background color is the translucent back wall temperature, not the gas temperature. The gas temperature is represented by the colors of the spheres. Minimal flow pathline traces are seen in the quench section.

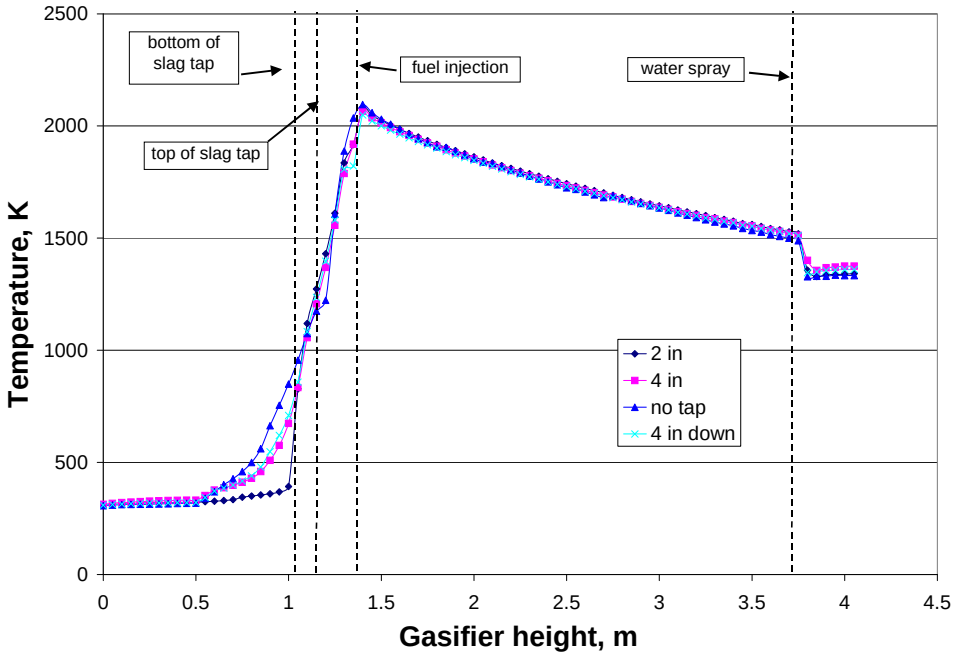

Figure 5.11 Mass-weighted temperature average at different gasifier heights.

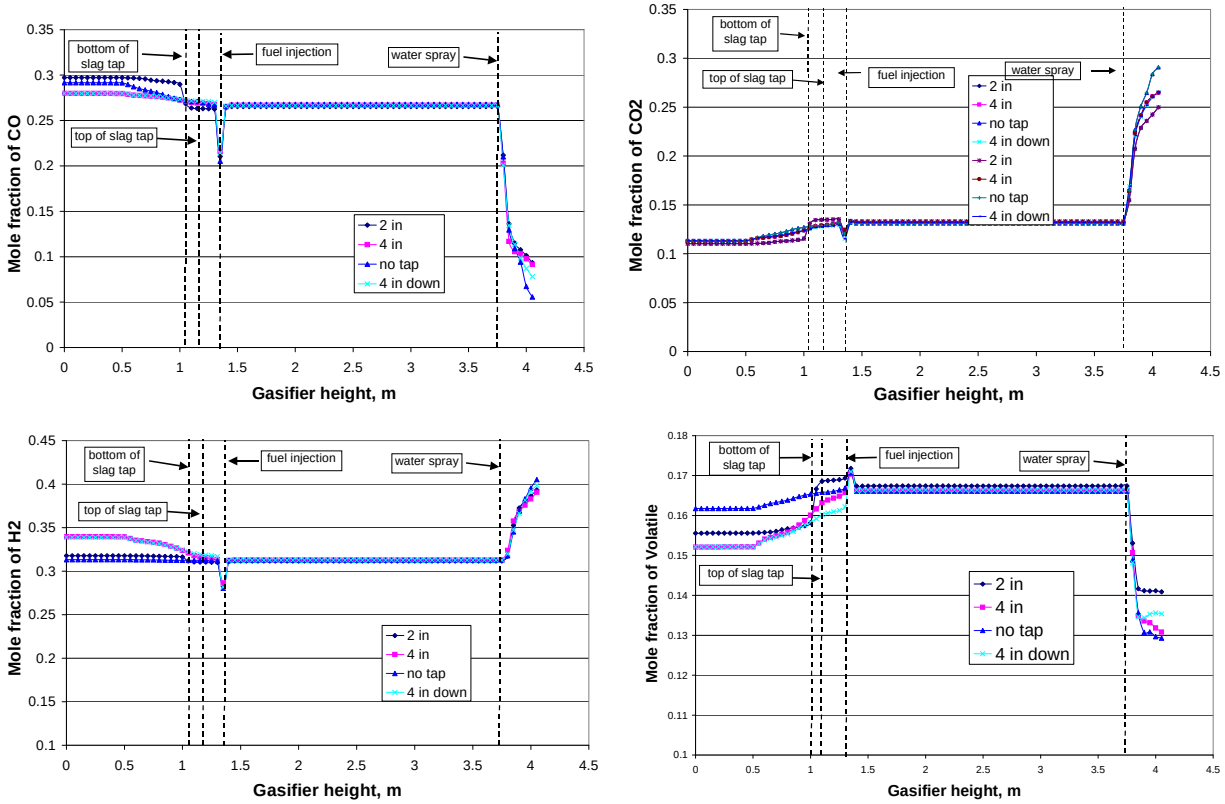

Figure 5.12 Mass-weighted gas mole fractions at different gasifier heights.

5.2.3 Conclusions of Slag Tap Study

Operation of a quench-type coal gasifier has frequently encountered the problem of clogged slag tap, especially for smaller gasifier. One possible means to avoid this problem is by widening the slag tap opening. The results show that the gas in the quenching section is almost stagnant. Opening up the slag tap only slightly increases flow motion in the quenching section. Temperature in the upper half of quenching section increases several hundred degrees, but it maintains the same in the lower half portion of the quenching section. This implies that radiation is the major heat transfer mode between the cold water bath and hot gas in the gasifier. Opening the slag tap increases shape factor and increases heat loss to the water bath. The overall gasification performance and syngas fuel heating values are downgraded approximately 10% when the slag tap opening widens from 2-inch to 6-inch in diameter. Unburned volatile fraction also increases as the slag tap widens. There is a concern that the increased unburned volatile could be quenched and condensed into tar in the cooler downstream of the gasifier during the cold-stream clean up process. Changing the injection direction from horizontal to 15 degrees downward does not make a noticeable difference to the gas temperature and gasification performance. The benefit of opening the slap tap wider by allowing slag to move successfully without clogging is compromised by increased heat losses, reduced gasification performance, downgraded syngas heating value, and increased unburned volatile matter.

5.3 Investigation of Heat Transfer and Gasification of Two Fuel Injectors

Fuel injectors in a gasifier operate in a very harsh environment. Extreme high pressure and hot temperatures often cause the injectors to fail in a short period of time, typically in 6 to 12 months. Each occurrence of a failed injector has caused an unwanted operation interruption that results in undesired expenses and reduced profit margin. Improvement of the operating life of fuel injectors has been identified as one of the most important research goals in the gasifier industry. ITRI's demonstration gasifier has faced this similar problem and has modified its fuel injectors in an attempt to lengthen the injector life expectancy and minimize the fuel injector failure problems. A study has been conducted to analyze the flow and temperature fields in the vicinity of the injector tip and the metal temperature of two different injectors. Because the focus of this study is the heat transfer on the fuel injectors, the instantaneous gasification model is chosen over the finite-rate model to save computational time.

Figures 5.13 and 5.14 show the schematics of fuel injectors before and after modification. The original injector consists of two concentric pipes. Fuel (pulverized coal) along with the transporting medium, nitrogen, is injected through the center pipe, while oxidant (95% O_2 and 5% N_2) is injected through the outer pipe. The conical nozzle of the original design of the injector allows the fuel and oxidant to premix before entering the gasifier. Due to the operational failures of this design, the tip of the injector has been modified by removing the conical nozzle as shown in Figure 5.14. Without the nozzle, the modified injector has a blunt tip. The outer pipe is sealed at the tip and small holes are drilled at the tip of the outer pipe to create a similar pressure drop as before the modification. Fuel enters the gasifier through the center hole, while oxidant enters through the 8 small outer holes. In the modified injector, the fuel and oxidant do not mix before entering the gasifier. CFD study has been performed to investigate the heat transfer on both injector designs. In this report, the simulation of the original injector design is referred as Case 1, and the simulation of the modified injector design is referred as Case 2.

The CFD model for each of the fuel injector design is divided into two steps: (1) calculate the fluid mechanics and reactions inside the gasifier and (2) use the calculated flow and thermal results as the boundary condition to calculate the heat transfer around and within the injector itself. Other than to provide boundary conditions, the purpose of performing step (1) is to investigate the effect of fuel injector designs on the gasification process.

The meshed computational domain for Case 1 is shown in Figure 5.15. The slag tap and the quenching section are not included in the calculation domain because we are interested in the region near the injectors. Finer meshes are created near the injectors and coarser mesh is used away towards the bottom and the top (exit). The domain includes a small part of the injector which is outlined with red lines. Figure 5.16 shows the computational domain for the injector heat transfer simulation. Temperature distributions on the injector outside/tip walls and at the mouth of the injector hole obtained in gasifier flow computation in step 1 is used as the boundary conditions in step 2, as shown in Figure 5.16. A total of 2,266,187 mesh cells are used for gasifier simulation and 890,556 mesh cells are used for injector heat transfer calculation.

The meshed computational domains for Case 2 are presented in Figures 5.17 and 5.18. Similar to the case of the original design, the temperature distributions on the modified injector tip wall and at the mouth of the injector holes in step 1 are used as boundary conditions in step 2.

Mass flow rates used in the study are listed in Table 5.7. The instantaneous gasification model is used.

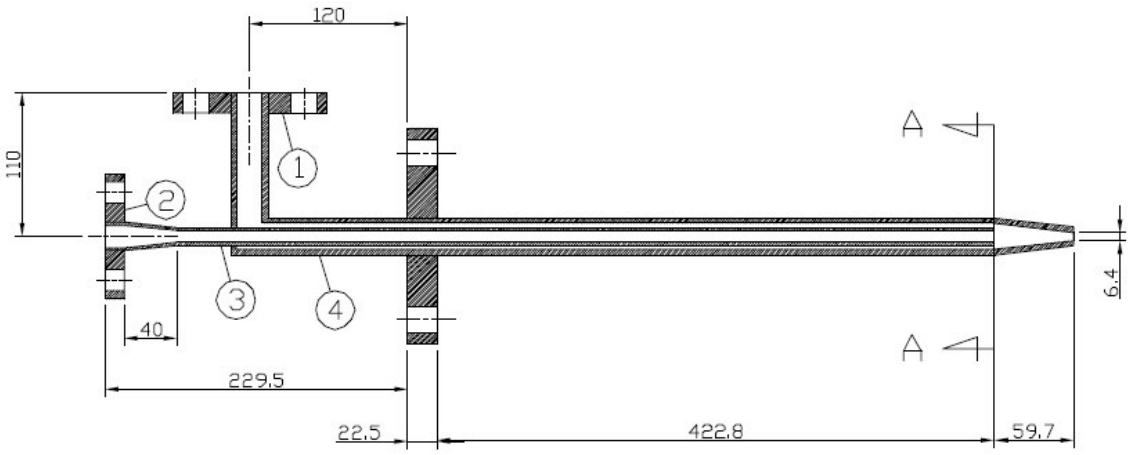

Figure 5.13 Schematic of the original fuel injector design with a conical nozzle tip (scale: mm).

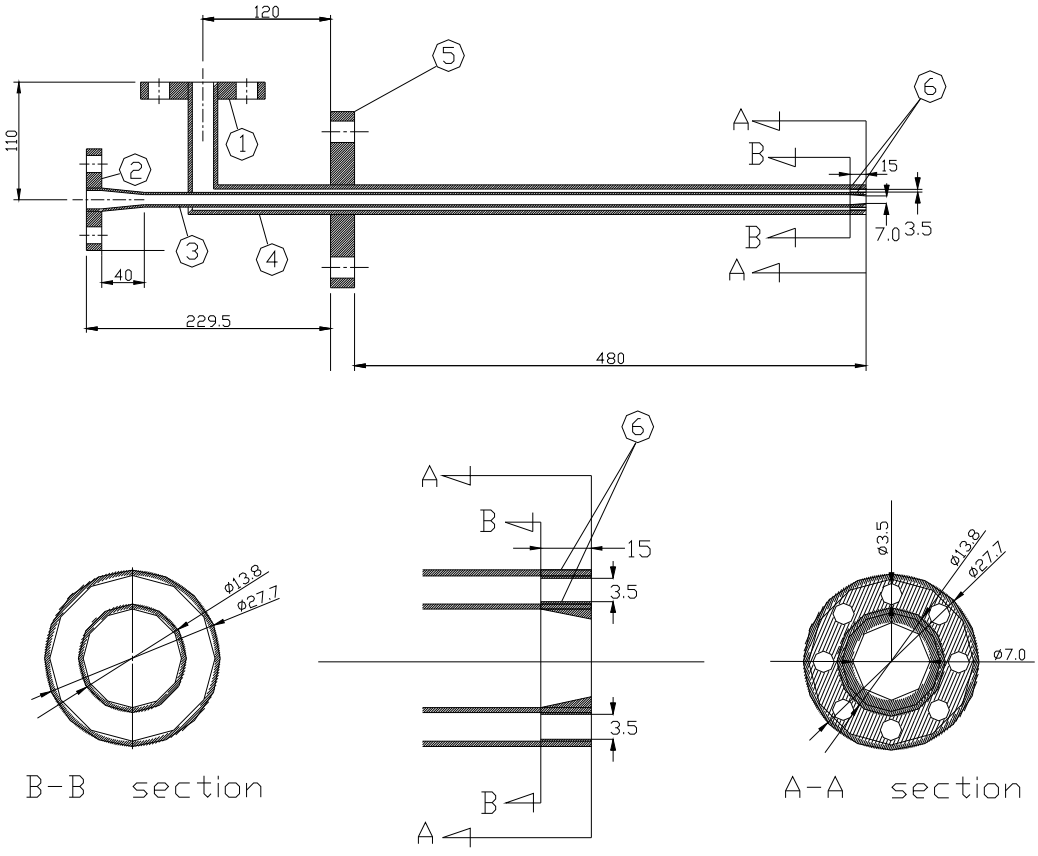

Figure 5.14 Schematic of new fuel injector design with a blunt tip (scale: mm).

Table 5.7 Mass flow rates and mass fractions at each inlet.

	Center pipe	*Outer pipe*
Mass flow rate, (kg/s)	0.01022	0.004972
Mass fraction:		
C	0.287	0.000
O_2	0.060	0.950
H2O	0.091	0.000
H2	0.050	0.000
volatile	0.290	0.000
N2	0.222	0.050

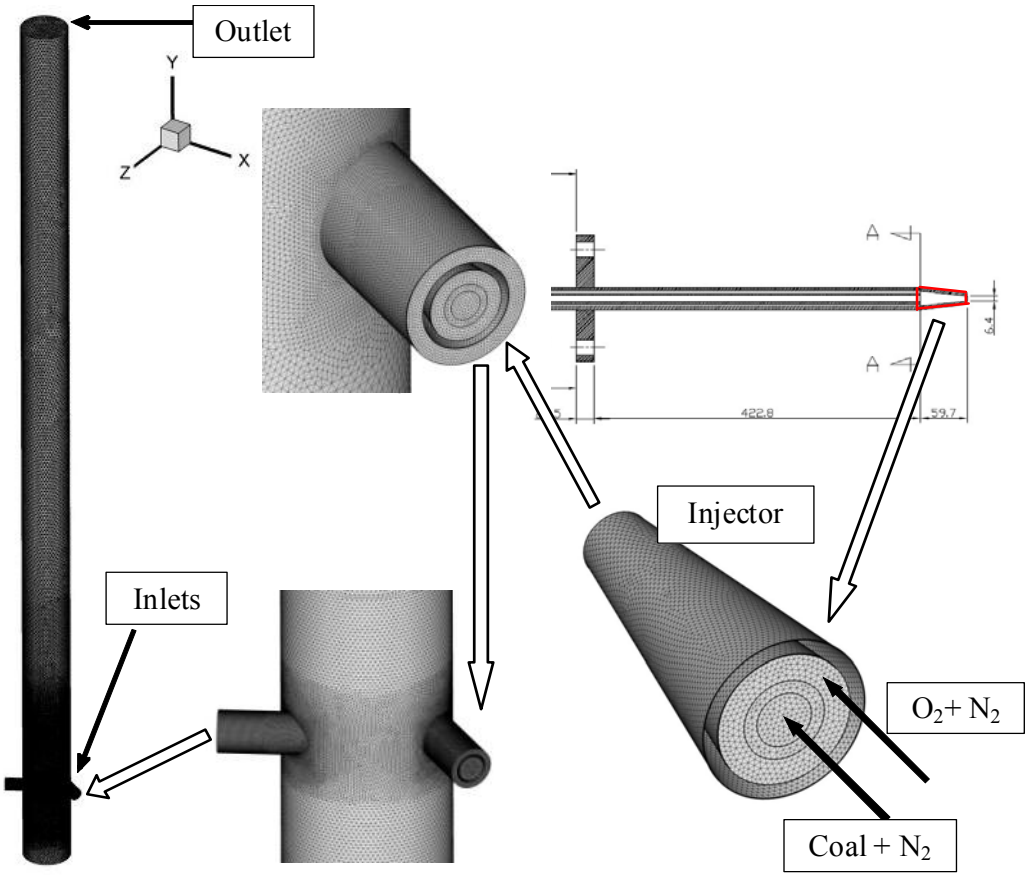

Figure 5.15 Meshed computational domain for entire gasifier with the original injector design (Case 1).

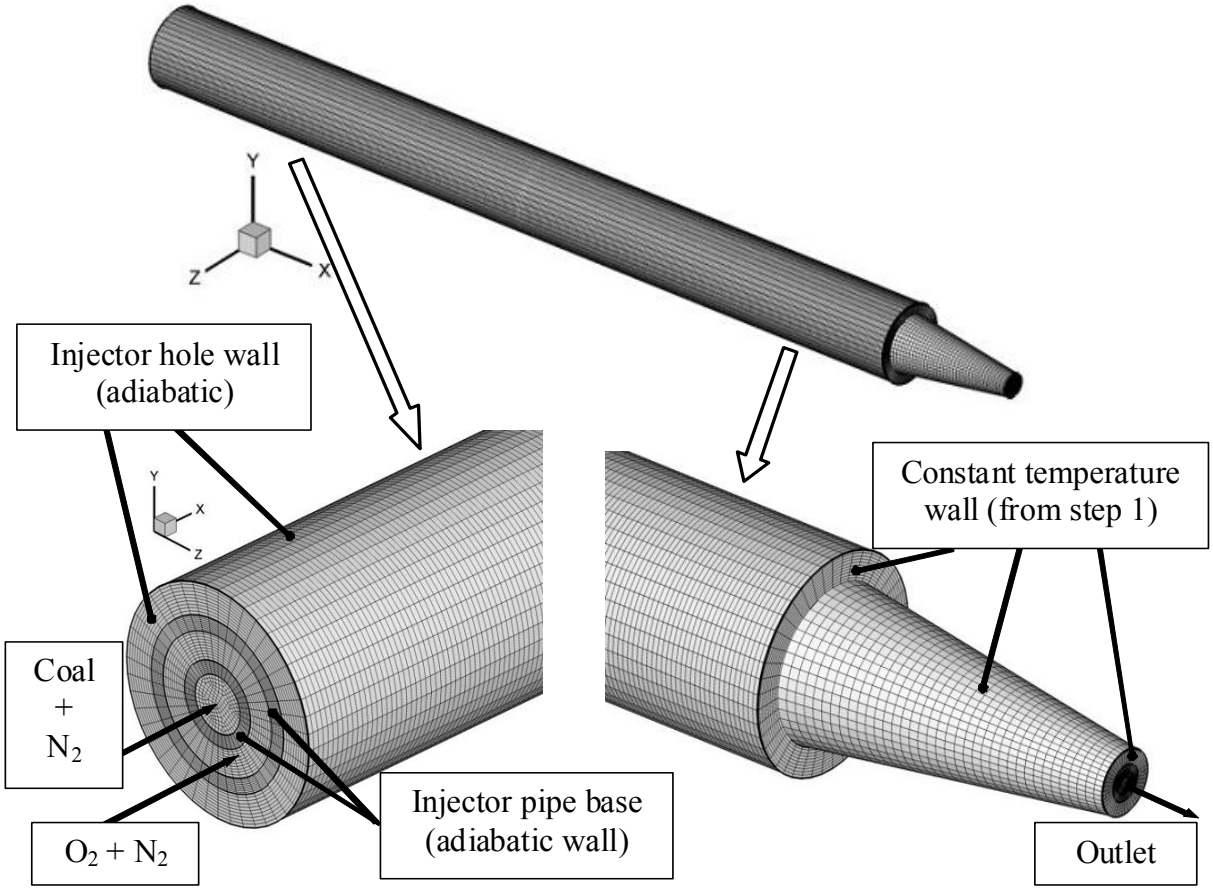

Figure 5.16 Meshed computational domain for heat transfer simulation within the original fuel injector (Case 1).

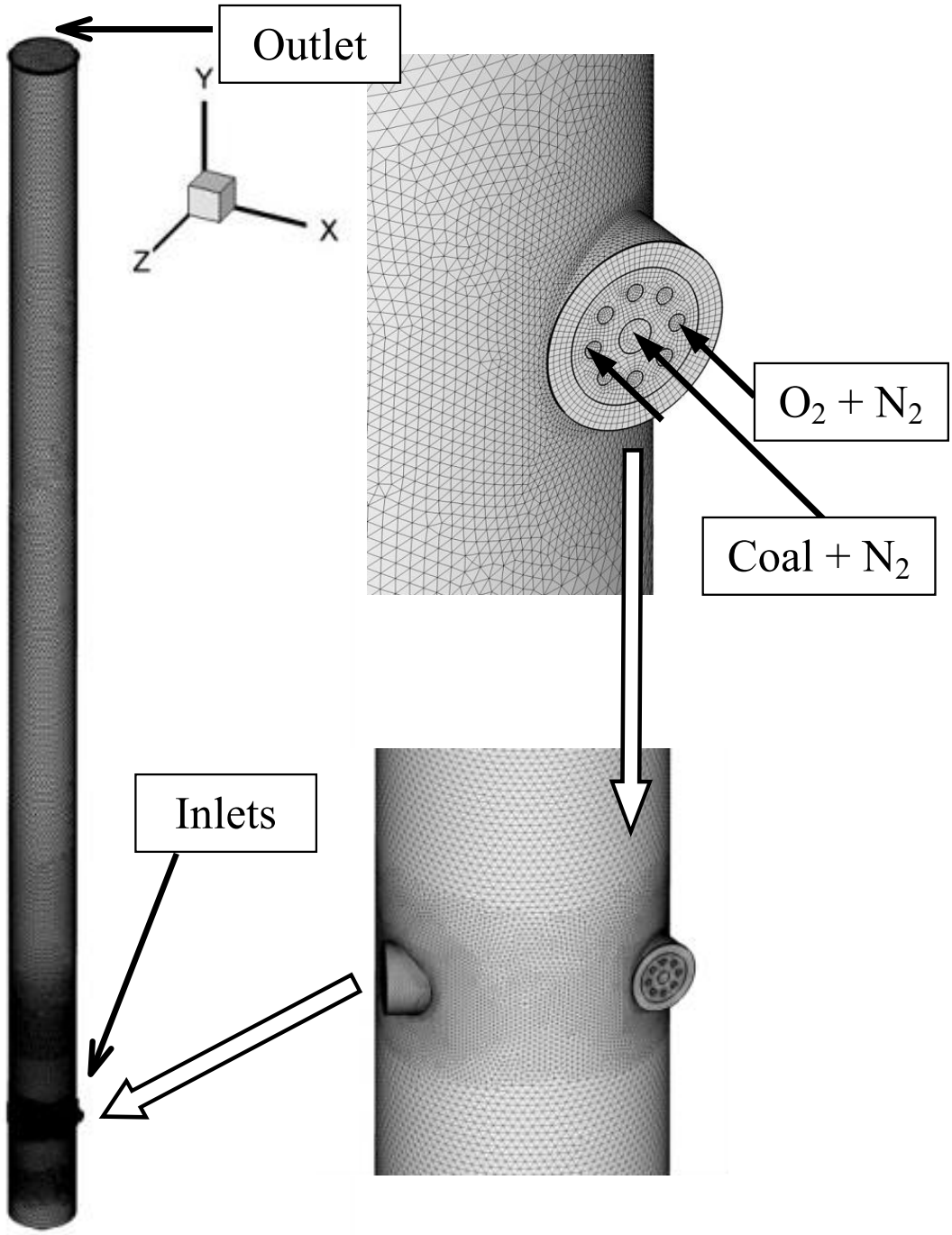

Figure 5.17 Meshed computational domain for fluid mechanics and reactions simulation inside gasifier for the modified injector design (Case 2).

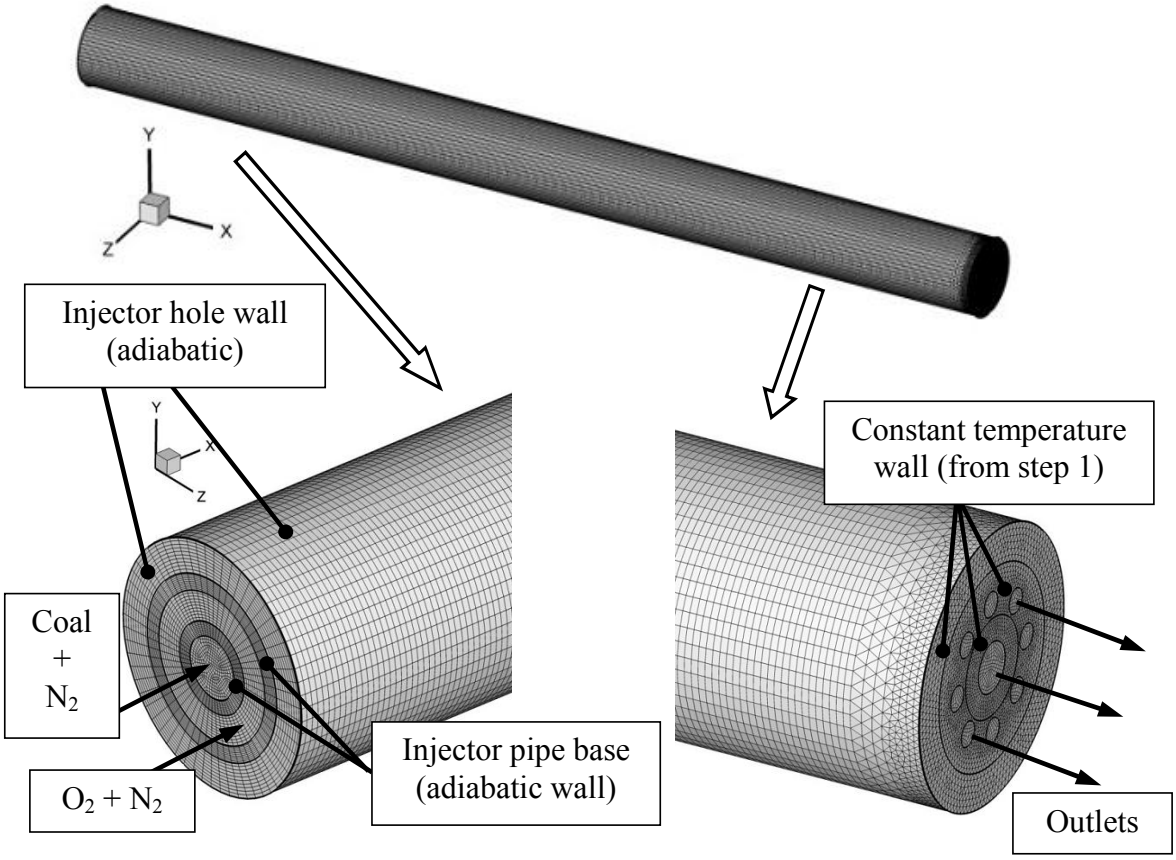

Figure 5.18 Meshed calculation domain for heat transfer simulation within the modified design fuel injector (Case 2).

5.3.1 Results

Gas temperature and species distributions inside the gasifier at the injector level for Case 1 are presented in Figure 5.19. In the temperature distribution, the blue regions are located at the inside of the injectors, where the fuel and oxidant mix before being injected into the gasifier. In eddy-dissipation combustion model, which was used in this study, reaction occurs as soon as fuel and oxidant mix. This created a problem during the initial stage of this simulation. The jump in temperature combined with the contraction of the flow path caused the calculation to diverge. To resolve this problem, the reaction calculation inside the injector was removed so that the reaction calculation only takes place after the fuel and oxidant enter the gasifier. In the real

situation flash back may occur in the injector nozzle when fuel and oxidant mix. The high temperature generated by the flash-back combustion inside the nozzle could have caused earlier failure of the injectors witnessed in the past operation.

The temperature distribution in Figure 5.19 shows that there is a core of very high temperature at the center of the gasifier. A close-up view of the injector's outside surface and its surrounding flow temperature are presented in Figure 5.20 in two opposite sides. The temperature is observed higher on one side of the injector than the other side. This is due to the swirling flow created by the tangential injection, which pushes the hot air to penetrate deeper into one side of the injector passage hole.

The contour of fixed C in Figure 5.19 indicates that C is immediately reacted. This is due to the fact that the fuel and the oxidant have already premixed in the converging nozzle of the injector and C undergoes the exothermic reaction $C + ½ O_2 \rightarrow CO$. The CO and CO_2 distributions presented in Figure 5.19 show that the distributions of CO and CO_2 are almost opposite to each other. CO fraction is highest when the CO_2 fraction is lowest. There is no CO in the center of the gasifier; on the other hand, the CO_2 is highest in the center of the gasifier. At the same time, the temperature is highest at the center of gasifier. This is due to the exothermic reaction $CO + ½ O_2 \rightarrow CO_2$. The volatiles are reacted very quickly, which will provide energy for gasification. Hydrogen is richly produced up to approximately 40% by moles at this stage.

The injector heat transfer study result is shown in Figure 5.21. In this simulation, any potential flashback combustion in the nozzle is removed. The heat source is assumed to be entirely located outside the injector as being calculated in step 1. Temperature which was obtained from the step 1 of the simulation mentioned earlier is imposed on the outside wall of the converging part of the injector at constant values. This constant temperature boundary condition allows thermal energy to transfer into step 2 computational domain without a limit, like a constant temperature reservoir. The fuel and oxidant moving inside the pipes actually act as coolants to carry away the heat conducted through the pipe walls. The gas in the narrow space between the outer pipe wall and the gasifier is almost stationary. The heat transfer in this air layer is dominated by heat conduction mode. Figure 5.21 shows the temperature distributions on the horizontal and vertical center planes of the computational domain, which include both the fluid and solid regions. The temperature calculated in the injector shows a very hot temperature,

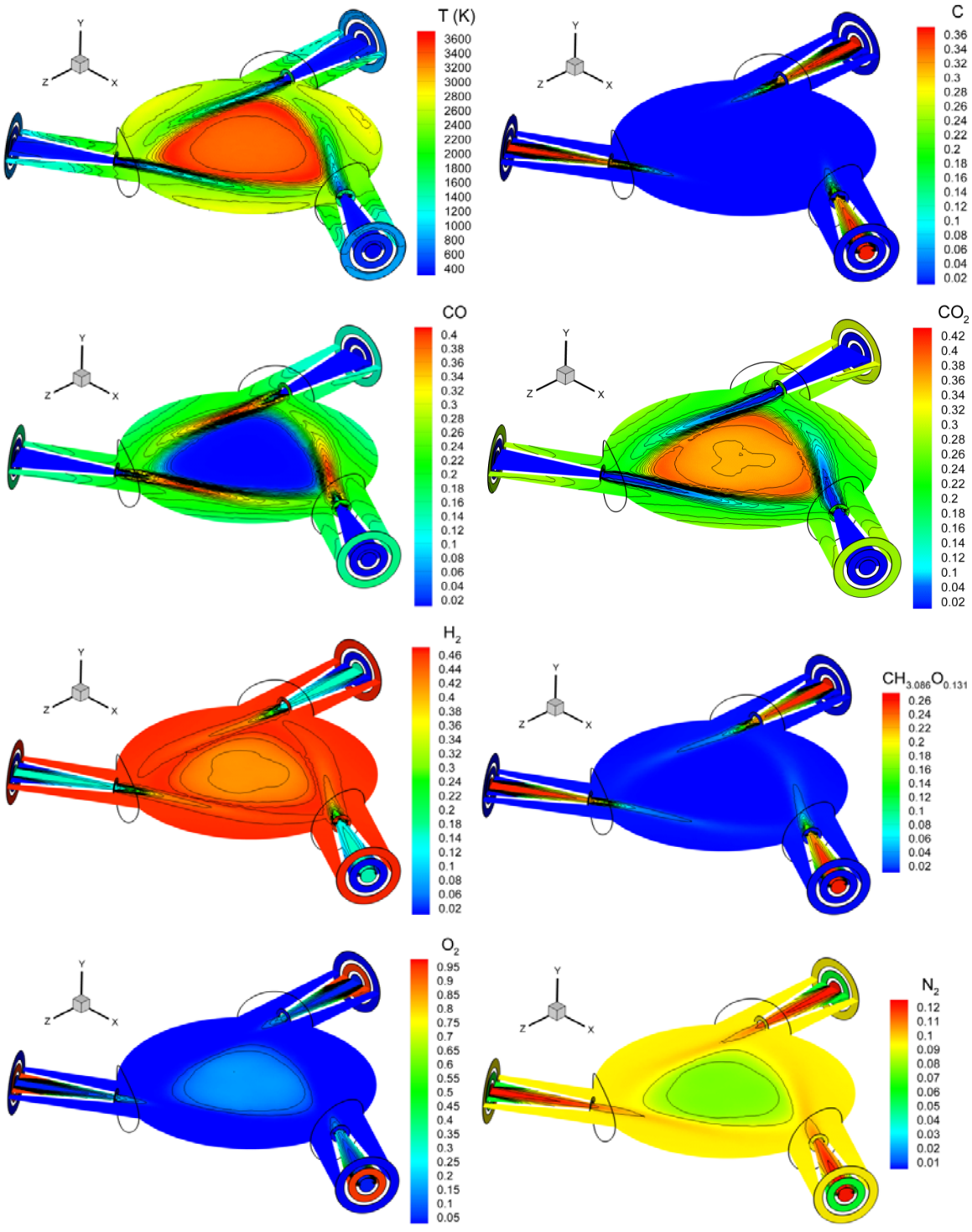

Figure 5.19 Temperature and species distributions on the horizontal plane at the injector height for Case 1.

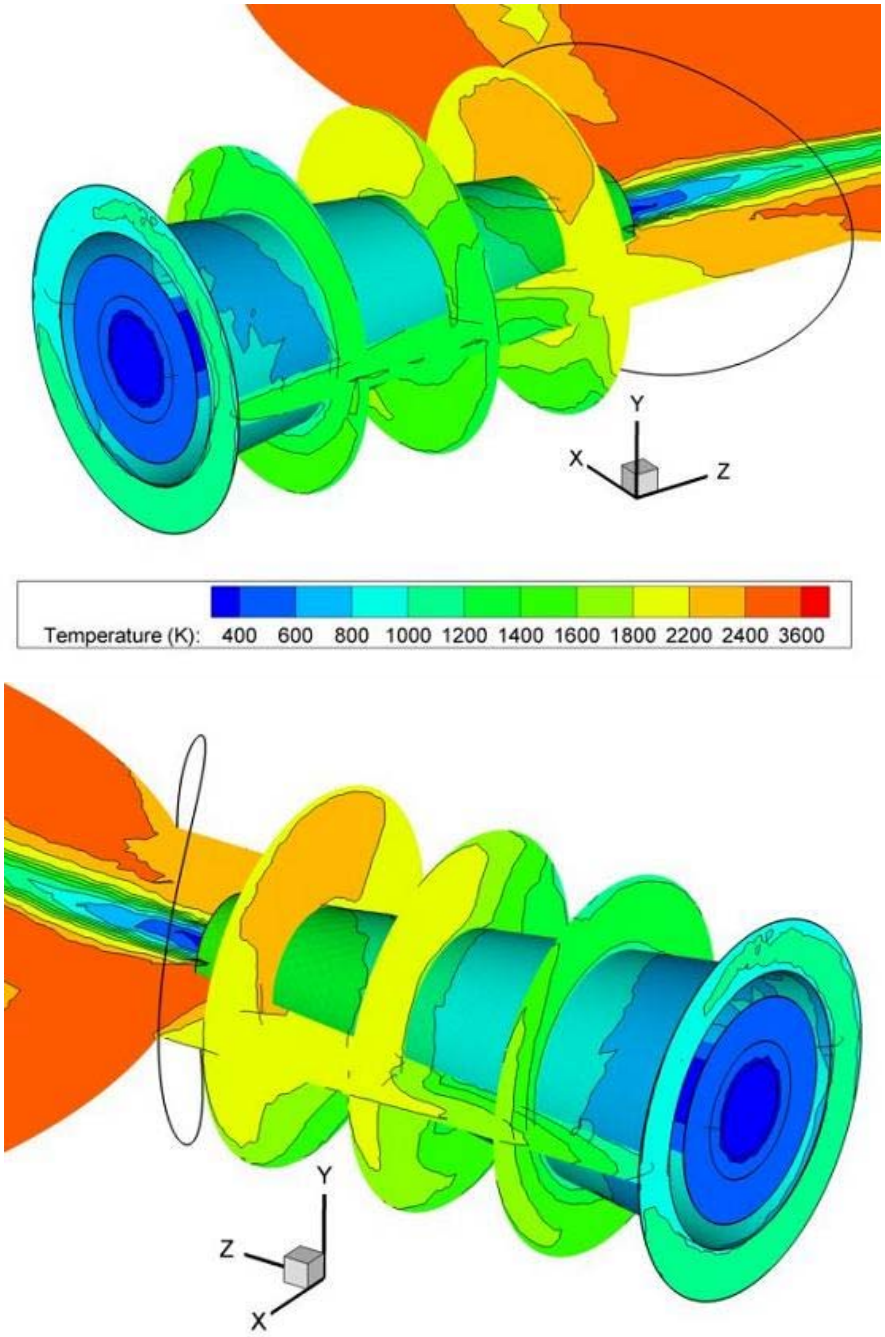

Figure 5.20 Temperature distribution on the injector outside surface and its surrounding flow for Case 1 seen from two opposite sides. Due to the tangential flow injection from the adjacent injector, one side has higher temperature than the other side. This is the result of the gasification simulation in the entire gasifier in step 1.

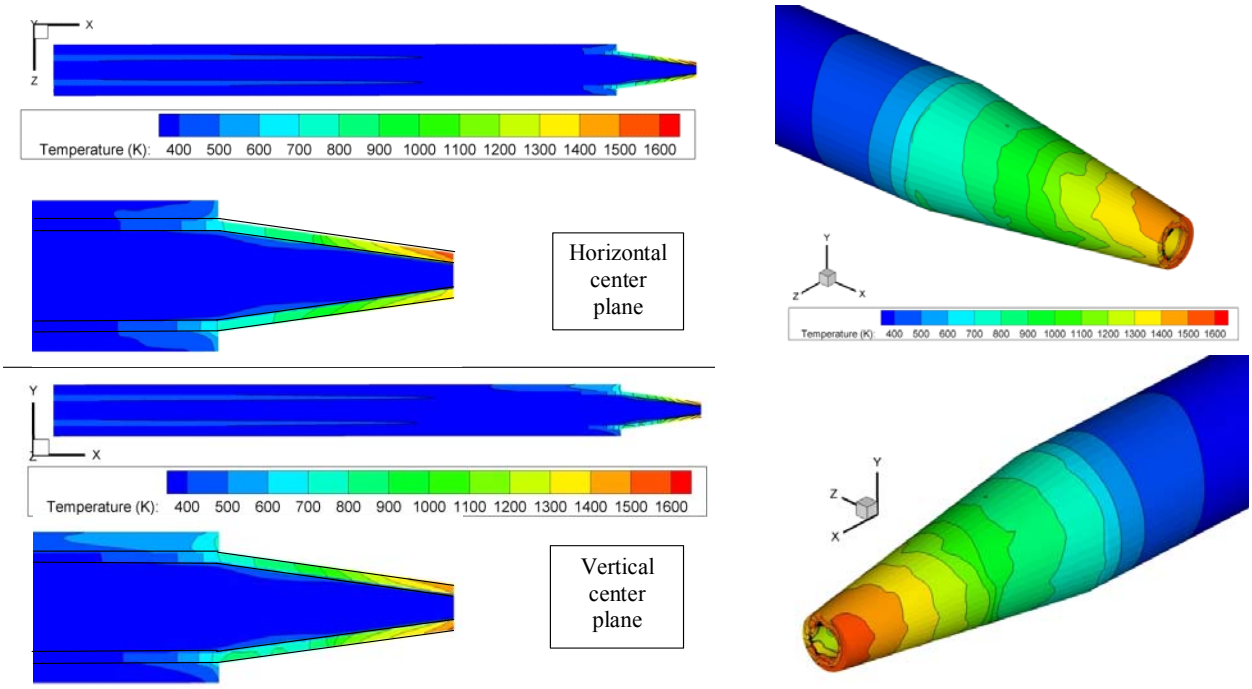

Figure 5.21 Temperature distribution on the horizontal and vertical center planes and outside wall of the injector for Case 1. This is the result of step 2 focusing on the entire injector.

around 1600 K, near the tip of the injector. The hot temperature on the surface of the injector decreases to 1100 K within 30 mm. This is sufficient to melt the injector tip. The temperature on the outside wall of the injector presented in Figure 5.21 shows the location where the highest temperature occurs on one side of the injector. This highest-temperature location is the side where the hot temperature hits from the adjacent injector as mentioned earlier.

The results of modified injector (Case 2) are given in Figure 5.22. The distribution of fixed carbon (C) shows that, very different from Case 1, C is not immediately consumed (reacted) because it is not premixed inside the injector as in Case 1. It is noted that O_2 injected facing the center side of the injector is immediately consumed and produces CO, while CO_2 is produced in the near wall region. Judging from the high temperature (near 3600K), high CO_2 and H_2, and low O_2 and volatiles in the near wall region, it can be concluded that two exothermic reactions, which are gasification of volatiles ($VM + O_2 \rightarrow CO + H_2$) and $CO + \frac{1}{2}O_2 \rightarrow CO_2$, prevail in the near-wall region and produces a lot of heat there. As soon as CO is produced by the gasification of volatiles, it is burned by O_2 to produce CO_2. Production of hydrogen is not as

much as in Case 1. A plenty amount of H_2 and CO are produced at this stage with H_2. An enlarged velocity vector plot superimposed with temperature in color is shown in Figure 5.23. Interaction of injected jet flow and the tangential momentum from the adjacent injector can be clearly seen in this figure.

Figure 5.24 presents the temperature contour on the outside wall of one of the injectors for Case 2. Again, this temperature contour was obtained from the gasification simulation of the entire gasifier. It was then used as the wall boundary condition at the injector tip. Similar to Case 1, the highest temperature observed is around 1600 K. However, this high temperature seems to be scatteringly distributed, as opposed to concentrated at one location in Case 1. Furthermore, Figure 5.24 shows the high temperature quickly decays to 1000 K within 2 mm (vs. 30 mm in Case 1). This means that the injector in Case 2 is less likely to fail due to the extreme temperature compared to the injector in Case 1.

Exit gas temperature and compositions for both Cases 1 and 2 are tabulated in Table 5.8. Even though the temperature and species distributions at the injection level seem very different, the exit syngas for both cases are pretty close to each other.

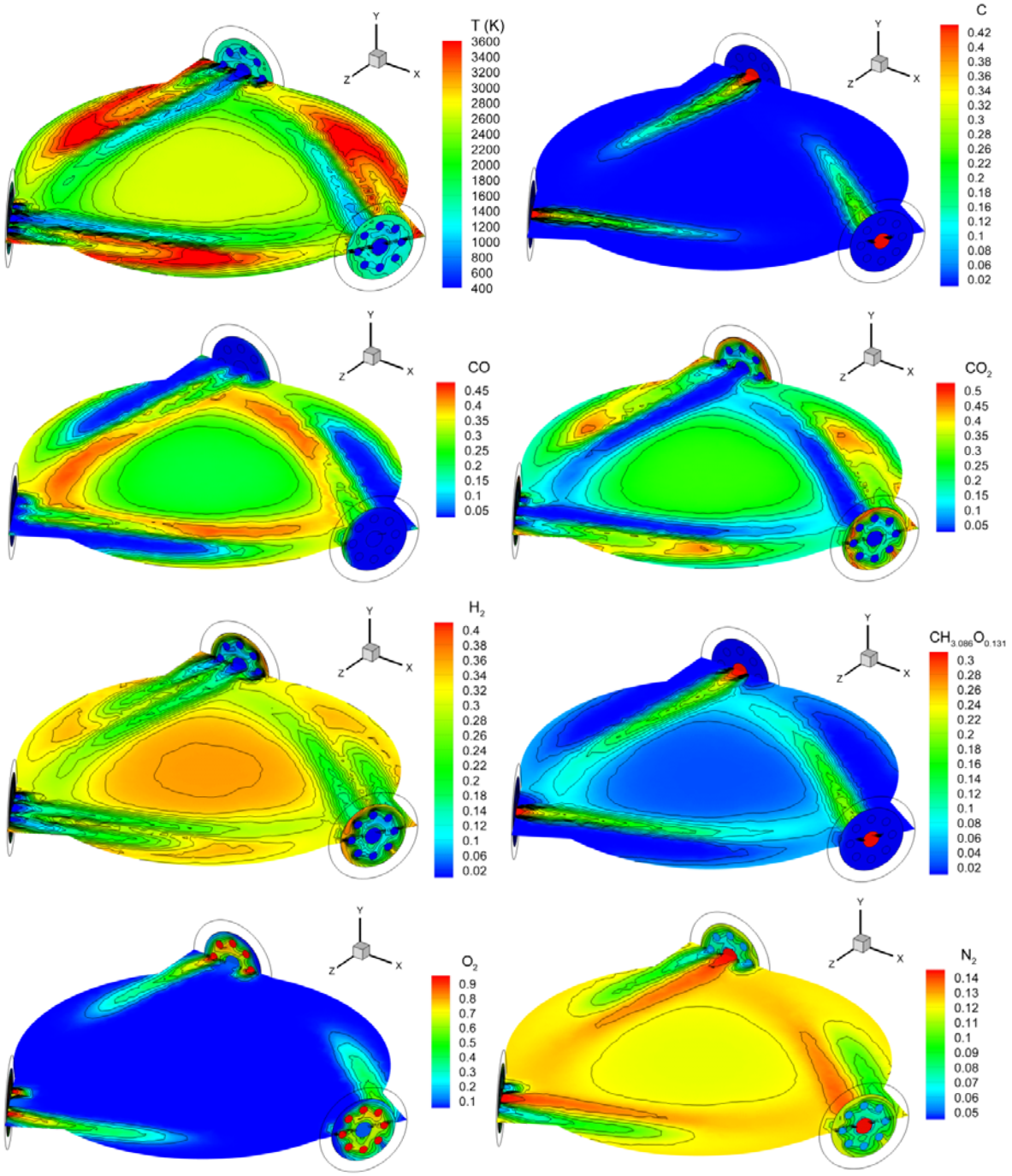

Figure 5.22 Temperature and species distributions on horizontal plane on injector height for Case 2.

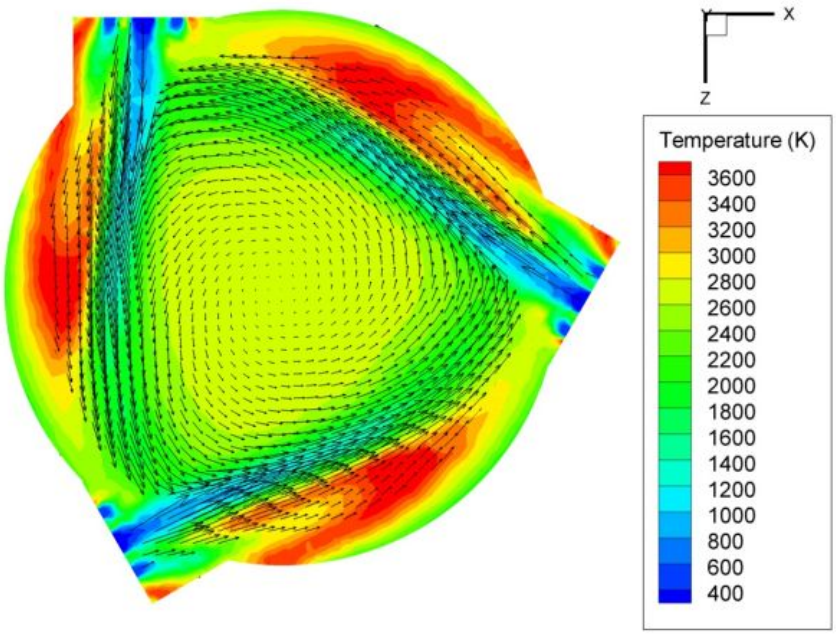

Figure 5.23 Velocity vectors and temperature distributions on horizontal plane on injector height for Case 2.

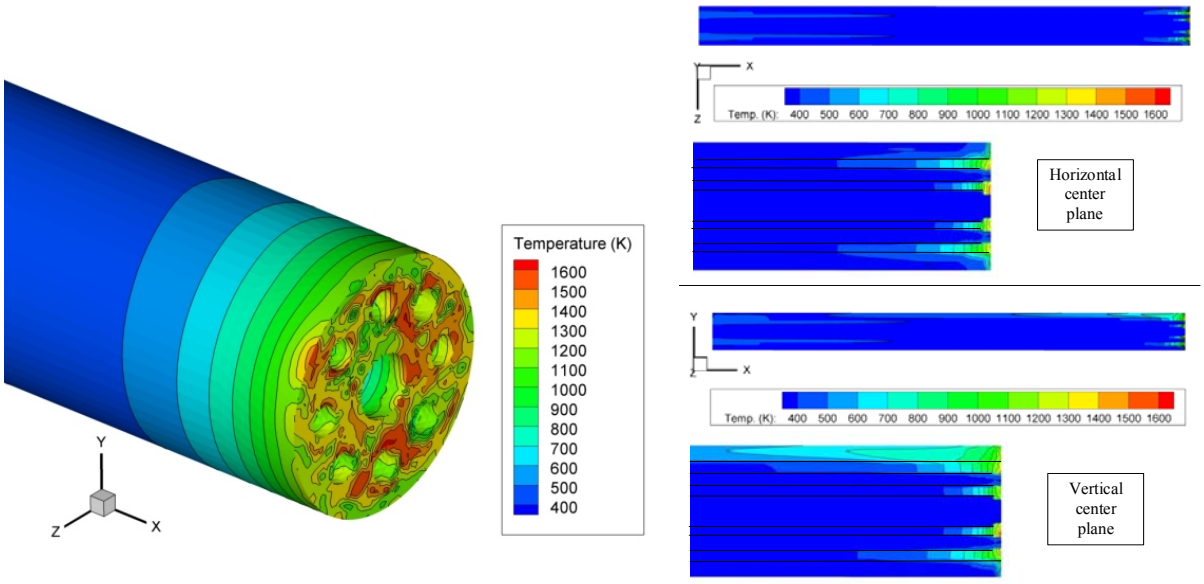

Figure 5.24 Temperature distribution on outside wall and on the horizontal and vertical center planes of injector for Case 2.

Table 5.8 Exit gas temperature and compositions for Cases 1 and 2.

Parameters	***Case 1***		***Case 2***	
Exit temperature, K	1265		1215	
Carbon fuel conversion efficiency, %	72%		86%	
Coal gasification conv. efficiency, %	66%		87%	
Fuel conversion efficiency, %	73%		80%	
Components at exit:				
	Mole fraction	Mole no. (mole)	Mole fraction	Mole no. (mole)
CO	41.9%	0.30	40.0%	0.30
H_2	33.4%	0.24	30.7%	0.23
CO_2	12.0%	0.08	10.1%	0.08
VM	0.7%	0.00	7.2%	0.05
H_2O	0.0%	0.00	0.0%	0.00
N_2	12.0%	0.08	12.0%	0.09
C	0.0%	0.00	0.0%	0.00
Heating value (MJ/kg)	10.2		13.9	

5.3.2 Experiment

As shown in the schematic of the original fuel injector in Figure 5.13, oxidant, transport gas and coal powder enter the gasification chamber in a premixed condition. This premixed type injector has not always been stable during operation. In test conditions, gasifier temperature reaches over 1400°C. During operation, sometimes coal particles have blocked the annular space in the injector, preventing continuous feed of coal into the gasifier. Flashback in the annular space of injector can potentially damage the injector. Shown in Figure 5.25 is the exterior wall of the gasifier where the red spot above the injector indicates the heat penetrates refractory insulation caused by the combustion of coal particles inside the injector. Figure 5.26 shows fuel injectors that failed due to very high operating temperature. It was speculated that the high temperature in the injector was caused by flash back combustion due to premixed combustion inside the conical nozzle. To remove this premixed design, the nozzle has been cut off as shown in Figure 5.27. The revised fuel injectors have performed stably and reliably for several months at 15 bars without any complication.

However, after a long period of testing, the thickness of the refractory-liner wall has been worn away and became thinner than the original contour of gasifier inside wall. The nozzle tip eventually protruded over the worn-out refractory-liner and is exposed to the extreme high temperature in the gasifier. As a result, the injector tips were eventually burned out as shown in Figure 5.28. Based on the test experience, it is suggested that the length of coal injector should be less than the thickness of refractory-liner by at least 10 mm. This will help ensure the gasifier will operate at a safe, continuous and stable condition.

Figure 5.25 Exterior wall of the gasifier using fuel injectors with pre-mixed fuel nozzles. Red spot indicates heat penetration through worn-out brick caused by premixed flash back combustion in the nozzle.

Figure 5.26 Burned out converging-tip fuel injectors.

Figure 5.27 Blunt-tipped (non-premixed) coal injector. Outer eight holes transfer oxygen; inner hole transfer coal and nitrogen.

Figure 5.28 The right blunt-tip injector shows it is in mint condition after a short service and the left injector shows a burned-out tip after extended service when the refractory brick has been worn away and the fuel injector eventually protruded out from the wall without protection.

5.3.3 Conclusions Heat Transfer and Gasification of Two Fuel Injectors

The two different fuel injector designs give very different temperature and species distributions inside the gasifier. In Case 1, the highest temperature inside the gasifier occurs at the center of the gasifier; whereas, in Case 2, it occurs near the wall. Case 1 produces high H_2 and low CO; whereas, Case 2 produces both rich H_2 and CO. There is a potential of flash back combustion in the nozzle at the tip of the conical injector due to its premixing feature of fuel and oxidant in the nozzle. The highest temperatures on both injectors are the same, around 1600 K. However, the highest temperature on the conical-tip injector (Case 1) is concentrated at one location with an extended region of 30 mm between 1600 K and 1100 K; whereas on the blunt-tip injector (Case 2), the maximum temperature distribution is scattered and the hot region (1600K - 1100K) only extends about 3 mm. Therefore, the blunt-tip injector is less likely to fail. Experimental results support simulated results and has demonstrated a short life for the conical tip fuel injector and an extended life for the blunt-tip fuel injector. However, eventually the

blunt-tip fuel injector did burn out after extended service when the refractory brick was worn away and the fuel injector tip protruded from the wall without any protection.

5.4 Investigation of Top Fuel Injection Design in a Coal Gasifier

The studies in the previous sections have been conducted in the existing gasifier at the Industrial Technology Research Institute (ITRI) in Taiwan. A new gasifier design is currently on the drawing board and a different fuel feeding scheme via injecting water slurry coal is under consideration. Instead of injecting the dry pulverized coal from the bottom of the gasifier, the water slurry coal will be injected from the top of the gasifier. Since there are many different means to inject the fuel, conducting experiments to investigate many different options is a time consuming and expensive process. To help narrow the number of experimental variables and guide design direction, Computational Fluid Dynamics (CFD) simulation is conducted to investigate the gasification performance by simulating various fuel injection schemes.

Several potential fuel injection configurations are studied. The schematic of the new gasifier is presented in Figure 5.29a. Instead of injecting tangentially, the fuel and oxidant are injected 45 degrees downward toward the center from the top of the gasifier. The gas and coal from both injectors will impinge at the center. With these new injectors, the gas and particles flow downward and exit from the bottom. The gasifier's inside diameter is enlarged to 0.6m from the existing 0.3m by replacing the current refractory brick with a thinner but higher thermal resistance brick. The outside diameter of the gasifier remains the same as 0.6m. The height remains the same at 3m. The coal is mixed with water to form a 60%-40% coal/water (by weight) slurry mixture before being fed into the gasifier.

This study focuses on the following two specific tasks:

(1) Coaxial dual jets impingement --- The fuel injector consists of two coaxial pipes. The water slurry coal is transported through the inner pipe, and the oxygen is transported through the outer annular passage. Two injectors (Figure 5.29a) are located diametrically and are oriented in a downward angle (θ) to impinge against each other at the centerline of the gasifier.

(2) Four jets impingement --- Four injectors are arranged as shown in Figure 5.29b. A pair of injectors is located diametrically and inject coal water slurry. The second pair of injectors is located 90^{o} from the first pair and injects oxygen only. Again, all four injectors are oriented

azimuthally in a downward angle of 45° to impinge against each other at the centerline of the gasifier.

Two meshed computational domains are shown in Figures 5.30 and 5.31. In Figure 5.30, coal slurry and oxidant are fed through two concentric pipes, with oxidant being injected through the inner pipe, and coal slurry being injected through the outer pipe. In Figure 5.31, coal slurry and oxidant are injected through separate injectors and are departed 90 degrees from each other. The grid size of both computational domains is roughly 0.8 millions cells each.

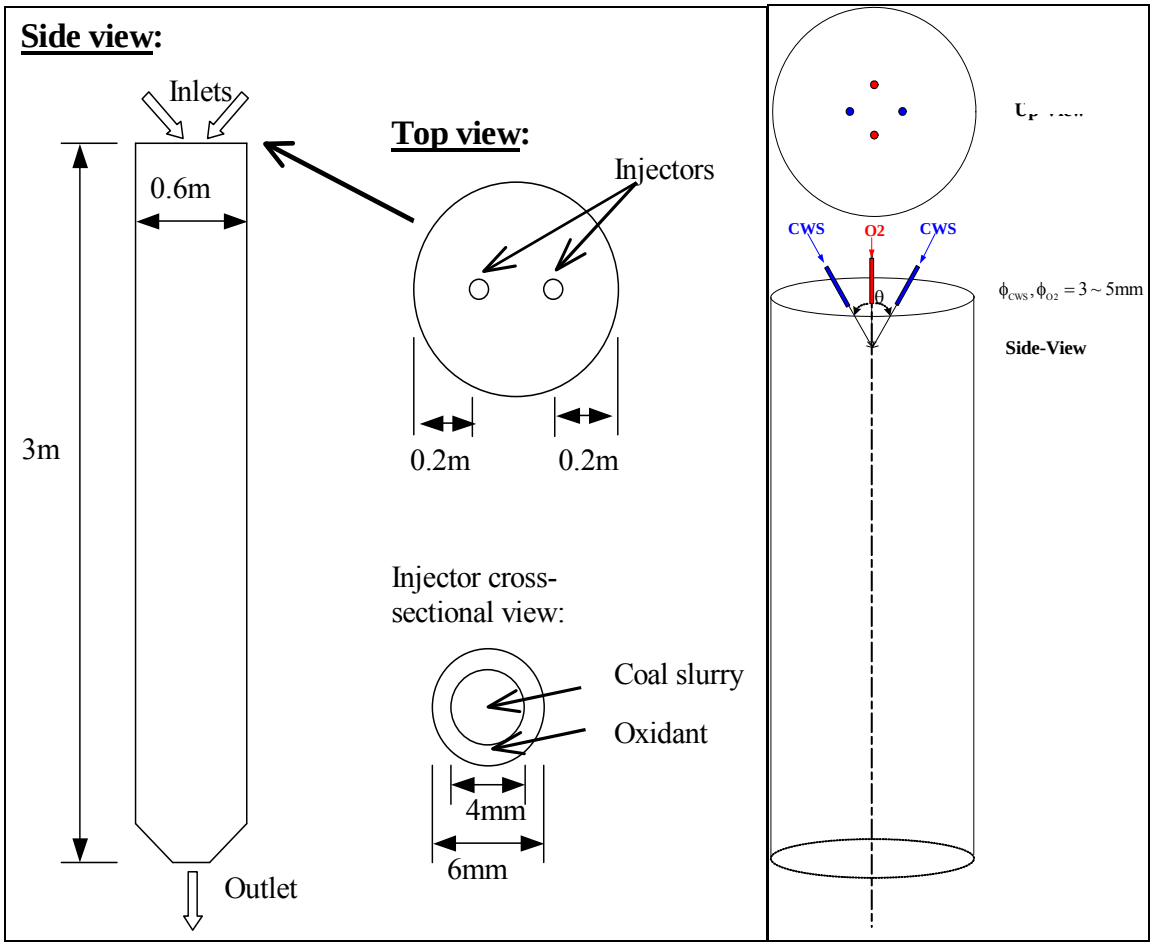

(a) (b)

Figure 5.29 (a) Modified gasifier with two inclined jets, and (b) four jets impinging.

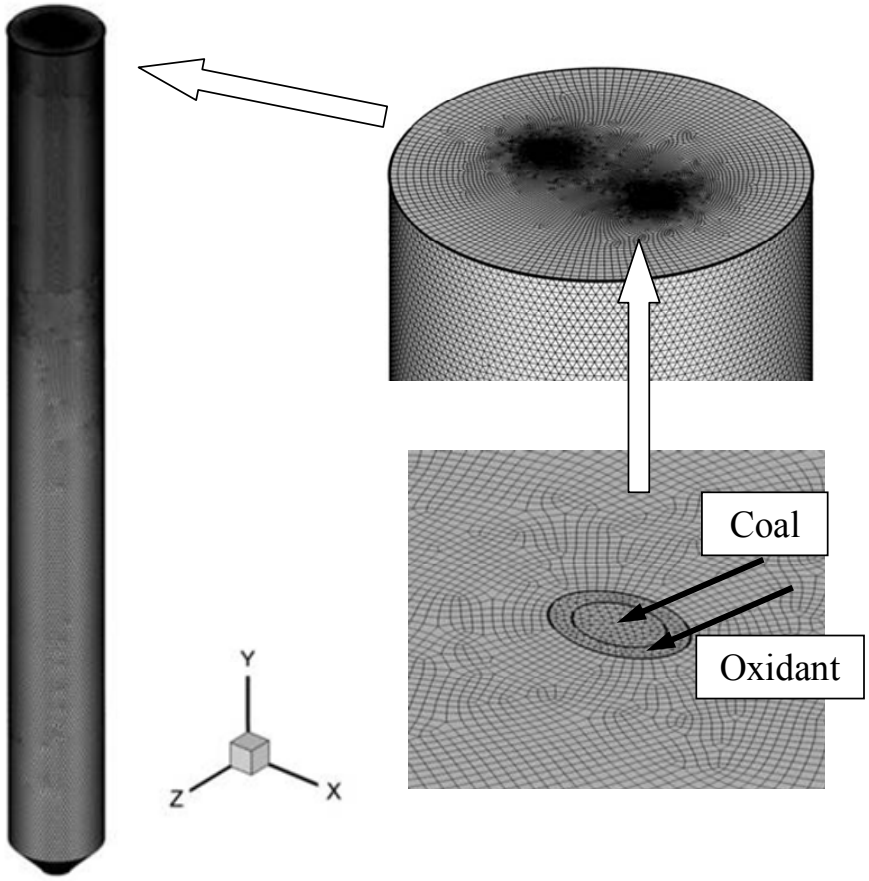

Figure 5.30 Meshed computational domain for two concentric injectors spraying with 45^{o} downward angle and 90^{o} interception angle.

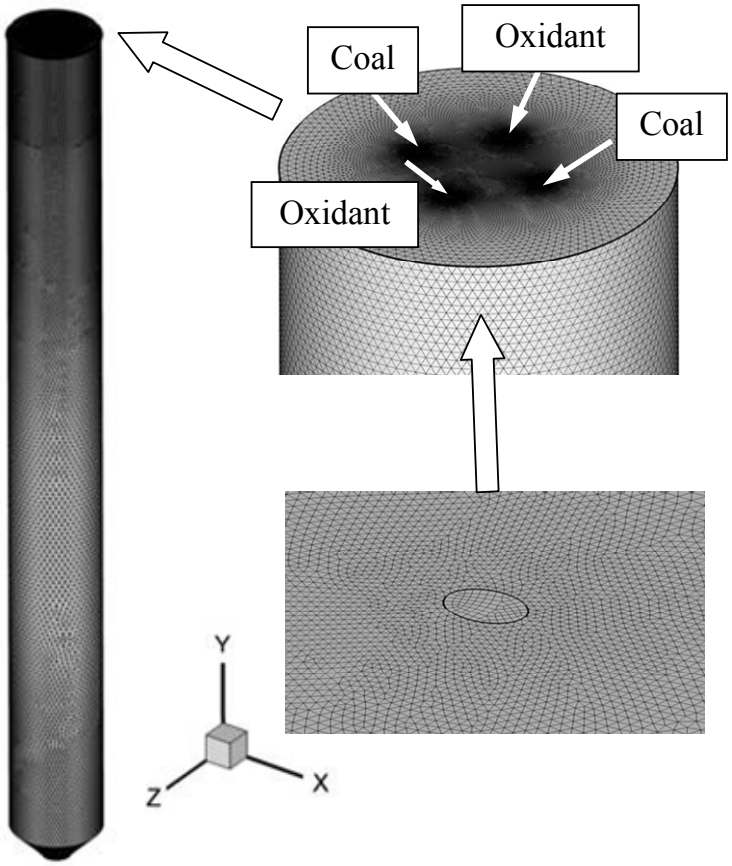

Figure 5.31 Meshed computational domain for four separate injectors spraying with 45^{o} downward angle and 90^{o} interception angle.

The total feed rates of coal slurry and oxidant are listed in Table 5.9. The coal/water weight ratio of the coal slurry is 60%/40%. The oxidant is 95% O_2 and 5% N_2. Two tons of coal per day are required to achieve the coal slurry feed rate of 0.0324 kg/s as listed in Table 5.9. The equivalence ratio between the fixed carbon contained in the coal and the oxygen feed rate is 0.4. The mass flow rate input for each injection is given in Table 5.10. The temperatures of the coal slurry and the oxidant are provided at 300 K and 420 K, respectively.

The walls are all adiabatic and with no slip condition (i.e. zero velocity). The particles are assigned to reflect if they hit any wall. The operating pressure inside the gasifier is initially set at 15 bars. The outlet is set as a constant pressure condition at 15 bars. After calculation, the pressure inside the gasifier and at the inlet will be adjusted to accommodate the pressure drop inside the gasifier.

Table 5.9 The feed rates of coal slurry and oxidant simulated in this study.

Composition	***Feed rate, kg/s***
Coal slurry (60% coal - 40% H_2O)	0.0324
Oxidant (95% O_2 - 5% N_2)	0.0113

Table 5.10 Mass flow rate input for four-injector case (2 coal injections and 2 oxidant injections).

Parameters	
Coal slurry injection mass flow rate, kg/s	0.0161
Oxidant injection mass flow rate, kg/s	0.0058
Mass fraction at oxidant injection	
O_2	0.930
N_2	0.070

The oxidant is considered as a continuous flow, and coal slurry is considered as a disperse phase consisting of many discrete coal particles, which are composed of the fixed carbon, the original water from the moisture content of coal, and the water added in the slurry. In other words, in the computational model the slurry is modeled as particles with each particle consisting of a fixed carbon particle inside a water droplet. Other components of the coal, such as N, S, and ash, are injected as gas together with the oxidant in the continuous flow. N is treated as N_2, while the masses of S and ash are lumped into N_2. The coal slurry size is uniformly given as spherical droplets with a uniform arithmetic diameter of 200 μm

5.4.1 Results of Two-Concentric Injectors

5.4.1.1 Finite-Rate Results

The result of particle tracks of two-concentric injectors is shown in Figure 5.32. In this figure, particles from each injection are seen to meet and pass each other at the center. No collisions among particles are seen because the particle reaction model can not be used together with the particle collision model in the current computational scheme. The reason for this is explained below.

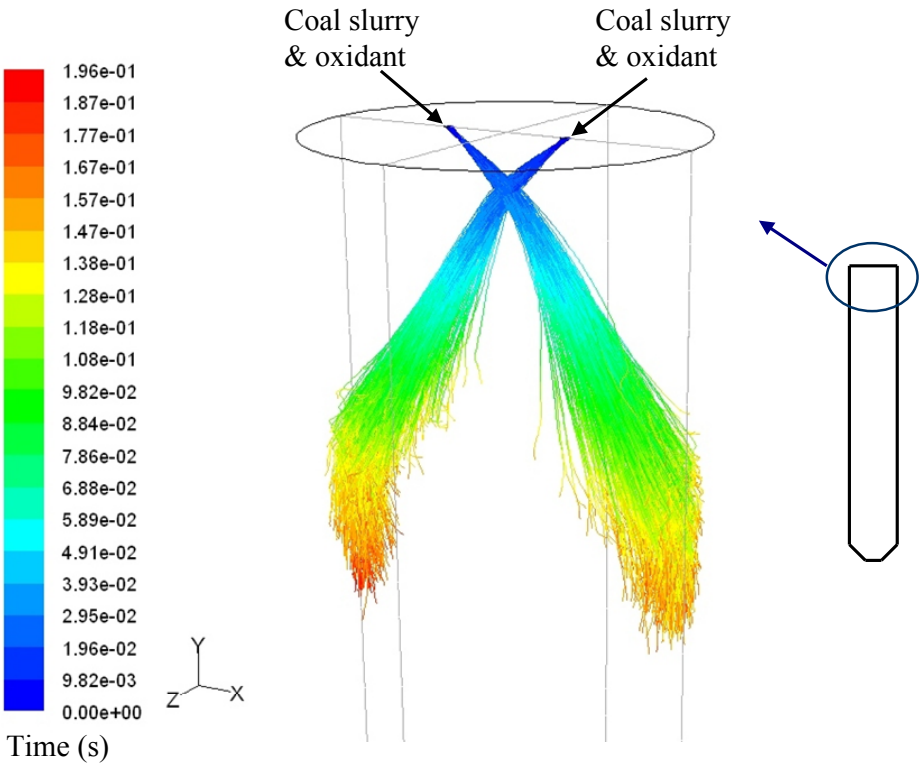

Figure 5.32 Particle tracks for two concentric coal slurry and oxidant injections with heterogeneous finite rate solid-gas reactions. (Note that Particle collision model can't be implemented together with the heterogeneous particle reaction model.)

To model particle collisions, the CFD model has to track all particles one by one at the same time. For each particle, the model has to predict the possibility of collision between that particle and other particles. So, if there are N particles, each particle will have N-1 possible collision partners. Because the collision between particle A and particle B is the same as the collision between particle B and particle A, the number of possible collision pairs is $\frac{1}{2}N^2$. To calculate $\frac{1}{2}N^2$ possible collisions for each time step is beyond the computational capability of a cluster of 64 nodes available for this study. Therefore, to save computational time and power, the collision model tracks particles in groups/parcels instead of individually; so each parcel is a statistical representation of a number of individual particles. As an example, if the model tracks a group of parcels, where each parcel represents 100 particles, the number of collision calculation is decreased by a factor of 10^4 (or 100^2). While the parcel tracking technique is good at saving collision calculation, it does not allow us to track the species fractions inside the

particles, which is required in the particle reaction model. Thus, the particle collision model cannot be used together with the particle reaction model in the current computational scheme.

Even with the current limitation of adequately simulating the coal particle collisions, the results are still very useful because they can be treated as a worst-case scenario of wall erosion with more coal particles hitting the wall than in the real case. The results show that the time needed for the particles to burn out is just less than 0.2 seconds. Many of the particles burn near the wall, which is after they hit the wall and reflect. Figure 5.33 shows the temperature and species distribution on two perpendicular vertical center planes inside the top 1/3rd of the gasifier. The gas species distributions in the lower 2/3rd of the gasifier are almost uniform, so they are not shown. The temperature distribution shows two hot spots near the wall. These are the locations where the coal particles hit the wall, reflect, and burn out. At the same locations, the CO species fraction is the highest while the CO_2 fraction is the lowest. But O_2 is already fully depleted by the time the particles reach the walls. It is suspected that reaction $C + CO_2 \rightarrow 2CO$ are dominant at those locations. The particles hitting the wall combined with the high gas temperature could damage wall refractory bricks. As explained earlier, the presented results are a worst-case scenario.

No CO is observed in the upper part of the gasifier near the inlets, but the CO_2 concentration is higher in that area. It seems complete combustion occurs there because CO reacts immediately with O_2 to produce CO_2 and release energy to support endothermic gasification reactions.

5.4.1.2 Instantaneous Gasification Results

As a compromise to resolving the limitation of modeling the particle-particle interactions when the particle reaction model is used, the "instantaneous gasification" method is employed as an alternative approach to examine the particle collision phenomenon. Under the "instantaneous gasification" approach, carbon particles are made to gasify instantaneously, thus the solid-gas reaction process can be modeled as homogeneous combustion reactions. This approach is based on the locally-homogeneous flow (LHF) model proposed by Faeth (1987), implying infinitely-fast interphase transport rates. The instantaneous gasification model can effectively reveal the overall combustion process and results without dealing with the details of the otherwise complicated heterogeneous particle surface reactions, heat transfer, species transport, and particle tracking in turbulent reacting flow.

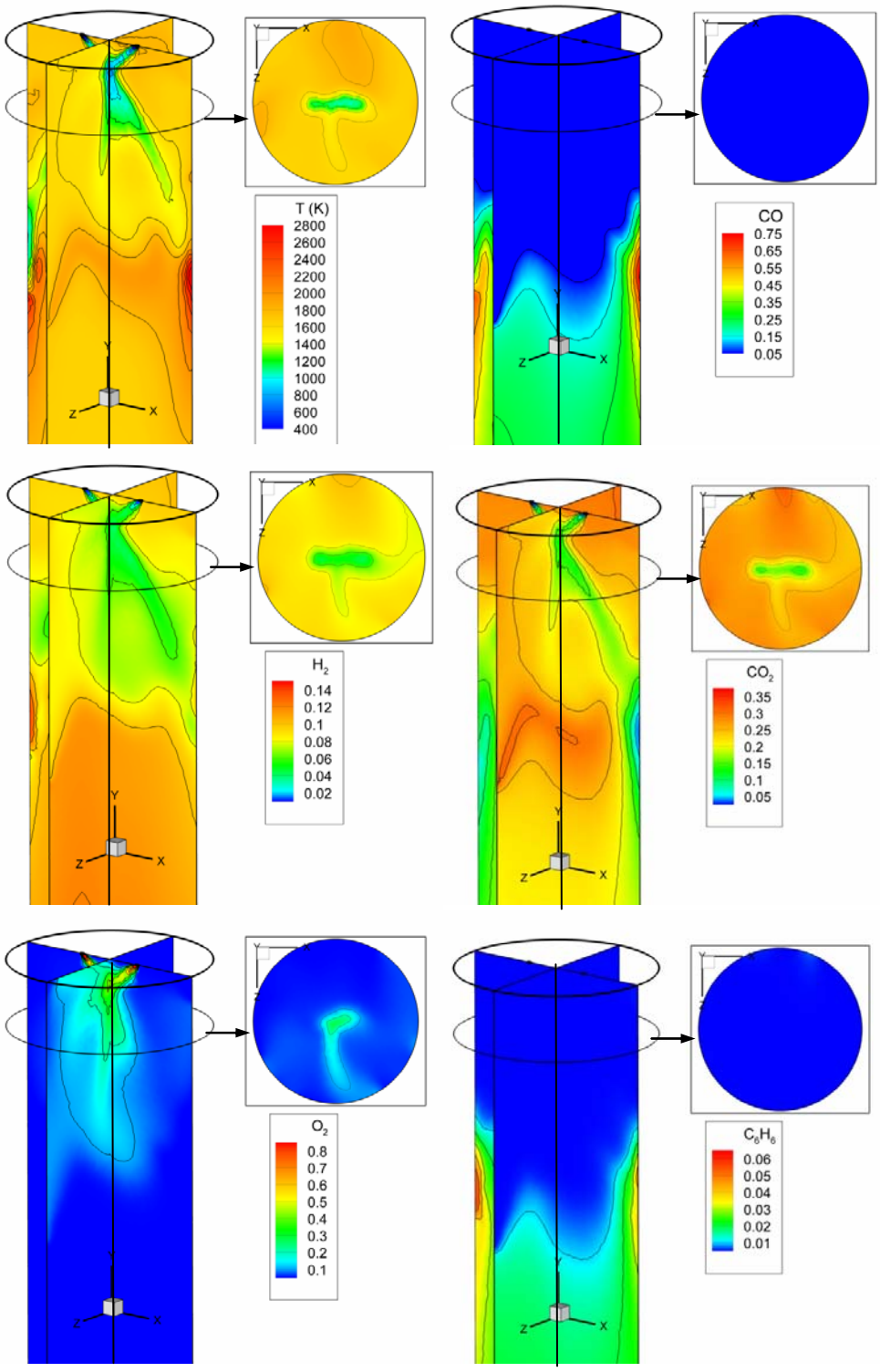

Figure 5.33 Temperature and species mole fraction distributions on two perpendicular vertical center plane inside gasifier for concentric coal-oxidant injection case with heterogeneous finite rate solid-gas reaction model.

Featured with a simpler mechanism, the gas combustion model is robust and less costly in computation. But it should be noted that this model lacks accuracy and detail in describing the physical process and usually over- predicts the reaction rate. With the instantaneous gasification approach, the fuel (fixed carbon and volatiles) is injected as gas, but the water component of the coal slurry and the moisture content of the coal are injected as water droplets (a discrete phase). The model is then able to track the particle-particle interactions among the droplets. Unsteady particle tracking is used to enable the tracking of the particle-particle interactions. The particle collision model includes elastic collision, particle breakup, and coalescence sub-models. From common intuition, the particles may be bounced off in different directions when the jets meet.

The temperature and species distributions on two vertical mid-planes in the top 1/3 of the gasifier is presented in Figure 5.34. Hot spots occur near the injection point, where the CO species fraction is also high. These are the locations where carbon actively reacts and is very different from the finite rate solid-gas reaction model simulated earlier where solid carbon burns near the wall. In the instantaneous gasification model, carbon is instantly converted into gas at the injection locations. As a result, carbon reacts much sooner than in the finite rate gasification model where the particle has to go through evaporation and devolatilization before it undergoes chemical reactions.

Figure 5.35 shows plots of the velocity vectors and water droplet tracks at two vertical mid-planes for the instantaneous gasification model case. The XY plane plots show that the water droplets deviate from the direction of the velocity vectors once they pass the impingement point. The result of droplet tracks shows that the droplets spread more but are not severely bounced around, as speculated, at the intersection where the jets meet, and majority of the droplets passes through the jet impingement section and hit the wall as the finite rate case. This implies that the results of the finite rate are acceptable even though the particle collision model is not implemented.

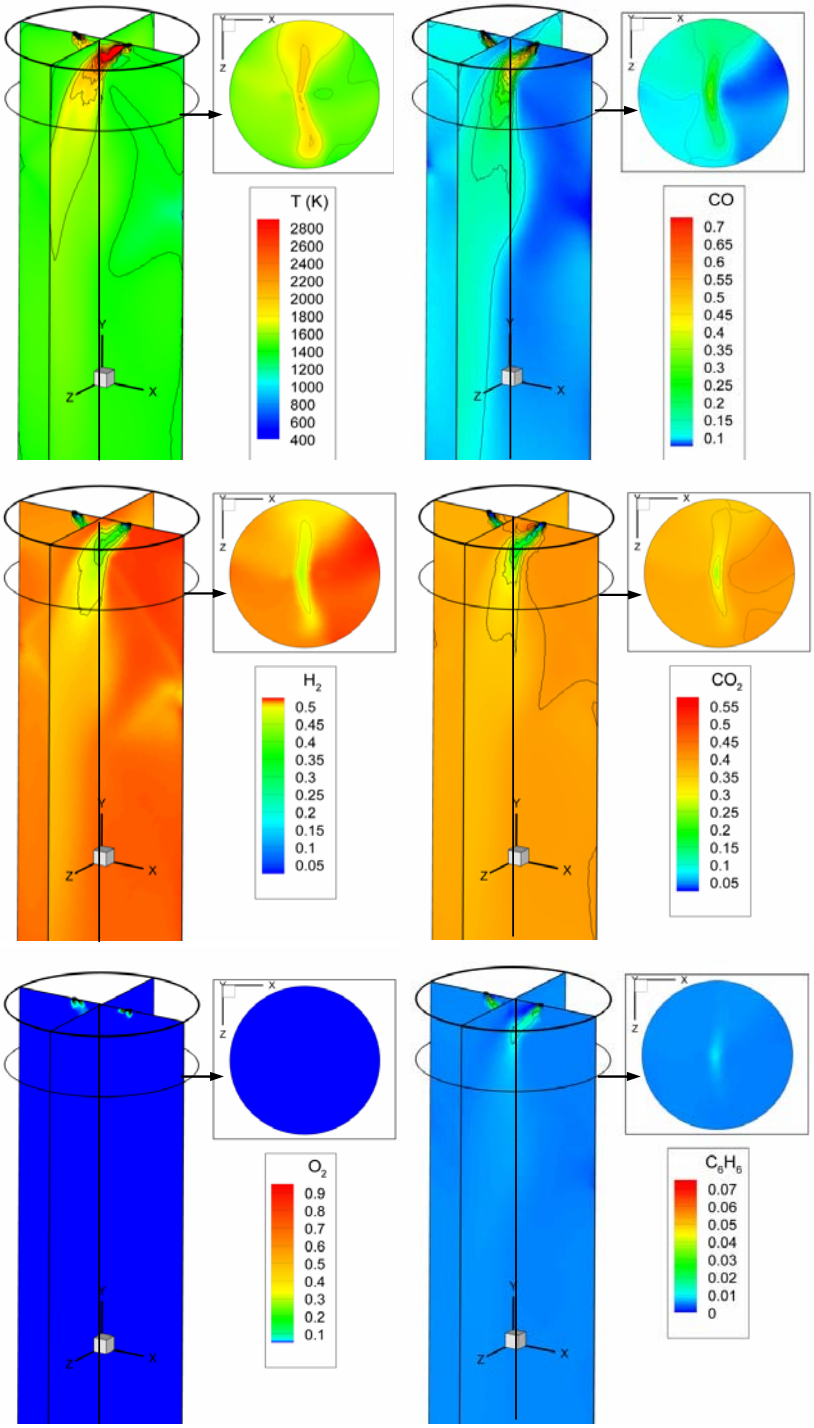

Figure 5.34 Temperature and species mole fraction distributions on two perpendicular vertical center-planes inside gasifier for concentric coal-oxidant injection case using the instantaneous gasification model implemented with particle collision model.

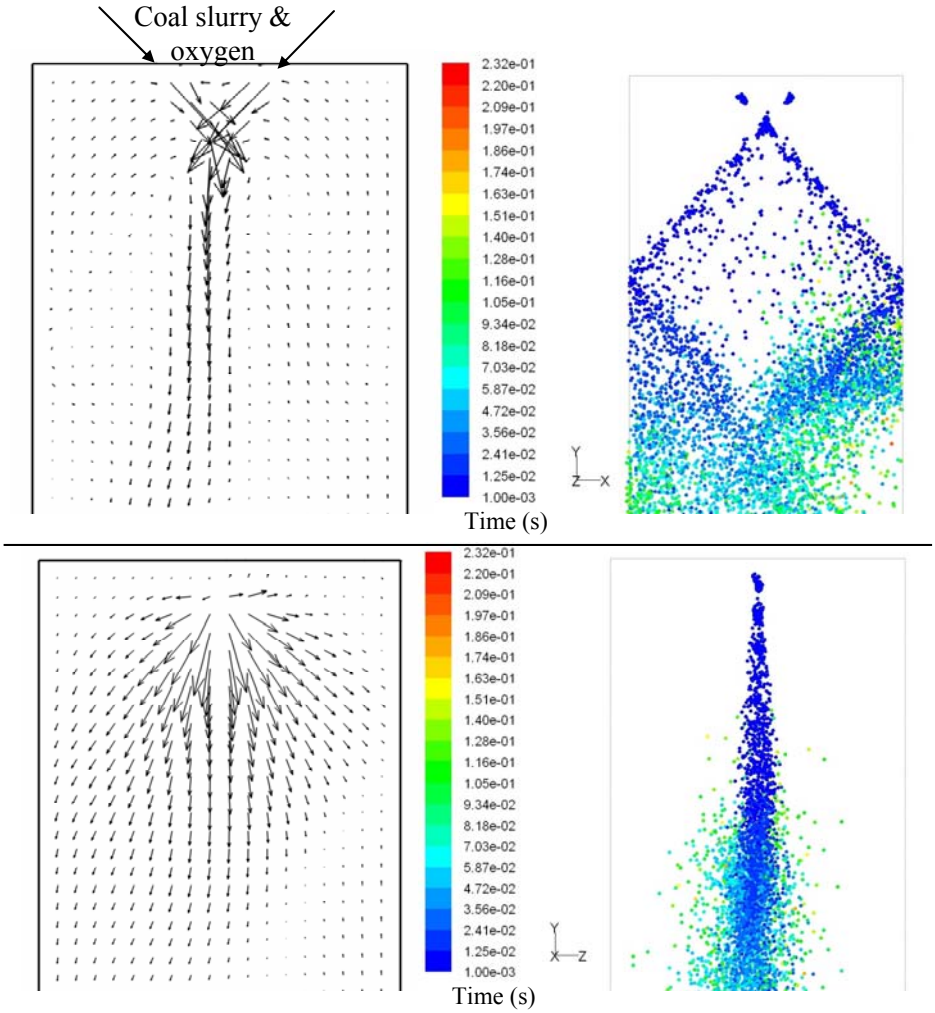

Figure 5.35 Velocity vectors and water droplet tracks on two perpendicular vertical center-planes for the concentric coal-oxidant injections using the instantaneous gasification model implemented with particle collision model.

5.4.2 Results of Four Separate Coal and Oxidant Injectors

5.4.2.1 Finite-Rate Results

A plot of particle tracks for the four separate coal and oxidant injection cases is presented in Figure 5.36. These cases show that the particles need longer time (~ 1 second) to burn out compared to approximately 0.2 seconds in the case of two concentric coal-oxidant injections. Injecting coal slurry separately from the oxidant does not provide good gas-particle mixing that is needed for effective heterogeneous reactions to occur. In a real situation, the reaction could be

faster than the predicted results because most particles would collide, change direction, and achieve a better mixing with the oxidant, which also impinges at the center.

The temperature and gas species distributions in Figure 5.37 show a few similar characteristics as those of the two concentric injections case in Figure 5.33. The hottest spots occur at the locations where the particles burn out, and the CO is highest and CO_2 is lowest at those locations. Also, there is no CO in the upper part near the inlet, but CO_2 is highest in the same area.

The exit gas temperature of the separate injection case is roughly 200K lower than that of the concentric injection case. Its H_2 concentration in the exit gas is higher by 4 percentage points, but its CO concentration is lower by 2.5 percentage points than the concentric injection case. The syngas heating value (listed in Table 5.11) for the separate injection is 5.5 MJ/kg and is 20% lower than the concentric injection (7.5 MJ/kg).

5.4.2.2 Instantaneous Gasification Results

Similar to the concentric coal-oxidant case, a simulation case using the instantaneous gasification model is conducted for the four separate injection configuration. The temperature distribution given in Figure 5.38 shows that the hot region occurs in the area near the injectors, which is different from the case using the finite-rate model where the hot region occurs near the wall away from the injectors. As mentioned earlier, this is due to the instantaneously conversion of carbon into gas at the inlets. The carbon can instantaneously react with other gases without having to wait for the evaporation and devolatilization process to occur as modeled in the finite-rate model.

Downstream of the impingement location, the water droplets deviate from the gas flow path and is shown in Figure 5.39. Again, the result of droplet tracks shows that the droplets spread broader but are not severely bounced around, as speculated, at the intersection where the jets meet, and majority of the droplets passes through the jet impingement section and hit the wall as the finite rate case. This implies that the results of the finite rate are largely acceptable even though the particle collision model is not implemented.

Table 5.11 Flow mass weighted average exit gas temperature and compositions for both 2 concentric and 4 separate injections cases.

	Concentric injection	Separate injection
	Finite-rate	Finite-rate
T (K)	1329	1182
Mole fraction:		
CO	23.1%	19.6%
H_2	17.3%	21.4%
CO_2	24.1%	30.0%
VM	0.0%	0.0%
H_2O	31.7%	27.0%
C_6H_6	2.3%	0.6%
N_2	1.5%	1.4%
C	0.0%	0.0%
HHV at 25°C (MJ/kg)	7.5	5.5

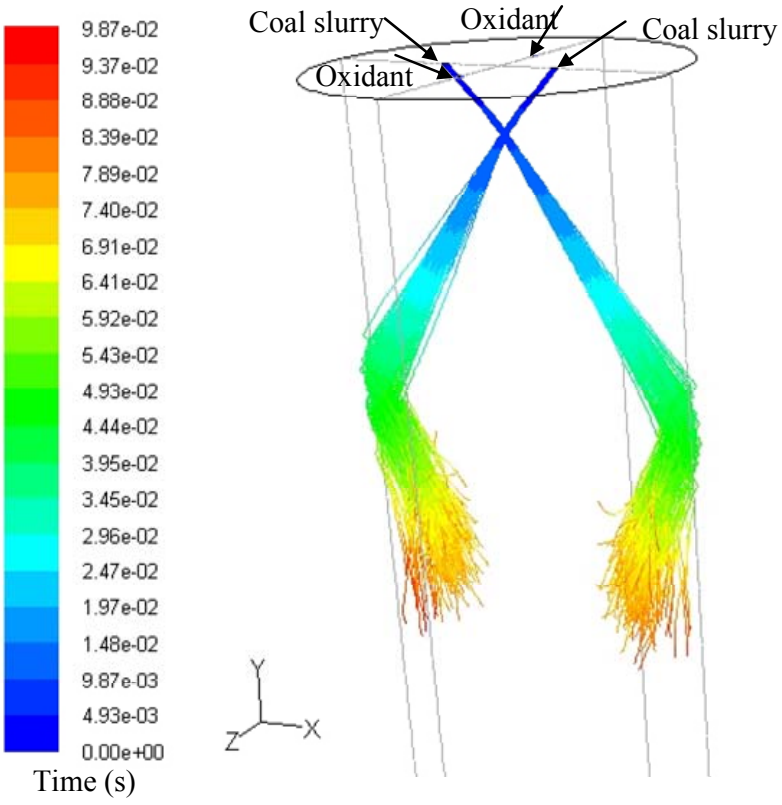

Figure 5.36 Coal particle tracks for four separate coal slurry and oxidant injections using finite rate reaction. (Note: Particle collision model can not be implemented.)

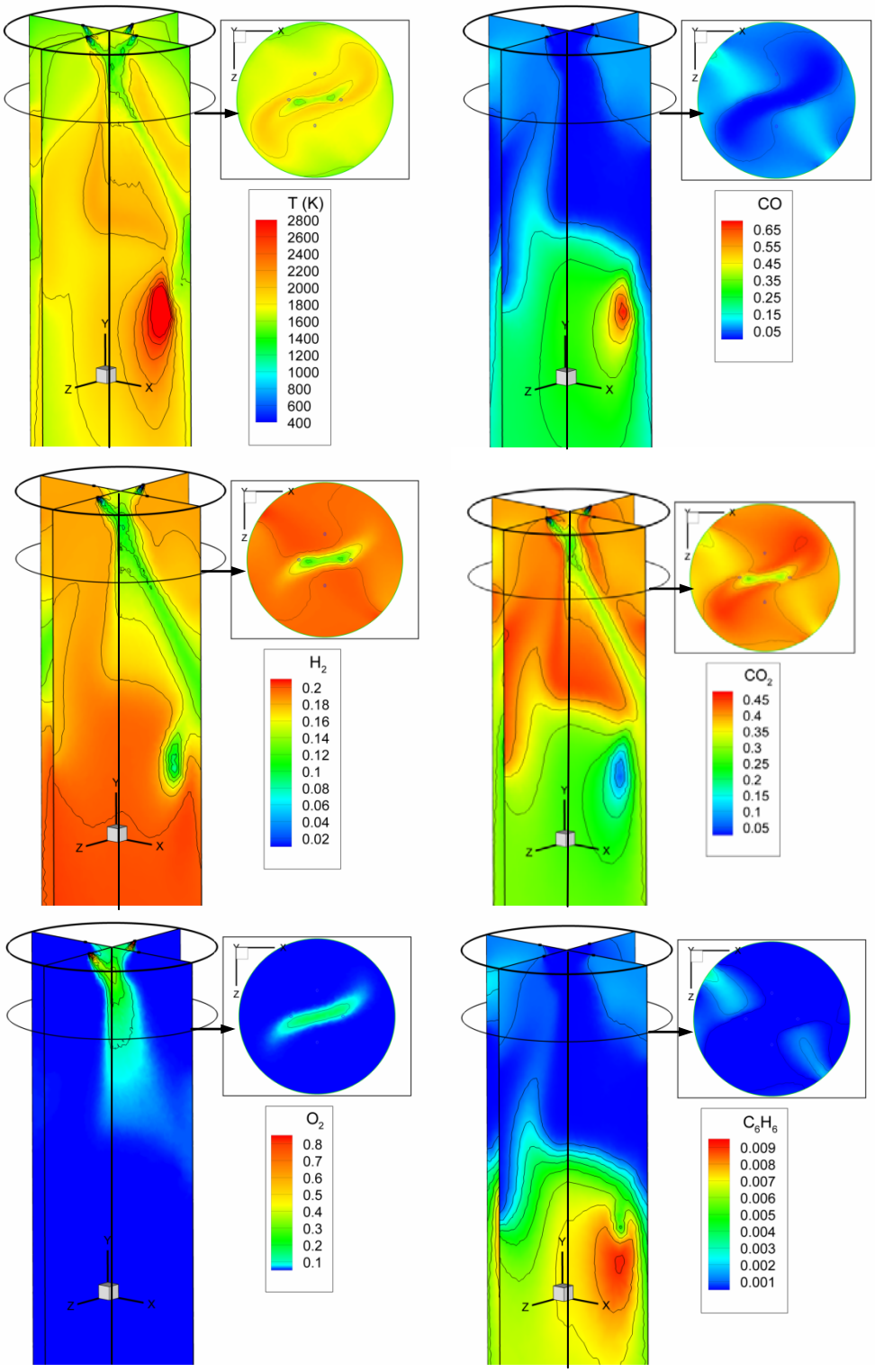

Figure 5.37 Temperature and species mole fraction distributions on two perpendicular vertical center-planes inside gasifier for separate coal-oxygen injection case with finite- rate reactions.

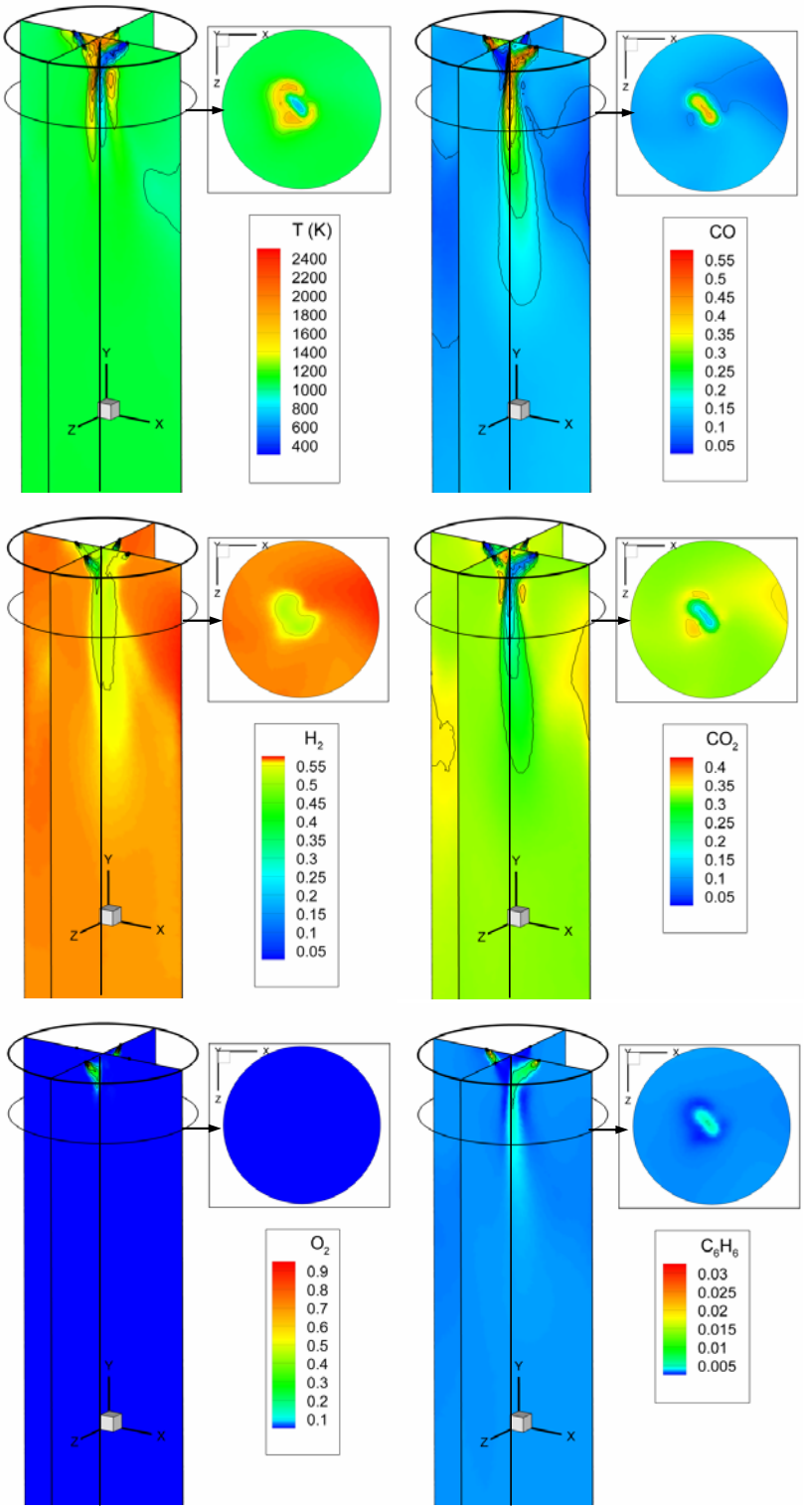

Figure 5.38 Temperature and species mole fraction distributions on two perpendicular vertical center-planes inside gasifier for separate coal-oxygen injection case modeled using the instantaneous gasification model implemented with particle collision model.

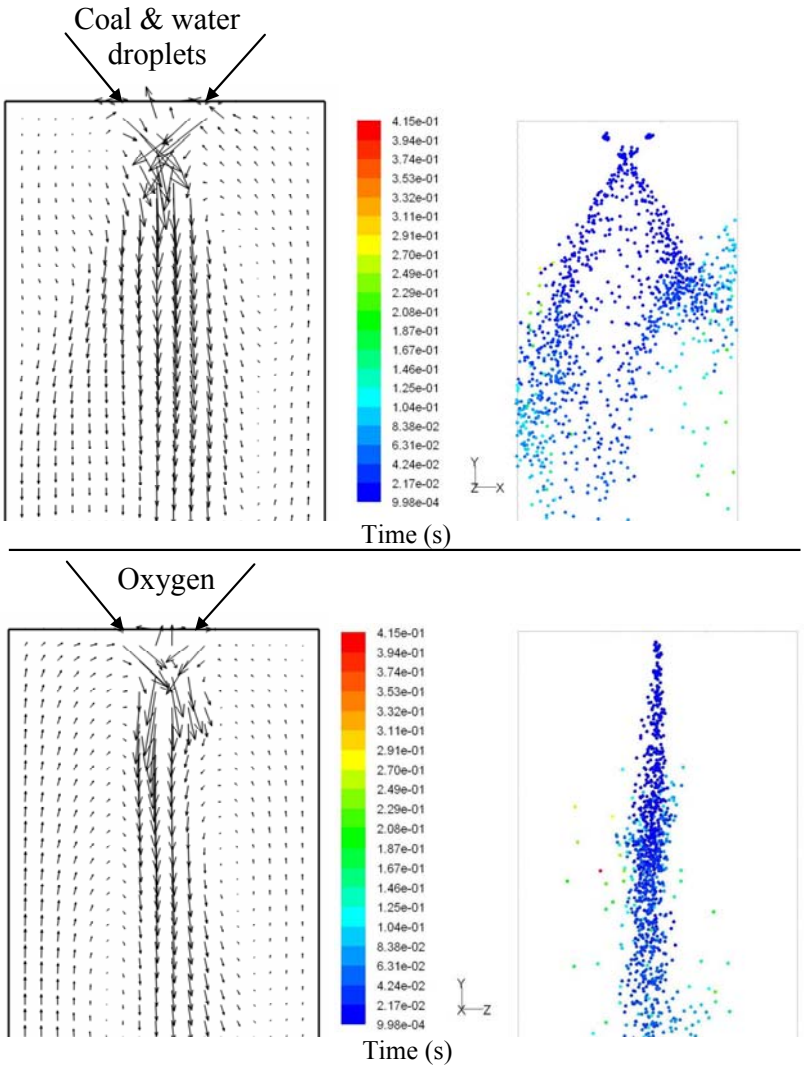

Figure 5.39 Velocity vectors and water droplet tracks for the four separate coal-oxygen injections case modeled using the instantaneous gasification model.

5.4.3 Conclusions of Top Fuel Injection Design

A computational study of two proposed coal-slurry fuel injection has been conducted in an entrained flow oxygen-blown gasifier. The limitation of the current computational model does not allow coal particle collision to be included in the heterogeneous finite-rate solid-gas reaction model. To examine the particle collision phenomenon, the instantaneous gasification model is implemented, in which the coal (consisting of carbon and volatiles) is injected as gas and the water is injected as droplets. The result of droplet tracks shows that the droplets are not bounced around, as speculated, at the intersection where the jets meet, and majority of the

droplets passes through the jet impingement section and hit the wall as the finite rate case. This implies that the results of the finite rate are acceptable even though the particle collision model is not implemented. The finite-rate result actually presents a worst-case scenario for predicting wall erosion. The particle tracks for both the 2 concentric and 4 separate injection configurations show that the coal particles hit the wall and can accelerate deterioration of the refractory bricks. The two concentric injection cases provide better fuel-oxidant mixing and higher heating value than the case using four separate injections

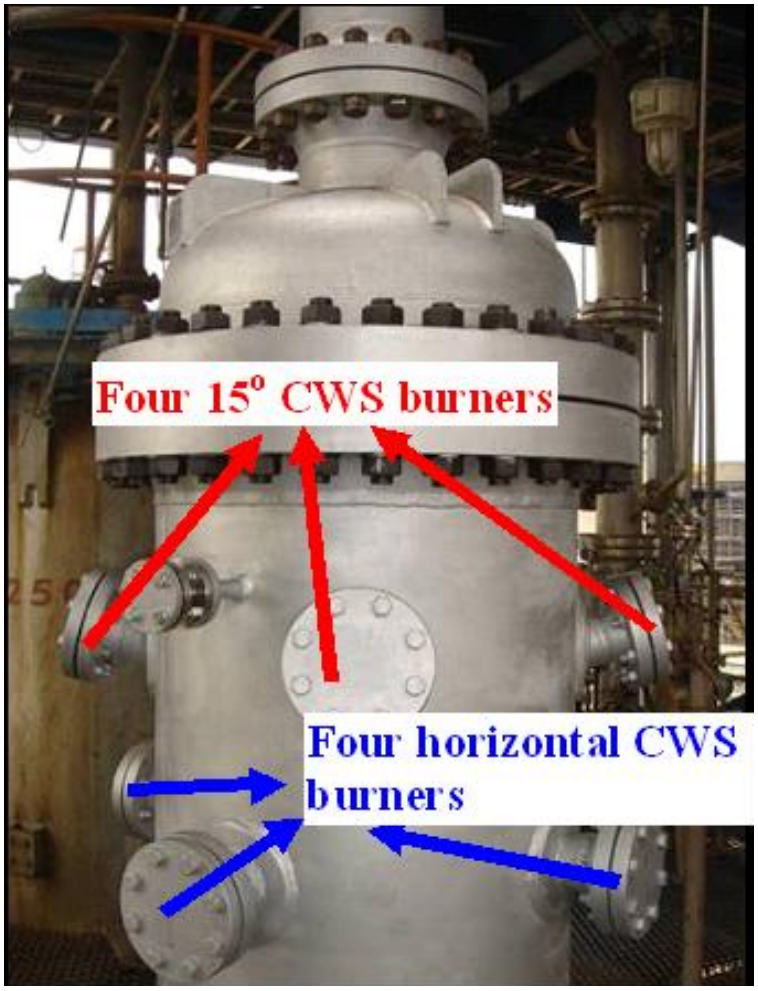

Figure 5.40 The top-loaded injectors in the ITRI experimental gasifier facility.

CHAPTER SIX
CONCLUSIONS

6.1 Summary

A comprehensive modeling and numerical investigation of entrained-flow coal gasifier have been conducted. The study begins with parametric study of effects of various models which are involved in the numerical simulation, such as turbulence and devolatilization models. Findings from parametric study are then applied to the investigation of finite-rate model vs. instantaneous gasification model. The parametric study is concluded with investigation of actually gasifier operation parameters, such as dry-fed vs. wet-fed, oxygen-blown vs. air-blown, and fuel distributions. A collaborative study has been conducted with the Industrial Technology Research Institute (ITRI) of Taiwan to help with its design and modifications of a demonstration coal gasifier. In return, ITRI's experimental data and operating experience are shared with the University of New Orleans.

6.2 Conclusions

6.2.1 Effect of Turbulence and Devolatilization Models on Gasification Simulation

Turbulence models significantly affect the simulated results. Among five turbulence models tested, the standard k-ε and the RSM models give consistent results. The time scale for employing stochastic time tracking of particles affects simulated result. Caution has to be exerted to select the appropriate time constant value. In this study, the time constant value of 0.015 and 0.00015 produce consistent results.

Among four devolatilization models, the Kobayashi model produces slower devolatilization rate than the other models. The constant rate model produces the fastest devolatilization rate. The single rate model and the chemical percolation model produces moderate and consistent devolatilization rate. Slower devolatilization rate produces lower H_2, but higher exit gas temperature, CO, and CO_2, and hence both the heating value and gasification efficiency are lower.

Usually smaller particles have larger surface/volume ratio and react more quickly than larger particles. However, when the particle size increases from 100 μm to 200 μm, it is discovered that larger particles possess higher inertia after injection. The higher inertia produces

higher slip velocity which increases higher convective transport and hence higher reaction rate. High inertia can also propel the particles to cross the gas streamlines and increase particle-gas mixing which results in enhanced reaction rate. When the inertia continue increases as particle size increases, the injection jet impinges on the opposite jet and results in strong recirculation zones which can trap the particles and increase the residence time. Using the results of parametric study in 2-D cases, appropriate models are selected for 3-D simulation to gain more confidence of the 3-D results.

6.2.2 Comparison Between Finite-Rate Model and Instantaneous Gasification Model

The instantaneous gasification model over-predicts the reaction rates. Gas temperature and species distributions indicate that reactions in the instantaneous gasification model occur very fast and finish very quickly. Its carbon conversion is 100%. Meanwhile, the reaction in the finite-rate model, which involves gas-solid reactions, occurs slower with some unburned chars and C_2H_2 at the exit. Varying the coal particle size of the finite-rate model shows that the syngas heating value of smaller particle size is closer to that of the instantaneous gasification model. The overall result reveals that the instantaneous gasification approach can provide an overall evaluation of relative changes of gasifier performance in terms of temperature, heating value, and gasification efficiency corresponding to parametric variations, but not adequately capture the local gasification process predicted by the finite rate model in most part of the gasifier

6.2.3 Parametric Study of Two-Stage Entrained-Flow Gasifier

For a two-stage entrained-flow gasifier with coal-slurry feed, the highest temperature (2400 K) occurs in the first stage. The dominant reaction in the first stage is the intense char combustion ($C + ½\ O_2 \rightarrow CO$ and $CO + ½\ O_2 \rightarrow CO_2$) in the first stage and gasification reactions (mainly char-CO_2 gasification, $C + ½\ CO_2 \rightarrow CO$) in the second stage. Char gasification is enhanced in the second stage with the injection of the remaining coal. Char is gasified with CO_2 produced in the first stage through reaction $C + CO_2 \rightarrow CO$ and with H_2O through reaction $C + H_2O \rightarrow CO + H_2$.

Effects of Coal Mixture (Slurry versus Dry)

The temperature in the first stage for the dry-fed case is approximately 3200 K, which is 800 K higher than that of the slurry-fed case. Unlike the slurry-fed case, the dry-fed case does not have a lot of H_2O to absorb the heat released by the char combustion, nor does much water react with char through the char-H_2O gasification. This higher gas temperature means that the refractory walls in the first stage will experience higher thermal loading than that in the coal slurry operation. The syngas high heating value of the dry coal case is also higher than that of the coal slurry case, 9.45 MJ/kg compared to 8.24 MJ/kg. However, the higher syngas temperature of the dry coal case means that it will have lower efficiency when it is put through the gas clean-up system downstream of the gasifier. A lot of energy will be downgraded via waste heat exchanger when the syngas is cooled down to the temperature acceptable for the gas clean-up system operation

Effects of Fuel Distribution between Two Stages

Reducing the fuel feed in the first stage results in higher gas temperature in the first stage. This is due to higher O_2/char ratio in the first stage, which causes more char to burn. One-stage operation yields higher H_2, CO and CH_4 combined than if two-stage operation is used, but with a lower syngas heating value. High heating value (HHV) of syngas for the one-stage operation is 7.68 MJ/kg, compared to 8.24 MJ/kg for two-stage operation with 72%-25% fuel distribution and 9.03 MJ/kg for two-stage operation with 50%-50% fuel distribution. This is due to the lower carbon conversion efficiency of one-stage operation (94.8%) compared to the other two cases (99.4% for 75%-25% fuel distribution and 98.3% for 50%-50% fuel distribution). The exit syngas of one-stage operation contains the most unreacted char, thus, combined with its high temperature, it has the lowest heating value.

Effects of Oxidant (Oxygen-Blown vs. Air-Blown)

Gas temperature inside the gasifier for the air-blown case is lower than that of the oxygen-blown gasifier due to the abundant presence of N_2. Carbon conversion efficiency of the air-blown case is 77.3%, which is much lower than that of the oxygen-blown case (99.4%). The syngas heating value for the air-blown case is 4.40 MJ/kg, which is almost half of the heating value of the oxygen-blown case (8.24 MJ/kg). To give a fair comparison, N_2 are removed from

syngas for both the air-blown and the oxygen-blown cases. The syngas heating value of the air-blown case is 7.26 MJ/kg which is still lower by roughly 1 MJ/kg than that of the oxygen-blown case (8.25 MJ/kg).

6.2.4 Part-Load Simulations of an Industrial Gasifier

Instantaneous gasification model is employed to investigate the part-load gasification process in an industrial gasifier operated by ITRI. It is found that that spraying water near the exit of the gasifier is not an effective approach to produce H_2 because the water shift process $CO + H_2O(g) \rightarrow CO_2 + H_2$, is likely to take place by converting CO (a good fuel) to CO_2 and H_2. The production of CO_2 during water shift process reduces the fuel heating value. Rather, it is more efficient to produce H_2 from the gasification reaction $C + H_2O \rightarrow CO + H_2$, in which no CO_2 is produced. If more H_2 is needed as the end product, it is recommended that steam be injected near the feedstock injection ports when plenty carbon is available and temperature is high. The steam can be generated from waste heat without consuming the gas flow energy. Spraying water will take energy away from the gas flow and reduce efficiency. Furthermore, with reduced temperature, the water shift reaction is more likely to take place than the more effective gasification reaction.

Comparison between the simulated and the part-load experimental data shows discrepancies. The CFD simulation usually overpredicts the carbon conversion efficiency and gasification performance. This could be attributed to the eddy-dissipation reaction rate model, which seems to produce faster than the actual reaction rates in this study. The simulation also overpredicts H_2 but underpredicts CO, possibly caused by injecting more water than the unknown actual amounts. The discrepancy in temperature comparison could be contributed by the uncertainty of thermocouple measurement location and the extremely large temperature gradients surrounding the measurement locations.

Employing fuel injection through a single injector unexpectedly performs better than applying three injectors. The results indicate the injection velocity speed and momentum strength of each injector, rather than the total momentum, could be more influential in affecting the gasification efficiency.

6.2.5 Effect of Slag Tap Size on Gasification Performance and Heat Losses in a Quench-Type Coal Gasifier

Operation of a quench-type coal gasifier has frequently encountered the problem of clogged slag tap, especially for smaller gasifier. One possible means to avoid this problem is by widening the slag tap opening. Instantaneous gasification model is employed to investigate the effect of slag tap size on gasification process in the ITRI gasifier. The results show that the gas in the quenching section is almost stagnant. Opening up the slag tap only slightly increases flow motion in the quenching section. Temperature in the upper half of quenching section increases several hundred degrees, but it maintains the same in the lower half portion of the quenching section. This implies that radiation is the major heat transfer mode between the cold water bath and hot gas in the gasifier. Opening the slag tap increases shape factor and increases heat loss to the water bath. The overall gasification performance and syngas fuel heating values are downgraded approximately 10% when the slag tap opening widens from 2-inch to 6-inch in diameter. Unburned volatile fraction also increases as the slag tap widens. There is a concern that the increased unburned volatile could be quenched and condensed into tar in the cooler downstream of the gasifier during the cold-stream clean up process. Changing the injection direction from horizontal to 15 degrees downward does not make a noticeable difference to the gas temperature and gasification performance. The benefit of opening the slap tap wider by allowing slag to move successfully without clogging is compromised by increased heat losses, reduced gasification performance, downgraded syngas heating value, and increased unburned volatiles.

6.2.6 Investigation of Heat Transfer and Gasification of Two Fuel Injectors

The two different fuel injector designs (conical tip and blunt tip) give very different temperature and species distributions inside the gasifier. When conical tip injectors are used, the highest temperature inside the gasifier occurs at the center of the gasifier; whereas, when blunt tip injectors are used, it occurs near the wall. Gasifier with conical tip injectors produces high H_2 and low CO; whereas gasifier with blunt tip injectors produces both rich H_2 and CO. There is a potential of flash back combustion in the nozzle at the tip of the conical injector due to its premixing feature of fuel and oxidant in the nozzle. The highest temperatures on both injectors are the same, around 1600 K. However, the highest temperature on the conical-tip injector is

concentrated at one location with an extended region of 30 mm between 1600 K and 1100 K; whereas on the blunt-tip injector, the maximum temperature distribution is scattered and the hot region (1600K - 1100K) only extends about 3 mm. Therefore, the blunt-tip injector is less likely to fail. Experimental results support simulated results and has demonstrated a short life for the conical tip fuel injector and an extended life for the blunt-tip fuel injector. However, eventually the blunt-tip fuel injector did burn out after extended service when the refractory brick was worn away and the fuel injector tip protruded from the wall without any protection.

6.2.7 Investigation of Top Fuel Injection Design in a Coal Gasifier

The limitation of the current computational model does not allow coal particle collision to be included in the heterogeneous finite-rate solid-gas reaction model. To examine the particle collision phenomenon, the instantaneous gasification model is implemented, in which the coal (consisting of carbon and volatiles) is injected as gas and the water is injected as droplets. The result of droplet tracks shows that the droplets are not bounced around, as speculated, at the intersection where the jets meet, and majority of the droplets passes through the jet impingement section and hit the wall as the finite rate case. This implies that the results of the finite rate are acceptable even though the particle collision model is not implemented. The finite-rate result actually presents a worst-case scenario for predicting wall erosion. The particle tracks for both the 2 concentric and 4 separate injection configurations show that the coal particles hit the wall and can accelerate deterioration of the refractory bricks. The two concentric injection cases provide better fuel-oxidant mixing and higher heating value than the case using four separate injections.

REFERENCES

Ajilkumar, A., Sundararajan, T., and Shet, U.S.P., "Gasification of Indian Coal in a Tubular Coal Gasifier", Proceedings of 2007 ASME-JSME Thermal Engineering Summer Heat Transfer Conference, Vancouver, Canada, 2007.

Badzioch, S., and Hawksley, P.G.W., "Kinetics of Thermal Decomposition of Pulverized Coal Particles", Industrial & Engineering Chemistry Process Design and Development, Vol. 9, 521-530, 1970

Baum, M.M. and Street, P.J., "Predicting the Combustion Behavior of Coal Particle", Combustion Science and Technology, Vol. 3, 231-243, 1971.

Beck, N.C., and Hayhurst, A.N., "The Early Stages of the Combustion of Pulverized Coal at High Temperatures I: The Kinetics of Devolatilization", Combustion and Flame, Vol. 79, 47-74, 1990.

Bhatia, K., and Perlmutter, D.D., "A Random Pore Model for Fluid-Solid Reactions I: Isothermal Kinetic Control", AIChE Journal, Vol. 26, 379-386, 1980.

Bockelie, M.J., Denison ,M.K., Chen, Z., Linjewile, T., Senior, C.L., and Sarofim, A.F., "CFD Modeling For Entrained Flow Gasifiers", Proceedings of the Gasification Technologies Conference 2002, San Francisco, CA, 2002(a).

Bockelie, M.J., Denison, M.K., Chen, Z., Linjewile, T., Senior, C.L., and Sarofim, A.F., "CFD Modeling For Entrained Flow Gasifiers in Vision 21 Systems", Proceedings of the Pittsburgh Coal Conference 2002, Pittsburgh, PA, 2002(b).

Bockelie, M.J., Denison, M.K., Chen, Z., Linjewile, T., Senior, C.L., and Sarofim, A.F., "Using Models to Select Operating Conditions for Gasifiers", Proceedings of the Pittsburgh Coal Conference 2003, Pittsburgh, PA, 2003.

Bouma, P.H., de Goey, L.P.H., Tummers, M.J., and Kiel, J.H.A., "Numerical Modeling of an Entrained-Flow Gasification Simulator", Proceedings of 1999 ASME Computational Technologies for Fluid/Thermal/Structural/Chemical Systems With Industrial Applications, 1999.

Boysan, F., Weber, R., Swithenbank, J., "Mathematical Modelling of an Entrained Coal Gasifier", 1983 International Gas Research Conference, 1983.

Brewester, B.S., Baxter, L.L., and Smoot, L.D., "Treatment of Coal Devolatilization in Comprehensive Combustion Modeling", Energy & Fuels, Vol. 2, 362-370, 1988.

Celik, I., and Chattree, M., "Numerical Simulation of Coal Gasification in an Entrained-Flow Reactor", Proceedings of 1990 ASME International Computers in Engineering Conference & Exposition, 1990.

Chapyak, E.J., Blewett, P.J., and Cagliostro, D.J., "Verification Studies of Entrained-Flow Gasification and Combustion Systems with the Simmer-II Code", 10th IMACS World Congress on System Simulation and Scientific Computation, 1983.

Chen, C., Miyoshi, T., Kamiya, H., Horio, M., and Kojima, T., "On the Scaling-up of a Two-Stage Air Blown Entrained Flow Coal Gasifier", The Canadian Journal of Chemical Engineering, Vol. **77**, 745-750, 1999.

Chen, C., Horio, M., and Kojima, T., "Numerical Simulation of Entrained Flow Coal Gasifiers. Part I: Modeling of Coal Gasification in an Entrained Flow Gasifier", Chemical Engineering Science, Vol. 55, 3861-3874, 2000(a).

Chen C., Horio M., and Kojima T., "Numerical Simulation of Entrained Flow Coal Gasifiers. Part II: Effects of Operating Conditions on Gasifier Performance", Chemical Engineering Science, Vol. 55, 3875-3883, 2000(b).

Choi, Y.C., Li, X.Y., Park, T.J., Kim, J.H., and Lee, J.G., "Numerical Study on the Coal Gasification Characteristics in an Entrained Flow Coal Gasifier", Fuel, Vol. 80, 2193-2201, 2001.

Choi, Y.C., Li, X.Y., Park, T.J., Kim, J.H., and Lee, J.G., "Numerical Analysis of the Flow Field Inside an Entrained-Flow Gasifier", Korean Journal of Chemical Engineering, Vol. 18, 376-381, 2001.

Choudhury, D., Introduction to the Renormalization Group Method and Turbulence Modeling, Technical Memorandum, TM-107, Fluent Inc., 1993.

Eaton, A.M., Smoot, L.D., Hill, S.C., and Eatough, C.N., "Components, formulations, solutions, evaluation, and application of comprehensive combustion models", Progress in Energy and Combustion Science, Vol. 25, 387-436, 1999.

Essenhigh, R.T., "Combustion and Flame Propagation in Coal Systems: A Review", Sixteenth Symposium (International) on Combustion, 1979.

Essenhigh, R.T., "Rate Equations for the Carbon-Oxygen Reaction: An Evaluation of the Langmuir Adsorption Isotherm at Atmospheric Pressure", Energy & Fuels, Vol. 5, 41-46, 1991.

Faeth, G.M., "Mixing, Transport and Combustion in Sprays", Progress in Energy and Combustion Science, Vol. 13, 293-345, 1987.

Faeth, G.M., "Evaporation and Combustion of Sprays", Progress in Energy and Combustion Science, Vol. 9, 1-76, 1983.

Fatemi, M., Scaroni, A.W., Lee, C.W., and Jenkins, R.G., "Effect of Pressure on Pyrolysis of a Sub-Bituminous Coal in an Entrained-Flow Reactor", American Chemical Society Division of Fuel Chemistry, 32, 117-124, 1987.

Field, M.A., "Rate of Combustion of Size-Graded Fractions of Char from a Low-Rank Coal Between 1200 K and 2000 K", Combustion and Flame, Vol. 13, 237-252, 1969.

Fletcher, T.H., "A Two-Dimensional Model for Coal Gasification and Combustion", PHD Dissertation, Birgham Young University, 1983.

Fletcher, T.H., Kerstein, A.R., Pugmire, R.J., and Grant, D.M., "Chemical percolation model for devolatilization: 2. Temperature and heating rate effects on product yields", Energy and Fuels, Vol. 4, 54-60, 1990.

Fletcher, T.H., Kerstein, A.R., Pugmire, R.J., and Grant, D.M., "Chemical percolation model for devolatilization: 3. Direct use of carbon-13 NMR data to predict effects of coal type", Energy and Fuels, Vol. 16, 414-431, 1992.

Fletcher, T.H., Smith, P.J., and Smoot, L.D., "Evaluation of a 2-D Coal Combustion Model", Proceedings of 1984 Spring Meeting of the Western States Section of the Combustion Institute, Boulder, CO, 1984.

Gale, T.K., Fletcher, T.H., and Bartholomew, C.H., "Effects of Pyrolysis Conditions on Internal Surface Areas and Densities of Coal Chars Prepared at High Heating Rates in Reactive and Nonreactive Atmospheres", Energy & Fuels, Vol. 9, 513-524, 1995.

Govind, R., and Shah, J., "Modeling and Simulation of an Entrained-Flow Flow Coal Gasifier", American Institute of Chemical Engineering Journal, Vol. 30, 79-91, 1984.

Grant, D.M., Pugmire, R.J., Fletcher, T.H., and Kerstein, A.R., "Chemical model of coal devolatilization using percolation lattice statistics", Energy and Fuels, Vol. 3, 175-186, 1989.

Hodge, E., Roberts, D., Harris, D., and Stubington, J., "The Char-CO_2 Reaction at High Temperatures and Pressures", Proceedings of the 23rd Pittsburgh Coal Conference, Pittsburgh, PA, 2006.

Holt, N., "Gasification Process Selection – Trade-offs and Ironies", Proceedings of the Gasification Technology Conference 2004, Washington, DC, 2004.

Hurt, R., Sun, J., and Lunden, M., "A Kinetic Model of Carbon Burnout in Pulverized Coal Combustion", Combustion and Flame, Vol. 113, 181-197, 1998.

Hurt, R.H., Calo, J.M., "Semi-Global Intrinsic Kinetics for Char Combustion Modeling", Combustion and Flame, Vol. 125, 1138-1149, 2001.

Hurt, R., and Mitchell, R.E., "Unified High-Temperature Char Combustion Kinetics for a Suite of Coals of Various Rank", Twenty-Fourth Symposium (International) on Combustion, 1243-1250, 1992.

Hsu, H. W., Shieh, C.L., and Lo, M. C., "Application and Outlook for Clean Coal Technologies in Taiwan," Clean Energy Technology Division, Energy & Resource Laboratories, Industrial Technology Research Institute, Taiwan, Proceedings of the 20th Pittsburgh Coal Conference, 2003.

Jaeger, H., "Outlook for Coal-Based IGCC Power Plant", Gas Turbine World, January-February, 2007.

Jones, W.P., and Lindstedt, R.P., "Global Reaction Schemes for Hydrocarbon Combustion, Combustion and Flame", Vol. 73, 233, 1998.

Kajitani, S., Hara, S., and Matsuda, H., "Gasification Rate Analysis of Coal Char With a Pressurized Drop Tube Furnace", Fuel, Vol. 81, 539-546, 2002.

Kobayashi, H., Howard, J.B., and Sarofim, A.F., "Coal Devolatilization at High Temperatures", 16th Symposium (International) on Combustion, 411-425, 1976.

Kumar, M., Zhang, C., Monaghan, R.F.D., Singer, S.L., Ghoniem, A.F., "CFD Simulation of Entrained Flow Gasification with Improved Devolatilization and Char Consumption Submodels", Proceedings of the ASME 2009 International Mechanical Engineering Congress & Exposition, Lake Buena Vista, FL, 2009.

Kuo, K.K., Principles of Combustion, John Wiley and Sons, New York, 1986.

Lasa, H., and Mok, L.K., "Entrained Coal Gasifiers: Modeling the Particle Acceleration", The Canadian Journal of Chemical Engineering, Vol. 59, 658-661, 1981.

Liu, G., Tate, A.G., Bryant, G.W., and Wall, T.F., "Mathematical Modeling of Coal Char Reactivity With CO_2 at High Pressures and Temperatures", Fuel, Vol. 79, 1145-1154, 2000.

Liu, H., Chen, C., Kojima, T., "Theoretical Simulation of Entrained-Flow IGCC Gasifers: Effect of Mixture Fraction Fluctuation on Reaction Owing to Turbulent Flow", Energy & Fuels, Vol. 16, 1280-1286, 2002.

Matsushita, Y., Goto, A., Morozumi, Y., Aoki, H., and Miura, T., "Numerical Analysis of 2 t/day Entrained-Flow Coal Gasifier – Effect of the Shape of Gasifier", Proceedings of 13th International Heat Transfer Conference, 2006.

Mayers, M.A., "The Rate of Reduction of Carbon Dioxide by Graphite", American Chemical Society Journal, 56, 70-76, 1934.

Mayers, M.A., “The Rate of Oxidation of Graphite by Steam”, American Chemical Society Journal, Vol. 56, 1879-1881, 1934.

Manton, N., Cor, J., Mul, G., Eckstorm, D., Malhotra, R., and Niksa, S., "Impact of Pressure Variations on Coal Devolatilization Products. 2. Detailed Product Distributions from 1.0 MPa", Energy & Fuels, Vol. 18, 520-530, 2004.

Menter, F., “Zonal Two Equation Model for Aerodynamic Flows,” AIAA Paper 93-2906, 1993

Mitchell, R.E., and Akanetuk, A.E.J., "The Impact of Fragmentation on Char Conversion During Pulverized Coal Combustion", Twenty-Sixth Symposium (International) on Combustion, 3317-3144, 1996.

Naredi, P., and Pisupati, S.V., "Numerical Modeling of the Effect of Aerodynamic on NO_x Emissions and Char Burnout for Combustion of Coal in O_2/CO_2", Proceedings of the 23rd International Pittsburgh Coal Conference 2006, Pittsburgh, PA, 2006.

Ni, Q., and Williams, A., "A Simulation Study on the Performance of an Entrained-Flow Coal Gasifier", Fuel, Vol. 74, 102-110, 1995.

Niksa, S., and Lau, C., "Global Rates of Devolatilization for Various Coal Types", Combustion and Flame, Vol. 94, 293-307, 1993.

Oka, S.N., Fluidized Bed Combustion, Marcel Dekker, Inc., 2004.

Pantankar, S.V., Numerical Heat Transfer and Fluid Flow, Taylor & Francis, 1980.

Pillai, K.K., “Influence of Coal Type on Devolatilization and Combustion in Fluidized Beds”, Journal of the Institute of Energy, Vol. 54, 1981.

Rabbitts, M.C., Van Den Houten, G.J., Glasser, D., and Bryson, A.W., "Modelling of Residence Time Distribution in an Entrained Flow Coal Gasifier Reactor", ChemSA, Vol. 9, 220-223, 1983.

Rezaiyan, J., and Cheremisinoff, N.P., Gasification Techonologies, Taylor & Francis, 2005.

Seebauer, V., Petek, J., and Staudinger, G., " Effects of Particle Size, Heating Rate and Pressure on Measurement of Pyrolysis Kinetics by Thermogravimetric Analysis", Fuel, Vol. 76, 1277-1282, 1997.

Serio, M.A., Hamblen, D.G., Markham, J.R., and Solomon, P.R., "Kinetics of Volatile Product Evolution in Coal Pyrolysis: Experiment and Theory", Energy & Fuels, Vol. 1, 138-152, 1987.

Silaen, A., Wang, T., "Effects of Fuel Injection Angles on Performance of A Two-Stage Coal Gasifier", Proceedings of the 23rd Pittsburgh International Coal Conference, Pittsburgh, PA, 2006.

Silaen, A., Wang, T., "Effects of Turbulence and Devolatilization Models on Gasification Simulation", Proceedings of the 35th Pittsburgh International Coal Conference, Pittsburgh, PA, 2008.

Singh, C.P.P., and Saraf, D.N., "Simulation of High-Temperature Water-Gas Shift Reactors", Industrial and Engineering Chemistry Process Design and Development, Vol. 16, 313-319, 1977.

Smith, I.W., "The Intrinsic Reactivity of Carbons to Oxygen", Fuel, Vol. 57, 409-414, 1978.

Smith, I.W., "The Combustion Rate of Coal Chars: A Review", 19th Symposium (International) on Combustion, 1045-1065, 1982.

Smith, K.L, Smoot, L.D., Fletcher, T.H., and Pugmire, R.J., Structure and Reaction Process of Coal, Plenum Press, 1994.

Smith, P.J., Fletcher, T.H., and Smooth, L.D., "Model for Pulverized Coal-Fired Reactors", Eighteenth Symposium (International) on Combustion, 1981.

Smoot, L.D., "Pulverized Coal Diffusion Flames: A Perspective Through Modeling", Eighteenth Symposium (International) on Combustion, 1981.

Solomon, P.R., Hamblen, D.G., Carangelo, R.M., Serio, M.A., and Deshpande, G.V., "General Model of Devolatilization", Energy & Fuels, Vol. 2, 405-422, 1988.

Souza-Santos, M.L., Solid Fuels Combustion and Gasification – Modeling, Simulation, and Equipment Operation, Marcel Dekker, Inc., 1996.

Sun, C.L., Xiong, Y.Q., Liu, Q.X., and Zhang, M.Y., "Thermogravimetric Study of the Pyrolysis of Two Chinese Coals Under Pressure", Fuel, Vol. 76, 639-644, 1997.

Tomeczek, J., Coal Combustion, Krieger Publishing Company, 1994.

Tominaga, H., Yamashita, T., Ando, T., and Asahiro, N., "Simulator Development of Entrained-Flow Coal Gasifiers at High Temperature and High Pressure Atmosphere", IFRF Combustion Journal, 2000.

Turns, S.R., An Introduction to Combustion, McGraw Hill, 2000.

Tyrkiel, E., and Cudnok, R., "Computer Modeling of Coal Combustion and/or Gasification in an Entrained-Bed System", Specialist Meeting on Coal Fired MHD Power Generation, Sydney, 1981.

Vicente, W., Ochoa, S., Aguillon, J., and Barrios, E., "An Eulerian Model for the Simulation of an Entrained Flow Coal Gasifier", Applied Thermal Engineering, Vol. 23, 1993-2008, 2003.

Ubhayakar, S.K., Stickler, D.B., Von Rosenberg, C.W. Jr., and Gannon, R.E., "Rapid Devolatilization of Pulverized Coal in Hot Combustion Gases", Sixteenth Symposium (International) on Combustion, 1979.

Wabash River Energy Ltd., "Wabash River Coal Gasification Report Repowering Project: Final Report", 2000.

Wall, T.F., Liu, G., Wu. H., Roberts, D.G., Benfell, K.E., Gupta, S., Lucas, J.A, and Harris, D.J., "The Effects of Pressure on Coal Reactions During Pulverized Coal Combustion and Gasification", Progress in Energy and Combustion Science, Vol. 28, 405-433, 2002.

Wang, T., Silaen, A., Hsu, HW., and Lo, MC., "Part-Load Simulations and Experiments of a Small Coal Gasifier", Proceedings of the 23rd Pittsburgh International Coal Conference, Pittsburgh, PA, 2006.

Wang, T., Silaen, A., Hsu, HW., and Shen, CH., "Effect of Slag Tap Size on Gasification Performance and Heat Losses in a Quench-Type Coal Gasifier", Proceedings of the 24th Pittsburgh International Coal Conference, South Africa, 2007.

Wang, T., Silaen, A., Hsu, HW., and Shen, CH., "Investigation of Heat Transfer and Gasification of Two Different Fuel Injectors in an Entrained-Flow Gasifier", Proceedings of the 24th Pittsburgh International Coal Conference, Pittsburgh, PA, 2008.

Watanabe, H., and Ichikawa, K., "Numerical Simulation of Coal Ash Particle Behavior in Entrained Flow Coal Gasifier", Proceedings of the 4th ASME-JSME Joint Fluids Engineering Conference, Honolulu, HI, 2003.

Watanabe, H., and Otaka, M., “Numerical Simulation of Coal Gasification in Entrained Flow Coal Gasifier”, Fuel, 85, 1935-1943, 2006.

Wen, C.Y., and Chaung, T.Z., “Entrainement Coal Gasification Modeling”, Industrial and Engineering Chemistry Process Design and Development, Vol. 18, 684-695, 1979.

Westbrook, C.K., and Dryer, F.L., "Simplified Reaction Mechanisms for the Oxidation of Hydrocarbon Fuels in Flames", Vol. 27, 31-43, 1981.

Wilcox, D.C., Turbulence Modeling for CFD, DCW Industries, Inc., La Canada, California., 1998.

Wildegger-Gaissmaier, A.E., and Agarwal, P.K., "Drying and Devolatilization of Large Coal Particles Under Combustion Conditions", Fuel, Vol. 69, 44-52, 1990.

Williams, A., Pourkashanian, M., Jones, J.M., and Skorupska, N., Combustion and Gasification of Coal, Taylor & Francis, 2000.

Wolfstein, M., "The Velocity and Temperature Distribution of One-Dimensional Flow with Turbulence Augmentation and Pressure Gradient", International Journal of Heat Mass Transfer, Vol, 12, 301-318, 1969.

Zeng, D., and Fletcher, T.H., "Effects of Pressure on Coal Pyrolysis and Char Morphology", Energy & Fuels, Vol. 19, 1828-1838, 2005.

APPENDIX

CALCULATING VOLATILE ENTHALPY

Moisture free proximate and ultimate analyses of Indonesian coal:

Table A.1 Moisture free proximate and ultimate analyses of Indonesian coal.

Proximate Analysis (MF), wt%		***Ultimate Analysis (MF), wt%***	
Volatile	51.29	C	73.32
Fixed Carbon (FC)	47.54	H	4.56
Ash	1.17	O	20.12
	100.00	N	0.72
		S	0.11
		Ash	1.17
			100.00

The moisture weight fraction of the coal is 8.25%. The heating value of the coal is 23.8 MJ/kg.

The proximate and ultimate analyses of Indonesian coal when moisture included is listed in Table A.2.

Table A.2 Proximate and ultimate analyses of Indonesian with moisture included.

Proximate Analysis, wt %		***Ultimate Analysis, wt %***	
Volatiles	47.06	Carbon	67.27
Fixed Carbon (FC	43.62	H	4.18
Moisture	8.25	O	18.46
Ash	1.07	N	0.67
	100.00	S	0.10
		Moisture	8.25
		Ash	1.07
			100.00

A.1 Volatile Composition

Calculate the weight percentage of each element in the volatiles using the moisture free proximate and ultimate analyses (Table A.1),

$$wt\%_{C,\,volatiles} = \frac{wt\%_{C}}{wt\%_{volatiles}} = \frac{wt\%_{C,\,ultimate} - wt\%_{FC,\,proximate}}{wt\%_{volatiles}} = \frac{73.32\% - 47.54\%}{51.29\%} = 50.26\%$$

$$wt\%_{H,\,volatiles} = \frac{wt\%_{H}}{wt\%_{volatiles}} = \frac{4.56\%}{51.29\%} = 8.89\%$$

$$wt\%_{O,\,volatiles} = \frac{wt\%_{O}}{wt\%_{volatiles}} = \frac{20.12\%}{51.29\%} = 39.23\%$$

$$wt\%_{N,\,volatiles} = \frac{wt\%_{N}}{wt\%_{volatiles}} = \frac{0.72\%}{51.29\%} = 1.40\%$$

$$wt\%_{S,\,volatiles} = \frac{wt\%_{S}}{wt\%_{volatiles}} = \frac{0.11\%}{51.29\%} = 0.22\%$$

The chemical formula of the volatiles is assumed to be in the form of $C_xH_yO_z$. The other elements, N and S, will be injected as gas, together with the oxidant through the inlet injections.

Weight percentages of C, H, and O in the volatiles after N and S have been removed are,

$$wt\%_{C\,in\,C_xH_yO_z} = \frac{wt\%_{C,\,volatiles}}{wt\%_{volatiles} - wt\%_{N,\,volatiles} - wt\%_{S,volatiles}} = \frac{50.26\%}{100\% - 1.40\% - 0.22\%} = 51.09\%$$

$$wt\%_{H\,in\,C_xH_yO_z} = \frac{wt\%_{H,\,volatiles}}{wt\%_{volatiles} - wt\%_{N,\,volatiles} - wt\%_{S,volatiles}} = \frac{8.89\%}{100\% - 1.40\% - 0.22\%} = 9.03\%$$

$$wt\%_{O\,in\,C_xH_yO_z} = \frac{wt\%_{O,\,volatiles}}{wt\%_{volatiles} - wt\%_{N,\,volatiles} - wt\%_{S,volatiles}} = \frac{39.23\%}{100\% - 1.40\% - 0.22\%} = 39.88\%$$

The volatile matters, $C_xH_yO_z$, are assumed to be composed of CO, H_2, and C_6H_6 (Tomeczek, 1994). The volatile matters are cracked into CO, H_2 and C_6H_6 according to the equation below,

$$C_xH_yO_z \rightarrow a\ CO + b\ H_2 + c\ C_6H_6$$

The coefficients a, b, and c are calculated by performing mass balance of the equation above.

Mass of each element in terms of the reaction coefficients are,

C: $m_C = (a + 6c) \times 12 = 12a + 72c$

H: $m_H = (2b + 6c) \times 1 = 2b + 6c$

O: $m_O = a \times 16 = 16a$

Assuming 1 kg of volatile, the actual mass of each element is calculated and is substituted into the equations above to determine the reaction coefficients.

$m_O = wt\%_{O \text{ in } CxHyOz} \times 1 \text{ kg} = 0.3988 \text{ kg}$

$\Rightarrow 16a = 0.3988 \Rightarrow a = 0.02493$

$m_C = wt\%_{C \text{ in } CxHyOz} \times 1 \text{ kg} = 0.5109 \text{ kg}$

$$\Rightarrow 12a + 72c = 0.5109 \Rightarrow c = \frac{0.5109 - 12(0.02493)}{72} = 0.002941$$

$m_H = wt\%_{H \text{ in } CxHyOz} \times 1 \text{ kg} = 0.0903 \text{ kg}$

$$\Rightarrow 2b + 6c = 0.0903 \Rightarrow b = \frac{0.0903 - 6(0.002941)}{2} = 0.03633$$

With the coefficients a, b, and c are known, the volatile matters split equation is rewritten as,

$$C_xH_yO_z \rightarrow 0.02493CO + 0.03633H_2 + 0.002941C_6H_6$$

Mass balance of each element is done to determine the values of x, y, and z.

$\Rightarrow x = 0.02493 + 6(0.002941) = 0.04258$

$\Rightarrow y = 2(0.03633) + 6(0.002941) = 0.09031$

$\Rightarrow z = 0.02493$

So, the volatile split equation becomes,

$$C_{0.04258}H_{0.09031}O_{0.02493} \rightarrow 0.02493\ CO + 0.03633\ H_2 + 0.002941\ C_6H_6$$

Normalizing the coefficients to have the volatile in CH_mO_n form yields,

$$CH_{2.121}O_{0.5855} \rightarrow 0.5855\ CO + 0.8532\ H_2 + 0.06907\ C_6H_6$$

The enthalpy of the volatile is not known and thus needs to be calculated. A correct enthalpy value of the volatile will ensure that energy is properly balanced in the volatile splitting reaction.

A.2 Volatile enthalpy

The steps taken to find the enthalpy of the volatile, $CH_{2.121}O_{0.5855}$, are as follow.

(a) Calculate the volatile's heating value.

The volatile's heating value is found by taking subtracting carbon's heating value from the coal's heating value, or as expressed below.

$$HV_{CH2.121O0.5855} = HV_{coal} - HV_C$$

where,

HV_{coal} = 5,690 kcal/kg of coal ≈ 23.8 MJ/kg of coal

$$HV_C = 393{,}546 \frac{\text{kJ}}{\text{kmole of C}} \times \frac{1\,\text{MJ}}{1000\,\text{kJ}} \times 0.03635 \frac{\text{kmole of C}}{\text{kg of coal}} = 14.31 \frac{\text{MJ}}{\text{kg of coal}}$$

Thus, the heating value of the volatiles is,

$$HV_{CH2.121O0.5855} = (23.8 - 14.31)\ \text{MJ/kg of coal} = 9.49\ \text{MJ/kg of coal}$$

Converting the volatile's heating value in terms of volatile's weight is,

$$HV_{CH2.121O0.5855} =$$

$$9.49 \frac{\text{MJ}}{\text{kg coal}} \times \frac{1\,\text{kg coal}}{0.4362\text{kmole volatiles}} = 20.50 \frac{\text{MJ}}{\text{kg volatiles}}$$

(b) Calculate volatile's enthalpy based on the volatile combustion reaction.

The chemical equation for the volatile combustion is

$$CH_{2.121}O_{0.5855} + 1.2378O_2 \rightarrow CO_2 + 1.061H_2O(g)$$

The equation of the volatile's heating value is expressed as,

$$HV_{CH_{2.121}O_{0.585}} = \left[\left(1 \times h_{f,CH_{2.121}O_{0.585}}\right) + \left(1.2378 \times h_{f,O_2}\right)\right] - \left[\left(1 \times h_{f,CO_2}\right) + \left(1.061 \times h_{f,H_2O(g)}\right)\right]$$

where,

$h_{f,CO2}$ = -393,546 kJ/kmole

$h_{f,H2O(g)}$ = -241,845 kJ/kmole

$h_{f,O2}$ = 0.

The equation is rearranged to give,

$$h_{f,CH_{2.121}O_{0.585}} = HV_{CH_{2.121}O_{0.585}} - \left(1.2378 \times h_{f,O_2}\right) + \left[\left(1 \times h_{f,CO_2}\right) + \left(1.061 \times h_{f,H_2O(g)}\right)\right]$$

Substituting the enthalpy values into the equation above gives,

$$h_{f,CH2.121O0.585} = 20.50x10^{3} - (1.2378 \times 0) + [1 \times (-393,546) + 1.061 \times (-241,845)]$$

$$h_{f,CH2.121O0.585} = -670,643 \text{ kJ/kg}$$

The enthalpy of the volatile ($CH_{2.121}O_{0.5855}$) is -670,643 kJ/kg.

VITA

Armin Silaen was born in Cairns, Australia, in 1979. He received his Bachelors degree in Mechanical Engineering from the University of New Orleans in 2002. He then continued to pursue Master's and Doctorate degrees also from the University of New Orleans. During the post-graduate program, he worked as a Research Assistant at the Energy Conversion and Conservation Center at the University of New Orleans under the supervision of Dr. Ting Wang. He received the Master's and Doctorate degrees in 2004 and 2010, respectively.